CENTRIFUGE MODELLING OF CONE PENETRATION TESTING IN COHESIONLESS SOILS

by

Lee Say Yong

A dissertation submitted for the degree of
Doctor of Philosophy at Cambridge University

Clare Hall
Cambridge

Jun, 1990

IN MEMORY OF MY MOTHER

SUMMARY

The quasi-static cone penetration test is becoming increasing popular as a site investigating tool to determine the geotechnical parameters for geotechnical design. As the result of complex changes in stress strain relationship, no comprehensive theoretical solution to this problem has yet been developed. Many of the available interpretations of cone penetration data are made with empirical correlations to obtain the required geotechnical parameters.

50 centrifuge tests at elevated g and 52 laboratory tests at 1g together with 23 triaxial tests with cell pressure ranging from 25kPa to 10MPa to determine the mobilised angle of shearing resistance and 13 direct shear tests to determine the friction angle of cone-soil interface were carried out. The penetration test results show that the stress level and the density of the soil are the most important factors that govern the penetration resistance.

Three different diameter cone penetrometers were employed in the investigation, i.e 6.35, 10.0 and 19.05mm which when tested on the same specimen such that they simulated a 'common prototype' of 400mm diameter in general gave an excellent "modelling of models" correlation. Experimental results show that no grain size effect on cone resistance was observed for $\frac{B}{d_{50}}$ greater than 12 where B is the cone diameter and d_{50} is the nominal grain size, whereas for $\frac{B}{d_{50}} = 7.5$, the grain size effect begins to appear and the difference on cone resistance is approximately 10% at $\frac{D}{B} = 25$ where D is the depth of penetration. The data indicate that difference in tip resistance between same sizes of cones but with quite different surface roughness, i.e knurled (rough) and unknurled (smooth) cones, is negligible for three different nominal grain sizes of sand (B.S 14/25, 25/52, 52/100 Leighton Buzzard sand). The data indicate that the rate of penetration does not significantly affect the tip resistance in dry sand where no excess pore pressure has been generated. The distance of the cone from the bottom boundary at which the bottom boundary effect becomes evident depends on the diameter of cone and the relative density of the soil and can be approximated from an empirical correlation as $\frac{X}{B} = 0.1139(R.D\%) - 1.238$ where X is the distance from the bottom boundary.

Correlation of the test results were carried out using :-

•the conventional approach to relate the tip resistance q_c, σ_v and the relative density R.D.

• the state parameter approach to relate the state parameter ψ' and the normalised factor of the tip resistance by mean normal effective stress $\left[\frac{q_c}{p'}\right]^{0.5}$.

Armed with these correlations, they can be used to determine the fundamental soil properties such as mobilised angle of shearing resistance for design or alternatively, to determine the insitu density of a model test sample such as is employed in a centrifuge test.

The theoretical solution to the deep penetration problem has been analysed using the method of characteristics taking into consideration the penetration up to a characteristic depth, thereafter a modified spherical cavity expansion theory is more appropriate. Classical bearing capacity theories used by other researchers are discussed. A parametric study on the effects of soil compressibility Δ has also been carried out for deep penetration.

PREFACE

I would like to thank the following people who have assisted me in many different ways throughout my studies in Cambridge:

Firstly, my supervisor Dr. R. G. James who suggested this topic of research. His experience, guidance and encouragement were a constant source of inspiration.

Secondly, all of the members of the Soil Mechanics Group and especially Professor Schofield who gave me the opportunity to join the group. I would also like to extend my gratitude to Mr. I. Nunez and Dr. R. Dean for proof reading the thesis and to Dr. R.H.G. Parry for his advice on the research. Dr. Q. Shi's original computer programme to solve surface footing problems proved invaluable in the solving of deep penetration problems based on the method characteristics and I would like to gratefully acknowledge his assistance.

I am also grateful to Mr. R. Julian, Mr B. Butler, Mr. R. Ward, Mr. W. Gwizdala, Mr P. Ford, Mr. N. Baker, Mr. S. Chandler and Mr. C. Collison for their help in making some of the equipment for my laboratory experiment and the centrifuge tests.

I would particularly like to acknowledge the financial support which I received from the Cambridge Commonwealth Trust which covered both my university fees and maintenance. I would also like to thank Clare Hall which, by means of a college bursary, took care of my college fees.

Finally, and most importantly, I owe so much to my wife Siew Fah for her constant encouragement and to my son Aaron who, by constantly seeking my attention, made my life both more exciting and more exhausting.

I hereby certify that this dissertation, which does not exceed the specified limit of 250 pages, is the result of my own experimental work, except where specific references have been made to the work of others. The contents of this dissertation are original and have not been submitted to any other university.

S.Y.Lee

TABLE OF CONTENTS

CHAPTER 1

INTRODUCTION AND REVIEW OF PREVIOUS WORK

1.1 Introduction

The quasi-static cone penetration test (QCPT) has been widely used as a site investigation tool to identify the stratigraphy and to reveal features that may have engineering significance for design and construction. The information that is obtained from penetration testing is the tip resistance, the sleeve resistance, the excess pore pressure generated during penetration in the case of a piezocone, and the depth of penetration; other sensors such as an inclinometer, temperature sensor can also be incorporated. This information is then correlated empirically to obtain the soil parameters such as shear strength or deformation moduli via some intermediate parameters such as relative density and the confining stress. Since there is no single curve for all soils, this makes the empirical correlation very local. Care must be exercised when using these parameters. Results should be supported by other methods of obtaining soil parameters if necessary, such as the laboratory triaxial test.

Insitu testing requires no sampling of the soil which means that visual study of the soil grain size, grain shape and the grain minerological content which are important characteristics affecting the strength and the deformation parameters cannot be carried out. Laboratory testing requires the extraction of a sample from the ground; sampling of soils usually causes great disturbance to the stress and hence the density of the sample which are two of the most important factors that control the strength. Therefore, insitu testing such as the QCPT should be carried out to determine the factors that can be determined insitu accompanied by laboratory testing to determine the factors that cannot be determined insitu.

Due to the complex changes in stress and strain of soils adjacent to the cone during penetration, there is no completely satisfactory theoretical prediction that is available. The theoretical analyses that are often used can be broadly classified into the following catergories:-

- Bearing capacity theory (Meyerhof 1961, De Beer 1967, Janbu and Sannest 1974).
- Cavity expansion theory (Ladanyi 1963, Vesic 1977, Baldi et al 1981).
- Strain path method (Baligh 1982, Teh 1987, Poorooshasb 1987)
- Kinematic Approach (Drescher et al 1984, 1987)

1.2 Literature Review

The idea of pushing a rod into the soil to identify the strength has long been in existence, Collin (1846). In those days, different sizes of cone and cone apex angle were used. It was not until 1957 that Van Der Veen asked for standardization of the cone. At present, a standard penetrometer has a cone diameter of 35.6mm and an apex angle of 60°. In recent years, much research on cone penetration testing has been carried out in the laboratory utilizing pressure chambers. Calibration of the cone data is based upon the known basic soil parameters such as the angle of shearing resistance ϕ, the deformation moduli, and the intermediate parameter, the relative density R.D. An example of such a test result is shown in fig (1.1). The tip resistance and the shaft friction are taken at the well defined plateau region, provided the cone data are free from boundary effects, otherwise calibration is very much dependent on the test that is carried out on the sample that is prepared in the laboratory calibration chamber. Examples of calibration chambers that are available are in Florida (Laier et al 1976), Australia (Chapman 1974), Italy (Belloti et al 1979), NGI (Parkin et al 1980), England (Wroth et al 1980). The overburden stress due to the self weight body force gradient that is present in the real field is simulated by applying pressure to the end boundaries of the specimen via a rubber bag in the chamber. The four different boundary conditions that are available is shown in fig (1.2). The desired stress history is obtained by loading and unloading of the pressure in the rubber bag. For normally consolidated sand, Veismanis (1974), Holden (1976) and Schmertmann (1978) have shown that the tip resistance q_c is a function of effective vertical stress σ'_v. For overconsolidated sand, it was reported that the cone resistance is controlled by the effective horizontal stress σ'_h, Baldi et al (1981). Schmertmann (1972, 1977) correlates the test results obtained from the calibration chamber tests between the tip resistance q_c, vertical stress σ_v and relative density R.D. for normally consolidated sand as shown in fig (1.3). It seems that no one has carried out any research on the QCPT in the centrifuge except that of Ferguson and Ko (1981) who have done some tests in the centrifuge at the University of Colorado; the equipment they used can only measure the total resistance to penetration.

1.2.1 Review on the Interpretation of Cone Data

Most of the available methods to correlate between cone resistance, relative density and soil parameters such as angle of shearing resistance ϕ and deformation moduli are in empirical form. Jamiolkowski et al (1985) presented a relationship between the relative density and normalised cone resistance with effective overburden stress as $\frac{q_c}{\sigma_v^{0.5}}$ for normally consolidated quartz sand as shown in fig (1.4), chamber size correction is then applied by dividing the tip resistance by factor k_q where

$$k_q = 1 + \frac{0.2(R.D - 30)}{60} \tag{1.1}$$

The value of k_q is obtained by an iterative method between equation (1.1) and the value of R.D in fig (1.4). Peak angle of shearing resistance ϕ_p can be estimated from fig (1.5) that was presented by Schmertmann (1978). Alternatively, ϕ can also be estimated from fig (1.6), presented by Durgunoglu and Mitchell (1975).

The deformation modulus such as the Constraint modulus $M=\frac{1}{m_v}$ from the 1-D consolidation test is generally expressed in the form $M = \alpha_m q_c$ where α_m is the constraint modular coefficient. Vesic (1970) suggested that α_m is in the range of 2 to 4 depending on the relative density of sand, later Veismanis (1974), Parkin (1980) show that for normally consolidated sand α_m lies in the region of 3 to 11 with higher values for overconsolidated sand (5 to 30). Lunne and Christoffersen (1983) show that the constraint moduli are stress dependent. The constraint modulus for vertical stress level changes from σ_v to $\sigma_v + \Delta\sigma_v$ is given as

$$M = M_0 \left(\frac{\sigma_v + \frac{\Delta\sigma_v}{2}}{\sigma_v} \right)^{0.5}$$

where M_0 is the initial tangent constraint for normally consolidated sand as shown in fig (1.7). Robertson and Campanella (1983) (based on Baldi's data that was obtained from calibration chamber tests) show that Young's modulus at 25% failure stress E_{25} varies in the range of $1.5q_c$ and $2.0q_c$ as shown in fig (1.8). They also correlate the dynamic shear modulus at small strain (10^{-3}) with cone resistance and effective overburden stress shown in fig (1.9).

1.2.2 Review on the Use of Cone Data

The empirically derived parameters and the tip resistance q_c can be used for foundation design, settlement calculation of footing and pile bearing capacity. It must be noted again that the empirically derived parameters must be used with caution. The ultimate bearing capacity can be calculated using the classical bearing capacity theory based upon a pseudo-constant ϕ obtained from the tip resistance correlation such as fig (1.6) to determine the bearing capacity factor.

De Beer and Martens (1957) presented a method to calculate the settlement of a footing which is given as

$$\rho_i = \sum_{H=H_1}^{H=H_n} \frac{1}{c} \left(log_e \frac{\sigma'_{v_z} + \Delta\sigma'_z}{\sigma'_{v_z}} \right) \Delta H \tag{1.2}$$

where $\Delta\sigma'_z$ is the increases in effective pressure at depth z below footing due to construction, σ'_{vz} is the overburden pressure at depth z below ground level, $c = \frac{1.5q_c}{\sigma'_{v_z}}$ is the compressibility factor and q_c is the tip resistance at depth z. This method tends to overestimate the settlement. Meyerhof (1961) suggested that $c = \frac{1.9q_c}{\sigma'_{v_z}}$, whereas Schmertmann (1970) proposed that $c = \frac{2.0q_c}{\sigma'_{v_z}}$. This method has now been superseded by Schmertmann's method (1970). The initial settlement of a footing is calculated as

$$\rho_i = c_1 c_2 q_n \sum_{0}^{2B} (\frac{I_z}{E}) \Delta H \tag{1.3}$$

where $c_1 = 1 - 0.5(\frac{\sigma_v}{q_n})$ is the embedment factor and $c_2 = 1 + 0.2\, log_{10}(\frac{times\ in\ years}{0.1})$ is the creeping factor, $E = q_c \times$factors in table (1.1) which depends on the type of soils I_z is the vertical strain influence factor which can be obtained from 2B-0.6 curve as shown in fig (1.10), for example, the influence factor to be used for layer Δ_{z1} is 0.1. σ'_v is the effective overburden stress at foundation level and q_n is the net bearing capacity.

The ultimate bearing capacity of a pile consists of 2 parts, the ultimate end bearing capacity and the shaft resistance. Ultimate end bearing capacity can be estimated from cone data as

$$Q_b = q_p A_b \tag{1.4}$$

where $q_p = \frac{q_{c1} + q_c 2}{2}$ as proposed by Heijnen (1974) and Schmertmann (1978) and A_b is the base area of pile. The procedure for obtaining q_p from cone data and values of q_{c1} and q_{c2} is shown in fig (1.11). Kemp (1977) limited the allowable end bearing calculated from cone data which depends on the O.C.R as shown in fig (1.12). The ultimate shaft resistance can be estimated from cone data proposed by Schmertmann (1978) as

$$Q_s = s \sum_{0}^{L} q_c \pi d \Delta L \tag{1.5}$$

where L is the embedded length of pile. The value of s to be used depends on the type of piles and is given in table (1.2), the limiting value of shaft resistance is 0.12 $\frac{MN}{m^2}$.

1.2.3 Review on Other Factors Influencing the Tip Resistance.

The two major factors that influence the tip resistance of a cone are the initial stress state and the relative density, Veismanis (1974), Schmertmann (1978), Baldi et al (1982). A more detailed review and discussion of these factors will be presented in chapter 3. The effect of the rate of penetration, roughness of cones, cone diameters and the overconsolidation on the tip resistance will be discussed and reviewed in more detail in chapter 3 and the compressibility effect in chapter 6.

Other factors that influence the tip resistance in the literature are :-

1.2.3.1 The Effect of the Wedge Angle

Meyerhof (1961), Durgunoglu and Mitchell (1975) carried out some research by varying the wedge angle of the penetrator and its effect on the bearing capacity. The results they obtained are presented in Fig (1.13)a and b which show the effect of wedge angle on the bearing capacity factor, N_γ and $N_{q\gamma}$. Clearly, they show that as the wedge angle decreases the bearing capacity factors increases for perfectly rough penetrators.

1.2.3.2 Variable ϕ with mean normal stress

As pointed out by Terzaghi (1925) the angle of internal friction ϕ for sand not only varies with the density but with mean normal stress as well for a given density. Since values of normal stress on a potential slip surface vary from point to point, Lee (1987), the simple linear function of the Mohr-Coulomb failure criterion does not hold for the shear strength characteristics of sand. For example, the ultimate bearing capacity increases with the width of the footing, so does the normal stresses along the potential slip surface. The mobilised angle of shearing resistance ϕ will thus decrease in value with an increase in normal stress. Therefore, the results of the laboratory tests on a small scale footing may lead to an overestimation of bearing capacity of a much larger actual footing.

1.2.3.3 Progressive Failure

In the process of gradual increases of load in a model test, the shear strength of soil is not immediately mobilised at all points along the potential rupture surface, but initially only at the point where the shearing stresses are highest. A rupture surface may gradually propagate to other points along the potential slip surface as load is increased further. This causes variation of soil properties along that slip surface. Due to compression, the density of soil increases in the highly stressed zone before rupture, so does the shear strength. At rupture, the shear strength corresponding to the initial density does not govern because of the variation of shearing strength along the rupture. In dense sand, the reverse is true. In the highly stressed zone before rupture, the soil begins to dilate causing reductions in density and thus ultimately reductions in shear strength.

1.2.4 Review on the Theoretical Analysis on Cone Penetration

As mentioned in the introductory section, the theoretical analysis of cone penetration can be broadly classified into four main catergories. The bearing capacity theory and the cavity expansion theory which will be used in the analysis will be reviewed in chapters 5 and 6 respectively. A brief review of the strain path method and the kinematic approach will be presented here.

The strain path method was developed at the Massachussetts Institute of Technology by Baligh et al (1985) during the past 10 years. The analysis assumed that the penetrator was brought to rest and a steady flow of incompressible soil passed over it, the path of the soil particles are defined as streamlines. Baligh et al (1985) used a line source to determine the stream function which is defined as the higher order of strain rates, whereas Teh (1987) obtained the stream function by solving the poisson equation from some assumed boundary conditions using the finite difference method. The poisson equation was obtained by combining the Navier-Stoke's equations, the continuity equation and the vorticity transport equation. By adopting an appropriate constitutive model, an estimate of the stresses corresponding to a given strain path can be obtained. Poorooshasb (1987) obtained the stream function by solving the biharmonic equation which he formulated by combining the equilibrium equation and the elastic equation of the stress-strain and hence the stream function relationship for the plane strain case, thus Poorooshasb's solution satisfied the equilibrium condition.

In the kinematic approach, the load required to penetrate in a rigid-plastic soil is calculated by postulating a mechanism of deformation. The deformation field consists of the rigid motion of blocks seperated by zones of intense deformation. The estimated load is obtained by equating the energy dissipated in the deformation and the energy supplied for the penetration, thus the kinematic approach becomes an upper bound type of solution. Drescher et al (1984, 1987) use this approach with a constitutive soil model to study the density variation in a pseudo-steady flow of granular material and also to determine the limit load of the steady penetration of a wedge.

1.3 Objectives of the Research

The research was undertaken at the Cambridge Geotechnical Centrifuge and in the University Engineering Laboratory. 50 centrifuge tests have been carried out together with 52 1g laboratory tests. These tests are supported by 26 triaxial tests with cell pressure ranging from 25kPa up to 10MPa to determine the basic soil parameters and direct shear tests to determine the surface roughness of cones. The objectives of the research were to investigate :-

- the behaviour of the shear strength of soils at high confining pressure.
- the stress level effects.
- the relative density effects.
- the scale effects.
- the grain size effects.

- the boundary effects.
- the penetration rate effects.
- the roughness effects.
- the overconsolidation effects.

The results are plotted such that they can be used to correlate field data to determine the relative density.

The results have also been analysed using the method of characteristics taking into consideration the rotation of the principal stress due to penetration effects up to a characteristic depth and the method was extended further by considering that the mobilised angle of shearing resistance is stress dependent. Beyond the characteristic depth, the extended theory based on the cavity expansion method is used. A parametric study on the influence of compressibility used in this theory was also carried out.

1.4 Layout of the Thesis

The thesis is divided into seven chapters. Chapter 1 introduces the topic of insitu cone penetration testing, followed by a literature review which touched on the application of cone data, the available theoretical analysis and the chapter ends by giving an outline of the objectives of the research.

Chapter 2 describes the properties of the materials used in the experiments, the procedure of triaxial testing which covered a wide range of cell pressure and a series of direct shear tests which were used to determine the surface roughness of the cones. Discussion of these results and descriptions of the experimental equipment are then presented.

The centrifuge modelling and the laboratory floor 1g experimental procedure and the test results are discussed in chapters 3 and 4 respectively. The centrifuge test results that are to be used as a calibration present the relationship between the tip resistance q_c, the relative density R.D, the effective vertical stress and the relative depth $\frac{D}{B}$ in chapter 3. The results of laboratory floor 1g tests of chapter 4 are then compared. Other parametric studies outlined in the objectives of research are also presented in these two chapters.

The experimental results are analysed using the stress characteristics theory for penetration depth up to a characteristic depth, thereafter, cavity expansion is more appropriate. Chapter 5 begins by reviewing the classical bearing capacity theory followed by mathematical formulation of the stress characteristics method which is valid for both plane strain and the axisymmetric case. The depth of penetration effect is also incorporated in the analysis. To validate the penetration effect, a plane strain pseudo-constant ϕ analysis is compared with the limit analysis solution. The triaxial test results in chapter 2 reveal that the mobilised angle of shearing resistance is stress level dependent, the relationship between the mean normal stress p′, ϕ and R.D are incorporated into the analysis, the results obtained are discussed and then compared with the experimental results. Beyond the characteristic depth, the experimental results are analysed using the extended cavity expansion theory in chapter 6. This chapter begins by outlining the assumptions in the analysis. Mathematical formulation for both elastic and plastic solutions are presented and incorporated. A parametric study is carried out by varying the compressibility of sand, the results obtained are discussed and contrasted with the experimental results.

Chapter 7 presents the major conclusions with respect to the centrifuge test results, triaxial test and laboratory floor 1g test results and the theoretical analysis. The thesis ends by making suggestions for future research with respect to the parametric study, the empirical correlations and the theoretical analysis of the quasi-static cone penetration test.

CHAPTER 2

SOILS PROPERTIES

2.1 Introduction

To solve the penetration tip resistance theoretically or more importantly, to correlate tip resistance with fundamental soil properties, values of the angle of shearing resistance for a given void ratio and stress level have to be determined. Drained triaxial tests with cell pressure σ_3 ranging from 25 kPa to 10 MPa were carried out. A series of direct shear tests were also performed to determine the friction angle of the cone-soil interface. The results from these tests can be used to determine the following:-

- The variation of mobilised angle of shearing resistance with mean effective stress for a given initial relative density.

- The approximate mean effective stress where the crushing of soil grains begins to occur.

- The friction angle δ of the cone-soil interface for different surface finishes for a given initial relative density and normal stress.

- The relative roughness $\frac{\delta}{\phi}$ for a given relative density.

The results were then used to predict the penetration resistance using the method of characteristics and the cavity expansion theory, thus enabling a comparison to be made between the theoretical predicted and the measured values.

2.2 Physical Properties

Four different type of sands were used in the penetration testing, they were a Fontainbleau sand, and 14/25, 25/52, 52/100 Leighton Buzzard sands. From now on, these sands will be referred as FB and their sieve sizes only. In triaxial testing, only 14/25 and 52/100 sands were used for the investigation. Particle size distributions were measured as shown in fig (2.1) and physical classifications are summarised in Appendix (A).

2.3 Shear Strength Characteristics

The triaxial compression test is the most common test used to determine the soil parameters for geotechnical design under fixed boundary conditions. The major and minor principal directions of stress and strain are normally assumed to coincide with the vertical and radial axes of the sample respectively. The change in size (volumetric strain) can be measured by the amount of water squeezed out or sucked in to the sample in the drained case, or the pore pressure measured in the undrained case. Cell pressure σ_3 and the deviatoric stress q can be altered independently to suit the requirement of the experiment. The sample can be tested under different paths (stress or strain) to failure.

Objectives of carrying out triaxial tests were to :-

• determine the relationship between mobilised angle of shearing resistance, ϕ_m and the mean effective stress p′ at various relative densities, R.D. So that an empirical correlation between ϕ, p′ and R.D could be obtained.

• determine the rigidity index I_r which will be discussed in section 6.3.3 for use with the cavity expansion theory.

• study the behaviour of soil under high cell pressure and at large strain.

Armed with the above results, they may then be correlated with the penetration test results obtained at 1g and at elevated g. Theoretical analysis based on the method of characteristics in which the mobilised angle of shearing resistance ϕ, which is stress level dependent can also be incorporated. Further to that, when sand particles are crushed, the mobilised angle of shearing resistance may decrease rapidly. This phenomenon is also included in the analysis which will be shown in chapter 5. In chapter 6 spherical expansion theory in which the compressibility of sand masses expressed in terms of a reduced rigidity index I_{rr} will be included in the analysis.

2.4 Sample Preparation

The triaxial samples were prepared by raining sand into a split mould which was held in position by the pedestal. Enclosed in the mould is a rubber membrane which has a thickness of 0.2mm for the low pressure tests and 1.1mm for the high pressure tests. The rubber membrane is secured on the pedestal by two o-rings, vacuum is applied between the mould and membrane interface so that the membrane conforms to a circular shape. Sand was then dropped from a funnel that hung from a tripod, the height of dropping and the rate of flow through the funnel was controlled to acquire the required density. An indented plastic can with a plastic tube glued to it sat on the split mould to trap the stray sand. The specimen top surface was then levelled off by suction machine. The weight of the sample was determined by subtracting the final weight from the initial weight of the sand in the funnel and the stray sand in the plastic can. The top cap is secured on the specimen by overlapping the rubber membrane on it and clamping by two o-rings. A negative back pressure of 20kPa is applied in the sample to prevent it from collapsing when dismantling the mould. The height and the diameter of the sample is measured with a pair of vernier callipers. All the samples had approximately 38mm diameter and an aspect ratio of 2:1. Calculation of density was based on the overall weight of the sand sample and its measured volume.

2.4.1 Low Pressure Triaxial System

Cell pressures of 25, 50, and 75 or 100kPa were chosen for the investigation. These tests were carried out on the computer controlled triaxial equipment setup by Airey (1987). Only a brief description of the apparatus will be presented here, a more detailed description of the apparatus can be found in the user's manual by Airey. The apparatus comprises a Geonor cell in a modified Wykeham Farrance loading frame, two stepper motors which can either be manual or computer programme operated are used for axial drive and winching of the mercury pots cell pressure system. Back pressure and volume change were measured by a GDS pressure controller. A stress path controlled test programme can be installed on the Sirius computer, all output signals are monitored via a Solatron Orion data logger.

The ram which connects the load cell to the top cap to measure the axial load passed through a rotating bush to reduce the friction. The connection between the ram and the top cap is by a friction grip which was first used by Loudon (1967) to prevent tilting of the top cap and also can be used for extension tests. To prevent water leaking out from the cell through the rotating bush, a thin layer of very viscous oil is introduced on top of the cell water. Fig (2.2) shows the layout of the triaxial apparatus.

Since all the samples were prepared dry, saturation of the sample was carried out by the following procedure:-

- After the cell was fixed to the loading frame, a cell pressure of 20kPa was applied equivalent to the vacuum pressure introduced in the sample which can then be removed.

- Carbon dioxide was introduced via the top drainage system into the sample slowly and let out via the bottom drainage system to flush the air out from the sample.

- Once the sample was saturated with CO_2 which could be detected when limewater turned chalky, de-aired water was then introduced into the specimen by the GDS pressure controller via the bottom drainage system and drained out via the top drainage system until full saturation was achieved. The specimen is allowed to stand for sometime, any gas bubbles (CO_2) entrapped in the specimen will dissolve in the water.

Back pressure and cell pressure were raised simultaneously by computer control keeping p′ constant until a back pressure of 200kPa was reached. The first stage involved drained isotropic compression tests, some undrained isotropic compression tests were also carried out and established that a value of Skempton parameter B of 0.91 or above was achieved. The second stage of a test was to carry out a standard drained test by increasing the deviatoric stress q. The axial deformation rate was $0.12\frac{mm}{min}$ for all tests.

2.4.2 High Pressure Triaxial System

Tests at four different cell pressures of approximately 930, 1930, 4780 and 9650 kPa were carried out on 52/100 and 14/25 sands to study the soil behaviour at high pressure. The triaxial apparatus consists of a stainless steel cell mounted in a 3 ton capacity Wykenham Farrance loading frame. The cell can withstand a maximum cell pressure of 14 MPa. Hydraulic oil was used as the cell fluid instead of water to minimise escape of cell fluid through the ram-bushing interface at high pressure. Cell pressure was measured by a pressure transducer, and was controlled by a valve which fed nitrogen gas from a pressurised cylinder to an accumulator. The accumulator consists of a steel cylinder and a rubber bag which separated the oil and nitrogen gas. If the nitrogen pressure in the cylinder is inadequate, the oil can be pressurised via a manual pump. Back pressure and volume change were measured using the Imperial College volume change transducer which has a capacity of 50 cc. The volume change transducer consists of a hollow cylinder and a double acting piston which is sandwiched between two bellofram rolling seals. The back pressure is applied to the bottom chamber, de-aired water is admitted to the top chamber which is sealed by a bellofram seal that allows displacement of the piston which is then measured by a displacement transducer. The displacement transducer is mounted on the outside of the cylinder. Calibration of the volume change is done against a burette. Applied load was measured by a load cell which was placed outside the cell. Friction on the ram-bushing interface is considered negligible because the applied axial load is high. The axial displacement of the sample is measured by an LVDT. All output signals were logged using the "Labtech Notebook" computer program which was installed on an IBM PC. The layout of the high pressure triaxial test system is shown in fig (2.3)

The procedure for saturation of the samples was similar to that for the low pressure triaxial system except that the de-aired water was introduced into the specimen through the volume change transducer. Back pressure and cell pressure were raised manually. As far as possible, p′ was kept constant until a back pressure of 690 kPa was reached. The first stage of the test was an isotropic compression drained test achieved by increasing the cell pressure manually up the the target cell pressure. The second stage of the test was a standard drained test and the axial deformation rate was 0.12 $\frac{mm}{min}$.

2.5 Test Results and Discussion

The results of the 26 triaxial drained tests are plotted. Fig (2.4)a, b and fig (2.5)a, b show the low pressure test results, and fig (2.6)a, b through fig (2.9)a, b show the high pressure test results. These plots show the value of deviatoric stress q versus axial strain ϵ_a, and in the case of the high pressure tests volumetric strain versus axial strain. The peak values of angle of shearing resistance of these tests were calculated as

$$\phi_p = \sin^{-1} \frac{q}{q + 2\sigma_3} \tag{2.1}$$

Shearing of the sample were carried out to an axial strain of 10% to 20%. By assuming that the strain is uniform throughout the sample, the shear strain ϵ_s due to change in shape is calculated from

$$\epsilon_s = \epsilon_a - \frac{\epsilon_v}{3} \tag{2.2}$$

Peak angles of shearing resistance are tabulated in the table (2.1) for a given initial void ratio e, at various confining pressures σ_3 and peak principal stress ratio $\frac{\sigma_1}{\sigma_3}$. This table shows that the principal stress ratios were decreasing with increasing confining pressure indicating that failure envelopes are curved, i.e the angle of shearing resistance has reduced for an increase in confining pressure. Fig (2.10)a and b show the plot of peak angle of shearing resistance ϕ_p against logarithmic scale of mean effective stress $p' = \frac{q}{3} + \sigma_3$ at various densities. Stroud (1972) carried out some plane strain tests on 14/25 sand using the simple shear apparatus. If the intermediate principal stress σ_2 is approximated equal to $\frac{\sigma_1+\sigma_3}{2}$, then ϕ_p obtained from the simple shear tests can be plotted in fig (2.10)a. Plane strain ϕ_p is slightly higher than the triaxial strain ϕ_p for the same value of mean effective stress p′ and R.D.

Bolton (1986) produced an empirical correlation between dilatancy rate at failure ν_{max}, mean effective stress p′, and relative density R.D. For triaxial strain, this is given as

$$\phi_{max} - \phi_{crit} = 3I_R \tag{2.3}$$

where I_R is the relative dilatancy index which is

$$I_R = R.D(10 - In\,p') - 1$$

From fig (2.10)a, it can be seen that the empirical correlation of equation 2.3 underestimates values of ϕ_p in the medium range of mean pressure p′, and overestimates in both high and low pressure range of p′.

In the author's theoretical analysis of the penetration test which will be outlined in chapter 5, the variation of p′ in the medium range of p′ is particularly important, to avoid this conservatism, it is best to correlate the author's experimental data by fitting two lines as shown in fig (2.10)a and b. It can be seen that ϕ_p decreases rapidly beyond certain values of p′. This may imply that at high mean pressure p′, particle crushing may have occured thereby reducing the maximum angle of dilation ν_{max} and hence the angle of shearing resistance. The region around the intersection point of two straight lines might be viewed as the region of mean pressure p′ where crushing of soil particles begins to occur. To investigate if the crushed sand will reach critical states during shearing, dilatancy rates and their mobilised angle of shearing resistance for the entire range of pressure are plotted in fig (2.11). This figure shows that critical states angle of 32° will eventually be reached i.e shearing at constant volume, irrespective of the confining pressure.

2.6 Discussion of Triaxial Tests

There are several factors which may influence the accuracy of the tests results. They are considered below and are classified as follows:-

2.6.1 Uniformity of Stress and Strain

It is usually assumed that the sample under straining remains in a cylindrical in shape, stress and strain distribution in the sample being uniform throughout. In actual fact, rupture planes will form in the sample as shown in fig (2.13). These rupture planes are the zone where volume change and shearing concentrate, other regions becoming relatively rigid. Therefore, strain calculations from external measurement do not represent the true behaviour of a uniformly straining soil element. In the deviatoric stress calculation, the change in cross-sectional area during straining can be taken into account by using average cross-sectional area, a, where

$$a = a_0 \frac{1 - \epsilon_v}{1 - \epsilon_a} \tag{2.4}$$

a_0 is the initial cross sectional area before straining.

Non-uniformity of straining may also cause progressive failure resulting in a reduction of the peak angle of shearing resistance.

2.6.2 Friction on End Platens

The horizontal planes of the specimen are assumed to be a principal plane. Inevitably, some friction must exist between the platen-sand interface, more seriously, end platens become roughened by scratches after high pressure tests. This was minimised by using end platens that were made of high carbon content steel, hardened by quenching. The friction on the end platen-sand interface was also reduced by application of grease to the interface.

At the middle of the platens there is a 10mm hole to house a porous stone for drainage. With this type of arrangement, friction on the surface platen can be significantly reduced and, more importantly with respect to the safety aspect of the test at high cell pressure, the membranes are less likely to burst which usually occurs near the edge of the end platen.

2.6.3 Friction on Ram-bushing Interface

The ram acts as the bridge between outside and inside of the cell. It passes through a bushing to guide its movement vertically. To avoid the escape of cell pressure, the fitting of the ram-bushing must be a very good fit. Inevitably, some friction must exist, the resistance against vertical movement becomes relatively more pronounced when the applied axial load is small, i.e in the low pressure triaxial test. This was overcome by rotating the bushing with a motor and oil is also fed into the interface. Taylor (1943), Casagrande (1948) overcame this problem by measuring the axial load inside the cell.

Additional friction may occur as the result of the ram pushing against the bushing if the applied axial load is eccentric or non-uniformity of axial strain of the sample due to inhomogenity about the central axis of the sample.

2.6.4 Membrane Penetration

The sand sample is isolated from the cell fluid by the rubber membrane, this membrane may fill part of the void between adjacent sand grains. The void is normally filled with deaired water, if sand grains do not crush and water is incompressible, any change in the volume of specimen will reflect the amount of water squeezed out or sucked in, but this will not be the case if the rubber membrane that filled part of the void, changes its volume. Two types of changes can be considered here, firstly, in the isotropic compression drained test, as the cell pressure σ_r is increased, the rubber membrane that fills part of the voids tends to occupy more space in the voids resulting in more pore fluid being expelled from the sample. Secondly, In the anisotropic compression drained test, the cell pressure is maintained constant, the sample can either dilate or compress depending on whether the sample is dense or loose. As a result the rubber membrane can be stretched, thus resulting in an error in the volumetric strain.

2.6.5 Crushing of Sand Grains

Volume change is one of the measurable quantities from the triaxial testing. Voids in between coarse grains are larger than those in between fine grains. From the shift of grading curves plotted after high pressure tests as shown in fig (2.1), one may conclude that crushing of particles has occured resulting the change in volumetric strain.

2.6.6 Rotation of Top Cap

The horizontal plane of the top cap has been assumed to be a principal plane, if the top cap rotates and its horizontal surface is not normal to the sample axis, shear stress will be induced on that plane when straining, this can be due to non-uniformity of strain of the sample resulting in under prediction of the failure stress. To avoid this, the sample is properly prepared to minimise inhomogenity and the top cap is placed horizontally with a spirit level. In the low pressure tests, the rotation of the top cap was prevented by using the friction grip method explained in section (2.4.1).

2.6.7 Oil as medium of cell or pore fluid

When oil is used either as a cell or pore fluid, the contact between the oil and the rubber membrane is unavoidable. Since the rubber membrane will expand when it is soaked in oil for a long time, it is likely that the amount of pore space occupied by the rubber membrane will increase resulting in an overestimate of the volume change measurement. To avoid this, the test should be carried out as soon as possible after saturation and with the shortest possible test duration.

2.7 Direct Shear Tests

A total of 13 direct shear tests were carried out to determine the friction angle δ of the cone-soil interface using the 100×100mm shear box. The lower half of the shear box housed a solid block of penetrometer cone material which had been machined and hardened. One face of the block is smooth and the other has the same surface profile as that of the knurled cone which will be termed as a rough face. The upper half of the shear box is filled with sand to the required density, vertical load is applied on top of the piston which sits on the sand surface. A cross-sectional view of the setup of shear box is shown in fig (2.12). Tests were done on both faces of the block, with 14/25 and 52/100 sands at different void ratios for these investigations. The shearing rate was maintained constant at 0.12 $\frac{mm}{sec}$.

2.7.1 Conclusions of the Direct Shear Test Results

The vertical normal stress that was applied during the tests were 98.1, 392.4 and 686.7 $\frac{kN}{m^2}$ The test results can be summarised as follows :-

• For the same normal stress and approximately same void ratio, the rough (knurled) surface will have a higher cone-soil interface friction angle δ then the smooth face as shown in fig (2.14). The figure also shows that δ is higher for larger nominal grain diameter, d_{50}

on the rough face and the reverse is true on the smooth face.

• The value of δ decreases as the normal stress increases for the same void ratio on both rough and smooth faces, but the rate of decreasing of δ for the rough face is greater as shown in fig (2.14), therefore it is possible that at some very high normal stress, the difference on the effect of roughness surface between that of a rough and a smooth face becomes smaller.

• Fig (2.15) shows that δ is also affected by the initial void ratio, being higher for dense sand, it decreases as the void ratio increases.

2.8 Summary

The angle of shearing resistance of 14/25 and 52/100 sand at different relative densities and confining stress was determined from drained triaxial tests. A series of direct shear test has also been carried out to determine the friction angle of cone-soil interface. The values of ϕ and δ are formulated in terms of void ratio or relative density and the mean normal stress. These results are used in chapter 5 and 6 to predict the penetration resistance theoretically. The triaxial test results also show that the shear strength is stress dependent and its strength decreses rapidly after sand grain crushing has occured.

CHAPTER 3

CENTRIFUGE MODELLING

3.1 Introduction

The quasi-static cone penetration test has been widely used as a site investigation tool to determine geotechnical parameters for geotechnical design. To date, most of the calibration of cone penetration tests have been performed in the laboratory with a calibration chamber. Empirical correlations relating tip resistance and sleeve resistance to fundamental soil properties such as relative density, shear strength and modulus are obtained for a variety of overburden pressures.

The calibration in the laboratory is done by applying surcharge to the soil surface to simulate the effect of overburden pressure. Some researchers use different boundary conditions by varying the lateral pressure around the circumference of the chamber via a rubber membrane. A reduced size of cone to minimise boundary effect is sometimes used, the results are then extrapolated to simulate the full scale. In either case, the effect of body force gradient due to self weight of the materials as in the real field cannot be guaranteed with the surcharge. Therefore the derived calibration from the laboratory 1g test that is used to determine the fundamental soil properties in the field always leaves room for questioning.

To study the effect of self weight body force gradient, centrifuge modelling is used. With a carefully prepared model with known soil properties, tested under different gravity environments, different tip resistance depth profiles will be produced. Detailed parametric studies based on the objectives of the research that were outlined in chapter 1 were then carried out.

3.2 Scaling Laws

The scaling laws in centrifuge modelling have been discussed by many centrifuge modellers relating the prototype and the model quantities. Since the tests were carried out on dry sand and in the static event, the time dependent scaling factors will not be discussed, only a brief description on scaling laws will be presented here.

Consider an n^{th} scale model which is tested under an acceleration field n times that of the earths gravity. Following are the scaling relationships between the prototype with subscript p and the model with the subscript m.

$$\text{Strain } \epsilon_p = \epsilon_m$$

$$\text{Stress } \sigma_p = \sigma_m$$

$$\text{Velocity } V_p = V_m$$

$$\text{Length } L_p = nL_m$$

$$\text{Unit Weight } \gamma_p = \frac{1}{n}\gamma_m$$

$$\text{Acceleration } a_p = \frac{1}{n}a_m$$

$$\text{Area } A_p = n^2 A_m$$

$$\text{Force } F_p = n^2 F_m$$

Application of dimensionless analysis requires that for geometric similarity,

$$(\frac{D}{B})_{prototype} = (\frac{D}{B})_{model}$$

From the above relationships, both stress and strain have a one to one relation between the prototype and the model. This implies that the stresses due to self weight are well replicated in a model of the prototype, which is one of the major factors influencing the tip resistance to penetration, thus making centrifuge modelling an attractive option.

3.3 Stress Variation with Depth in Flight

As pointed out by Schofield (1980), the radial accelaration field in the centrifuge ($\omega^2 r$) varies with radius for a given angular velocity ω. Hence to assume a single linear scaling factor relating a model to its equivalent prototype will introduce an error. The magnitude of the error being the difference between the linear variation in vertical stress in the prototype and the radially varying vertical stress in the centrifuge can be calculated as follows:-

Consider a model of thickness d in flight with angular velocity ω. Its surface at radius R_i has zero stress, then the vertical stress σ_{v1} at depth z in the model is

$$\sigma_{v1} = \int_{R_i}^{R_i+z} \rho\omega^2 r dr = \frac{\rho\omega^2}{2}\left(z^2 + 2R_i z\right)$$

where ρ is the density.

In the prototype, the corresponding vertical stress σ_{v2} at depth nz is

$$\rho(gn)z \tag{3.1}$$

If the gravity level(ng) is assumed to be equal to $\omega^2 R_i$ Then, the percentage error between that of model and prototype is

$$\frac{z}{(z+4R_i)} \times 100\% \tag{3.2}$$

Most of the centrifuge modelling has $\frac{d}{R_i} \leq 0.1$ and $\frac{z}{R_i} \leq 0.05$. The maximum difference in stress between the model and prototype is only 1.2% which therefore does not pose a serious problem in the penetration testing.

3.4 Instrumentation, A Review

Campanella and Robertson (1981) have highlighted the importance of equipment design and procedure to obtain accuracy and repeatibility of results. Some effort must be put in to design proper equipment before any experiment is carried out.

In Cambridge, the development of the penetrometer goes back to 1981 when Cheah modified the vane apparatus of Davies and Parry which was used in clay as shown in fig (3.1). The probe shaft was 8mm diameter and was coated with teflon hoping to eliminate the effect of shaft friction. A 10mm diameter 60° cone was fixed at one end, and on the other a load cell to measure the tip resistance to penetration. The probe was driven in by a D.C motor. Almeida and Parry (1983) show that this system can only measure the total resistance and there is no way to uncouple the tip resistance and shaft friction. This lead to the development of a mark II penetrometer which has two load cells to measure the tip resistance and total resistance separately, see fig (3.2). Initial tests using this penetrometer shows that the output signals from the columnar load cell were very small and susceptible to electrical noise from slip rings.

In order to improve the measurement, a mark III penetrometer probe was developed as shown in fig (3.3) with a rosette load cell mounted at the top of the probe. The output signals were seven times higher to give more reliable results. Unfortunately, the new design could not measure the total resistance to penetration.

A piezocone was also developed at that time for use in studies of the behaviour of embankment on soft clay as in fig (3.4). The porous element is located at the tip of the cone. The excess pore pressure generated is measured using a PDCR 81 Druck pressure transducer. For each operation, the porous stone and the pressure transducer have to be deaired. Springman (1987) used the piezocone probe for her centrifuge tests in layered soils consisting of clay overlaid by sand. The location of the porous stone proved to be vulnerable to breakage. Since then no more effort has been put in to improve the piezocone probe.

Randolph, Nunez, Airey and Phillips (1986) developed a hydraulically actuated penetrometer for use in cohesionless soils. Two units of probe diameter 9.525 and 19.05mm were designed. The 9.525mm diameter probe is fitted with a 10mm diameter cone and is universally used by the Cambridge Soils Mechanics Group. For the purpose of author's research, the unit with the 19.05mm diameter probe was used.

3.4.1 Cone Penetrometer

The unit with 19.05mm diameter probe designed by Randolph and et al has been modified so that three different sizes of probe of 6.35, 10, and 19.05mm diameter are interchangeable. At one end of the probe, a tip load cell was fixed to measure the tip resistance. To the other, was coupled a common total load cell via a separable glass seal. The common total load cell was fixed to the lower part of the piston. A bush bearing which is interchangeable depending on the size of probe, used to guide the probe, is fitted at the lower cap of the hydraulic cylinder. The depth of penetration is measured by a rotary potentiometer. Previously, the rotation of the rotary potentiometer relied upon the strain energy stored in the spring, this arrangement unfortunately did not work at high g-level because the spring tended to be pulled down due to gravity effects instead of coiling around the pulley of the rotary potentiometer. Modification to this arrangement was made by using a rubber roller directly in contact with the probe in use without using a spring whereby transforming the linear motion of the shaft to a rotary motion of the rotary potentiometer. To eliminate the slippage between the roller and the probe, a finger tight pressure is applied when tightening the rotary potentiometer in position. A plot of penetration against time is shown in fig (3.5). When the 19.05 mm probe was used, the previous arrangement was adopted because there was insufficient space available in the cylinder to accomodate the new design. This did not pose a problem because the 19.05mm probe was used at a lower g-level. Other measurements included the H_2O and

N_2 transducers to monitor the pressure in the cylinder. The penetrometer assembly is shown in fig (3.6).

3.4.2 Design of Load Cells

All the three load cells were made of aluminium alloy designated as BS-6082 HE-30-TF which has $295 \times 10^3 \frac{kN}{m^2}$ compressive strength. The output signals depend on the magnitude of strain on the active face. To obtain a reasonable signal output, the wall thickness of the load cell must be thin. On the other hand, it must be thick enough to withstand the load without breakage. Aluminium alloy has Young's Modulus E of approximately $70 \frac{kN}{mm^2}$. If the allowable strain on the load cell is 1500 microstrain, then the wall thickness of the load can be calculated. A check must be carried out to ensure that the design stress does not exceed that of the compressive strength. Specifications of all load cells are shown in table (3.1) and their schemetic diagrams are shown in fig (3.7)a, b and c.

Strain gauges are cemented onto the surface of the active face to measure the change in electrical resistance with strain. Two types of gauges were used, the 6.35mm load cell was cemented with 2n/120/PC17 strain gauges whereas the 10mm and the total load cell were cemented with 3s/350/EC23. Due to the small circumference available in the 6.35mm load cell, the legs of the strain gauges were cut to accommodate the available space. This did not cause any problems because the active part was not disturbed. A simple method to measure the change in electrical resistance is by means of a wheatstone bridge. To obtain a fully active bridge arranged for temperature compensation and also not to be affected by bending stresses of the load cell, the bridge is arranged as shown in fig (3.8)a and b. Strain gauges are powered at 3 volts as recommended by the supplier and are protected by a sleeve over the load cell.

Calibrations of the load cells were done on a loading machine by straining the load cell to just beyond the design load, the process was repeated several times until the shift of the calibration curves ceased. By this procedure it was possible to eliminate hysteresis effects.

Before the penetrometer assembly was put to full operation, it was also checked against the Euler's buckling load of the probe, $P_e = \frac{\pi^2 EI}{L_e^2}$. Fig (3.9) shows the safe range of operation for zero eccentricity (i.e the buckling load for that portion of the probe remaining within the cylinder).

3.4.3 Roughness of Cones

The cone to be used for each test depends on the objective of test and the diameter of the probe. All cones have an apex angle of 60°. They are made of high carbon content steel and are hardened by quenching to keep a consistent surface finish in all tests. To investigate the roughness effects on a 19.05mm diameter cone-soil interface, the cone surface was knurled before hardening. Fig (3.10) shows the surface finish of knurled and unknurled cones which will be termed as rough and smooth cones.

This method of roughening the surface is used instead of glueing sand on the cone face as many researchers had done because by doing so, the diameter can be kept the same as the smooth cone. Comparison of results due to roughness effect on cones is then possible. Otherwise, for example, tests on the 14/25 sands which has a mean grain diameter of 0.9mm: if they were to glued onto the 10mm diameter cone, the diameter would have increased to 11.8mm. Simple calculations will reveal that for the same failure stress, the force due to the increase in size of the cone would have increased by approximately 30%, therefore this is inappropriate for comparison.

3.4.4 Data Acquisition

All raw signals from load cells, pressure transducers and rotary potentiometer passed through a junction box which was mounted on the centrifuge model package. These raw signals were amplified 100 times before passing through the slip rings of the centrifuge. The amplified raw signals were then logged into the newly installed logging system, i.e

Labtech Notebook which is installed in an IBM PC. The signals were also recorded on RACAL tape recorders and stored in a magnetic tape. Processing of the raw data was done using a program package called Lotus 1-2-3. Methods of using these packages can be found in the user's manual which will not be explained here.

3.5 Model Preparation and Test Procedure

The model was prepared by raining sand from a single-holed hopper into the 850mm diameter by 400mm high tub. The relative density of the sand model depends on the height of pouring and the size of the partial eclipse aperture formed from overlapping two perforated plates. Phillip (1987) has shown that this method of model preparation can achieve a fairly uniform sample. In the preparation of the sample, the flow rate and the height of drop were maintained constant. Loose samples tend to densify when disturbed. To avoid this during model handling, the samples were prepared in the centrifuge compound. Calculation of the relative density is based on the overall weight of sample and its volume measured after the package had been mounted on to the centrifuge arm. The volume of the sample are also been checked after each test to ensure that no serious settlement and hence densification of the sample has occured.

The penetrometer assembly is mounted asymmetrically on the rectangular box section beam which is then mounted on top of the tub. It is therefore possible to perform four to five tests on each sample by changing the position of the box section after each test. In the modelling of models, the penetrometer is stripped down, and the required probe is assembled.

This method of setup is used because it is robust, penetration in flight is guaranteed, and more importantly, the unformity of the relative density in a single model preparation is better than four or five model preparations to acquire the same relative density, noting that relative density is one of the two major factors that influences the tip resistance. It will be shown later that with this type of setup, there is no significant side boundary effect. The assembled package for the centrifuge tests is shown in fig (3.11).

Before penetration testing at the required g-level is carried out, the gravity effect tends to pull the probe downwards. To prevent this, the lower chamber of the penetrometer cylinder was pressurised with nitrogen gas at about 135 p.s.i (931 kPa) to counteract the self weight of the piston, the probe and the head of water in the external piping along the centrifuge arm.

During penetration testing, the probe was pushed into the soil by releasing pressurised mixture of water and rust inhibitor i.e fernox-B (4:1 ratio), that was stored in two accumulators mounted near the axis of the centrifuge, to the top chamber of the cylinder. As penetration occured, the build-up of nitrogen pressure at the bottom chamber required that, the nitrogen pressure was bled at about 150 p.s.i (1035 kPa) via a pressure relief valve. A schematic diagram of hydraulic and pressure control system is shown in fig (3.12)a and b and the calculation of nitrogen pressure required to be stored in the accumulators is shown in Appendix B.

When the test was completed and the centrifuge was stopped, the pressure in the accumulators was released. The probe was retracted by the pressure in the bottom chamber and the mixture of water in the top chamber of the cylinder flowed back to the accumulators. Changing of the probe was then carried out if so required and the process was repeated for the next test at another location. The amount of the mixture of water that was stored in the accumulators was also checked to ensure that it was adequate for the penetration required during the next test to be carried out.

3.6 Discussions of Experimental Results

Some 50 centrifuge tests were carried out and the test programme is summarised in table (3.2). Parametric studies of the results are discussed in the following sections.

3.6.1 Stress Level Effects at Different g-level

Section 3.3 has shown that the maximum difference in vertical stress with depth between that of prototype and centrifuge model is not greater than 1.2% at 200mm depth, which is insignificant. In the present setup of experiment, the centrifuge needed to be stopped to change the location after each penetration test in the same soil model. This procedure of stopping and starting of the centrifuge leads to a stress cycle on the soil. Since this investigation is on the stress level effects on normally consolidated sand, the sequence of testing is to run the tests at 10, 20, 40, 80g respectively. The vertical stress at depth D in the model and in prototype is $(\rho \times n \times g \times D)$.

Test series II (T5 through T8) on dense 14/25 sand are plotted in fig (3.13). They showed that the tip resistance to penetration due to increase in vertical stress level increased at a decreasing rate, replotting of $\frac{D}{B}$ of q_c against σ_v for various values of $\frac{D}{B}$ are shown in fig (3.20)a through e. This pheonomenon can be explained by the fact that dilation effects along the failure surfaces have been supressed due to increases in stress level. In a previous study of the strain field (Lee, 1987), a plot of relative displacement across a discontinuity between two lead shots taken from X-rays has shown that the dilatancy effect is not a material constant, but depends on the normal stress acting on the failure plane. That is to say mobilised angles of shearing resistance varying along failure surfaces and are stress dependent.

Test series I on fontainbleu sand (T1 through T4) and test series V on dense 52/100 sand (T18 through T21) are plotted in fig (3.14) and fig (3.15). Replotting the graphs as before (see fig 3.20), they show the same effect at high vertical stress, whereas at low vertical stress, 14/25 sand shows a higher gradient, this is because coarse sand tends to dilate more than fine sand. Test series VII and VIII on 52/100 sand (T26 through T29), (T30 through T33) and test series III and IX on medium to loose 14/25 sand (T9 through T12), (T34 through T37) are plotted in fig (3.16) through fig (3.19). Replotting the graphs, see fig (3.20), they show a linear increase in tip resistance with stress level.

It must be pointed out here that it would be erroreous if fig (3.13) through fig (3.19) were plotted together for q_c against σ'_v directly because for the same value of σ'_v, the values of $\frac{D}{B}$ are different depending on the g-level. For example, the vertical stress of $27.7\frac{kN}{m^2}$ running at 10g in test T5 will correspond to $\frac{D}{B} = 16$, whereas for the same vertical stress running at 20g in test T6 would correspond to $\frac{D}{B} = 8$. Different $\frac{D}{B}$ values mean that the 'failure mechanism' is different, and hence relative depth and stress are inseparable.

3.6.2 Relative Density Effects

The main purpose of field penetration testing as a site investigation tool is to determine the density of soils insitu. For dry sand, the void ratio e is calculated from $\rho = \frac{\rho_w G_s}{1+e}$ where G_s is the specific gravity and ρ_w is the density of water. The known void ratio is then correlated with the laboratory determined angle of shearing resistance for geotechnical design. Engineers normally prefer to use relative density which is

$$R.D = \frac{e_{max} - e}{e_{max} - e_{min}}$$

The replotted curves in fig (3.20)a through e for different relative densities have similar profiles to those produce by Schermertmann (1976) and Veismanis (1974) (see fig 1.3). Plots showing the relationship between tip resistance and relative depth for 14/25 sand and 52/100 sand for three relative density at four different g-level are shown in fig (3.21) through fig (3.28). Retabulation of these results is shown in table (3.3). Other relative depths can also be shown or expressed as vertical stress if so required. It can be seen that the ratio of tip resistance of 14/25 to that of 52/100 sand for 54% relative density is relatively constant throughout the different g-level, whereas in the 80% relative density, the ratio is higher at low g-level, i.e low stress level, and decreases to become relatively constant at high g-level, i.e high stress level. In all tests, 14/25 sand shows higher tip resistances than 52/100 sand for same relative density. The effect of relative density on tip resistance is because the tip resistance is very much dependent on the mobilised angle of shearing resistance. The mobilised angles are high for high relative density but are reduced with increasing mean stress level, whereas, low relative density sand tends to be compressed and the mobilised angles of shearing resistance are not so significantly affected by the stress level. In the previous studies on the propagation of rupture beneath a strip footing, Lee (1987), a strain controlled model footing test reveals that rupture always starts at the corner of the footing and subsequently develops progressively downward and changing in direction up towards the free surface, similar behaviour was also observed in the X-radiograph recorded in a plane strain test utilising a wedge as shown in the front cover. When the sample is gradually brought to failure, localisation of deformation into a shear band started to develop at the tip of the penetrator. As the penetrator advances, the soil at the tip of the advancing shear band will be dilating at a certain rate until maximum and further back along the shear band, the rate of dilation will fall and the mobilised angle of friction will reduce to the critical state angle. The amount of soil at any one time exhibiting this phenomenon will influence the average values of the mobilised angle of friction. This phenomenon occurs in a much greater degree in a fine sand, therefore the judder in fig (3.25) and the low penetration resistance in the fine sand maybe due to this progressive failure effect. Hence one can write

$$\phi = f(\sigma, e_0, d_{50}) \tag{3.4}$$

i.e the mobilised angle of friction ϕ is some function f of the stress stresses, the initial voids ratio e and the d_{50} particle size.

3.6.3 Scale Effects

De Beer (1965) investigated the scale effect associated with the pheonomenon of progressive rupture in cohesionless soils and concluded that the bearing capacity factors due to self weight body force N_γ for a large footing will be smaller than for a smaller footing. Therefore, care must be exercised when extrapolating the bearing capacity factors found on small model tests to be used in prototype footings of much larger size. Yamaguchi (1977) and Abghani (1987) also investigated these effects in bearing capacity problems. Oversen (1981) and Tagaya (1987) studied the same effects with respect to the pull-out of anchors. All investigators concluded that, the bearing or the pull-out capacity are different for different sizes of footings or anchors.

Strictly speaking, to study the scale effects related to penetration problems in the centrifuge, different sizes of probe diameter should be used and the centrifuge run at constant g-level, so that, the same stress level at the same depth can be achieved, the pattern of the failure mechanisms may then be similar but with a quite different size dependent on the probe diameter used. Hence, the effect of scale on the tip resistance can be compared.

Tests T10 and T13 on 14/25 sands are presented in fig (3.29). They were carried out using 10mm and 19.05mm probe diameter running at nominal accelerations of 20g and 21g, these will correspond to prototype diameters of 200mm and 400mm respectively. Similarly, tests T19 and T22 on 52/100 sand using 10mm and 19.05mm probe diameter are shown in fig (3.30). An interpolation of tests T20 and T21 running at 40g and 80g to 63g using the 10mm diameter probe, is made for comparison with the test T25 using the 6.35mm probe diameter, these will correspond to prototype diameters of 630mm and 400mm respectively. The plots are shown in fig (3.31). It should be noted here that tests T11 and T12 have not been interpolated to 63g using the 10mm probe diameter and compared to test T16 using the 6.36mm probe diameter in the 14/25 sand because it will be shown in the next section that there is some influence due to grain size effects, hence the comparison is invalid.

In all these tests, it can be seen that the smaller the diameter, the higher is the resistance to penetration. The reason is that, the mobilised angle of shearing resistance depends on the mean stress, density and nominal grain size, as indicated in equation (3.4) of the previous section. If same nominal grain size and density are used, then the only variable is the mean effective stress, i.e $\phi = f(\sigma)$. The big probe diameter will induce a larger plastic zone than the small one, this means that the self weight body force, and hence the stress acting on the potential rupture is higher to give a lower mobilised angle of shearing resistance, hence the smaller probe will show a higher bearing capacity factor then the bigger probe. A similar effect has also been reported by Meyerhof (1983) in model pile tests to study the scale effect at 1g.

3.6.4 Particle Size Effects

The influence of particle size effect on model structures is a topic of major interest in the present research. This is particularly important in model studies especially when the model structure is small in relation to the nominal grain diameter, d_{50}. Relative grain diameter ratio which is defined here as the ratio of the diameter of model structure B to the nominal grain diameter d_{50}, i.e $\frac{B}{d_{50}}$ which will be used throughout this study. In centrifuge modelling, the grain size of sand used in the model will therefore correspond to a prototype grain size that is coarser by the modelling scale factor. To study the behaviour of sand therefore one may require ideally to use silt size particles in the model which would then however have different strength characteristics. In many cases, the same sands are used in the model to study the prototype behaviour, therefore it is necessary to investigate the grain size effect.

Yamaguchi (1977) studied the grain size effect with relative grain diameter ratio ranging from 21 to 289 in the footing problem, Oversen (1981) investigated the pull out of anchors, employing relative grain diameter ratios in the range of 25 to 128. Both reported that no significant grain size effect was observed.

To study the grain size effect on cones in the QCPT, modelling of models has been employed. Three different sizes of cones of 19.05, 10 and 6.35 mm diameter were used in gravity fields of 21g, 40g and 63g respectively, these are therefore all equivalent to a prototype diameter of 400mm. Other gravity fields can also be used if so required provided an identical prototype diameter is achieved.

Test series VI (T22, T24, T25) was performed on dense 52/100 sand which has a nominal grain diameter d_{50} of 0.225mm, this gave relative grain diameter ratios of 85, 44 and 28. Fig (3.32) shows the plot of tip resistance against relative depth, no grain size effect was observed. Note that the last portion of each curve should be ignored since the cone resistance is becoming influenced by the proximity of the base of the sample container. Test series XI (T42, T43, T45) performed on loose 52/100 sand, unfortunately, at high g-level, loose samples tend to densify, 1mm settlement of the sample was measured after test T45 running at 63g and also the 6.35mm probe was found to have bent slightly after the test, this is because the probe was not assembled properly, thus correct penetration in flight was not guaranteed. Fig (3.33) shows that the 19.05 and 10mm diameter cones which have the same prototype diameter modelled very well. Test series XII (T46, T48, T49) was done on dense 25/52 sand which has a nominal grain diameter of 0.4mm, this will correspond to relative grain diameter ratios of of 48, 25, and 16. Plots of tip resistance against relative depth are presented in fig (3.34), again they show that grain size effect was not very significant, however the 6.35mm probe does give a slightly higher result and may therefore be influenced by grain size. Test series X (T38, T40, T41) and test series III (T13, T15, T17) were carried out on 14/25 sand which has a nominal grain diameter of 0.85mm, this will correspond to relative grain diameter ratios of 22, 12 and 7.5. Plots of tip resistance against relative depth are shown in fig (3.35) and fig (3.36). Clearly, grain size effects begin to appear for a relative grain diameter ratio of 7.5. For example, in the dense 14/25 sand, at $\frac{D}{B} = 30$,the difference in tip resistance is approximately 10% . Fig (3.37) shows from the test results T16 and T17 using the 6.35mm probe thereby giving an indication of the variability in the results for this probe. Thus, it can be concluded that if the relative grain diameter ratio is greater than 12, no significant grain size related errors will influence the tip resistance. It is also evident that in general, within certain grain size restrictions, and outside of the region of the 'bottom boundary effect', the modelling of models of a common prototype gave an excellent correlation, as of course it should if grain size effects are small and the principles of centrifuge modelling are valid.

3.6.5 Boundary Effects

Before cone penetration testing in the field can be correlated theoretically or experimentally, calibration of penetration testing must be done in the laboratory and related to the known properties of soils. The chamber diameter D_T is usually designed to be as large as possible, however it is still finite, and the question arises if the chamber test is true by representative of insitu soils of large lateral extent. However, if the cone penetration test is free from boundary effects, then the correlation to the field test will be correct to some degree. In this study, the relative chamber size is defined as the ratio of chamber diameter to the diameter of probe in used, i.e $\frac{D_T}{B}$.

Parkin and Lunne (1982) investigate the boundary effects using two different sizes of probe and calibration chambers, tests were performed under two different boundary conditions, namely $BC1$ and $BC3$ of fig (1.2). It was reported that the boundary effect is dependent on the relative density of sands. Plots of cone resistance against relative chamber size are presented in fig (3.39). The curves show that for dense sand with relative density of 90%, the relative chamber size must be at least 50 for normally consolidated sand and about 100 for overconsolidated sands with O.C.R of 8. In loose sand with relative density of 15% to 30% the side boundary effect on the tip resistance is apparently negligible.

In the author's research, the chamber used in centrifuge tests and laboratory 1g tests is a rigid-walled tub. Tests by Phillips (1987) with same boundary conditions are shown in fig (3.38)a and b. In fig (3.38)a, test 4A, B, and C were done on fontainbleau sand with relative density of 87%, the distance from the rigid-wall to the probe ranges from $10B$, $20B$ and $42B$ where B is the probe diameter and is equal to 10mm. No boundary effect was observed. Fig (3.38)b shows tests on 14/25 sand with relative density of 97% using the 19.05mm probe diameter, the distance from the probe to the rigid boundary wall in test 5A, B, C and D ranges from $22.3B$, $10.5B$ and $5.2B$. Equally, no boundary effect was observed. Thus it may be concluded that, with the present method of setup for the experiments, no boundary wall related errors should influence the tip resistance.

In author's study on the bottom boundary effect, it was observed that the influence of the rigid bottom boundary started to affect the tip resistance by increasing rapidly at some distance X from the base as the cone approaches the bottom of the tub. Data collected from tests using 6.35, 10 and 19.05mm probe diameter shows that the bottom boundary effect is dependent on relative density. Plot of $\frac{X}{B}$ against relative density in fig (3.40) show an empirical correlation as

$$\frac{X}{B} = 0.1139(R.D) - 1.238$$

where X is the distance from the cone tip to the bottom boundary when the bottom boudary effect started to emerge and R.D is the relative density expressed in %.

3.6.6 Penetration Rate Effects

In the calibration tests, the penetrometer probe is pushed into the sand hydraulically at a rate controlled by a constant flow rate valve. The rate of penetration is in the range of 3 to 5 $\frac{mm}{sec}$. Since it is impossible to adjust the constant flow rate valve to give a constant flow rate for all tests, it is necessary to study if different penetration rates have any significant effect on the tip resistance.

Tests T14 and T15 were done on 14/25 sand and tests T43 and T44 were done on 52/100 sand, the penetration rates are 27.0, 3.6, 3.51 and 6.10 $\frac{mm}{sec}$ respectively. All these tests were carried out using the 10mm diameter probe. Plots of tip resistance against relative depth are shown in fig (3.41)a and b one may conclude that for penetration rates in the range of 3.5 to 27 $\frac{mm}{sec}$ there is no significant effect on the tip resistance. This would not of course be the case in low permeability saturated soils where excess pore pressure would be generated. Springman (1987) carried out a test using the piezocone probe describe earlier on clay overlying 30/52 sand which has a nominal grain diameter of approximately 0.4mm, the rate of penetration was 10 $\frac{mm}{sec}$. Comparison of static water pressure to the total pore pressure measured during penetration is shown in fig (3.42). Clearly, in the clay layer, where the permeability is low, excess pore pressure is generated because it is an undrained event. Once the piezocone has reached the sand layer, the excess pore pressure dropped to zero quickly which indicates a drained event, in that case, penetration rate should not affect the tip resistance significantly.

Kamp (1982) studied the rate of penetration effect and reported that higher tip resistance was measured for a rate of penetration in excess of 20 $\frac{mm}{sec}$ also tests carried out in very dense North Sea sands show that very high tip resistances were measured at shallow depth. This can be explained by the fact that dense sand tends to dilate during shearing at shallow depth where the mean effective stress acting on the potential rupture surface is low, therefore, negative excess pore pressure was generated and this will correspond to an increase in the tip resistance.

3.6.7 Roughness Effects

Most of the available investigations on the roughness effect are on flat strip or circular surface footings. Meyerhof (1955), Hansen and Christensen (1969), Graham and Stuart (1971) have shown that the bearing capacity of a rough flat surface footing is significantly higher than that of a smooth footing. Durgunoglu and Mitchell (1973) investigated the roughness effect in a wedge penetration test by glueing sand on the wedge surface. Wedge penetration resistance was then converted to a cone penetration resistance by a shape factor. The conclusion they drew was that the penetration resistance is higher for a rough surface.

It seems that no one has investigated the roughness effect of a cone in deep penetration except Tumay (1981), and Schaap and Zuidberg (1982) who studied the wear and tear of the cone face after a long usage. Fig (3.43) shows the wear and tear of a cone face. In practice, a new cone is not perfectly smooth, not to mention after a long usage. An investigation of roughness effect was carried out by the author using the 19.05mm smooth and rough cones. Tests T22 and T23 were done on 52/100 sand, tests T38 and T39 were done on 14/25 sand and tests T46 and T47 were done on 25/52 sand. All these tests were at 21g. Plots of tip resistance against relative depths are shown in fig (3.44)a. b and c. Paradoxically, they show that roughness of the cone does not appear to influence the tip resistance at all! The reason could be due to the fact that at such a high mean stress level in the vicinity of the cone face, even a smooth cone would be roughened and behave similar to the rough cone.

3.6.8 Overconsolidation Effects

In centrifuge modelling, the sand model can be stress cycled resulting in overconsolidation depending on the sequence of testing at different g-levels. For example, if a test is done on a model at 50g where in the past, this model had subjected to higher g-level, say 100g, then the model would be overconsolidated with an O.C.R of 2. Tests T48 and T50 were done on 25/52 sand with a relative density of 92% using the 10mm diameter probe. They were carried out at a nominal accelaration of 40g, but test T50 was done after the model had been stress cycled to 63g, i.e corresponding to an O.C.R of 1.575. Plots of tip resistance against relative depth are shown in fig (3.45), they indicate that overconsolidation affects the tip resistance considerably. This is because coefficient of earth pressure, k_0 has been increased after consolidation, resulting in an increased in insitu horizontal effective stress. Veismanis (1974), Jamiolkowski et al (1982) in their calibration chamber tests have shown that insitu horizontal effective stress becomes important for overconsolidated sands.

In Durgunoglu and Mitchell's (1972) theoretical analysis, horizontal stress have to be determined first which depends on the coefficient of earth pressure k_0 as shown in fig (5.1) before total equilibrium of forces can be considered. For normally consolidated sand this has been taken as $(1 - \sin \phi)$, subsequently, higher values of k_0 were used for overconsolidated sand. Therefore, Durgunoglu and Mitchell's method of calculation can consider the overconsolidation effect directly in the analysis. An example of the plot of bearing capacity factors $N_{q\gamma}$ against ϕ for different k_0 is shown in fig (3.46).

Schmertmann (1975) suggested an empirical relationship of tip resistance between normally consolidated and overconsolidated sand as

$$\frac{q_{(o.c)}}{q_{(n.c)}} = 1 + \chi\left[(O.C.R)^{\kappa} - 1\right]$$

The values of χ and κ are 0.75 and 0.42 respectively. By adopting Schmertmann's empirical correlation, the results are shown in fig (3.45).

In the field tests where the history of the soil is unknown, if the increase in tip resistance is due to overconsolidation effect, one would tend to misinterpret the result as a higher insitu density rather then the overconsolidation effect, unless maximum density of the soil insitu is known in which case the excess tip resistance can be attributed to overconsolidation effect. Therefore it is necessary to study the history of the soil insitu before interpreting the results from the CPT.

3.7 Summary

A set of accurate and consistent data from the centrifuge tests have been produced. The two major factors that govern the penetration resistance are the stress level and the density. The results are plotted as shown in fig (3.20)a to e so that they can be used to determine the fundamental soil properties either in a field test or in a centrifuge model test such as in the drum centrifuge where the void ratio of the sample is difficult to determine.

From the parametric studies that were carried out it was concluded that, no grain size related error was observed if $\frac{B}{d_{50}}$ is greater then 12, the penetration rate and the roughness of the cone surface has no significant effect on the tip resistance, the depth X at which the rigid bottom boundary started to influence the tip resistance depends on the relative density and can be empirically correlated as

$$\frac{X}{B} = 0.1139(R.D) - 1.238$$

The O.C.R and the scale of the probe affect the penetration resistance considerably, being higher for higher O.C.R or smaller scale of the probe diameter.

CHAPTER 4

1G LABORATORY TESTS

4.1 Introduction

Most of the cone penetration data that are available are obtained from tests on samples with either rigid or flexible boundaries with a surcharge applied to simulate the overburden stress that exists at depth in the field. The main objective of carrying out 1g laboratory tests is to compare the results with the centrifuge test results. Such a comparison provides an opportunity to study the validity of simulating self weight overburden stress by the application of surcharge pressure.

Further to that, it is an easier and less expensive way to carry out parametric studies into the influence of effects such as roughness, penetration rate and boundary effects, but more importantly, to check the cone penetration equipment by carrying out repeatable tests on the different sizes of probe designed by the author.

4.2 The Experimental Setup

The circular tub that was used for the centrifuge test was also used for the laboratory floor 1g test. The sand sample was prepared to the required density in a similar way to that outlined in chapter 3. The surcharge pressure was applied on top of the sand surface by means of a 12.7mm thick plate resting on it, the plate was reinforced with a 101.7×101.7mm box section cruciform and the load was applied to it by a pneumatic jack in a consolidation press frame. Eight holes with three different diameters were drilled into the plate as shown in fig (4.1) where the penetration testing is to be carried out. The reason for doing so is because eight tests can be performed for each sample prepared, but

CHAPTER 4

1G LABORATORY TESTS

4.1 Introduction

Most of the cone penetration data that are available are obtained from tests on samples with either rigid or flexible boundaries with a surcharge applied to simulate the overburden stress that exists at depth in the field. The main objective of carrying out 1g laboratory tests is to compare the results with the centrifuge test results. Such a comparison provides an opportunity to study the validity of simulating self weight overburden stress by the application of surcharge pressure.

Further to that, it is an easier and less expensive way to carry out parametric studies into the influence of effects such as roughness, penetration rate and boundary effects, but more importantly, to check the cone penetration equipment by carrying out repeatable tests on the different sizes of probe designed by the author.

4.2 The Experimental Setup

The circular tub that was used for the centrifuge test was also used for the laboratory floor 1g test. The sand sample was prepared to the required density in a similar way to that outlined in chapter 3. The surcharge pressure was applied on top of the sand surface by means of a 12.7mm thick plate resting on it, the plate was reinforced with a 101.7×101.7mm box section cruciform and the load was applied to it by a pneumatic jack in a consolidation press frame. Eight holes with three different diameters were drilled into the plate as shown in fig (4.1) where the penetration testing is to be carried out. The reason for doing so is because eight tests can be performed for each sample prepared, but more importantly, three different sizes of probe for the penetration test can be used in the same sample. To minimise stress relief on the surface from these holes, the diameter is kept close to the diameter of the probe to be used in the test so long as the probe can pass through without touching the plate.

Since most of the investigations in the centrifuge tests were done on normally consolidated sand, the surcharge pressures applied in the laboratory floor tests are in the sequence of 50, 100, 150 kPa for each series of tests using the three different sizes of probe.

4.3 Instrumentation

The instruments that were required for the laboratory floor test were the cone penetrometers and the logging system to collect the data, as outlined previously in chapter 3. The penetrometer is mounted either on the cruciform or on the plate with a packing depending on the position of the test. With this kind of arrangement, vertical penetration is guaranteed and it is robust. The assembled package for the laboratory floor test is shown in fig (4.1).

The hydraulic system in the laboratory floor test is very much simplified, unlike the elevated g tests, the nitrogen pressure to counteract the weight of the piston and probe at the bottom chamber of the penetrometer cylinder is not required.

During penetration testing, the pressurised water mixture to push the probe into the soil is released from the accumulator via a valve. The required pressure that was needed to be stored in the accumulator depends on the capacity of the load cell, i.e the size of the probe that was used, and is summarised in table (4.1). A schemetic diagram of the hydraulic and pressure control system is shown in fig (4.2).

After the test is completed, the pressure in the accumulator is released. The probe is retracted by supplying nitrogen gas to the bottom chamber of the penetrometer assembly, the mixture of water in the top chamber of the cylinder flows back to the accumulator.

Changing of the probe is then carried out or same probe diameter is used in a further test at another location.

4.4 Test Procedure

The procedure of carrying out a series of tests on a sample can be summarised into the following steps:-

- (1) A newly prepared sample in the tub is placed in the consolidometer frame. The plate which was mounted under the cruciform is placed on the sand surface and the hydraulic ram is lowered on it. Pressure is applied to the ram from a cylinder of pressurised nitrogen gas up to the required value of surcharge. The sample is then left for sometime until vertical consolidation has ceased which is monitored by a dial gauge.

- (2) The penetrometer assembly is mounted onto the plate at the position where the test is to be carried out. Hydraulic pipes are connected between the accumulator and the top chamber of the penetrometer.

- (3) The accumulator consists of two chambers, one of them is filled with approximately 10 litres of water mixture with fernox-b. The other chamber is pressurised with nitrogen gas which can be charged up at this stage. The required charge pressure depends on the size of the probe used and is shown in table (4.1).

- (4) Check that the logging system and the electric system of the penetrometer is functioning.

- (5) Test is performed by releasing the pressurised mixture of water from the accumulator to the top chamber of the penetrometer via a valve.

- (6) After the test has been completed, the nitrogen pressure in the accumulator is released, the probe is retracted by supplying air pressure to the bottom chamber of the penetrometer, thus the water mixture is caused to flow back to the accumulator.

• (7) The penetrometer assembly is removed and the probe is changed if required, step (2) to step (6) are repeated for next test.

4.5 Discussion of Test Results

As mentioned in earlier section that the main objective of carrying out 1g tests was to check the equipment and to make some parametric studies that can be performed at 1g. The test programme is summarised in table (4.2). The test results discussed in this section are :-

4.5.1 Check for Repeatibility

Before any empirical correlation to determine the fundamental soil properties or theoretical studies on the experimental results can be carried out, a set of good data must be produced from the experiment so that comparison is possible. To do this, the equipment must be capable of repeating the test results if they were to be carried out on the same sample at the same vertical stress. Checking the repeatibility of the test results was done employing the three different sizes of probes on the four types of sands that were used in the centrifuge tests.

Plots of tip resistance versus the depth of penetration for tests LT4, LT5 on 25/52 sand, LT18, LT19 on 52/100 sand and LT20, LT26 on FB sand using the 6.35mm diameter probe are shown in fig (4.3)a, b, c. Tests LT16, LT17 on 52/100 sand and LT24, LT25 on FB sand using the 10.0mm diameter probe are shown in fig (4.4) a, b. and tests LT9, LT10 on 14/25 sand and LT13, LT14 on 52/100 sand using the 19.05mm diameter probe are shown in fig (4.5)a, b respectively. The results indicate that the repeatibility of the test results is generally good, hence the equipment is capable of producing a set of accurate and consistent data.

4.5.2 Boundary Effects

The centrifuge test results have shown that no boundary effects have been observed if the distance from the probe to the rigid wall boundary is greater than 5.2B. Since the location of the holes on the surcharge plate are fixed, only the 10.0mm probe can be used for this investigation at 1g.

Plots of tests for LT1, LT2 on 25/52 sand and LT6, LT7 on 14/25 sand which have a relative density of 79.3% and 98.5% were shown in fig (4.6)a, b, the distance from the probe to the rigid wall boundary were 20B and 15B respectively. Clearly, the plots show that no boundary related error was observed.

4.5.3 Roughness Effects

The investigation of the roughness effect were carried out using the rough and the smooth cones that have been discussed in chapter 3. Plots of the tip resistance versus the depth of penetration for tests LT1, LT3 on 25/52 sand, LT6, LT8 on 14/25 sand, LT15, LT17 on 52/100 sand and LT25, LT26 on FB sand using the 10.0mm diameter probe are shown in fig (4.7)a, b, c, d and tests LT9, LT11 on 14/25 sand, LT12, LT13 on 52/100 sand and LT22, LT23 on FB sand using the 19.05mm diameter probe are shown in fig (4.8)a, b, c respectively. These plots show that surface roughness of cones has little or no influence on the tip resistance and agreed well with the centrifuge test which also showed similar results.

4.5.4 Penetration Rate Effects

These tests were carried out on dry sand similar to that used in the centrifuge tests. Tests LT51 and LT52 were carried out on 52/100 sand using the 10.0mm diameter probe with a surcharge of 100kPa, the penetration rates were 3.2 and 4.9$\frac{mm}{sec}$ respectively. Plots of the tip resistance versus the depth of penetration are shown in fig (4.9). They show that this amount of variation to the penetration rate had little or no influence on the tip resistance.

4.5.5 Scale Effects

To investigate the scale effects, tests were carried out using three different sizes of probes that were used for the centrifuge tests at a constant applied surcharge.

Plots of tests for LT22, LT25, LT20 on FB sand with surcharge of 50kPa, LT12, LT15, LT18 on 52/100 sand with surcharge of 150kPa using the 19.05, 10.0 and 6.35mm and LT31, LT32 on 14/25 sand with surcharge of 100kPa using the 19.05 and 10.0mm probe diameter are shown in fig (4.10)a, b, c respectively. They show that the smaller the diameter, the higher is the tip resistance which is a similar result to that obtained from the centrifuge test results.

4.5.6 Stress Level Effects

The investigation of stress level effects was performed on 14/25 sand with surcharge pressure increased in the sequence of 50, 100, 150kPa. Plots of tests LT29, LT30 and LT37, LT38 using the 6.35mm diameter probe are shown in fig (4.11)a, b. It must be noted that for the 6.35mm diameter probe test on 14/25 sand, grain size related errors may have influenced the tip resistance. The tests using the 10.0mm diameter probe are LT27, LT32, LT33 and LT36, LT39, LT48 which are shown in fig (4.12)a, b. Plots of tests for (LT28, LT31, LT34), (LT35, LT40, LT41) and LT44, LT47, LT50 using the 19.05mm diameter probe are shown in fig (4.13)a, b, c. Clearly, those plots show that the tip resistance is increasing at a decreasing rate for an increase in vertical stress which is a similar trend to that observed in the centrifuge test results. This phenomenon can be explained on the basis that as the normal stress increases, the mobilised angle of shearing resistance decreases which is consistent with the shear box and triaxial data presented in fig (2.10).

4.5.7 Relative Density Effects

The test results of laboratory floor 1g test have shown that the tip resistance increases rapidly in the initial penetration follow by a relatively gentle constant increase in tip resistance with depth, when the tip approaches the bottom boundary, the tip resistance increases rapidly again. The initial portion of the curve is due to the top boundary effect and the last portion is due to the bottom boundary effect, therefore the only useful information is the central portion of the curves, their magnitude depends on the surcharge and the relative density of the sand. It must be pointed out here that over the central portion of the curves where top and bottom boundary effects are considered to be absent, the tip resistance do not remain constant but increased slightly with depth. Parkin and Lunne (1982) reported a similar effect in their flexible-walled chamber tests.

In this investigation, the relative density of the 14/25 sand samples are 86.1, 47.1, and 24%, the plots of tests LT31, LT40, LT47 and LT34, LT41, LT51 using the 19.05mm diameter probe with applied surcharges of 100 and 150kPa respectively are shown in fig (4.14)a, b and tests (LT27, LT36, LT43), (LT32, LT39, LT48) and LT33, LT42, LT49 using the 10.0mm probe with surcharges of 50, 100, 150kPa respectively are shown in fig (4.15)a, b, c.

The plots show that the difference in tip resistance between the dense and the medium loose sand is very much higher than the difference in tip resistance between the medium loose and the loose sand. A similar trend was also observed in the centrifuge tests for 14/25 sand. This phenomenon is due to the angle of dilation ν, which makes a large contribution to the strength of dense sand, the rate of dilation is a function of density of the soil rather than ϕ and may even be zero as in the case of loose sand although ϕ is not. Therefore the angle of shearing resistance ϕ on the rupture plane may be considered to be comprised of two components, ϕ_{crit} and ν i.e

$$\phi = \phi_{crit} + f(\nu)$$

Bolton (1986) has shown that for plane strain

$$\phi = \phi_{crit} + 0.8\nu$$

Rowe's (1962) stress-dilatancy theory link ν and ϕ as

$$\left(\frac{1+\sin\phi_{crit}}{1-\sin\phi_{crit}}\right)\left(\frac{1+\sin\nu_m}{1-\sin\nu_m}\right) = \left(\frac{1+\sin\phi_m}{1-\sin\phi_m}\right)$$

where the subscript m refers to mobilised angle. Therefore the dilatancy effect affects the penetration resistance considerably in the case of coarse dense sand.

4.6 Comparison of the Test Results.

To compare the tip resistance between the centrifuge tests and the 1g laboratory floor test results for a comparable relative density, average values of the central portion of curves of the 1g tests have been used i.e at $\frac{D}{B} = 12$, and are presented in table (4.3). They show that at low stress level, the centrifuge test and the 1g test results agreed very well. At the higher stress level, the laboratory 1g test results tend to underestimate the strength of the soil. This is probably due to the stress gradient effect that is present in the centrifuge modelling, but absent in the 1g laboratory test where the whole sample is assumed to be subjected to a uniform stress distribution with depth. Hence a smaller average value of ϕ is mobilised compared to the higher average value of ϕ that is mobilised when the distribution of stress increases with depth as in the case of centrifuge modelling and also in the rigid top plate 1g tests, it is likely that the simulated overburden stress distribution has been significantly modified as the penetrator advances, being higher in the vicinity of the penetrator and tapering off to the surcharge value at some radial distance. Thus it is concluded that perhaps it is improper to simulate the overburden stress due to the self weight body force gradient that is present in the real field by simply using a a rigid plate.

4.7 Correlation of Test Results using the State Parameter

The state parameter concept was introduced by Been and Jefferies (1985) to correlate the state of a sand with the tip resistance. This concept was introduced because for the same relative density and stress level of same sand but with quite different grain size, the tip resistance obtained is not the same. The state of a sand ψ' has combined the effects of the void ratio and the effective stress and is defined as

$$\psi' = e + \lambda \text{In}\, p' - e_{ss}$$

where e is the void ratio of the sand, λ is the slope of the steady state line, p' is the mean normal effective stress and e_{ss} is the void ratio on the steady state line at $\text{In}\,\text{p}' = 1\frac{\text{kN}}{\text{m}^2}$ as shown in fig (4.16).

The values of λ and e_{ss} to determine the state parameter of a sand were obtained by carrying out undrained triaxial tests. For Leighton Buzzard sand, these parameters have been taken as 0.08 and 1.000 (Jefferies et al (1985)).

To correlate the laboratory 1g test and the centrifuge test results of the tip resistance q_c with shear strength of soil, the state parameter approach has been followed. To estimate the mean stress p′, values of k_o are calculated from $(1 - \sin\phi)$ for normally consolidated sand, whereas for overconsolidated sand of the centrifuge test T50, the value of k_o is estimated from the known O.C.R using the Schmertmann's relationship (1975) $\text{k}_o(o.c)=(\text{O.C.R})^{0.42}\times\text{k}_o(n.c)$. Fig (4.18) shows the correlation between the tip resistance and the state parameters of different grain sizes and an O.C.R, fig (4.17) shows the plot of the mobilised angle of shearing resistance from drained triaxial test against the state parameters. which show quite a good correlation. This means that the concept of state parameter to combine the effect of grain size, effective stress and overconsolidation ratio which was introduced in the first place is satisfactory. (Note that only shown for O.C.R=1.575)

4.8 Summary

The equipment that was designed and machined by the author has proved to be able to produce consistent data. The results of the 1g test also show that the rate of penetration and roughness surface of cone has no significant effect on the tip resistance. Comparison of the test results between the centrifuge and the laboratory floor 1g tests reveal that ϕ is highly sensitive to the stress distribution with depth, hence it is improper to use a surcharge to simulate the stress distribution with depth that exist in the real field.

CHAPTER 5

THEORETICAL FRAMEWORK I

5.1 Introduction

The theoretical analysis of quasi-static cone penetration testing will be divided into two parts, namely, classical bearing capacity theory which will be considered to apply to deep penetration but only up to a characteristic depth, and spherical expansion theory which is considered to be valid at depths greater than the characteristic depth.

5.2 Classical Bearing Capacity Theory

Most bearing capacity solutions for a rigid perfectly plastic, incompressible weightless material with shear strength characteristic governed by the Mohr-coulomb failure criterion $\tau_f = c + \sigma \tan\phi$ are attributed to Prandtl (1921) and Reisnner (1924). The solution for the bearing capacity under a strip footing is

$$\begin{aligned} q_f = c\cot\phi \Big[\big(\exp(\pi\tan\phi)\big)\tan^2\big(\frac{\pi}{4}+\frac{\phi}{2}\big) - 1 \Big] \\ + q\Big[\big(\exp(\pi\tan\phi)\big)\tan^2\big(\frac{\pi}{4}+\frac{\phi}{2}\big) \Big] \end{aligned} \tag{5.1}$$

Terzaghi (1943) included the self-weight term as $0.5\gamma_s BN_\gamma$ into the Prandtl-Reisnner equation. Shape factors were then employed to consider other foundation configurations.

Meyerhof (1951), Brinch Hansen (1961), De Beer (1967) suggested that for deep foundation, the depth effects can be taken into account by a depth factor. The general bearing capacity equation becomes

$$q_f = cN_c s_c d_c + qN_q s_q d_q + 0.5\gamma_s BN_\gamma s_\gamma d_\gamma \tag{5.2}$$

where

N_c,N_q,N_γ = bearing capacity factor for cohesion, surcharge and self-weight terms.

s_c,s_q,s_γ = shape factors for cohesion, surcharge and self-weight terms.

d_c,d_q,d_γ = depth factors for cohesion, surcharge and self-weight terms.

Since the general bearing capacity equation was formulated from the strip footing case, Terzaghi (1943), Skempton (1951) suggested the following shape factors to be used for other footing configurations.

$$\begin{matrix} s_c \\ s_\gamma \end{matrix} = \begin{matrix} 1.3 \\ 0.6 \end{matrix} \qquad \textbf{circular}$$

$$\begin{matrix} s_c \\ s_\gamma \end{matrix} = \begin{matrix} 1+0.2(\frac{B}{L}) \\ 1-0.2(\frac{B}{L}) \end{matrix} \qquad \textbf{square or rectangular}$$

where B is the width and L is the length of the footing.

For deep foundations, the assumed failure mechanisms are shown in fig (5.1)a and b. Terzaghi (1943) assumed that the soil above the foundation level can be considered as surcharge. Later Brinch Hansen (1961), Meyerhof (1951,1961,1963) and De Beer (1967,1970) each suggested their own shape and depth factor to take account of these effects.

Durgunoglu and Mitchell (1973) used an equilibrium analysis to analyse the penetration data obtained from the lunar surface by the Appolo 15 self-boring penetrometer. The assumed failure mechanism shown in fig (5.2) comprised a plane shear zone AOB adjacent to the wedge, a logarithmic spiral BC approximated the slip surface of the radial shear zone which either intersects with the ground surface for small relative depth ratio $\frac{D}{B}$ or reaches a vertical tangent CD for large relative depth. Static equilibrium was then considered by summing all moments about point O to zero. New bearing capacity factors $N_{q\gamma}$ which included the self weight and depth of penetration were formulated. The analysis did not assume the curvealinear nature of the shear strength envelope which occurs with increasing stress level. This means that ϕ was constant along the potential rupture surface which is unlikely to be true. Brinch Hansen's shape factor is then introduced to consider the circular configuration of the penetrometer. The resistance to penetration is

$$q_c = s_{q\gamma} N_{q\gamma} B. \tag{5.3}$$

where B is the width of the penetrometer and $s_{q\gamma}$ is the shape factor and can be obtained from fig (5.3). The bearing capacity factor $N_{q\gamma}$ for different relative depths and roughnesses of the wedge are shown in fig (5.4)a to c.

From the information of the shape and depth factors that are available, it is not clear as to which one to adopt. Consequently this leads one to the development of direct solutions using the method of characteristic based on plasticity theory. The method can handle slightly more complicated problems such as both plane strain and the axisymmetric case, and different relative depth ratios can be incorporated.

5.3 Review of the Method of Characteristics

Most of the available solutions based on the method of characteristics are for either plane strain or axisymmetric flat surface footings. Shield (1955) has presented a solution for an axisymmetric surface footing on a weightless Tresca material. Cox (1961,1962) pointed out that if a large region of soil is undergoing plastic deformation, the effect of the self-weight body force of the material is likely to be important and must be included in the analysis. Relative cohesion $c^* = c + p_a \tan\phi$ is used in place of true cohesion c, where p_a is the atmospheric pressure. A dimensionless factor $G = \frac{\gamma B}{2c^*}$ is then introduced. In Cox's analysis, a small value of factor G is equivalent to the neglect of the soil self-weight body force.

Sokolovski (1965) presented the method of characteristics in detail and obtained solutions to a number of important problems, thereafter many researchers adopted the Sokolovski kind of calculation and extended it to other problems such as rough and partially rough flat surface footings, for example (Graham and Stuart, 1971). Larkin (1968) investigated the shallow footing by using Cox's analysis, slip lines were generated from the surface and the major principal stress direction maintained horizontal in the passive zone as for the surface footing, see fig(5.10). Graham and Hovan (1986) extended the method further by considering that mobilised angles of shearing resistance are stress dependent using the critical state soil model. Shi (1988) studied the jack-up spud problem in the centrifuge and concluded that method of characteristic analysis can predict the experimental results satisfactorily.

Though the method is powerful, it seems that it has not been used to analyse the quasi-static cone penetration resistance in cohesionless soils at different relative depths for a given relative roughness except by Nowartzki (1971) who analysed the S.P.T by assuming that the slip lines revert back to the penetrometer shaft. Later Nowartzki and Karafiath (1972) assumed that the slip lines end at base level. They adopted this new assumption because their theoretical prediction due to the previous assumption overpredicted the experimental values. It is considered that the reason for this overprediction is that he assumed that the mobilised angle of shearing resistance is independent of mean stress level along the slip surface. Since the radial fan zone is the region where major changes of mean stress level take place as a result of the rotation of major principal stress direction, it is equally likely that mobilised angles of shearing resistance has been reduced from ϕ_p at the equivalent free surface to ϕ_{crit} in the vicinity of cone tip for a large relative depth. Therefore, it is improper to use constant ϕ analysis that obtained from the triaxial test, especially when the changes of normal stress along the potential rupture surface is large as in the case of penetration resistance test and ϕ is a variable which depends on the stress level which has demostrated in fig (2.10), unless a pseudo-constant ϕ analysis is carried out which is independent of stress.

5.4 Governing Equations

All stress components acting on an element as shown in fig (5.5) and must satisfy the following equilibrium equations. With z-axis acting vertically downward, they can be expressed as:-

$$\frac{\partial \sigma_r}{\partial r} + \frac{\partial \tau_{rz}}{\partial z} + \frac{n}{r}(\sigma_r - \sigma_\theta) = 0$$

$$\frac{\partial \tau_{zr}}{\partial r} + \frac{\partial \sigma_z}{\partial z} + \frac{n}{r}\tau_{zr} = \gamma_s$$

in which

$$n = \begin{cases} 0 & \text{Plane Strain} \\ 1 & \text{Axisymmetric} \end{cases}$$

where σ_θ is the circumferential stress for the axisymmetric case and is equivalent to the intermediate principal stress, σ_z is the vertical stress and σ_r is the radial (horizontal) stress.

If γ represents the bulk unit weight at an orientation η to the vertical axis, then the radial body force becomes $\gamma \sin \eta$ and the axial body force becomes $\gamma \cos \eta$, these equilibrium equations can then be written as:-

$$\frac{\partial \sigma_r}{\partial r} + \frac{\partial \tau_{rz}}{\partial z} + \frac{n}{r}(\sigma_r - \sigma_\theta) = \gamma \sin \eta \tag{5.4}$$

$$\frac{\partial \tau_{zr}}{\partial r} + \frac{\partial \sigma_z}{\partial z} + \frac{n}{r}\tau_{zr} = \gamma \cos \eta \tag{5.5}$$

If the soil is assumed to be a rigid-perfectly plastic material, i.e a special case where the failure condition is identical to the yield condition and the elastic modulus is infinite, then the Mohr-Coulomb failure criterion can be used to specify the yield surface. From fig (5.6)

$$(\sigma_z + \sigma_r)\sin\phi = \left[(\sigma_r - \sigma_z)^2 + 4\tau_{rz}^2\right]^{\frac{1}{2}}$$

From Mohr's circle which represents stresses on planes as shown in fig (5.8), the directions of the two characteristic lines can be determined from the pole at point P. By adopting the sign convention α characteristic as positive shear and β characteristic as negative shear, these two characteristic lines α and β make an equal angle $\mp\epsilon$ with the direction of major principal stress σ_1 as shown in fig (5.7) where

$$\epsilon = \frac{\pi}{4} - \frac{\phi}{2} \tag{5.6}$$

By introducing two dependent variables representing the mean stress σ and the orientation of the major principal stress direction ψ with the z-axis as

$$\sigma = \frac{\sigma_r + \sigma_z}{2} \tag{5.7}$$

and

$$\psi = \frac{1}{2}\tan^{-1}\frac{2\tau_{rz}}{(\sigma_r - \sigma_z)} \tag{5.8}$$

the stress components written in terms of σ and ψ are

$$\sigma_r = \sigma(1 - \sin\phi\cos 2\psi) \tag{5.9}$$

$$\sigma_z = \sigma(1 + \sin\phi\cos 2\psi) \tag{5.10}$$

$$\tau_{rz} = \tau_{zr} = \sigma\sin\phi\sin 2\psi \tag{5.11}$$

In the plane strain case, it will be shown later that the equilibrium equations combined with the Mohr-coulomb failure criterion make the stress components statically determinate. In the axisymmetric case, the extra stress component due to the circumferential stress σ_θ makes them statically indeterminate. Consequently, an assumption with regard to σ_θ is necessary. Haar and Von Karman hypothesized that σ_θ is equal to either the major or the minor principal stress. Detailed studies of Shield (1955), Cox (1961) and Chen (1975) have pointed out that σ_θ is equal to the major or the minor principal stress depending on whether the soil under loading is moving inward or outward.

In the following analysis, σ_θ is assumed to be equal to the minor principal stress σ_3 because the soil adjacent to the penetrator is moving away during penetration. Thus σ_θ

can be expressed in terms of the mean stress σ as

$$\sigma_\theta = \sigma(1 - \sin\phi) \tag{9}$$

Partially differentiating the stress equations (5.9) through (5.12) with respect to r and z to give

$$\frac{\partial \sigma_r}{\partial r} = \frac{\partial \sigma}{\partial r}(1 - \sin\phi\cos 2\psi) + 2\sigma\sin\phi\sin 2\psi\frac{\partial \psi}{\partial r} \tag{5.13}$$

$$\frac{\partial \sigma_z}{\partial z} = \frac{\partial \sigma}{\partial z}(1 + \sin\phi\cos 2\psi) - 2\sigma\sin\phi\sin 2\psi\frac{\partial \psi}{\partial z} \tag{5.14}$$

$$\frac{\partial \tau_{zr}}{\partial r} = \frac{\partial \sigma}{\partial r}\sin\phi\sin 2\psi + 2\sigma\sin\phi\cos 2\psi\frac{\partial \psi}{\partial r} \tag{5.15}$$

$$\frac{\partial \tau_{rz}}{\partial z} = \frac{\partial \sigma}{\partial z}\sin\phi\sin 2\psi + 2\sigma\sin\phi\cos 2\psi\frac{\partial \psi}{\partial z} \tag{5.16}$$

and substituting equations (5.13) through (5.16) into the equilibrium equations in (5.4) and (5.5), a set of partial differential equations is obtained

$$\begin{aligned}(1 - \sin\phi\cos 2\psi)\frac{\partial \sigma}{\partial r} + 2\sigma\sin\phi\sin 2\psi\frac{\partial \psi}{\partial r} + 2\sigma\sin\phi\cos 2\psi\frac{\partial \psi}{\partial z} + \\ \frac{\partial \sigma}{\partial z}\sin\phi\sin 2\psi + \frac{n}{r}\sigma\sin\phi(1 - \cos 2\psi) = \gamma\sin\eta\end{aligned} \tag{5.17}$$

$$\begin{aligned}(1 + \sin\phi\cos 2\psi)\frac{\partial \sigma}{\partial z} - 2\sigma\sin\phi\sin 2\psi\frac{\partial \psi}{\partial z} + 2\sigma\sin\phi\cos 2\psi\frac{\partial \psi}{\partial r} + \\ \frac{\partial \sigma}{\partial r}\sin\phi\sin 2\psi + \frac{n}{r}\sigma\sin\phi\sin 2\psi = \gamma\cos\eta\end{aligned} \tag{5.18}$$

Taking advantage of equation (5.6), equations (5.17) and (5.18) can further be simplified by equation (5.17)$\times\cos(\psi - \epsilon)$-equation (5.18)$\times\sin(\psi - \epsilon)$ to give

$$\begin{aligned}&\left[\cos\phi\frac{\partial \sigma}{\partial r} + 2\sigma\sin\phi\frac{\partial \psi}{\partial r} - \gamma\sin(\eta - \phi)\right]\sin(\psi + \epsilon) + \\ &\left[\cos\phi\frac{\partial \sigma}{\partial z} + 2\sigma\sin\phi\frac{\partial \psi}{\partial z} - \gamma\cos(\eta - \phi)\right]\cos(\psi + \epsilon) + \\ &\frac{n}{r}\sigma\sin\phi\left[\cos(\psi - \epsilon) - \cos(\psi + \epsilon)\right] = 0\end{aligned} \tag{5.19}$$

similarly, $equation(5.17) \times \cos(\psi+\epsilon) - equation(5.18) \times \sin(\psi+\epsilon)$ to give

$$\begin{aligned}&\left[\cos\phi\frac{\partial\sigma}{\partial r} - 2\sigma\sin\phi\frac{\partial\psi}{\partial r} - \gamma\sin(\eta+\phi)\right]\sin(\psi-\epsilon)+\\&\left[\cos\phi\frac{\partial\sigma}{\partial z} - 2\sigma\sin\phi\frac{\partial\psi}{\partial r} - \gamma\cos(\eta+\phi)\right]\cos(\psi-\epsilon)+\\&\frac{n}{r}\sigma\sin\phi\left[\cos(\psi-\epsilon) - cos(\psi+\epsilon)\right] = 0\end{aligned} \tag{5.20}$$

Since the two characteristic lines are

$$\frac{dr}{dz} = \tan(\psi \mp \epsilon) \tag{5.21}$$

where the upper sign holds for an α characteristic and the lower sign holds for a β characteristic. The solution along these characteristic lines from equations (5.19) and (5.20) are

$$\begin{aligned}d\sigma\cos\phi \mp 2\sigma\sin\phi d\psi + \frac{n}{r}\sigma\big(\sin\phi\cos\phi dr \mp (\sin^2\phi - \sin\phi)dz\big) =\\ \gamma\big(\sin(\eta\pm\phi)dr + \cos(\eta\pm\phi)dz\big)\end{aligned} \tag{5.22}$$

where again the upper sign holds along α characteristics and lower sign holds along β characteristics.

5.4.1 Numerical Analysis

The variation of the dependent variables σ and ψ along the characteristic curves are expressed in first order differential equations (5.22). To solve these equations by direct integration seems remote, hence, numerical analysis using finite difference has been employed. A point within the plastic field is determined by solving equations (5.21) and (5.22). Suppose that to solve an unknown point p which lies on the intersection of α and β characteristics from either a known boundary condition or from two previously computed points $p_1(r,z,\sigma,\psi)_1$ and $p_2(r,z,\sigma,\psi)_2$ as shown in fig (5.9). The values of $(r,z,\sigma,\psi)_p$ at point p can be obtained by solving the following finite difference equations from equations (5.21) and (5.22) for $\eta = 0$

$$(r - r_2) = (z - z_2)\tan(\psi_2 - \epsilon)\cdots\alpha\ characteristic$$

$$(r - r_1) = (z - z_1)\tan(\psi_1 + \epsilon) \cdots \beta \; characteristic$$

$$\begin{gathered}(\sigma - \sigma_2) - (\sigma + \sigma_2)\tan\phi(\psi - \psi_2) = \\ -n\frac{\sigma + \sigma_2}{r + r_2}\Big[\sin\phi(r - r_2) - (\frac{\sin^2\phi - \sin\phi}{\cos\phi})(z - z_2)\Big] + \quad along\; \alpha\; characteristic \\ \gamma\Big[\tan\phi(r - r_2) + (z - z_2)\Big]\end{gathered}$$

$$\begin{gathered}(\sigma - \sigma_1) + (\sigma + \sigma_1)\tan\phi(\psi - \psi_1) = \\ -n\frac{\sigma + \sigma_1}{r + r_1}\Big[\sin\phi(r - r_1) + (\frac{\sin^2\phi - \sin\phi}{\cos\phi})(z - z_1)\Big] + \quad along\; \beta\; characteristic \\ \gamma\Big[-\tan\phi(r - r_1) + (z - z_1)\Big]\end{gathered} \tag{5.23}$$

It will be more convenient to use dimensionless terms by normalising the mean stress σ as $\varrho = \frac{\sigma}{0.5B\gamma}$ and the coordinates r and z expressed in units of 0.5B. Unfortunately the equations are implicit. Shi(1988) suggested the following substitution. Rewriting equations (5.23)

$$z = \left(\frac{z_1\tan(\psi_1 + \epsilon) - z_2\tan(\psi_2 - \epsilon) + r_2 - r_1}{\tan(\psi_1 + \epsilon) - \tan(\psi_2 - \epsilon)}\right) \tag{5.24}$$

$$r = r_1 + (z - z_1)\tan(\psi_1 + \epsilon) = r_2 + (z - z_2)\tan(\psi_2 - \epsilon) \tag{5.25}$$

and

$$\begin{aligned}(\varrho - \varrho_2) - 2\varrho_2\tan\phi(\psi - \psi_2) &= A \\ (\varrho - \varrho_1) + 2\varrho_1\tan\phi(\psi - \psi_1) &= B\end{aligned} \tag{5.26}$$

where

$$\begin{aligned}A = -n\frac{2\varrho_2}{r + r_2}\Big[(\sin\phi(r - r_2) - \left(\frac{\sin^2\phi - \sin\phi}{\cos\phi}\right)(z - z_2)\Big] + \\ \tan(r - r_2) + (z - z_2) + \varrho_2 - 2\varrho_2\tan\phi\psi_2 \\ B = -n\frac{2\varrho_1}{r + r_1}\Big[(\sin\phi(r - r_1) + \left(\frac{\sin^2\phi - \sin\phi}{\cos\phi}\right)(z - z_1)\Big] - \\ \tan\phi(r - r_1) + (z - z_1) + \varrho_1 + 2\varrho_1\tan\phi\psi_1\end{aligned}$$

$$(r - r_1) = (z - z_1)\tan(\psi_1 + \epsilon) \cdots \beta \; characteristic$$

$$\begin{aligned}(\sigma - \sigma_2) - (\sigma + \sigma_2)\tan\phi(\psi - \psi_2) = \\ -n\frac{\sigma + \sigma_2}{r + r_2}\left[\sin\phi(r - r_2) - (\frac{\sin^2\phi - \sin\phi}{\cos\phi})(z - z_2)\right] + \\ \gamma\left[\tan\phi(r - r_2) + (z - z_2)\right]\end{aligned} \quad along\ \alpha\ characteristic$$

$$\begin{aligned}(\sigma - \sigma_1) + (\sigma + \sigma_1)\tan\phi(\psi - \psi_1) = \\ -n\frac{\sigma + \sigma_1}{r + r_1}\left[\sin\phi(r - r_1) + (\frac{\sin^2\phi - \sin\phi}{\cos\phi})(z - z_1)\right] + \\ \gamma\left[-\tan\phi(r - r_1) + (z - z_1)\right]\end{aligned} \quad along\ \beta\ characteristic \tag{5.23}$$

It will be more convenient to use dimensionless terms by normalising the mean stress σ as $\varrho = \frac{\sigma}{0.5B\gamma}$ and the coordinates r and z expressed in units of 0.5B. Unfortunately the equations are implicit. Shi(1988) suggested the following substitution. Rewriting equations (5.23)

$$z = \left(\frac{z_1\tan(\psi_1 + \epsilon) - z_2\tan(\psi_2 - \epsilon) + r_2 - r_1}{\tan(\psi_1 + \epsilon) - \tan(\psi_2 - \epsilon)}\right) \tag{5.24}$$

$$r = r_1 + (z - z_1)\tan(\psi_1 + \epsilon) = r_2 + (z - z_2)\tan(\psi_2 - \epsilon) \tag{5.25}$$

and

$$(\varrho - \varrho_2) - 2\varrho_2\tan\phi(\psi - \psi_2) = A$$

$$(\varrho - \varrho_1) + 2\varrho_1\tan\phi(\psi - \psi_1) = B \tag{5.26}$$

where

$$\begin{aligned}A = -n\frac{2\varrho_2}{r + r_2}\left[(\sin\phi(r - r_2) - \left(\frac{\sin^2\phi - \sin\phi}{\cos\phi}\right)(z - z_2)\right] + \\ \tan(r - r_2) + (z - z_2) + \varrho_2 - 2\varrho_2\tan\phi\psi_2\end{aligned}$$

$$\begin{aligned}B = -n\frac{2\varrho_1}{r + r_1}\left[(\sin\phi(r - r_1) + \left(\frac{\sin^2\phi - \sin\phi}{\cos\phi}\right)(z - z_1)\right] - \\ \tan\phi(r - r_1) + (z - z_1) + \varrho_1 + 2\varrho_1\tan\phi\psi_1\end{aligned}$$

Equation (5.26) can now be written in an explicit form as

$$\varrho - 2\varrho_2 \tan\phi\psi = A$$

$$\varrho + 2\varrho_1 \tan\phi\psi = B$$

or

$$\varrho = \frac{A\varrho_1 + B\varrho_2}{\varrho_1 + \varrho_2} \tag{5.27}$$

$$\psi = \frac{-(A-B)}{2\tan\phi(\varrho_2 + \varrho_1)} \tag{5.28}$$

Numerical computation is required to solve equations (5.24), (5.25), (5.27), (5.28) respectively. The accuracy of the numerical analysis depends on the size of network and the criterion of errors as the slip lines are curves between two known points and an unknown point. To improve the accuracy and to reduce the iteration times, the computing process is repeated by using $\varrho_2^\star = 0.5(\varrho + \varrho_2)$ and $\psi_2^\star = 0.5(\psi + \psi_2)$ along α characteristic, $\varrho_1^\star = 0.5(\varrho + \varrho_1)$ and $\psi_1^\star = 0.5(\psi + \psi_1)$ along β characteristic where asterisk represent the new values to be used for each process until convergence is satisfied.

5.4.2 Depth of Penetration effects

The increase in penetration resistance due to penetrating effects can be assumed to be because of the following reasons:-

• (1) Increase in overburden pressure and neglecting the shear strength of the overburden.

• (2) The shear strength of the overburden has been mobilised but neglecting the rotation of principal stress direction.

• (3) The shear strength of the overburden has been mobilised and the rotation of principal stress direction has been incorporated.

Nowatzki and Karafiath (1972) analysed deep foundations by assuming that slip surface ends at base level, as was assumed by Terzaghi (1943) in fig (5.1)b means that shear strength of overburden has been neglected. Larkin (1968) extended Cox's (1963) slip line analysis on footing problems in cohesionless soils has shown that the bearing capacity is sensitive to depth of burial. The anlysis assumed that the shear strength of the overburden has been mobilised, but the major principal stress direction is horizontal throughout the overburden and the included angle of the radial fan zone has been maintained as in fig (5.10). This means that the angle of rotation of principal stresses direction is similar to the case of a surface footing. Consequently, it is not possible to distinguish between assumption (1) and (2), Hence, the theoretical solutions of bearing capacity due to penetrating effects with increasing overburden pressure will be conservative.

Meyerhof (1951) used the limit equilibrium analysis to analyse a deep strip footing on weightless material and Nowartzki (1971) adopted the slip line analysis for the S.P.T by including the shear strength of the overburden and allowing the rotation of principal stress direction. The assumption to account for the penetration effect is that the included angle θ_0 in fig (5.11) of the radial fan zone has been increased. Fig (5.12)a and b shows how the radial fan zone has been increased for $\phi = 40°$ at $\frac{D}{B} = 3$ and $\frac{D}{B} = 10$ in a perfectly rough 60° wedge. As $\frac{D}{B}$ is increased to $\frac{D_c}{B}$ the slip surface reverts back to the shaft, no additional rotation of the principal stress is allowed beyond this depth D_c. Many researchers refer to this depth as a critical depth where maximum bearing capacity factor is reached. The existence of such a depth is questionable. However, in order to clarify the terminology, this depth will be defined as the characteristic depth from now on. For convenience, three different depths will be defined i.e as shallow as in fig (5.12)a, as deep as in fig (5.12)b and very deep for depths greater than the characteristic depth.

5.4.2.1 Determination of Angle γ_T in the Plane Shear Zone

Angle OAB of the plane shear zone adjacent to the wedge in fig (5.11) is determined from the Mohr's circle in fig (5.13) and making use of the known base angle ψ_c, and the relative friction angle $\frac{\delta}{\phi}$ where ϕ is the mobilised angle of friction and δ is friction angle at the wedge sand interface. OB is the slip line where the shear strength has been fully mobilised, This will correspond to point b on the Mohr's circle in fig (5.13), and will have a normal stress σ_b and a shear stress τ_b. The stresses on plane OA are τ_a and σ_a where

$$\tau_a = \frac{(\sigma_1 - \sigma_3)}{2} \cos(2\gamma_T - \phi) \tag{1}$$

$$\sigma_a = \frac{(\sigma_1 + \sigma_3)}{2} + \frac{(\sigma_1 - \sigma_3)}{2} \sin(2\gamma_T - \phi)$$

and

$$\tau_a = \sigma_a \tan \delta \tag{5.29}$$

The ratio of major to minor principal stress is

$$\frac{\sigma_1}{\sigma_3} = \frac{1 + \sin \phi}{1 - \sin \phi}$$

equation (5.29) can be rewritten as

$$\tan \delta = \frac{\sin \phi \cos(2\gamma_T - \phi)}{1 + \sin \phi \sin(2\gamma_T - \phi)} \tag{5.30}$$

Hence angle γ_T can be obtained by iteration for a given roughness δ, and angle of internal friction ϕ.

For a purely smooth face $\sin \phi \cos(2\gamma_T - \phi) = 0$ and for $\phi \neq 0$ $\gamma_T = \frac{\pi}{4} + \frac{\phi}{2}$. Point a on the Mohr circle in fig (5.11) coincide with σ_1. For a perfectly rough face $\delta = \phi$ equation (5.30) becomes $1 + \sin \phi \sin(2\gamma_T - \phi) - \cos \phi \cos(2\gamma_T - \phi) = 0$ or $1 - \cos 2\gamma_T = 0$ therefore $\gamma_T = 0$ and point a coincides with point b in fig (5.13). Values of γ_T for given values of δ and ϕ are summarised in table (5.1).

5.4.2.2 Determination of Characteristic Depth D_c

The characteristic depth is defined as the depth at which the slip lines revert back to the probe and touch the surface as in fig (5.14). The angle $\psi_s = \frac{\pi}{4} - \frac{\phi}{2}$ assuming that the probe is smooth. If the radial shear zone BC in fig (5.11) is of log spiral form, then $r_2 = r_1 \exp(\theta \tan\phi)$ and $r_1 = r_0 \frac{\cos(\gamma_T - \phi)}{\cos\phi}$. From triangle OCE

$$D = 2\cos(\frac{\pi}{4} - \beta_0 + \frac{\phi}{2})\cos(\frac{\pi}{4} - \frac{\phi}{2})r_2 \tag{5.31}$$

For a 60° wedge $r_0 = B$, equation (5.31) becomes

$$\frac{D}{B} = 2\frac{\cos(\gamma_T - \phi)}{\cos\phi}\cos(\frac{\pi}{4} - \frac{\phi}{2})\cos(\frac{\pi}{4} - \beta_0 + \frac{\phi}{2})\exp(\pi - \psi_c - \gamma_T + \beta_0)\tan\phi \tag{5.32}$$

By substituting $\beta_0 = \frac{\pi}{4} + \frac{\phi}{2}$ in equation (5.32), $\frac{D_c}{B}$ can be determined. Fig (5.15) shows the variation of $\frac{D_c}{B}$ for different roughness δ and angle of shearing resistance ϕ.

5.4.3 Organisation of Computations

Armed with equations (5.24) through (5.28), slip lines can be generated from a known boundary condition OE in fig (5.11). It is generally assumed that the major principal stress in zone OCE is greater than the applied hydrostatic surcharge which is equivalent to the minor principal stress. The mean stress at the boundary is therefore $\sigma = \frac{p_o}{1-\sin\phi}$ where $p_o$is the hydrostatic surcharge. Meyerhof (1951) studied the effects of bearing capacity by varying the shear stress on the equivalent free surface and showed that the bearing capacity is not sensitive to the shear stress. Therefore, it is realistic to assume that soil in zone OEF is a hydrostatic fluid. Since OE is the equivalent free surface, it is a non-characteristic, the solution throughout the region OCE can be obtained and is referred as the Cauchy problem.

OC is now the known boundary conditions for the fan zone OCB. Point O is a singularity point, the stress at that point will increase exponentially according to the amount of rotation of the major principal stress direction. For example, when the major principal stress direction has rotated by $\Delta\theta$, then the new boundary condition corresponding to the α characteristic has mean stress

$$\sigma_{\Delta\theta} = \sigma \exp(2\Delta\theta \tan\phi)$$

the direction that the major principal stress makes with the vertical z-axis is

$$\psi_{\Delta\theta} = \psi + \Delta\theta$$

By marching across each fan, the solution can be obtained throughout region OBC through that degenerate point O of fig (5.11). Zone OBC is viewed as a degenerate boundary problem. The maximum angle of rotation of principal stresses direction is $\theta = 180° - \psi_c - \gamma_T + \beta_0$. Methods to obtain γ_T and β_0 were shown in the previous section.

Along the boundary OA, coordinates r,z and the direction of major principal stress ψ are known. The value of γ_T depends on the friction angle δ of cone-soil interface and mobilised angle ϕ which can be obtained from equation (5.30), or from Mohr circle of stress in fig (5.21)

$$\gamma_T = \frac{\pi}{4} + \frac{\phi}{2} - 0.5(\delta + \sin^{-1}(\frac{\sin\delta}{\sin\phi}))$$

Previously computed values in the radial fan zone become the boundary conditon in zone OAB. Values of ϱ at each point on OA can be computed by sweeping across that mixed boundary problem in fig (5.16), (numbers show how points are generated respectively).

Knowing the mean stress $\sigma = \varrho \times \gamma 0.5B$ at each point and the direction of major principal stress ψ, stress components σ_r, σ_z, $\tau_{rz} = \tau_{zr}$ and σ_θ at each point can be obtained by back substitution into equations (5.9) through (5.12). A Mohr's circle of stress for each point is now available. Fig (5.17) a to c show the changes of stress components on the Mohr circle for different roughness on OA. By drawing a line parallel to plane OA through the pole P, the normal stress at each point is given by

$$\sigma_{n_i} = \frac{\sigma_{r_i} + \sigma_{z_i}}{2} + \cos(\Delta + \delta)\sqrt{(\frac{\sigma_{r_i} - \sigma_{z_i}}{2})^2 + \tau_{rz_i}^2}$$

where i is the point number. The normal force can be determined from the average of the normal stress of two adjacent points, their spacing and radii from the central axis. The penetration resistance can now be computed from the equilibrium of forces as

$$q_c = (\frac{4}{\pi B^2})\frac{\cos(\psi_c - \delta)}{\cos\delta}\sum_{i=1}^{i=i} F_{ni} \cdots for \quad cone$$

where F_{ni} is the normal force acting on each element. It must be noted here that the stress distribution on the cone face is not constant.

5.4.3.1 Procedure of Computations

The procedure of computation can be summarised as follows:-

• (1) Determination of top angle γ_T for a given $\frac{D}{B}$, $\frac{\delta}{\phi}$, the included angle in the radial fan zone $\theta = \theta_0 + \beta$ and the boundary conditions along OE by assuming the size of the plastic zone R.

• (2) Generation of α and β characteristic from equations (5.24) through (5.28).

• (3) Checked to see if the β characteristic starts at E actually ends at A. If not, another R is assumed and the process is repeated until correct R is found.

• (4) Determination of stress components on the cone face, equilibrium of forces will reveal the penetration resistance.

It is important to note in step (3) that the geometric relationship between $\frac{D}{B}$, and θ has to be maintained in the axisymetric case because for a given value of $\frac{D}{B}$, $\frac{\delta}{\phi}$ and base angle ψ_c, there is one value of β_0. Reducing the plastic zone R means that characteristic lines are generated from E' in fig (5.11). It is not unreasonable to assume that the effect of the soil above F'E' can be considered as a surcharge, since, afterall zone OEF has been assumed to be equivalent to a hydrostatic surcharge anyway.

5.5 Theoretical Prediction

In author's previous study on rupture propagation beneath a strip footing (1987), it has been shown that dilation angle ν_m along the failure line is not a material constant but varies with the stress level. Triaxial tests in chapter (2) from low (25kPa) to high (10MPa) cell pressure have shown that peak mobilised angle of friction is reduced as the mean effective stress is increased. The Mohr-coulomb strength envelope is therefore generally curved instead of straight as for constant ϕ_m, Baligh (1976). Hence to use a constant value of peak ϕ in the theoretical analysis will overpredict the experimental results. On the other hand, to use a constant value of critical mobilised angle ϕ_{crit} will be too conservative.

In author's variable ϕ analysis, slip lines are generated from known boundary values of σ, ψ, r, z. The mobilised angle ϕ_m on that boundary depends on the mean stress level, i.e the g-level and the depth of penetration. This means the mobilise angle ϕ_m varies with depth of penetration and the g-level which is certainly true. For each layer of characteristic lines generated, new values of σ, ψ, r, z emerge. With these new values of mean stress and mobilised angle of shearing resistance obtained from fig (2.10)b in chapter (2), new values of mobilised angle ϕ is used to generate next layer of characteristic lines. These processes are then repeated. Hence, the analysis incorporate the dependent ϕ on stress level and also the value of ϕ after crushing of sand grain beyond certain values of mean stress. Note that this technique adopted for the characteristics solution is not perfect, since each new values of mean stress generate, a new mobilised angle of shearing resistance which is used to generate the next layer of characteristics line. Hence, the whole characteristic net tends to be pulled towards the penetrator. The limitation of this method of analysis is that the curvalinear nature of the Mohr-Coulomb envelope has not been satisfied. For more rigorous method of analysis based on the curvalinear of Mohr-Coulomb envelope, refer to Lau (1988). The theoretical predicted results are marked in circles in fig (3.32), (3.36) and fig (3.22) through (3.28) for various depth to diameter ratio that are less than the "characteristic depth". These results are also tabulated in table (5.2). An example of a stress characteristic net generated with penetration effect and varying ϕ for test T25 is shown in fig (5.12)c. From fig (3.32) and fig (3.25) through (3.28), it may be seen that the theory predicts well for the three different relative densities of 52/100 sand. However, the prediction tends to overestimate the experimental results for large $\frac{D}{B}$. For the 14/25 sand, the theory also predicts well for the medium to low relative densities up to 40g as shown in fig (3.36), (3.22) and (3.23). Whereas, for the high relative density and high gravity level (80g) as shown in fig (3.22) and fig (3.24), the theory tends to underpredict the experimental results.

5.5.1 Determination of Bearing Capacity Factors N_q

If a pseudo-constant mobilised angle ϕ_{pc} is assumed along the characteristic lines, then the bearing capacity factor due to surcharge can be obtained by increasing the applied surcharge until its effect on the solution is negligible. Such factors would be applicable for example in the laboratory 1g tests where surcharge has been applied in some way and the self-weight body force of the material in the plastic zone has been neglected. Plots of bearing capacity factor N_q against mobilised friction angle at different relative depth $\frac{D}{B}$ for different relative roughness $\frac{\delta}{\phi}$ for both the plane strain and axisymmetric cases are shown in fig (5.18)a, b, c and fig (5.19)a, b, c, the results are also tabulated in table (5.3)a, b, c and table (5.4)a, b, c respectively. Note that the line marked AB in fig (5.18)a and subsequently for all figures of (5.18), (5.19) and (5.22) are the limiting lines where the 'characteristics depth' has been reached and no additional rotation of the principal stress is allowed beyond this depth, i.e to the left of AB one must change over to the cavity expansion theory.

5.5.2 Limit Analysis of N_q

To check that penetration effects are correctly formulated using the method of characteristic, a comparison is made with a plane strain closed form solution on weightless Mohr-coulomb type of material using the limit analysis.

Fig (5.20)a shows the major principal stress direction across a discontinuity which has rotated by $\Delta\theta$ and the corresponding Mohr-circles are shown in fig (5.20)b. The stress conditions between the two sides of the discontinuity need not be the same but conditions of equilibrium must be satisfied, $\sigma_{na} = \sigma_{nb}$, $\tau_{na} = \tau_{nb}$. Mohr-circle of stresses on either side of the discontinuity passed through a common point c. It can be shown that for a single discontinuity (Atkinson)

$$\frac{s_2}{s_1} = \frac{\cos(\delta\theta - \phi')}{\cos(\delta\theta + \phi')}$$

where ϕ' is the mobilised angle of shearing resistance on that plane. Therefore, the change in stress conditions across the discontinuity simply relate to the rotation of major principal stress direction.

In the radial fan zone where the angle of shearing resistance has been fully mobilised, ϕ' approaches ϕ. It can be viewed as an infinity of discontinuities corresponding to an infinity of Mohr circles each representing a stress condition in a sector of fan. From the geometry in fig (5.20)b and in the limit $\delta\theta \to 0$, $\sin\delta\theta \to \Delta\theta$. By applying the sine rule

$$\frac{ds}{2d\theta} = \frac{s\sin\phi}{\cos\phi}$$

intergrating the above equation through the fan to give

$$\frac{s_2}{s_1} = \exp\left[2\Delta\theta\tan\phi\right] \tag{5.34}$$

5.5.2.1 Formulation

Assume that the failure mechanism comprises plane shear OAB, radial fan zone OBC and passive zone OCE as shown in fig (5.11). The angle γ_T of plane shear zone is controlled by the degree of roughness on the face OA and can be determined from equation (5.30) for a given δ and ϕ.

The included angle of fan zone BOC comprises θ_0 and β_0. The value of β_0 is fixed for a given depth to diameter ratio $\frac{D}{B}$, ϕ, γ_T and base angle ψ_c. and can be determined from equation (5.32) The stress on the cone can be determined from the stress across the discontinuity using Mohr's circle of stress and Mohr-coulomb failure line.

Considering fig (5.21)a, OB is a slip line where full strength has been mobilised, that corresponds to point b on the Mohr's circle and where P is the pole for planes. Stresses on plane OA can be determined by drawing a line through the pole and parallel to the plane OA to cut the Mohr's circle at point a. From fig (5.21)b

$$\frac{OC}{\sin\Delta} = \frac{OA}{\sin\delta}$$

therefore

$$\Delta = \sin^{-1}\frac{\sin\delta}{\sin\phi}$$

and

$$S_1 = \frac{p_0}{(1 - \sin\phi)} \tag{5.35}$$

$$S_2 = \frac{\sigma_a}{(1 + \sin\phi\cos(\Delta + \delta))} \tag{5.36}$$

where p_0 is the surcharge as shown in fig (5.11) and σ_a is the normal stess on plane OA. The stress across the discontinuities in fan zone from equation (5.34) has the relationship

$$\frac{S_2}{S_1} = \exp(2\theta\tan\phi)$$

By combining equations (5.35) and (5.36). It can be shown that

$$\sigma_a = p_0\frac{1 + \sin\phi\cos(\Delta + \delta)}{1 - \sin\phi}\exp(2(\theta_0 + \beta)\tan\phi) \tag{5.37}$$

Equilibrium of forces in the plane strain wedge analysis from fig (5.23) and Appendix C reveals that

$$q_p = \sigma_a \frac{\cos(\psi_c - \delta)}{\cos\delta \cos\psi_c} \tag{5.38}$$

where ψ_c is the wedge angle and q_p is the bearing capacity. Substituting equation (5.37) into (5.38),

$$q_p = N_q p_o \tag{5.39}$$

, where N_q, the plane strain bearing factor is

$$N_q = (1 + \tan\delta \tan\psi_c) \frac{1 + \sin\phi \cos(\Delta + \delta)}{1 - \sin\phi} \exp(2(\pi - \psi_c - \gamma_T + \beta_0)\tan\phi) \tag{5.40}$$

Plots of bearing capacity factors N_q are shown in fig (5.22)a, b and c. The factors are also tabulated in table (5.5)a, b, and c.

5.6 Discussion of Theoretical Results

A theoretical three dimensional analysis of the quasi-static cone penetration using plastic theory and Coulomb's failure criterion is presented. The plastic equilibrium differential equations are solved numerically for an ideal homogeneous dry sand.

The numerical analysis of the slip line fields are computed using the Phoenix link to the university main frame. Variables like $\delta, \frac{D}{B}$, γ_T, g-level and the relationship between mobilised angles of shearing resistance and mean effective stress p' from low pressure and high pressure triaxial tests in fig (2.10)b are identified and defined. The governing differential equations were then solved numerically by varying the extent of the slip line fields on the boundary. The theoretical correct solution is when the far end of the β slip line converged to the cone tip, provided no β slip lines have crossed.

It can be seen that, as the mobilised angle of shearing resistance increases as the result of increasing relative density, the extent of the plastic zone increases thus indicating that a larger volume of soil has been influenced resulting in a larger resisting force which is in agreement with what has been observed experimentally.

5.6.1 Effect of Surcharge

As the surcharge is increased, the self-weight body force of the plastified soil becomes negligible resulting in straight characteristic lines adjacent to the penetrator and below the equilivalent free surface. In the radial sheared zone, characteristic lines are an undisturbed network of straight lines and logarithmic spirals. Since the computation starts from a known boundary, the bearing capacity factor due to surcharge can be determined by increasing the surcharge at the boundary until the effect on the bearing capacity factor is negligible. This can be explained by the fact that the surcharge contributed proportionally to both the major and minor principal stress resulting in increase in resisting force with increasing surcharge proportionately. To validate this effect, a plane strain limit analysis which has a unique solution based upon straight and logarithmic spiral slip lines as shown in table (5.5)a, b, c and the plane strain stress characteristic numerical analysis as shown in table (5.3)a, b, c are compared. They show good agreement in the bearing capacity factors for different values of δ, $\frac{D}{B}$, and friction angles ϕ.

5.6.2 Effect of Self Weight

As surcharge is reduced to a small value, the self-weight body force of the material becomes important. Since characteristic lines are generally curves, the radial shear zone has been disturbed and the included angle θ reduced substantially, the top angle γ_T has to be increased. Unlike the surface footing, the bearing capacity factor due to self-weight N_γ for deep penetration cannot be plotted simply . The reason is that there is no single unique solution, the bearing capacity factors diverge as the 'small surcharge' is reduced and finally instability of numerical analysis occurred as the result of cross over of characteristic lines, and the principal stress directions have been over rotated. In centrifuge modelling, the self-weight body force is a finite value, and is known for a given density, penetration depth, and g-level, and hence a theoretical correct solution can be computed and plotted as shown in fig (3.32), fig (3.36) and fig (3.22) through fig (3.28).

5.6.3 Effect of friction angle on cone-soil interface

Theoretically, the characteristic line fields have shown that an increase in δ is accompanied by an increase in the extent of plastic field. The distortion of the characteristic line network adjacent to the cone tip means that for a perfectly rough cone, the top angle γ_T vanishes, this is at the expense of the active zone AOB in fig (5.11). Consequently, the included angle in the radial fan zone θ has to be increased, together with an increase in the rotation of major principal stress direction. The effects of increasing δ is to shift the resultant forces closer to the vertical, thereby, increasing the magnitude of the vertical component of the resultant force. Hence, theoretically, δ has a significant influence on the penetration resistance but this effect has not been observed in the experimental results.

5.6.4 Critical review

Stress characteristics analysis has both advantages and disadvantages when compared with other methods of analysis. They can be summarised as follows:-

<u>**Advantages**</u>

• In the real situations where the overburden stress increses with depth, i.e self-weight body force of the soil can be considered and included in the analysis. This is particularly important in the centrifuge modelling which can simulate the real field situation.

• Can consider either plane strain or axisymmetric analysis. Application of shape factors to convert from plane strain to axisymmetric (circular) may not be correct.

• Dependence of mobilised angle of friction on mean effective stress p' along characteristic lines can be incorporated in the numerical analysis. This is particularly important especially when the extent of characteristic lines and changes of mean effective stresses p' along these characteristic lines are large.

• Shear strength of soil above the cone base can be included by extending the characteristic lines fields for deep penetration.

• In the analysis when shear strength is stress dependent, a relationship between mobilised angle of shearing resistance and mean effective stress p' is required for various relative densities means that the angle of shearing resistance and the unit weight of the soil are interdependent variables.

• Bearing capacity factors due to surcharge can be put into a simple graph (see fig 5.18, 5.19 and 5.22) for various values of $\frac{D}{B}, \frac{\delta}{\phi}$ and pseudo-constant angle of shearing resistance ϕ.

Disadvantages

• The set of differential equations describing the axisymmetric loading of ideally plastic material are statically indeterminate. Therefore it is required to postulate that the circumferential stress, σ_θ which is the intermediate principal stress does not affect the shear strength and is equivalent to the minor principal stress. (Haar and Von Karman's hypothesis).

• The bearing capacity factor due to the self-weight body force of the soil for deep penetration cannot be put into a simple graph, since each test requires the start of a new analysis in which the extent of the characteristic line field is adjusted until it converges to the correct location.

• The fact that the method of stress characteristics does not make use of a stress-strain relationship means that statically correct solutions may be kinematically inadmissible. An ideal perfectly plastic Mohr-coulomb material is neither work hardening nor work softening when failing, the yielding and failure lines coincide and the flow rule is associated. This implies that volume changes do not affect the shear strength which is certainly not true, i.e this material dilates at ϕ which is statically and kinematically admissible, but generally, real soil may experience dilatation rates considerably different from ϕ, thus the solution becomes kinematically inadmissible.

5.7 Summary

The theoretical analysis on the general shear failure based on the method of characteristics is presented. The method include the rotation of the major principal stress direction due to penetration effects and mobilised angle of shearing resistance is a variable and is a function of stress level.

The method has predicted well for fine sand and loose to medium loose sand for coarse sand. It underpredict the coarse dense sand because the dilatancy effects which is a major contribution to the strength cannot be incorporated in the analysis at this stage.

CHAPTER 6

THEORETICAL FRAMEWORK II

6.1 Introduction

As mentioned in chapter 5 that beyond the characteristic depth spherical expansion theory is appropriate because the deformation zone becomes very localised. Bishop (1945) applied this theory to indentation and hardness tests, whereas Vesic (1977) applied it to the problem of the bearing capacity of piles. The observation of deformation in the vicinity of pile tip as shown in fig (6.1) resembles that of a spherical expansion, a similar observation was also reported by Chen (1986) who studied the strain fields from the displacement of lead shot markers taken from x-rays. Therefore, the author feels that it is justifiable to use this theory for very deep penetration problems.

6.2 Review of Spherical Expansion Theory

Consider a spherical cavity with initial radius R_i as shown in fig (6.2)a which is expanded by a unformly distributed internal pressure p, a spherical zone around the cavity will undergo plastic deformation as the internal pressure is increased. Bishop, R.F Hill and Mott (1945), Gibson (1961) assumed that the material in this plastic zone was rigid-perfectly plastic. Vesic (1972) included the volumetric strain in this region which he obtained from the known stress in the plastic zone and a volumetric strain-stress relationship.

As the pressure p is increased to reach the ultimate value p_u as shown in fig (6.3) with cavity radius R_u, the radius of the plastic zone increases to R_p, beyond that zone, the material is in a state of elastic equilibrium and can be defined in terms of the deformation modulus E and Poisson ratio μ.

6.2.1 Underlying Assumptions

The problem of spherical expansion can be assumed to be comprised of three stages, and can be summarised as follows :-

- Stage I :- Increment of cavity pressure to $p = p_0 + \Delta p$, and the soil surrounding the cavity is in the state of elastic equilibrium as shown in fig (6.2)a, where p_0 is the initial cavity pressure and Δp is the pressure increment.

- Stage II :- Increment of cavity pressure to critical pressure $p = p_{crit}$ where the soil surrounding the cavity is now in a state of plastic equilibrium as shown in fig (6.2)b.

- Stage III :- Further increment of cavity pressure to ultimate pressure $p = p_u$ causing annular growth of plastic zone as shown in fig (6.3).

6.3 Mathematical Formulation

Consider the origin of the coordinate system to be coincident with the centre of sphere and the applied forces in the form of uniformly distributed pressure. The element considered is then subjected to the stress system as shown in fig (6.4). By symmetry there will be no shearing stress on the cavity boundary and the circumferential stress σ_θ will be the same in all directions at a particular radius r. If the soil is assumed to be weightless, the only equilibrium equation refers to the radial direction and is as given below

$$\begin{aligned}(\sigma_r + \frac{\partial \sigma_r}{\partial r}\delta r)(r+\delta r)\delta\theta(r+\delta r)\delta\theta - \sigma_r r\delta\theta r\delta\theta - \\ 2\sigma_\theta \delta r r\delta\theta \sin\frac{\delta\theta}{2} - 2\sigma_\theta \delta r r \delta\theta \sin\frac{\delta\theta}{2} = 0\end{aligned} \tag{6.1}$$

The equilibrium equation can be reduced to an ordinary differential equation as

$$\frac{d\sigma_r}{dr} + \frac{2(\sigma_r - \sigma_\theta)}{r} = 0 \tag{6.2}$$

partial derivatives are not required since σ_r is independent of θ.

6.3.1 The Elastic Solution

For simplicity, the sign convention in this section is tensile positive. Consider the solution for the elastic zone of fig (6.3) where $r \geq R_p$ and the soil is assumed to be linearly elastic. Hooke's law and the principal of superposition can be applied and the stress and strain relationship can be written as :-

$$\epsilon_r = \frac{1}{E}(\sigma_r - 2\mu\sigma_\theta) \tag{6.3}$$

$$\epsilon_\theta = \frac{1}{E}(-\mu\sigma_r + (1-\mu)\sigma_\theta \tag{6.4}$$

To obtain the stresses in terms of radial displacement u, multiply equation (6.3) by μ and add to equation (6.4) to give

$$\frac{\sigma_r}{E} = \epsilon_r + \frac{2\mu}{1-\mu-2\mu^2}(\mu\epsilon_r + \epsilon_\theta) \tag{6.5}$$

the strain components expressed in terms of radial displacement u, are

$$\epsilon_r = \frac{du}{dr} \tag{6.6}$$

$$\epsilon_\theta = \frac{u}{r} \tag{6.7}$$

substituting for ϵ_r and ϵ_θ in terms of u into equation (6.4) and (6.5) give

$$\frac{\sigma_r}{E} = \frac{(1-\mu)\frac{du}{dr} + 2\mu\frac{u}{r}}{1-\mu-2\mu^2} \tag{6.8}$$

and

$$\frac{\sigma_\theta}{E} = \frac{\mu\frac{du}{dr} + \frac{u}{r}}{1-\mu-2\mu^2} \tag{6.9}$$

Differentiate equation (6.8) with respect to r and substituting the values of $\frac{d\sigma_r}{dr}$, σ_r, and σ_θ into the equilibrium equation (6.2), a second order ordinary differential equation is obtained as

$$\frac{d^2u}{dr^2} + \frac{2}{r}\frac{du}{dr} - 2\frac{u}{r^2} = 0 \tag{6.10}$$

The general solution to equation (6.10) is

$$u = Ar + \frac{B}{r^2} \tag{6.11}$$

where u is the radial displacement which is a function of radius r and constants A and B are dependent on the boundary conditions of the sphere which are yet to be determined. Differentiate equation (6.11) with respect to r and substitute these values of $\frac{du}{dr}$ and u into stress equations, the stress distribution and the strain distribution in r direction in the elastic zone are :-

$$\sigma_r = 3KA - 4G\frac{B}{r^3} \tag{6.12}$$

and

$$\sigma_\theta = 3KA + 2G\frac{B}{r^3} \tag{6.13}$$

where $K = \frac{E}{3(1-2\mu)}$ is the bulk modulus and $G = \frac{E}{2(1+\mu)}$ is the shear modulus of the material, and

$$\epsilon_r = \frac{du}{dr} = A - \frac{2B}{r^3}$$

$$\epsilon_\theta = \frac{u}{r} = A + \frac{B}{r^3}$$

6.3.1.1 Boundary Conditions

To determine constants A and B, the boundary conditions must be known and are as shown in fig (6.3), i.e

- At r=Rp, i.e the boundary between the plastic and elastic zone, $\sigma_r = \sigma_p$
- At r=∞, $\sigma_r = \sigma_h$, and radial displacement u=0.

substitute these values into equations (6.11) and (6.12) to give

$$0 = A\infty + \frac{B}{\infty^2}$$

$$\sigma_p = 3KA - 4G\frac{B}{R_p^3}$$

The value of these constant are

$$A = 0$$

and

$$B = -(\frac{\sigma_p}{4G})R_p^3$$

Substitute the value of A and B into equations (6.12) and (6.13), it can be shown that the radial and the hoop stresses are

$$\sigma_r = \sigma_p(\frac{R_p}{r})^3 \tag{6.14}$$

$$\sigma_\theta = -\frac{\sigma_p}{2}(\frac{R_p}{r})^3 \tag{6.15}$$

6.3.2 The Plastic Solution

The solution applied to the plastic zone of fig (6.3), where $R_p \geq r \geq R_u$. From Mohr-Coulomb's failure criterion for cohesionless soil

$$\sigma_1(1 - \sin\phi) - \sigma_3(1 + \sin\phi) = 0$$

for the spherical problem, this is

$$\sigma_r(1 - \sin\phi) - \sigma_\theta(1 + \sin\phi) = 0 \tag{6.16}$$

Substituting equation (6.16) into equation (6.2) and note that for r=R$_u$, $\sigma_r = p_u$, the solution derived by Vesic (1972) to this differential equation is

$$\sigma_r = p_u(\frac{R_u}{r})^{\frac{4\sin\phi}{(1+\sin\phi)}} \tag{6.17}$$

The equation shows the decrease in radial stress with increase in radius in the plastic zone. At the boundary between the plastic and elastic zone, radial stress is $\sigma_r = \sigma_p$ at radius r=R$_p$, equation (6.17) becomes

$$\sigma_p = p_u(\frac{R_u}{R_p})^{\frac{4\sin\phi}{(1+\sin\phi)}} \tag{6.18}$$

To determine the ultimate pressure to cause expansion and the radius of plastic zone, a relationship between volume change of cavity and the volume change in the elastic and plastic zone is required. Vesic (1972) assumed that

$$R_u^3 - R_i^3 = R_p^3 - (R_p - u_p)^3 + (R_p^3 - R_u^3)\Delta$$

where u_p is the radial displacement at the boundary between the elastic and plastic zone obtained from the Lame's solutions, Vesic has shown that the extent of plastic zone is

$$(\frac{R_p}{R_u})^3 = (\frac{I_r}{1 + I_r\Delta}) = I_{rr}$$

where $I_r = \frac{E}{2(1+\nu)(p\tan\phi)} = \frac{G}{s}$ is defined as the rigidity index and I_{rr} is the reduced rigidity index, p is the intial mean effective stress, Δ is the volumetric strain in the plastic region, s is the intial shear strength and G is the shear modulus.

6.3.3 Soil Compressibility

As mentioned in the above section the compressibility of the sand mass can be expressed in terms of its rigidity index. If the soil is assumed to be incompressible, i.e no volume changes occuring in the soil mass surrounding the penetrator, then $\Delta = 0$ and $I_{rr} = I_r$, as in the case of general shear failure. If the soil is assumed to be compressible, $I_{rr} < I_r$, then the bearing capacity factor calculated on the assumption that ultimate pressure on the dead zone I of fig (6.5) under the flat bottom pile that has transmitted to the vertical face OB is equal to the ultimate pressure needed to expand a spherical cavity of the same soil mass and is much lower than for incompressible soil. Hence, in the very deep penetration local shear failure is likely to occur and soil compressibility becomes of greater importance.

6.3.4 Input Parameters

The basic soils data required for the analysis are :-

Elastic Modulus E_{50}

The elastic modulus is calculated from triaxial tests and is taken at 50% of the ultimate stress. It is a function of density and confining pressure. A summary of moduli at various densities and confining pressures is shown in table (6.1).

Poisson's ratio μ

The intial value of poisson's ratio μ is estimated from initial zero lateral strains. From elastic equations, it can be shown that

$$\frac{\sigma_3}{\sigma_1} = k_0 = \frac{\mu}{1-\mu}$$

or

$$\mu = \frac{k_0}{1+k_0} \tag{6.19}$$

where k_0 is taken as $(1 - \sin\phi)$ for sand, Jaky (1948).

Volumetric Strain Δ in Plastic Zone

Since no volume change device can be conveniently incorporated to measure the volumetric strain of soil in the vicinity of the cone, a parametric study by varying the volumetric strain will be discussed. Volumetric strain obtained from the triaxial test is not comparable to the volumetric strain in the penetration test because the soil adjacent to the cone is subjected to very high stress which is not in the range of the high pressure triaxial test results and it is likely that compression is taking place, see for example in the high pressure triaxial plot of fig (2.6)b.

Chen (1986) who studied the strain field from the displacement of lead shots recorded by x-rays also concluded that a highly compressed zone existed adjacent to the cone followed by a highly sheared transition zone. Therefore, if the insitu stress is considered and volumetric strain is calculated from low pressure triaxial test results, it is likely that for dense sand dilation will occur which would be misleading if it was used to determine the reduced rigidity index.

6.3.5 Limiting Equilibrium

Consider an element of soil at the boundary between the plastic and elastic regime of fig (6.3), the Mohr's circle of stresses will just touch the Mohr-Coulomb's failure line as shown in fig (6.6). By adopting Von Karman's hypothesis where the intermediate principal stress is equal to the minor principal stress, The mean normal stress σ_u for that element is

$$\sigma_u = \frac{\sigma_\theta + \sigma_r}{2} \tag{6.20}$$

By combining equation (6.20) and the Mohr-Coulomb failure criterion in equation (6.16) , note that $\sigma_r = p_u$. It can be shown that

$$\sigma_u = \frac{1}{(1 + \sin\phi)} p_u \tag{6.21}$$

6.3.6 Variation of Radial Stress with Radius r

The elastic solution of equation (6.14) and the plastic solution of equation (6.17) show a decrease in radial stress with increasing radius r. From equation (6.18) by substituting the value of σ_p into elastic equation (6.14). It can be shown that

$$\frac{\sigma_r}{p_u} = \frac{I_{rr}^{\frac{3-\sin\phi}{3(1+\sin\phi)}}}{(\frac{r}{R_u})^3} \qquad for \quad r \geq R_p \tag{6.22}$$

and rearranging the plastic equation (6.17) that

$$\frac{\sigma_r}{p_u} = (\frac{r}{R_u})^{-\frac{4\sin\phi}{1+\sin\phi}} \qquad for \quad R_p \geq r \geq R_u \tag{6.23}$$

From the above two equations, the value of $\frac{\sigma_r}{p_u}$ can be plotted against $\frac{r}{R_u}$, an example of the plot for $\phi = 44°$ and $I_r = 200$ and $\Delta = 0$ is shown in fig (6.7).

6.4 Flat-Bottom Piles

Vesic (1977) applied the spherical expansion concept to a flat-bottom pile to predict the end bearing capacity. The failure mechanism assumed is shown in fig (6.5), which comprises a dead zone I which pushes the highly sheared zone II radially outward. The included angles FOA and OFA in the dead zone I are $(\frac{\pi}{2}+\frac{\phi}{2})$, the stress induced at the base of the pile OF transmitted to the face OB was then taken as the cavity pressure p_u to cause a spherical expansion of plastic zone III, i.e to say that penetration of pile is possible by lateral expansion of soil along the circular ring OB as well as any possible soil compression in these zones. The end bearing capacity of the pile q_p is given as

$$q_p = N_\sigma \sigma_m$$

where

$$N_\sigma = \frac{3}{3-\sin\phi}\exp\left((\frac{\pi}{2}-\frac{\phi}{2})\tan\phi\right)\tan^2(\frac{\pi}{4}+\frac{\phi}{2})I_{rr}^{\frac{4\sin\phi}{3(1+\sin\phi)}}$$

and σ_m is the insitu mean hydrostatic stress and is

$$\sigma_m = \frac{(1+2k_0)}{3}\sigma_v$$

where k_0 is the lateral earth pressure at rest and σ_v is the insitu vertical stress.

6.5 Author's Extended Theory for 60° Cone

To compute the penetration resistance for a cone with 60° apex angle beyond the characteristic depth, spherical cavity expansion theory is used but with a simplified factor taking into consideration that the soil adjacent to the cone is a highly sheared zone where full strength has been mobilised. The mean normal stress at C of fig (6.5) in the plastic zone is (Sokolovski 1965)

$$\sigma_c = \sigma_u \exp(2\theta\tan\phi) \tag{6.24}$$

where σ_u is the mean hydrostatic stress at the transition surface and is assumed to be equal to the mean pressure in the cavity to cause a spherical expansion of same mass of soil. From Mohr's circle of stress in fig (6.8) and applying the sine rule

$$\sigma_c = p_c \frac{\sin \Delta}{\sin(\Delta + \delta)} \tag{6.25}$$

where $\Delta = \sin^{-1}\left(\frac{\sin \delta}{\sin \phi}\right)$ Combining equations (6.21), (6.24) and (6.25). It can be shown that

$$p_c = \frac{\sin(\Delta + \delta)}{\sin \Delta} \frac{1}{(1 + \sin \phi)} \exp{(2\theta \tan \phi)} p_u \tag{6.26}$$

where p_u is the cavity pressure. Substituting p_u from equation (6.18) into equation (6.26) gives

$$p_c = \frac{\sin(\Delta + \delta)}{\sin \Delta} \frac{1}{(1 + \sin \phi)} \exp{(2\theta \tan \phi)} (\frac{R_p}{R_u})^{\frac{4 \sin \phi}{(1+\sin \phi)}} \sigma_p \tag{6.27}$$

6.5.1 Equilibrium of Forces

To determine the tip resistance q_c, equilibrium of forces at the cone face is required. The stresses acting on the cone face as shown in fig (6.9)a are σ_n and τ_n, consider an annular ring of fig (6.9)b which has an area of $2\pi r \cos \psi_T dr$. Total vertical force acting downward is

$$q_c \pi R^2 \cos^2 \psi_T$$

and total force acting upward assuming that the normal stress σ_n and the shear stress τ_n are constant on the cone face is

$$\int_0^R (\sigma_n \cos \psi_T + \tau_n \sin \psi_T) \cos \psi_T 2\pi r dr$$

From Mohr's circle of stress in fig (6.8), $\sigma_n = p_c \cos \delta$ and $\tau_n = p_c \sin \delta$. Equilibrium of forces reveals that

$$q_c = \frac{1}{\pi R^2} \int_0^R p_c \frac{\cos(\delta - \psi_T)}{\cos \psi_T} 2\pi r dr \tag{6.28}$$

and substituting the value of p_c from equation (6.27), It can be shown that

$$q_c = N\sigma_p \tag{6.29}$$

where

$$N = \frac{\cos(\delta - \psi_T)}{\cos\psi_T}\frac{\sin(\Delta + \delta)}{\sin\Delta}\frac{1}{(1 + \sin\phi)}I_{rr}^{\frac{4\sin\phi}{3(1+\sin\phi)}}\exp(2\theta\tan\phi)$$

Since radial stress σ_r is decreasing in the elastic zone up to a certain value of r where the insitu stress is approached, many researchers believe that the insitu mean hydrostatic stress σ_m is more appropriate to be used in the analysis. Vesic (1977) has shown that a factor N_q related to the vertical insitu stress and a factor N_m relate to the mean hydrostatic stress have the following relationship :-

$$N_q = \frac{1 + 2k_o}{3}N_m$$

By adopting vesic's method relating to the mean hydrostatic stress and the insitu mean stress and assuming thay $k_o = 1 - \sin\phi$, then σ_p in equation (6.29) is to be substituted by equation (6.14) until the insitu stress is approach to give

$$q_c = \frac{\cos(\delta - \psi_T)}{\cos\psi_T}\frac{\sin(\Delta + \delta)}{\sin\Delta}Irr^{\frac{4\sin\phi}{3(1+\sin\phi)}}\exp(2\theta\tan\phi)\frac{1}{(1 + \sin\phi)}\frac{3}{3 - 2\sin\phi}(\frac{r}{R_p})^3\sigma_m \tag{6.30}$$

If the change in radial stress in the elastic zone is not incorporated, i.e to say that to use σ_p from the insitu mean hydrostatic stress σ_m, then the tip resistance to penetration computed will be underpredicted. On the other hand, if the soil is assumed to be incompressible, i.e $I_{rr} = I_r$, then the computed result of the tip penetration resistance will be overpredicted which will be discussed later.

6.5.2 Procedure of Analysis

The procedure of the analysis can be summarised into following steps :-

- (1) For a given $\frac{D}{B}$ and g-level, the vertical stress can be calculated for an assumed value of relative density of the soil.

• (2) From fig (2.10) and the assumed relative density, assume a value of ϕ which will correspond to a cell pressure σ_3, the horizontal stress σ_h is calculated as $\sigma_h = k_0\sigma_v$ where $k_0 = (1 - \sin\phi)$.

• (3) If $\sigma_h \neq \sigma_3$, step (1) and (2) are repeated until an acceptable value is obtained.

• (4) Knowing ϕ and σ_3, Young's Modulus E_{50} can be obtained from table (6.1). Poisson's ratio μ and insitu mean hydrostatic stress σ_m can be calculated from k_0 and σ_v, hence I_r is known.

• (5) Plot of $\frac{\sigma_r}{p_u}$ against $\frac{r}{R_u}$ to approximate the value of $\frac{r}{R_p}$ where the insitu stress is approached by assuming that $\Delta = 0$ i.e $I_{rr} = I_r$.

• (6) The ratio of $\frac{r}{R_p}$ is not very sensitive to the change of Δ, hence $\frac{r}{R_p}$ for $\Delta = 0$ will be used for parametric studies by varying the volumetric strain $\Delta = 0\%$, 2.5%, 5.0%.

• (7) Obtaining cone-soil interface friction angle, δ, from shear box tests shown in fig (2.14), the value of q_c from equation (6.30) can be calculated.

6.6 Discussion of Theoretical Results

A theoretical solution based on the spherical expansion of a cavity is presented. Both the elastic theory and the plastic theory are incorporated in the analysis. The radial stress p_u on the transition surface which is a major principal stress is assumed to be equal to the cavity pressure to cause a spherical expansion of the same mass of soils. It must be pointed here that the stress distribution from a spherical cavity to the cone face cannot be drawn, therefore the value of p_u is merely an assumption in a cavity sphere. This assumption also adopted by Vesic (1977) for his flat bottom piles analysis except that the minor principal stress on the transition face has been taken as the cavity pressure p_u which is unusual.

To determine the value of p_u, soil adjacent to the cone is assumed to be subjected to high shear and the stress distribution from the cone face to the transition ring obey a logarithmic spiral, Sokolovski (1965).

6.6.1 Effect of Volumetric Strain Δ

As mentioned earlier that soil compressibility becomes important in the case of local shear failure, Meyerhof (1962). A parametric study has been carried out analytically by varying the values of Δ=0, 2.5, 5.0%. A comparison is also made with the available volumetric strain Δ from the high pressure triaxial tests.

From the theoretical analysis of the previous chapter, it is likely that the angle of shearing resistance has reached a critical state value for the stress level in the vicinity of the cone. The tip resistances calculated using ϕ_{crit} are summarised in table (6.2)b. The analytical results show that for the same $\frac{D}{B}$ and insitu stress in the same mass of sand, the results show a decreasing of tip resistance at a decreasing rate as Δ is increased. For example, in test T25 at $\frac{D}{B} = 30$, the analytical results from equation (6.30) for Δ=0, 2.5 and 5.0% are 43.8, 23.18 and 18.07 MPa respectively. The tip resistance of the experimental results is 38.3 MPa, therefore, if soil compressibility had not been incorporated, i.e Δ=0, the analytical result will overpredict by approximately 10%. It must noted here that volumetric strain in the elastic zone is not included.

Loose sand tends to be more compressible then dense sand, therefore the influence of Δ on the tip resistance will be more pronounced. This effect is also shown in the analysis, for example in tests T27 and T19 which had relative densities of 53.9% and 79% respectively. At $\frac{D}{B} = 20$ the analytical results for Δ=0 are 13.36 and 15.97 MPa, whereas for Δ=2.5%, the analytical results are 6.35 and 6.91 MPa compared with the experimental results of 8.07 and 13.0 MPa respectively.

In many engineering studies (Vesic, 1972), values of insitu ϕ is used in the analysis. The tip resistance calculated using insitu ϕ are summarised in table (6.2)a, which is considered inconsistent in relation to the stress level generated as the penetrator advances. Consider tests T19 and T27 at $\frac{D}{B}$ again, from the high pressure triaxial tests of fig (2.8)b and fig (2.9)b with cell pressures of 4780 and 1930 MPa, the corresponding volumetric strains are 0.8 and 1.5%. An analysis using ϕ_{crit} will give 14.42 and 7.6 MPa, whereas if insitu ϕ of 45° and 39° are used, the calculated tip resistances are 19.66 and 10.8 MPa which overpredict the experimental results by 35% and 25% respectively.

6.6.2 Effect of radial stress σ_r

As mentioned earlier, equation (6.14) of the elastic theory and equation (6.17) of the plastic theory shows the variation of radial stress σ_r with radius r. Many researchers have excluded the variation of radial stress in the elastic zone, though the insitu mean stress σ_m has been used in the analysis, resulting in an underprediction of the theoretical results.

The value of $\frac{r}{R_p}$ that is to be used in equation (6.30) is obtained from the plot of $\frac{\sigma_r}{p_u}$ against $\frac{r}{R_u}$, the value of $\frac{r}{R_u}$ is determined when its effect upon $\frac{\sigma_r}{p_u}$ is negligible. Knowing the value of $\frac{r}{R_u}$ from the plot, then the value of $\frac{r}{R_p}$ can then be calculated from $(\frac{R_p}{R_u})^{\frac{1}{3}} = I_{rr}$.

6.7 Summary

The theoretical analysis on the local shear failure based on the extended theory of the cavity expansion method is presented. A parametric study on the compressibility factor Δ, variation of the radial stress σ_r in the elastic zone has also been incorporated in the analysis.

Comparison of the theoretical analysis and the experimental results reveal that compressibility effect is important in the deep penetration and its effect reduced the bearing capacity considerably. If this effect is not taken into consideration, then the analytical result tends to overpredict the experimental value.

CHAPTER 7

CONCLUSIONS AND SUGGESTIONS FOR FUTURE RESEARCH

7.1 Conclusions

Centrifuge Test Results

• A set of accurate and consistent data from the centrifuge tests have been produced, they show that the two major factors that influence the cone tip resistance are the confining stress and the density. It was found that the tip resistance can be correlated with the vertical stress and the density for normally consolidated sand, but there isn't a single curve to represent the same type of sand with different gradations. However by carrying out a series of model tests which represent the prototype scale in the centrifuge, the model test results can be normalised and extrapolated to the prototype. The correlated results are presented in graphical form and can be used to determine the relative density in the field or of samples used in Centrifuge tests for example. In general, tests employing different diameter cones on the same specimen simulating a 'common prototype' gave an excellent 'modelling of models' correlation.

• It was found that if the relative grain diameter ratio $\frac{B}{d_{50}}$ is greater than 12, then no particle size related error will influence the tip resistance.That is to say there is no grain size effects.

• The bottom boundary effect is dependent on the relative density of sand, the empirical correlated results from the three diffent sizes of probe in the centrifuge tests data can be estimated as

$$\frac{X}{B} = 0.1139(R.D\%) - 1.238$$

where X is the distance from the bottom boundary where the boundary effects begin to influence the tip resistance. For R.D less than 11%, no serious bottom boundary effect related error will influence the tip resistance.

• For the same size of cones but with quite different roughness surface, the roughness paradoxically has little influence on the tip resistance.

• For dry sand where no pore pressure is generated, the rate of penetration has little influence on the tip resistance.

• Stress cycle effect resulting in overconsolidated of sand in the centrifuge increases the tip resistance significantly.

Triaxial Test and Laboratory 1g Penetration Test Results

• From the high pressure triaxial test results, it is evident that sand can still reach a critical state, i.e approximately 32° for Leighton Buzzard sand, and that dense sand can exhibit behaviour similar to loose sand at low pressures, i.e volumetric compression occurs during shearing.

• Peak mobilised angles of shearing resistance are stress dependent, and beyond a certain crushing mean stress, the mobilised angle of shearing resistance decreases rapidly.

• Results of 1g laboratory penetration testing also reveals that surface roughness and the rate of penetration in dry sand has little influence on the tip resistance. Similarly, the two major factors that control the tip resistance are the vertical stress and the density.

Theoretical Analysis

• For penetration depths of less than a 'characteristic depth', general shear failure is likely to be true. By using the method of characteristics with an extended theory such that ϕ is a variable which depends on the stress level and the rotation of the principal stress due to the penetrating effect, the extended theory can predict the experimental results reasonably well.

• Beyond the 'characteristic depth', local shear failure is more appropriate and the compressibility of sand becomes increasingly important as it is able to accomodate the volume of the embeddded penetrator. The extended theory based on the cavity expansion method which can handle the compressibility effects gave a good prediction of the experimental results.

General Comment

From the experimental results that have been discussed, it may be improper to simulate the overburden stress by surcharge as is done in the "chamber test", since the stress gradient effect due to the self weight body force that occurs in a real prototype situation is not simulated. Centrifuge modelling however can correctly simulate the self weight body force stress gradient effect, therefore, it is likely that the 1g model tests with surcharge (chamber tests) will underestimate the strength of soils in the prototype situation where the stress gradient effect is present.

7.2 Suggestions for Future Research

The investigations conducted during the research have to some extent thrown new light on various aspects of the quasi-static cone penetration test (QCPT) as outlined in the previous sections. Inevitably, these investigations will pose some new questions. For future extension of the research, the author would like to put forward the following suggestions.

Parametric Study

• Investigate the scale effect in more detail in the centrifuge. This can be carried out with the existing three different sizes of cones by testing at the same g-level with 52/100 sand for example.

• Investigate the overconsolidation effects further by testing at different sequences of g-levels in the centrifuge. It is also desirable that a moveable penetrator with gantry be mounted on the tub, so that tests can be carried out at various location without stopping the centrifuge.

• More tests should be carried out on other types of sand which have different particle shape, particle size and minerological content to produce a data bank. Such a data bank would be of use in the field or as an index for assessing the densities and uniformity of sample prepared for the beam and drum centrifuge model tests.

• Test should also be carried out on clay to investigate the excess pore pressure generated using a piezocone (undrained event).

Empirical Correlations and the Theoretical Analysis

• One of the objectives of the use of QCPT in the field is to obtain empirical correlations with soil properties that may be used to assist in the solution of bearing capacity, pile or settlement problems. Since many centrifuge tests on footings and piles have been carried out by the Cambridge Soils Mechanics Group in the past, these data are readily available. Now, with these penetration test results, research should be carried out to correlate them empirically.

• An empirical correlation relationship between normally consolidated and overconsolidated cone data should be determined from the centrifuge test data, so that in future this correlation can be used in the field.

• The theoretical analysis based on the cavity expansion method should incorporate the dilatancy effect, say some distance away, and the crushibility effects of sand in the vicinity of cone. The stress dependent ϕ should also be incorporated.

Type of materials	Factors
silts, sandy silts, and slight cohesive silty sands	2
clean fine to medium sands, slightly silty sands	3.5
coarse sands and sands with a little gravel	5
sandy gravel and gravel	6

Table 1.1 Multiplication factors (after Schmertmann, 1970).

Type of pile	S_t (reference tip, R*)
Timber	1.2
Parallel-sided concrete or steel:	
flat end	0.6
pointed end	1.1
Driven *cast-in-situ*†	1.6
Open steel tube and H-pile	0.7

*For f_s measured with a Dutch friction sleeve tip (M), the values of S_t are halved
† S_t may be higher if the concrete is rammed as the casing tube is withdrawn

Table 1.2 Values of s to be used in equation 1.5

Type of sands	Relative density (%)	Cell pressure (kPa)	$\frac{\sigma_1}{\sigma_3}$	ϕ_p (°)
14/25	28	25	4.344	38.05
	36	50	4.470	38.1
	38.8	75	4.493	39.36
	48.6	935	3.495	33.7
	52.3	1925	3.009	30.1
14/25	90.5	25	8.200	51
	99.7	50	6.440	46.9
	95.7	75	6.067	45.7
	77.5	930	3.874	36.6
	81.8	1920	3.699	35.1
52/100	47	25	4.560	35.6
	49.7	50	4.480	38.3
	53.4	100	4.800	40.76
52/100	80.8	25	5.96	45.45
	81.05	50	5.700	44.55
	78.13	100	5.120	42.31
	81.92	915	4.449	39.3
	84.0	1915	3.924	36.4
	84.5	4780	3.264	32.1

Table 2.1 Peak angle of shearing resistance ϕ_{peak} at different confining pressure and void ratio.

Probe diameter (mm)	Max. capacity of load cell (kN)	Calibration constant ($\frac{kN}{mV}$)
6.35	3.68	0.295
10.0	7.6	0.45
19.05	10	1.346

Table 3.1 Specifications of load cells.

Test Series	Sand Type	Void Ratio	Cone Dia (mm)	Test No	G-Level
I	FB Sand	0.622	10.00	T1	10
				T2	20
				T3	40
				T4	80
II	14/25	0.495	10.00	T5	10
				T6	20
				T7	40
				T8	80
III	14/25	0.671	10.00	T9	10
				T10	20
				T11	40
				T12	80
IV	14/25	0.674	19.05	T13	21
			10.00	T14◇	40
			10.00	T15	40
			6.35	T16	63
			6.35	T17	63
V	52/100	0.657	10.00	T18	10
				T19	20
				T20	40
				T21	80
VI	52/100	0.646	19.05	T22	21
			19.05	T23*	21
			10.00	T24	40
			6.35	T25	63
VII	52/100	0.743	10.00	T26	10
				T27	20
				T28	40
				T29	80
VIII	52/100	0.909	10.00	T30	10
				T31	20
				T32	40
				T33	80
IX	14/25	0.741	10.00	T34	10
				T35	20
				T36	40
				T37	80
X	14/25	0.519	19.05	T38	21
			19.05	T39*	21
			10.00	T40	40
			6.35	T41	63
XI	52/100	0.710	19.05	T42	21
			10.00	T43	40
			10.00	T44◇	40
			6.35	T45	63
XII	25/52	0.524	19.05	T46	21
			19.05	T47*	21
			10.00	T48	40
			6.35	T49	63
			10.00	T50	40

⋆ To investigate the roughness effects
◇ To investigate the penetration rate effects

Table. 3.2 Summary of Test Programmes in Centrifuge Modelling

R.D (%)	54%		80%		54%	80%
$\frac{D}{B}$	14/25	52/100	14/25	52/100	$\frac{q_{c_{14/25}}}{q_{c_{52/100}}}$	$\frac{q_{c_{14/25}}}{q_{c_{52/100}}}$
12	6.92	5.00	11.5	7.67	1.38	1.50
16	10.0	6.5	16.15	10.0	1.54	1.62
20	12.31	8.4	20.4	14.0	1.46	1.47

Table 3.3a Ratio of tip resistance between 14/25 and 52/100 sand at 20g.

R.D (%)	54%		80%		54%	80%
$\frac{D}{B}$	14/25	52/100	14/25	52/100	$\frac{q_{c_{14/25}}}{q_{c_{52/100}}}$	$\frac{q_{c_{14/25}}}{q_{c_{52/100}}}$
12	9.6	6.9	16.0	12.6	1.40	1.27
16	13.0	8.9	21.7	17.7	1.46	1.23
20	14.8	10.9	27.0	22.6	1.36	1.2

Table 3.3b Ratio of tip resistance between 14/25 and 52/100 sand at 40g.

R.D (%)	54%		80%		54%	80%
$\frac{D}{B}$	14/25	52/100	14/25	52/100	$\frac{q_{c_{14/25}}}{q_{c_{52/100}}}$	$\frac{q_{c_{14/25}}}{q_{c_{52/100}}}$
12	18.0	12.58	27.8	22.13	1.43	1.26
16	21.7	16.1	34.3	29.3	1.35	1.17
20	26.1	17.9	40.4	33.3	1.46	1.21

Table 3.3c Ratio of tip resistance between 14/25 and 52/100 sand at 80g.

Probe dia. (mm)	g-level	weight of piston+probe (kN)	accumulator pressure (kPa)
19.05	21	0.0094	3730
6.35	63	0.0048	1944
10	10	0.006	2926
	20		2805
	40		2565
	80		2083

Table 3.4 Required pressure in accumulator for different g-level and probe diameter.

Probe diameter (mm)	Pressure in accumulator (kPa)
6.35	1370
10.0	2030
19.05	3025

Table 4.1 Required pressure to be stored in the accumulator (inclusive of pressure losses through bends, joints and friction)

Test Series	Sand Type	Void Ratio	Cone Dia (mm)	Test No	Surcharge (kPa)
I	25/52	0.570	10.0	LT1	100
			10.0	LT2	100
			10.0*	LT3	100
			6.35	LT4	100
			6.35	LT5	100
II	14/25	0.50	10.0	LT6	50
			10.0	LT7	50
			10.0*	LT8	50
			19.05	LT9	50
			19.05	LT10	50
			19.05*	LT11	50
III	52/100	0.640	19.05	LT12	150
			19.05*	LT13	150
			19.05*	LT14	150
			10.0	LT15	150
			10.0*	LT16	150
			10.0*	LT17	150
			6.35	LT18	150
			6.35	LT19	150
IV	FB	0.620	6.35	LT20	50
			6.35	LT21	50
			19.05	LT22	50
			19.05*	LT23	50
			10.0	LT24	50
			10.0	LT25	50
			10.0*	LT26	50
V	14/25	0.54	10.0	LT27	50
			19.05	LT28	50
			6.35	LT29	50
			6.35	LT30	100
			19.05	LT31	100
			10.0	LT32	100
			10.0	LT33	150
			19.05	LT34	150
VI	14/25	0.667	19.05	LT35	50
			10.0	LT36	50
			6.35	LT37	50
			6.35	LT38	100
			10.00	LT39	100
			19.05	LT40	100
			19.05	LT41	150
			10.0	LT42	150
VII	14/25	0.742	10.0	LT43	50
			19.05	LT44	50
			6.35	LT45	50
			6.35	LT46	100
			19.05	LT47	100
			10.0	LT48	100
			10.0	LT49	150
			19.05	LT50	150
VIII	52/100	0.632	10.0	LT51	100
			10.00	LT52	100

Table 4.2 Summary of the laboratory 1g tests programme.

sand	Vertical stress (kPa)	Centrifuge		Laboratory 1g	
		void ratio	q_c (MPa)	void ratio	q_c (MPa)
FB	50	0.622	20	0.62	20
14/25	50	0.50	25.0	0.50	25.3
14/25	50	0.741	4.0	0.742	2.0
	100	0.741	7.56	0.742	3.89
	150	0.741	11.3	0.742	5.15
14/25	50	0.682	5.56	0.667	5.17
	100	0.682	10.89	0.667	9.17
	150	0.682	16.44	0.667	14.58
14/25	100	0.50	38.9	0.54	34.5
	150	0.50	49.3	0.54	40.7

Table 4.3 Comparison of tip resistance between centrifuge and laboratory 1g test results at $\frac{D}{B} = 12$.

ϕ \ δ/ϕ	0.0	0.25	0.5	0.75	1.0
15	52.5	43.3	33.6	22.5	0.0
20	55.0	45.1	34.7	22.9	0.0
25	57.5	46.9	35.8	23.4	0.0
30	60.0	48.7	36.9	23.8	0.0
35	62.5	50.4	37.9	24.1	0.0
40	65.0	52.2	38.9	24.5	0.0
45	67.5	53.9	39.9	24.9	0.0
50	70.0	55.6	40.9	25.3	0.0

Table 5.1 Values of ψ_T at different $\frac{\delta}{\phi}$ and ϕ

Table (5.2) Comparison of theoretical predicted and experiment test results.

Test No:	$\frac{D}{B}$	plastic zone $\frac{R}{B}$	$q_{c(theory)}$(MPa)	$q_{c(exp)}$(MPa)
T24	5	9.5	3.84	3.91
	10	8.7	10.13	11.3
	15	8	17.92	19.01
	20	6.9	27.18	26.96
	25	5.4	37.93	33.04
	30	3.8	51.19	38.26
T15	5	7.4	1.77	2.17
	10	6.47	5.23	5.91
	15	4.1	10.48	11.18
	18	2.3	14.46	12.69
T10	5	7	1.16	2.27
	10	6	3.4	4.55
	15	4	6.6	7.35
T11	5	7.4	1.8	3.39
	10	6.5	5.29	6.96
	15	4.4	10.61	12.17
T12	5	8.4	2.9	6.08
	10	6.6	8.48	12.61
	15	4.25	17.29	16.52
T19	5	9.1	2.4	1.61
	10	9	6.31	5.31
	15	8.2	11.48	9.81
T20	5	9.5	3.61	3.48
	10	9.2	9.57	9.26
	15	8	17.1	16.34
T21	5	10	5.7	6.12
	10	9	14.54	17.63
	15	7.2	25.6	27.83
	20	6.3	39.7	33.22

Continue....

Test No:	$\frac{D}{B}$	plastic zone $\frac{R}{B}$	$q_{c(theory)}$ (MPa)	$q_{c(exp)}$(MPa)
T27	5	8	2.34	1.48
	10	7	6.46	4.01
	15	6	12.24	9.81
T28	5	7.5	1.534	3.04
	10	7	4.2	6.09
	15	5.7	7.89	8.52
T29	5	8.5	3.73	4.91
	10	7.5	10.1	10.16
	15	5.7	19.65	15.03
	20	3.5	32.4	
T31	5	5.5	0.67	1.15
	10	3.8	2.17	1.64
T32	5	5.7	1.06	1.43
	10	4.4	3.68	2.17
T33	5	6	1.81	2.63
	10	4.7	6.5	3.95
T35	5	6	0.808	1.51
	10	4.7	2.51	2.65
	15	3.5	3.46	4.17
T36	5	6.7	1.27	2.61
	10	5.08	4.08	4.35
	12	3.8	5.75	5.65
T37	5	7.2	2.08	5.21
	10	5	6.91	9.56
	12	4	9.8	10.87

Table (5.3)a Numerical analysis bearing capacity factors N_q.
(Plane strain)

ϕ	$\frac{\delta}{\phi}$	$\frac{D}{B}$	N_q
28	0	0	5.02
30	0	0	5.73
32	0	0	6.56
34	0	0	7.51
36	0	0	8.64
38	0	0	10.01
40	0	0	11.63
42	0	0	13.69
44	0	0	16.15
46	0	0	19.43
48	0	0	23.75
28	0	3	13.98
30	0	3	15.86
32	0	3	18.2
34	0	3	20.71
36	0	3	23.77
38	0	3	27.38
40	0	3	31.58
42	0	3	36.78
44	0	3	42.97
46	0	3	50.59
48	0	3	60.12
28	0	5	26.14
30	0	5	27.47
32	0	5	30.06
34	0	5	33.45
36	0	5	37.63
38	0	5	42.55
40	0	5	48.57
42	0	5	55.77
44	0	5	64.44
46	0	5	75.1
48	0	5	88.28
38	0	10	107.52
40	0	10	113.87
42	0	10	123.52
44	0	10	137.4
46	0	10	155.71
48	0	10	177.87

Table (5.3)b Numerical analysis bearing capacity factors N_q.
(Plane strain)

ϕ	$\frac{\delta}{\phi}$	$\frac{D}{B}$	N_q
28	0.5	0	9.72
30	0.5	0	11.74
32	0.5	0	14.24
34	0.5	0	17.42
36	0.5	0	21.47
38	0.5	0	26.75
40	0.5	0	33.74
42	0.5	0	43.06
44	0.5	0	55.72
46	0.5	0	73.11
48	0.5	0	97.31
28	0.5	3	20.82
30	0.5	3	25.08
32	0.5	3	30.22
34	0.5	3	36.78
36	0.5	3	44.6
38	0.5	3	54.74
40	0.5	3	67.67
42	0.5	3	84.45
44	0.5	3	106.52
46	0.5	3	136.03
48	0.5	3	176.35
28	0.5	5	31.51
30	0.5	5	36.88
32	0.5	5	43.77
34	0.5	5	52.22
36	0.5	5	62.86
38	0.5	5	76.26
40	0.5	5	93.25
42	0.5	5	115.17
44	0.5	5	143.61
46	0.5	5	181.43
48	0.5	5	232.46
34	0.5	10	113.5
36	0.5	10	127.56
38	0.5	10	147.1
40	0.5	10	174.38
42	0.5	10	208.64
44	0.5	10	254.07
46	0.5	10	313.39
48	0.5	10	392.42

Continue....

ϕ	$\frac{\delta}{\phi}$	$\frac{D}{B}$	N_q
38	0.5	15	263.71
40	0.5	15	291.92
42	0.5	15	335.91
44	0.5	15	396.16
46	0.5	15	476.57
48	0.5	15	584.28
40	0.5	20	475.998
42	0.5	20	511.36
44	0.5	20	579.34
46	0.5	20	677.68
48	0.5	20	812.89

Table (5.3)c Numerical analysis bearing capacity factors N_q.
(Plane strain)

ϕ	$\frac{\delta}{\phi}$	$\frac{D}{B}$	N_q
28	1	0	14.69
30	1	0	18.36
32	1	0	23.15
34	1	0	29.46
36	1	0	37.89
38	1	0	49.35
40	1	0	65.16
42	1	0	87.42
44	1	0	119.42
46	1	0	166.54
48	1	0	237.85
28	1	3	27.69
30	1	3	34.29
32	1	3	42.72
34	1	3	53.59
36	1	3	67.79
38	1	3	86.6
40	1	3	111.87
42	1	3	146.49
44	1	3	194.83
46	1	3	263.9
48	1	3	365.27
28	1	5	38.73
30	1	5	47.29
32	1	5	58.19
34	1	5	72.18
36	1	5	90.33
38	1	5	114.17
40	1	5	145.93
42	1	5	189.01
44	1	5	248.51
46	1	5	332.51
48	1	5	454.26
30	1	10	101.39
32	1	10	114.5
34	1	10	134.57
36	1	10	161.87
38	1	10	198.16
40	1	10	246.37
42	1	10	311.14
44	1	10	399.4
46	1	10	521.97
48	1	10	696.24

Continue....

ϕ	$\frac{\delta}{\phi}$	$\frac{D}{B}$	N_q
34	1	15	245.91
36	1	15	270.06
38	1	15	313.73
40	1	15	376.16
42	1	15	461.97
44	1	15	579.34
46	1	15	741.68
48	1	15	970.41
38	1	20	483.4
40	1	20	548.34
42	1	20	650.13
44	1	20	794.56
46	1	20	996.37
48	1	20	1280.7
40	1	25	786.17
42	1	25	887.77
44	1	25	1052.54
46	1	25	1291.09
48	1	25	1630.68

Table (5.4)a Numerical analysis bearing capacity factors N_q. (Axisymmetric)

ϕ	$\frac{\delta}{\phi}$	$\frac{D}{B}$	N_q
28	0	0	10.22
30	0	0	12.35
32	0	0	14.99
34	0	0	18.31
36	0	0	22.55
38	0	0	27.95
40	0	0	34.93
42	0	0	44.14
44	0	0	55.98
46	0	0	71.93
48	0	0	94.03
28	0	3	33.48
30	0	3	40.92
32	0	3	50.23
34	0	3	61.9
36	0	3	76.57
38	0	3	95.21
40	0	3	119
42	0	3	149.84
44	0	3	189.72
46	0	3	242.61
48	0	3	313.31
30	0	5	70.53
32	0	5	85.24
34	0	5	103.9
36	0	5	127.75
38	0	5	157.8
40	0	5	196.3
42	0	5	245.9
44	0	5	310.26
46	0	5	394.93
48	0	5	507.68
40	0	10	476.11
42	0	10	590.14
44	0	10	734.97
46	0	10	925.64
48	0	10	1178.18

Table (5.4)b Numerical analysis bearing capacity factors N_q.
(Axisymmetric)

ϕ	$\frac{\delta}{\phi}$	$\frac{D}{B}$	N_q
28	0.5	0	20.15
30	0.5	0	25.93
32	0.5	0	33.68
34	0.5	0	44.14
36	0.5	0	58.47
38	0.5	0	78.47
40	0.5	0	106.78
42	0.5	0	147.81
44	0.5	0	208.61
46	0.5	0	300.59
48	0.5	0	442.12
28	0.5	3	50.57
30	0.5	3	65.22
32	0.5	3	84.55
34	0.5	3	110.36
36	0.5	3	145.1
38	0.5	3	192.41
40	0.5	3	257.92
42	0.5	3	351.99
44	0.5	3	481.58
46	0.5	3	674.61
48	0.5	3	962.76
28	0.5	5	78.45
30	0.5	5	100.2
32	0.5	5	128.88
34	0.5	5	167.04
36	0.5	5	218.4
38	0.5	5	287.8
40	0.5	5	383.01
42	0.5	5	516
44	0.5	5	703.79
46	0.5	5	976.58
48	0.5	5	1378.95
34	0.5	10	367.06
36	0.5	10	469.85
38	0.5	10	607.63
40	0.5	10	795.07
42	0.5	10	1053.75
44	0.5	10	1415
46	0.5	10	1929.88
48	0.5	10	2677.64

Continue....

ϕ	$\frac{\delta}{\phi}$	$\frac{D}{B}$	N_q
38	0.5	15	1044.21
40	0.5	15	1361.02
42	0.5	15	1782.77
44	0.5	15	2365.31
46	0.5	15	3185.39
48	0.5	15	4361.84
42	0.5	20	2691.5
44	0.5	20	3558.35
46	0.5	20	4755.54
48	0.5	20	6449.41

Table (5.4)c Numerical analysis bearing capacity factors N_q.
(Axisymmetric)

ϕ	$\frac{\delta}{\phi}$	$\frac{D}{B}$	N_q
28	1	0	30.29
30	1	0	40.26
32	1	0	54.08
34	1	0	73.47
36	1	0	101.33
38	1	0	141.84
40	1	0	202.21
42	1	0	294.01
44	1	0	437.49
46	1	0	668.57
48	1	0	1053.35
28	1	3	65.59
30	1	3	87.46
32	1	3	116.7
34	1	3	156.79
36	1	3	213.28
38	1	3	293.16
40	1	3	408.48
42	1	3	578.55
44	1	3	835.24
46	1	3	1232.75
48	1	3	1869.23
28	1	5	96.31
30	1	5	126.79
32	1	5	167.82
34	1	5	224.69
36	1	5	303.17
38	1	5	413.53
40	1	5	571.3
42	1	5	801.31
44	1	5	1143.94
46	1	5	1666.84
48	1	5	2492.61
30	1	10	265.42
32	1	10	343.44
34	1	10	448.68
36	1	10	593.74
38	1	10	795.02
40	1	10	1078.82
42	1	10	1486.22
44	1	10	2080.85
46	1	10	2970.85
48	1	10	4340.75

Continue....

ϕ	$\frac{\delta}{\phi}$	$\frac{D}{B}$	N_q
36	1	15	989.45
38	1	15	1306.29
40	1	15	1745.72
42	1	15	2369.09
44	1	15	3269.55
46	1	15	4597.55
48	1	15	6615.13
38	1	20	1928.51
40	1	20	2578.14
42	1	20	3463.85
44	1	20	4725.99
46	1	20	6569.71
48	1	20	9334.86
40	1	25	3510
42	1	25	4763.09
44	1	25	6458.98
46	1	25	8867.37
48	1	25	12522.2

Table (5.5)a Limit analysis bearing capacity factors N_q.

ϕ	$\frac{\delta}{\phi}$	$\frac{D}{B}$	N_q
28	0	0	4.83
30	0	0	5.49
32	0	0	6.26
34	0	0	7.17
36	0	0	8.24
38	0	0	9.53
40	0	0	11.07
42	0	0	12.95
44	0	0	15.26
46	0	0	18.12
48	0	0	21.71
28	0	3	13.37
30	0	3	15.12
32	0	3	17.16
34	0	3	19.53
36	0	3	22.32
38	0	3	25.59
40	0	3	29.47
42	0	3	34.1
44	0	3	39.67
46	0	3	46.43
48	0	3	54.72
28	0	5	24.92
30	0	5	26.14
32	0	5	28.43
34	0	5	31.47
36	0	5	35.21
38	0	5	39.72
40	0	5	45.13
42	0	5	51.62
44	0	5	59.43
46	0	5	68.9
48	0	5	80.49
38	0	10	100.23
40	0	10	105.24
42	0	10	114.15
44	0	10	126.36
46	0	10	142.02
48	0	10	161.67

Table (5.5)b Limit analysis bearing capacity factors N_q.

ϕ	$\frac{\delta}{\phi}$	$\frac{D}{B}$	N_q
28	0.5	0	9.52
30	0.5	0	11.48
32	0.5	0	13.94
34	0.5	0	17.06
36	0.5	0	21.03
38	0.5	0	26.17
40	0.5	0	32.89
42	0.5	0	41.82
44	0.5	0	53.86
46	0.5	0	70.48
48	0.5	0	93.75
28	0.5	3	20.35
30	0.5	3	24.36
32	0.5	3	29.3
34	0.5	3	35.42
36	0.5	3	43.07
38	0.5	3	52.72
40	0.5	3	65.06
42	0.5	3	81.01
44	0.5	3	101.95
46	0.5	3	129.93
48	0.5	3	167.97
28	0.5	5	30.62
30	0.5	5	35.85
32	0.5	5	42.38
34	0.5	5	50.5
36	0.5	5	60.64
38	0.5	5	73.39
40	0.5	5	89.58
42	0.5	5	110.38
44	0.5	5	137.42
46	0.5	5	173.21
48	0.5	5	221.36
34	0.5	10	109.84
36	0.5	10	122.75
38	0.5	10	141.88
40	0.5	10	167.11
42	0.5	10	199.88
44	0.5	10	242.45
46	0.5	10	298.33
48	0.5	10	372.61

Continue....

ϕ	$\frac{\delta}{\phi}$	$\frac{D}{B}$	N_q
38	0.5	15	252.59
40	0.5	15	279.31
42	0.5	15	320.45
44	0.5	15	376.87
46	0.5	15	452.39
48	0.5	15	553.15
40	0.5	20	454.44
42	0.5	20	487.13
44	0.5	20	550.04
46	0.5	20	641.66
48	0.5	20	767.52

Table (5.5)c Limit analysis bearing capacity factors N_q.

ϕ	$\frac{\delta}{\phi}$	$\frac{D}{B}$	N_q
28	1	0	14.73
30	1	0	18.41
32	1	0	23.19
34	1	0	29.49
36	1	0	37.92
38	1	0	49.36
40	1	0	65.13
42	1	0	87.29
44	1	0	119.14
46	1	0	165.94
48	1	0	236.63
28	1	3	27.62
30	1	3	34.2
32	1	3	41.78
34	1	3	53.39
36	1	3	67.51
38	1	3	86.18
40	1	3	111.27
42	1	3	145.58
44	1	3	193.44
46	1	3	261.73
48	1	3	361.72
28	1	5	38.6
30	1	5	47.1
32	1	5	57.94
34	1	5	71.84
36	1	5	89.86
38	1	5	113.5
40	1	5	145
42	1	5	187.56
44	1	5	246.35
46	1	5	329.19
48	1	5	456.13
30	1	10	100.77
32	1	10	113.73
34	1	10	133.59
36	1	10	160.58
38	1	10	196.42
40	1	10	244.03
42	1	10	307.88
44	1	10	394.76
46	1	10	515.23
48	1	10	686.14

Continue....

ϕ	$\frac{\delta}{\phi}$	$\frac{D}{B}$	N_q
34	1	15	243.62
36	1	15	267.27
38	1	15	310.2
40	1	15	371.62
42	1	15	455.85
44	1	15	570.95
46	1	15	729.89
48	1	15	953.36
38	1	20	476.91
40	1	20	540.46
42	1	20	639.93
44	1	20	781.02
46	1	20	977.89
48	1	20	1254.66
40	1	25	773.26
42	1	25	871.91
44	1	25	1032.18
46	1	25	1264.07
48	1	25	1593.47

Relative density (%)	Confining pressure (kPa)	Young's modulus E_{50} (kPa)
95.7	75	68486
99.7	50	53746
90.5	25	40174
38.8	75	44107
36.0	50	28704
28.0	25	19475

Table 6.1a Summary of Young's modulus for 14/25 sand.

Relative density (%)	Confining pressure (kPa)	Young's modulus E_{50} (kPa)
78.13	100	43770
81.05	50	23548
80.8	25	13769
53.4	100	36611
49.7	50	17982
47.0	25	10218

Table 6.1b Summary of Young's modulus for 52/100 sand.

TEST	$\frac{D}{B}$	σ_v	ϕ	I_r	$\frac{r}{R_p}$	$q_{c\Delta=0\%}$ (MPa)	$q_{c\Delta=2.5\%}$ (MPa)	$q_{c\Delta=5\%}$ (MPa)	$q_{c_{exp}}$ (MPa)
T25	30	189.5	44°	97.11	2.176	91.72	46.77	34.9	38.3
	40	252.7	44°	72.8	2.155	101.52	57.61	43.88	45.0
T27	20	59.6	39°	143.5	1.987	19.53	8.91	6.62	8.07
	26	77.5	39°	110.4	2.085	25.62	12.95	9.76	10.0
T19	20	62.76	45°	171.4	1.818	25.86	10.3	7.43	13.0
	26	81.59	45°	103.1	1.782	27.2	12.2	8.94	17.0
T11	20	124.5	38°	195.8	1.911	38.5	15.7	11.5	12.6
	29	161.8	37.5	173.2	1.956	49.14	21.11	15.62	14.3
T12	20	248.9	37°	152.8	2.02	75.3	34.3	25.6	21.0
	26	323.6	37°	133	2.057	96.4	46.3	34.8	27.5

(a) Analysis using insitu ϕ

TEST	$\frac{D}{B}$	σ_v	ϕ	I_r	$\frac{r}{R_p}$	$q_{c\Delta=0\%}$ (MPa)	$q_{c\Delta=2.5\%}$ (MPa)	$q_{c\Delta=5\%}$ (MPa)	$q_{c_{exp}}$ (MPa)
T25	30	189.5	32°	116.5	2.15	43.8	23.18	18.07	38.3
	40	252.7	32°	87.36	2.25	58.7	34.39	27.02	45.0
T27	20	59.6	32°	160.59	2.024	13.36	6.35	4.84	8.07
	26	77.5	32°	123.5	2.209	20.0	10.44	8.05	10.0
T19	20	62.76	32°	205.7	2.033	15.97	6.91	5.22	13.0
	26	81.59	32°	158.2	2.126	21.03	10.05	7.66	17.0
T11	20	124.5	32°	216.1	2.000	30.5	12.94	9.76	12.6
	26	161.8	32°	166.3	2.091	40.14	18.82	14.32	14.3
T12	20	248.9	32°	166.1	2.092	61.84	29.0	22.08	21.0
	26	323.6	32°	127.8	2.184	81.03	41.8	32.18	27.5

(b) Analysis using critical ϕ

Table 6.2 Values of qc from equation (6.30) with different volumetric strain Δ

LIST OF SYMBOLS

B	Cone diameter or width of wedge
C.E.M	Cavity Expansion Method
D	Depth of penetration
D_c	Characteristic depth
E	Young's modulus
F	Capacity of load cell
G	Shear Modulus
G_s	Specific gravity
I_r	Rigidity index
I_{rr}	Reduced rigidity index
K	Bulk modulus
M	Constraint modulus
M.C	Method of Characteristics
M_0	Initial tangent constraint modulus
N.C	Normally Consolidated
N_2	Nitrogen
N_q	Bearing capacity factor
N_γ	Bearing capacity factor
$N_{q\gamma}$	Bearing capacity factor
O.C	Overconsolidated
P	Pole for plane
R_i	Initial radius of cavity
R_p	Radius of plastic zone
R_u	Final radius of cavity
X	Distance to the rigid boundary
d	Internal diameter of cylinder
d_{50}	Nominal grain diameter

e	Void ratio
f_s	Skin friction
i	point numbers
k_o	Coefficient of earth pressure at rest
m	Weight of probe+piston
ng	gravity level
p'	Mean hydrostatic effective stress
p_i	Initial pressure
p_{crit}	Critical pressure
p_u	Ultimate pressure
q_c	Tip resistance
s	Mean normal stress
z	Thickness of strata

Greek letters

α, β Characteristic lines.

β_0 Radial fan angle.

γ Unit weight.

γ_T Active wedge angle.

δ Cone-soil interface friction angle.

ϵ Angle of the characteristic lines made with the major principal stress direction.

ϵ_a Axial strain.

ϵ_s Shear strain.

ϵ_v Volumetric strain.

θ Total angle of radial fan.

θ_0 Radial fan angle.

μ Poisson ratio.

ν dilatancy angle.

ρ Density.

ρ_i Immediate settlement.

ϱ Dimensionless factor.

τ_{ij} Shear stress tensor.

σ_{ij} Cauchy stress tensor

ϕ_m Mobilised angle of shearing resistance.

ϕ_p Peak angle of shearing resistance.

ϕ_{pc} Pseudo-constant angle of shearing resistance.

ψ Angle of the direction of major principal stress makes with the vertical z-axis.

ψ_c, ψ_T Cone base angle.

ω Angular velocity.

$\Delta\sigma$ Change in normal stress.

i, j all possible direction in space

REFERENCES

Airey, D.W, Budhu, M, Wood, D.M (1984) Some aspects of the behaviour of soils in sample shear. Cambridge University Engineering Department Technical Reports. CUED/D-SOILS TR.155.

Almeida, M.S.S and Parry, R.H.G (1983) Studies of vane and penetrometer tests during centrifuge flight. Cambridge University Engineering Department Technical Reports. CUED/D-SOILS TR142.

Atkinson, J.H (1981) Foundations and slopes. McGraw-Hill, London.

Atkinson, J.H and Bransby P.L (1978) The mechanics of soils. McGraw-Hill, London.

Baldi, G et al (1981) Cone resistance in dry NC and OC sand. Proc. Cone Penetration Testing and Experience. ASCE St.Louis Missouri, pp. 145-177.

Baligh, M.M (1976) Cavity expansion in sands with curved envelope. J. Geotechnical Engineering Div. ASCE, pp. 1131-1147.

Baligh, M.M (1985) Strain path method. J. Geotechnical Engineering Div. ASCE, pp. 1108-1135.

Been, K and Jefferies, M.G (1986) A state parameter for sand. Geotechnique 35, pp. 99-112.

Been, K. Jefferies, M.G. Crooks, J.H.A and Rothenburg, L (1987) The cone penetration test in sands: part II, general inference of state. Geotechnique 37, pp. 285-299.

Benham, P.P and Warnock, F.V (1979) Mechanics of solids and structure. The Pitman Press, Bath, pp.316-326.

Bolton, M.D (1979) A guide to soil mechanics.
The Macmillan Press Ltd.

Bolton, M.D (1986) The strength and dilatancy of sands.
Geotechnique 36, pp 65-78.

Borst, R. and Vermeer, P (1982) Finite element analysis of static penetration tests.
Proc. Second European Sym. on Penetration Testing,
Amsterdam. pp 457-462.

Calladine, C.R (1985) Plasticity for engineers.
Ellis Harwood Ltd, England.

Chapman, G.A (1974) A calibration chamber for field test equipment.
Proc. First European Sym. on Penetration Testing, Stockholm. pp 59-65.

Chen, W.F (1975) Limit analysis and soil plasticity.
Elsevier Scientific Publishing Company, New York.

Cox, A.D, Eason, G and Hopkins, H (1961) Axially symmetric plastic deformations
in soils. Proc. Roy. Society, Vol 254. pp 1-45.

Cox, A.D (1962) Axially symmetric plastic deformation in soil-II indentation
of ponderable soils. Int. J. Mech. Sci. pp 371-380.

Dahlberg, R (1974) The effect of the overburden pressure on the penetration
resistance in a preloaded natural fine sand deposit.
Proc. First European Sym. on Penetration Testing, Stockholm. pp 89-91.

De Beer, E.E (1970) Experimental determination of the shape factors and the bearing
capacity factors of sand. Geotechnique 20. pp 387-411.

De Beer, E.E (1974) Scale effects in results of penetration tests performed in stiff clay.
Proc. First European Sym. on Penetration Testing, Stockholm. pp 105-114.

Drescher, A and Kang, Y (1987) Kinematic approach to limit load for steady penetration in rigid-plastic soil. Geotechnique 37. pp 233-246.

Drescher, A and Michalowski (1984) Density variation in pseudo-steady plastic flow of granular media. Geotechnique 34. pp 1-10

Durgunoglu, H.T and Mitchell, J.K (1975) Static Penetration resistance of soils. I-Analysis, II-evaluation of theory and implications for practice. Proc. Speciality Con. on Insitu Measurement of Soil Properties, ASCE. Vol I.

Ferguson, K.A and Ko, H.Y (1981) Centrifuge model of the cone penetrometer. Proc. Cone Penetration Testing and Experience. ASCE, St. Louis, Missouri. pp 108-127.

Folque, J (1974) Compressibility of sands determined by means of penetration testing. Proc. First European Sym. on Penetration Testing, Stockholm. pp 141-145.

Graham, J. and Hovan, J (1986) Stress characteristics for bearing capacity in sand using a critical state model. Canadian Geotechnical J. pp 195-202.

Graham, J. and Stuart, J (1971) Scale and boundary effects in foundation analysis. J. Soil Mechanics and Foundation Div. ASCE. pp 1533-1549.

Hansen, B and Christensen, N (1969) Theoretical bearing capacity of very shallow footings. J. Soil Mechanics and Foundation Div. ASCE. pp 1568-1572.

Houlsby, G.T and Withers, N (1988) Analysis of the cone pressuremeter test in clay. Geotechnique 38. pp 575-587.

Houlsby, G.T and Wroth, C.P (1980) strain and displacement discontinuity in soil. Journ. of the Eng. Mech. Div. ASCE 106. pp 753-771.

Houlsby, G.T and Wroth, C.P (1982) Direct solution of plasticity problems in soils by the method of characteristics. Proc. Forth Conf. Num. Anal. Methods in Geomechanics 3, Edmonton. pp 1059-1071.

James, R.G and Bransby, P.L (1971). A velocity field for some passive earth pressure problems. Geotechnique, 21, 61-83.

Kemp, W.G.B (1982) The influence of the rate of penetration on the cone resistance q_c in sand. Proc. Second European Sym. on Penetration Testing, Amsterdam. pp 627-634.

Kimura, T. Kusakabe, O and Sattoh, K (1985) Geotechnical model tests of bearing capacity problems in a centrifuge. Geotechnique 35. pp 33-45

Ko, H.Y and Scott, R.F (1973) Bearing capacities by plasticity theory. J. Soil Mechanics and Foundations Div. ASCE. pp 25-43

Koumoto, T and Kaku, K (1982) Three dimensional analysis of static cone penetration in clay. Proc. Second European Sym. on Penetration Testing, Amsterdam. pp 635-640.

Ladanyi, B (1963) Expansion of a cavity in a saturated clay medium. J. Soil Mechanics and Foundation Div. ASCE. pp 127-161.

Larkin, L (1968) Theoretical bearing capacity of very shallow footings. J. Soil Mechanics and Foundation Div. ASCE. pp 127-161.

Lee. S.Y (1987) Propagation of ruptures beneath strip footings. MPhil Thesis, University of Cambridge.

Meigh, A.C (1987) Cone penetration testing. CIRIA Ground Engineering Report. Butterworth Publication.

Meyerhof, G (1951) The ultimate bearing capacity of foundations.
Geotechnique 2. pp 301-331

Meyerhof, G (1953) The bearing capacity of foundation under
eccentric and inclined load.
Proc. Third Int. Conf. Soil Mech. pp 440-445.

Meyerhof, G (1955) Influence of roughness of base and groundwater conditions
on the ultimate bearing capacity of foundation.
Geotechnique 5. pp 227-242.

Meyerhof, G (1961)a The ultimate bearing capacity of wedge-shaped foundation.
Proc. Fifth Int. Conf. on Soil Mech. and Found. Eng. vol 2. pp 105-109.

Meyerhof, G (1976) Bearing capacity and settlement of pile foundations.
J. Geotechnical Engineering Div. ASCE. pp 197-227.

Mitchell, J.K and Lunne, Tom (1978) Cone resistance as measure of sand strength.
J. Geotechnique Engineering Div. ASCE. pp 995-1011.

Nowatzki, E.A (1971) A theoretical assessment of the S.P.T.
Proc. Forth Pan-American Conf. on soil Mechanics and
Foundation Engineering. pp 45-61.

Nowatzki, E.A and Karafiath, L (1972) Effect of cone angle on penetration resistance.
51^{st} Am. meeting of the Highway Research Board. pp 102.

Ovesen, N.K (1981) Centrifuge tests of the uplift capacity of anchors.
Proc. Tenth Int. Conf. S.M.F.E, Stockholm, Sweden. vol 1 pp 717-722.

Parkin, A.K and Lunne, T (1982) Boundary effects in laboratory calibration
of a cone penetrometer for sand. Proc. Second European
Sym. on Penetration Testing, Amsterdam. pp 761-767.

Phillip, R et al (1987) An experimental investigation of factors affecting penetration resistance in granular soils in centrifuge modelling. Cambridge University Technical Report. CUED/D-SOILS, TR 210.

Poorooshasb, F (1988) The dynamic embedment of a heat emitting projectile. Ph.D Thesis, Cambridge University.

Robertson, P and Campenella, R (1983) Interpretation of cone penetration tests, part-I: sand. Canadian Geotechnical J. vol 20. pp 718-733.

Robertson, P and Campanella, R (1986) S.P.T-C.P.T correlations. J. Geotechnical Engineering Div. ASCE. pp 1449-1459.

Roscoe, K.H (1970). The influence of strain in soil mechanics. Geotechnique 20 (2), 129-170.

Rowe, P.W (1962) The stress-dilatancy relation for static equilibrium of an assembly of particles in contact. Proc. R. Soc, 269, pp 500-527.

Schaap, L and Zuidberg, H (1982) Mechanical and electrical aspects of the electric cone penetrometer tip. Proc. Second European sym. on Penetration Testing, Amsterdam. pp 841-852.

Schofield, A.N (1980) Cambridge geotechnical centriguge operation. 20^{th} Rankine Lecture, Geotechnique 30. pp 227-268.

Schofield, A.N and Wroth, C.P (1968) Critical state soil mechanics. McGraw-Hill , London.

Shi, Q (1988) Centrifuge modelling of surface footings subjected to combine loading. Ph.D Thesis, University of Cambridge.

Shield, R.T (1953) Mixed boundary value problems in soil mechanics. Quart. of the Applied. Maths (11). 61-75.

Smits, E.P (1982) Cone penetration tests in dry sand.
Proc. Second European Sym. on Penetration Testing. pp877-882.

Sokolovski, V.V (1965) Statics of granular media.
Pergamon Press, Oxford.

Stone, K.J.L (1988) Modelling of rupture development in soils.
Ph.D Thesis, University of Cambridge.

Stroud, M.A (1971) The behaviour of sand at low stress level in the simple shear apparatus. Ph.D Thesis, University of Cambridge.

Taylor, D.W (1948) Fundamentals of soil mechanics. J. Wiley, New York. 329-361.

Teh, C.I (1987) An analytical study of the cone penetration test.
D.Phil Thesis, Oxford University.

Terzaghi, K and Peck, R.B (1948) Soil mechanics in engineering practice. J.Wiley, New York. 217-225.

Veismanis, A (1974) Laboratory investigation of electric friction cone penetrometers in sand. Proc European Sym. on Penetration Testing, Stockholm. pp 407-419.

Venter, K.V (1987) Modelling the response of soils to cyclic loading.
Ph.D Thesis, University of Cambridge.

Vesic, A (1963) Bearing capacity of deep foundation in sand.
Highway Research Record No. 39. pp 112-153.

Vesic, A (1972) Expansion of cavities in finite soil mass.
J. Soil Mechanics and Foundations Div. ASCE. pp 265-290.

Phillip, R et al (1987) An experimental investigation of factors affecting penetration resistance in granular soils in centrifuge modelling. Cambridge University Technical Report. CUED/D-SOILS, TR 210.

Poorooshasb, F (1988) The dynamic embedment of a heat emitting projectile. Ph.D Thesis, Cambridge University.

Robertson, P and Campenella, R (1983) Interpretation of cone penetration tests, part-I: sand. Canadian Geotechnical J. vol 20. pp 718-733.

Robertson, P and Campanella, R (1986) S.P.T-C.P.T correlations. J. Geotechnical Engineering Div. ASCE. pp 1449-1459.

Roscoe, K.H (1970). The influence of strain in soil mechanics. Geotechnique 20 (2), 129-170.

Rowe, P.W (1962) The stress-dilatancy relation for static equilibrium of an assembly of particles in contact. Proc. R. Soc, 269, pp 500-527.

Schaap, L and Zuidberg, H (1982) Mechanical and electrical aspects of the electric cone penetrometer tip. Proc. Second European sym. on Penetration Testing, Amsterdam. pp 841-852.

Schofield, A.N (1980) Cambridge geotechnical centriguge operation. 20^{th} Rankine Lecture, Geotechnique 30. pp 227-268.

Schofield, A.N and Wroth, C.P (1968) Critical state soil mechanics. McGraw-Hill , London.

Shi, Q (1988) Centrifuge modelling of surface footings subjected to combine loading. Ph.D Thesis, University of Cambridge.

Shield, R.T (1953) Mixed boundary value problems in soil mechanics. Quart. of the Applied. Maths (11). 61-75.

Smits, E.P (1982) Cone penetration tests in dry sand.
Proc. Second European Sym. on Penetration Testing. pp877-882.

Sokolovski, V.V (1965) Statics of granular media.
Pergamon Press, Oxford.

Stone, K.J.L (1988) Modelling of rupture development in soils.
Ph.D Thesis, University of Cambridge.

Stroud, M.A (1971) The behaviour of sand at low stress level in the
simple shear apparatus. Ph.D Thesis, University of Cambridge.

Taylor, D.W (1948) Fundamentals of soil mechanics. J. Wiley, New York. 329-361.

Teh, C.I (1987) An analytical study of the cone penetration test.
D.Phil Thesis, Oxford University.

Terzaghi, K and Peck, R.B (1948) Soil mechanics in engineering practice. J.Wiley,
New York. 217-225.

Veismanis, A (1974) Laboratory investigation of electric friction cone
penetrometers in sand. Proc European Sym. on
Penetration Testing, Stockholm. pp 407-419.

Venter, K.V (1987) Modelling the response of soils to cyclic loading.
Ph.D Thesis, University of Cambridge.

Vesic, A (1963) Bearing capacity of deep foundation in sand.
Highway Research Record No. 39. pp 112-153.

Vesic, A (1972) Expansion of cavities in finite soil mass.
J. Soil Mechanics and Foundations Div. ASCE. pp 265-290.

Vesic, A (1977) Design of pile foundations. National Co-operative Highway Research Programme Report 42. Transport Research Board, Washington D.C.

Villet, W.C.B and Mitchell, J.K (1981) Cone resistance, relative density and friction angle. Proc. Cone Penetration Testing and Experience, ASCE. St. Louis, Missouri. pp 178-208.

Wroth, C.P and Bassett, R.H (1965) A stress-strain relationship for the shearing behaviour of sand. Geotechnique 15, 32-56.

Yamaguchi, H. Kimura, T and Fuji, N (1977) On the scale effect of footings in dense sand. Proc. Ninth Int. Conf. on S.M.F.E, Tokyo, Japan. vol 1. pp 795-798.

Chen P,K-H (1986) Axisymmetric deformations during cone penetration of sand Ph.D Thesis, University of London.

Lau, C.K (1988) Scale effects in Tests on footing, Ph.D Thesis, University of Cambridge

Appendix A

Physical Characteristic of Sands

Fontainbleau Sand

e_{max}	0.920
e_{min}	0.548
G_s	2.69
d_{50}	$0.176mm$

14/25 Leighton Buzzard Sand

e_{max}	0.820
e_{min}	0.495
G_s	2.65
d_{50}	$0.900mm$

25/52 Leighton Buzzard Sand

e_{max}	0.859
e_{min}	0.495
G_s	2.65
d_{50}	$0.400mm$

52/100 Leighton Buzzard Sand

e_{max}	0.928
e_{min}	0.585
G_s	2.65
d_{50}	$0.225mm$

Appendix B

Calculation of nitrogen pressure required to be stored in the accumulator.

F=capacity of load cell (kN).

N_2=blow-off pressure (1034 kPa).

m=weight of probe + piston at 1g

p=pressure in the top chamber (kPa).

R=radius from centrifuge axis to the c.g of piston+probe (3.51m).

d=internal diameter of the cylinder (m).

ng=gravity level.

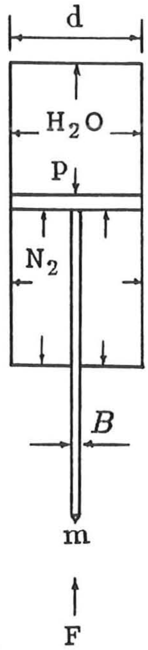

w=weight of piston and probe at n gravity level is

$$w = mng \quad \text{(kN)}$$

Equilibrium of forces as shown in the figure is

$$F + N_2\left(\frac{\pi}{4}(d^2 - B^2)\right) = w + p\left(\frac{\pi}{4}d^2\right)$$

or

$$p = \left(F + N_2\left(\frac{\pi}{4}(d^2 - B^2)\right) - m\frac{R}{4}n\right)\frac{4}{\pi d^2}$$

water pressure due to change g level is

$$\int_{0.63}^{3.062} \rho\omega^2 r dr = 11n \quad \textbf{(kPa)}$$

Pressure losses across bent, joint and friction assume to be 1034kPa (150 psi). Therefore required pressure to be stored in the accumulator is

$$\left(F + N_2\left(\frac{\pi}{4}(d^2 - B^2)\right) - m\frac{R}{4}n\right)\frac{4}{\pi d^2} - 11n + 1034. \qquad \textbf{(kPa)}$$

Summary of the required pressures to be stored in the accumulator for different probe diameter and g-level is shown in table 3.4

Appendix C

Force equilibrium

Refer to figure 5.22, force acting on plane OA is

$$\sigma_a(\frac{0.5B}{\cos\psi_T})$$

assuming that the stress distribution is uniform throughout that plane.

Resolving the force vertically,

$$q_c(0.5B) = \sigma_a(\frac{0.5B}{\cos\psi_T})\left(\frac{\cos(\psi_T - \delta)}{\cos\delta}\right)$$

or

$$q_c = \sigma_a\left(\frac{\cos(\psi_T - \delta)}{\cos\psi_T \cos\delta}\right)$$

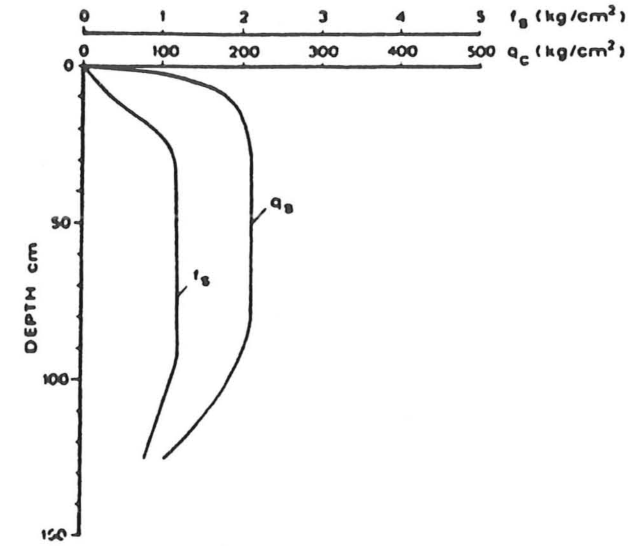

Fig 1.1 Example of a CPT test result.

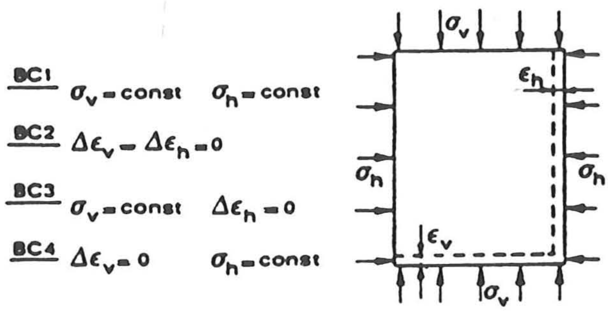

Fig 1.2 Boundary conditions that can be applied during calibration chamber test.

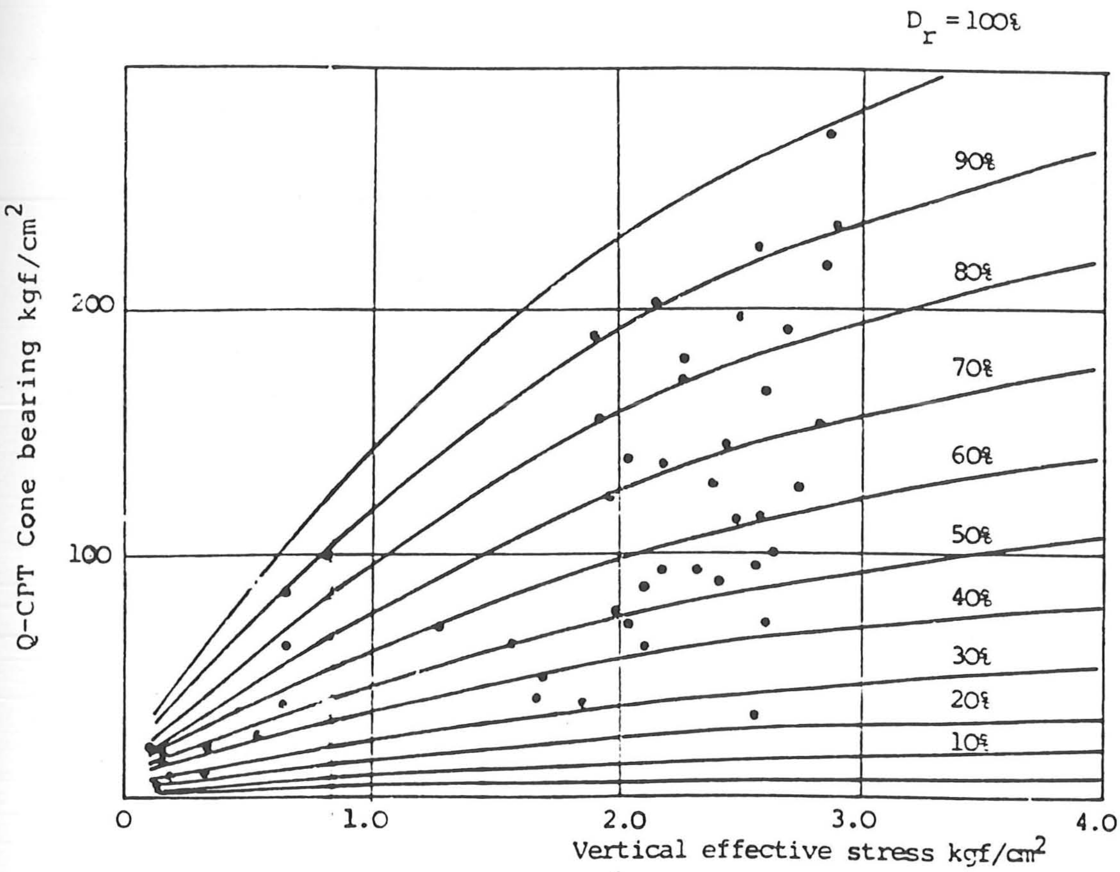

Fig 1.3 Relationship between q_c, σ'_v and R.D for normally fine sand (after Schmertmann, 1975).

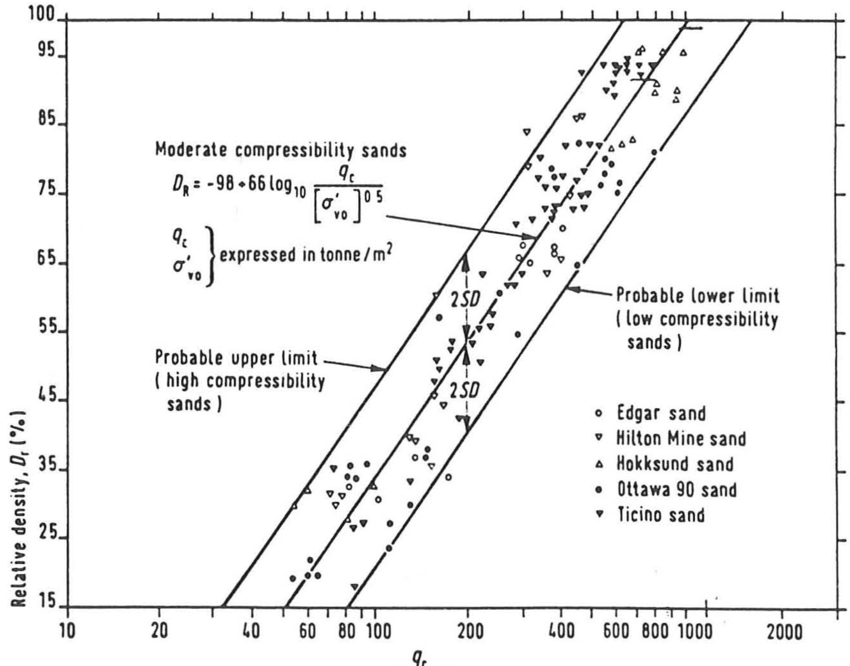

Fig 1.4 Relationship between q_c, σ'_v and R.D for normally consolidated quartz sand (after Jamiolkowski et al, 1985).

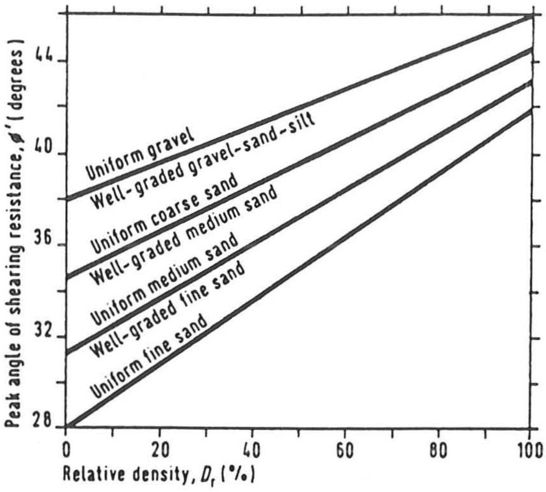

Fig 1.5 Relationship between ϕ_p, and R.D for quartz sand (after Schmertmann, 1978).

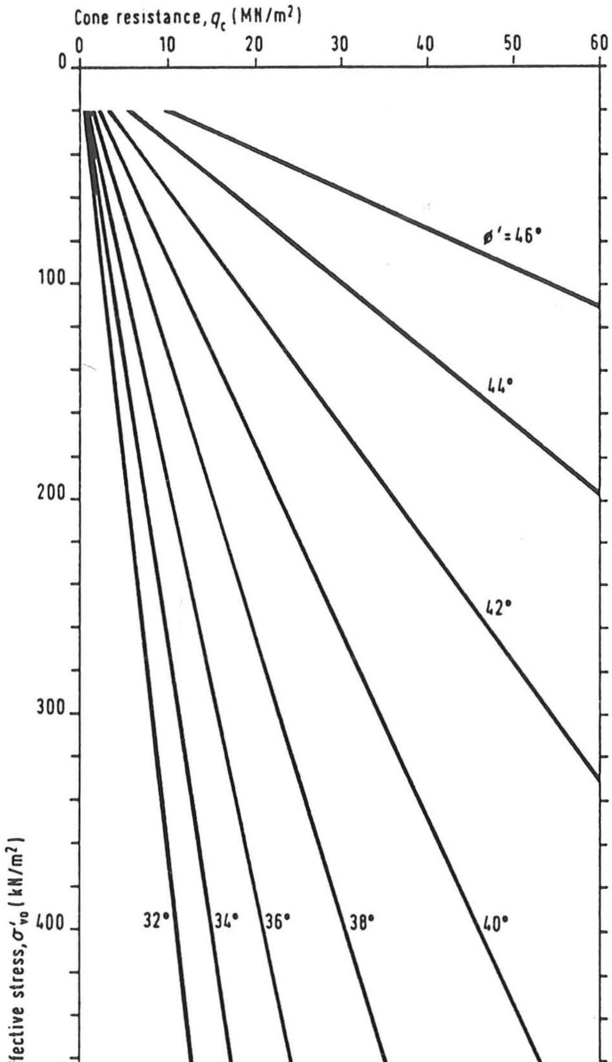

Fig 1.6 Relationship between q_c, σ'_v, and R.D for normally consolidated quartz sand (after Durgunoglu and Mitchell, 1975).

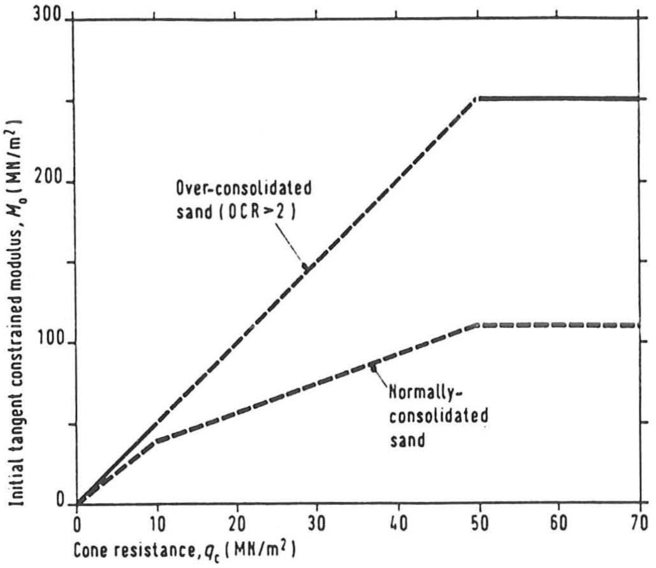

Fig 1.7 Initial tangent constraint modulus M_0 for normally consolidated sand (after Lunne and Christoffersen, 1983).

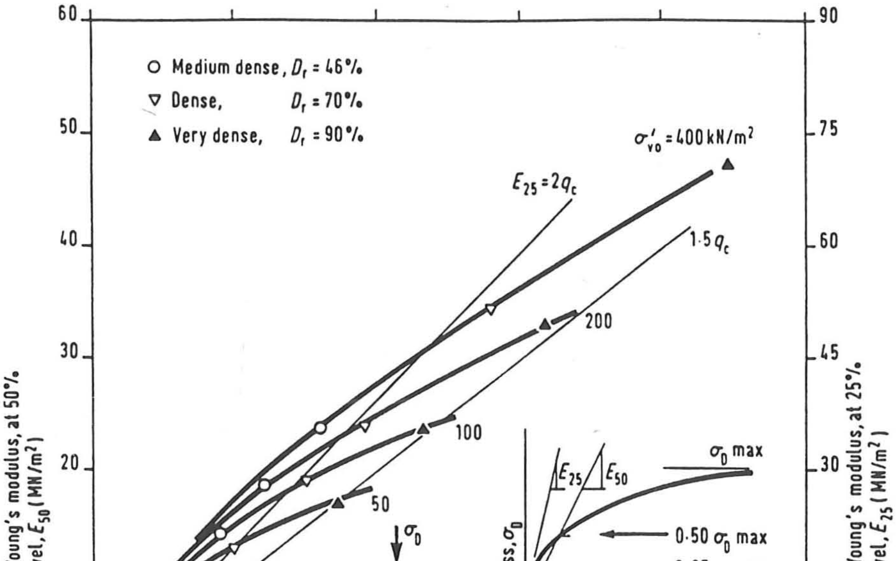

Fig 1.8 Young's modulus for normally consolidated quartz sand (after Robertson and Campenella, 1983).

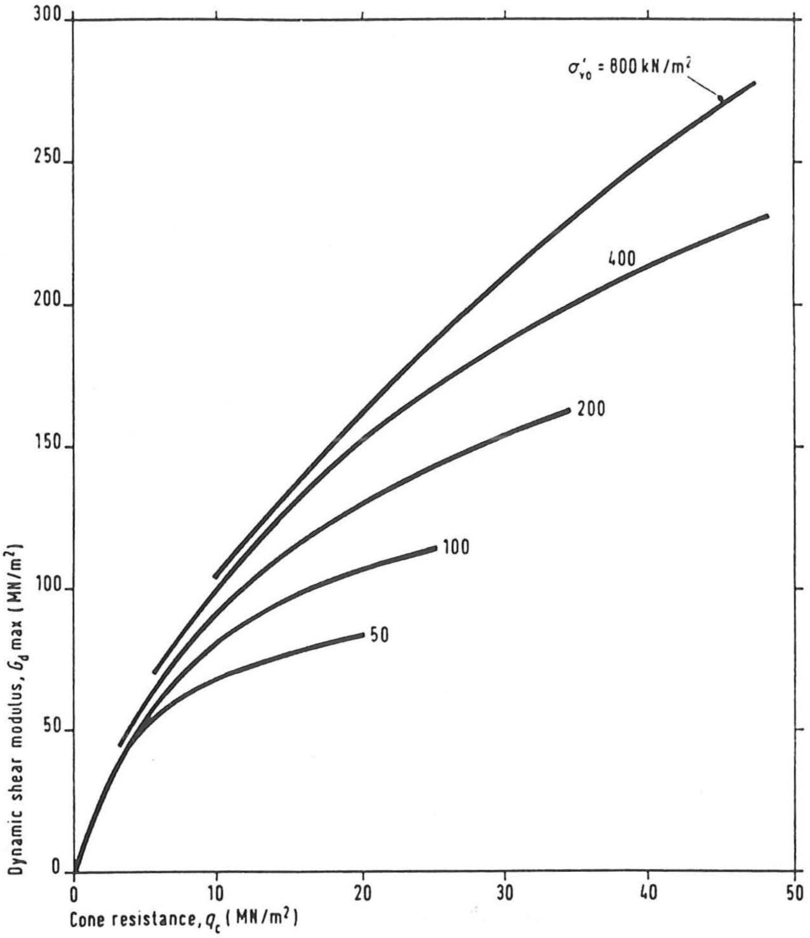

Fig 1.9 Dynamic shear modulus for normally consolidated quartz sand at small strain (after Robertson and Campenella, 1983).

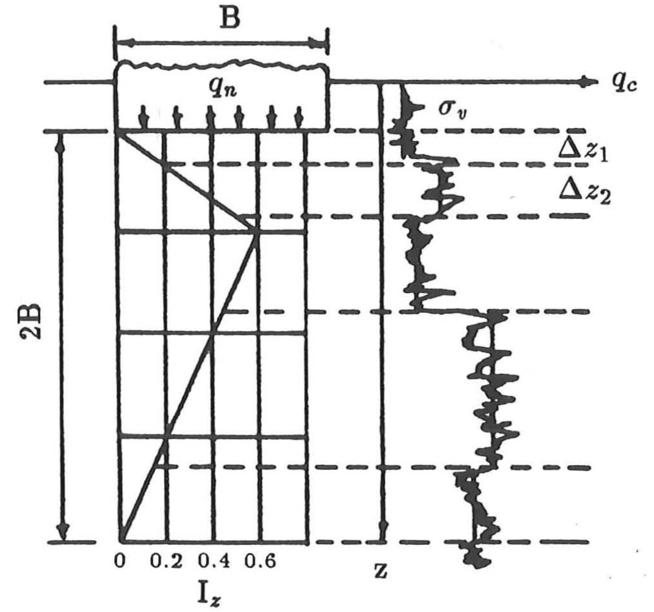

Fig 1.10 2B-0.6 curve Influence factor I_z

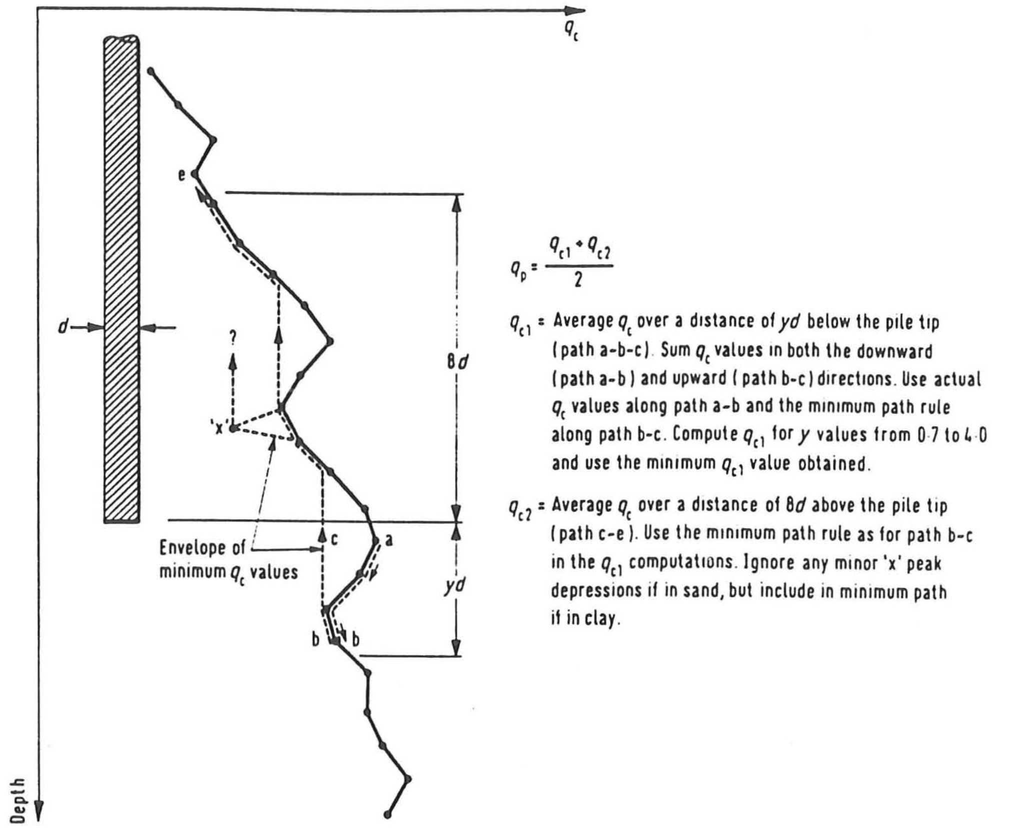

Fig 1.11 Procedure to determine q_p from CPT (after Schmertmann, 1978 and Heijnen, 1974).

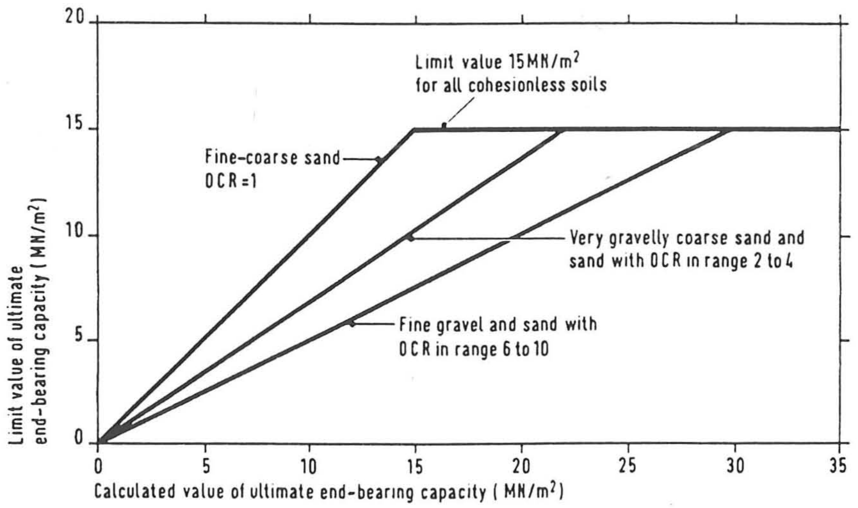

Fig 1.12 Limit values of ultimate pile end-bearing capacity (after Kemp, 1977)

(a)

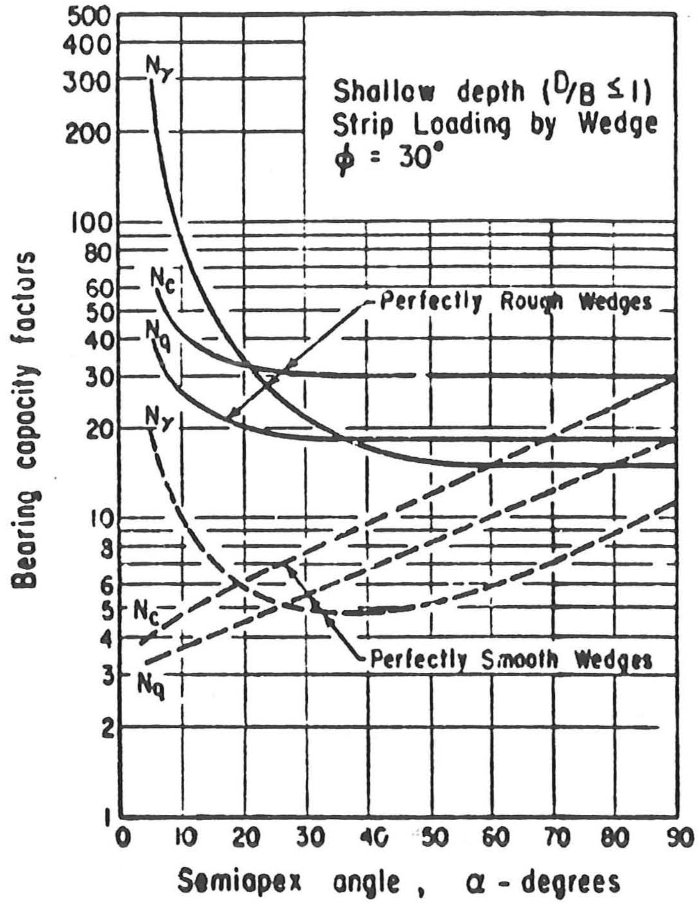

(b)

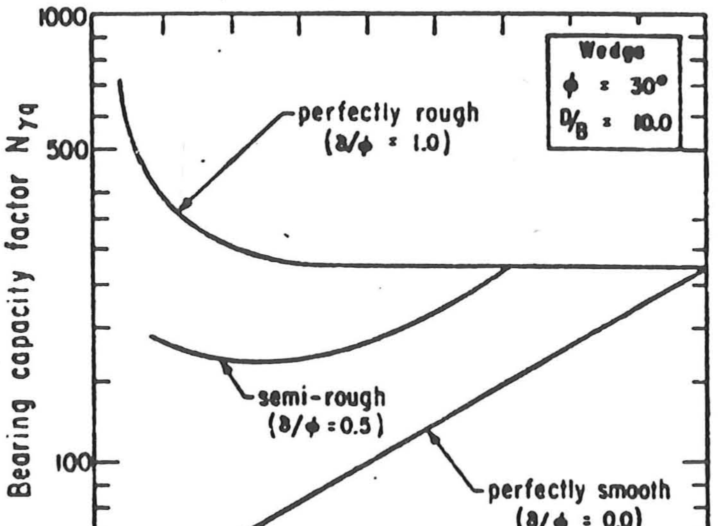

Fig 1.13 Effects of wedge angle on the bearing capacity factor
(after Meyerhof, 1961, Durgunoglu and Mitchell, 1975)

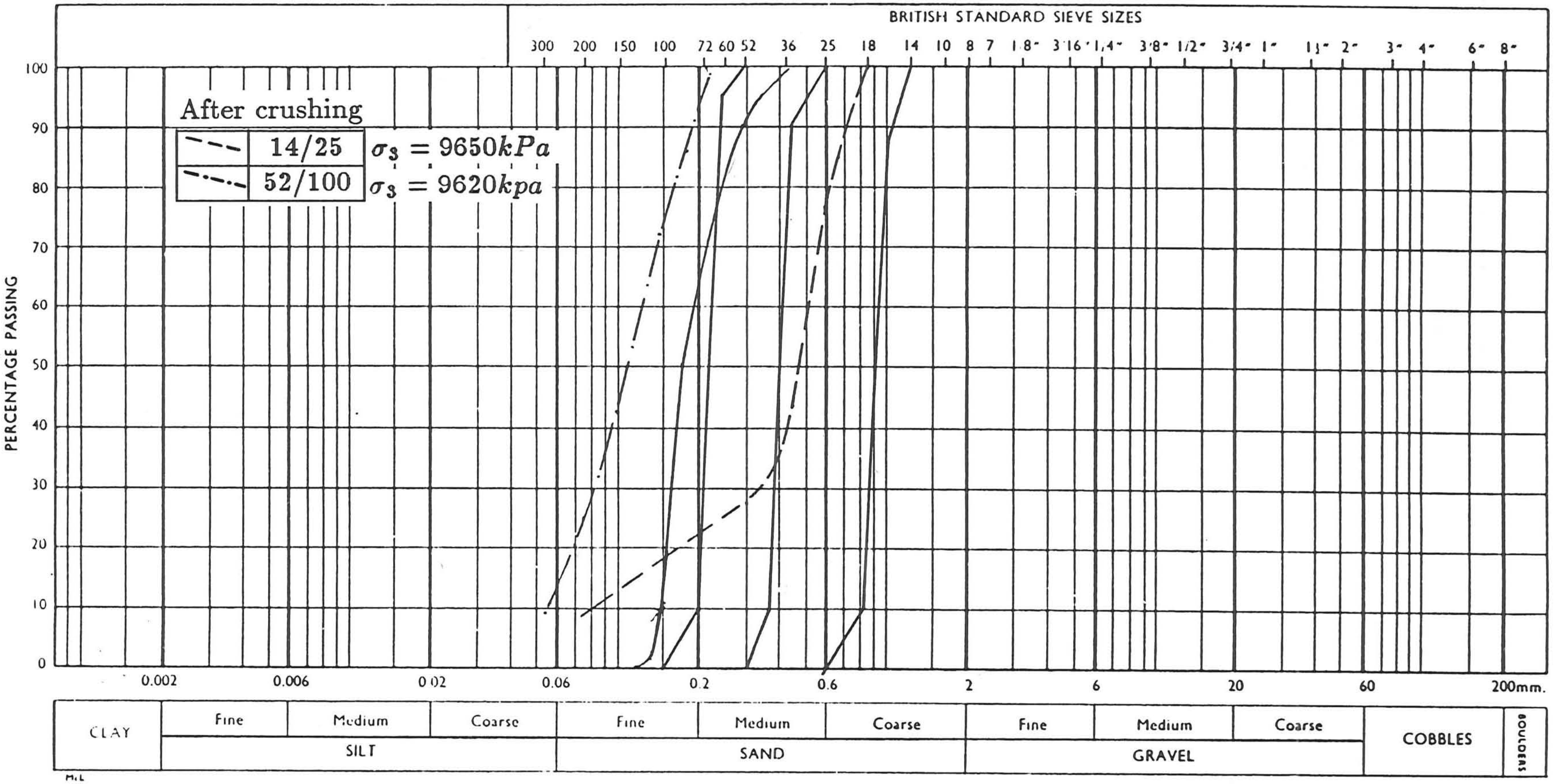

Fig 2.1 Particle size distributions curves before and after crushing.

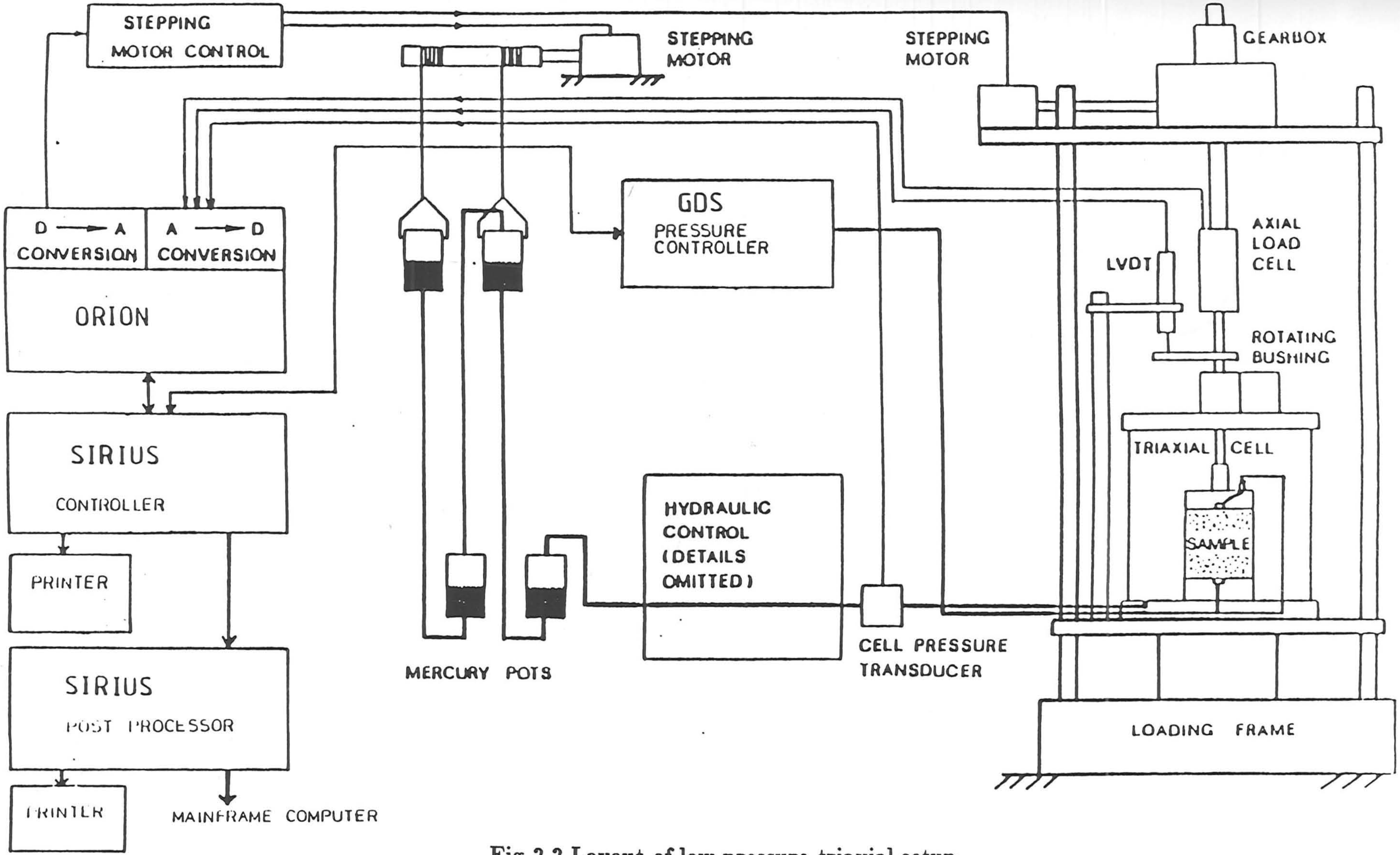

Fig 2.2 Layout of low pressure triaxial setup.

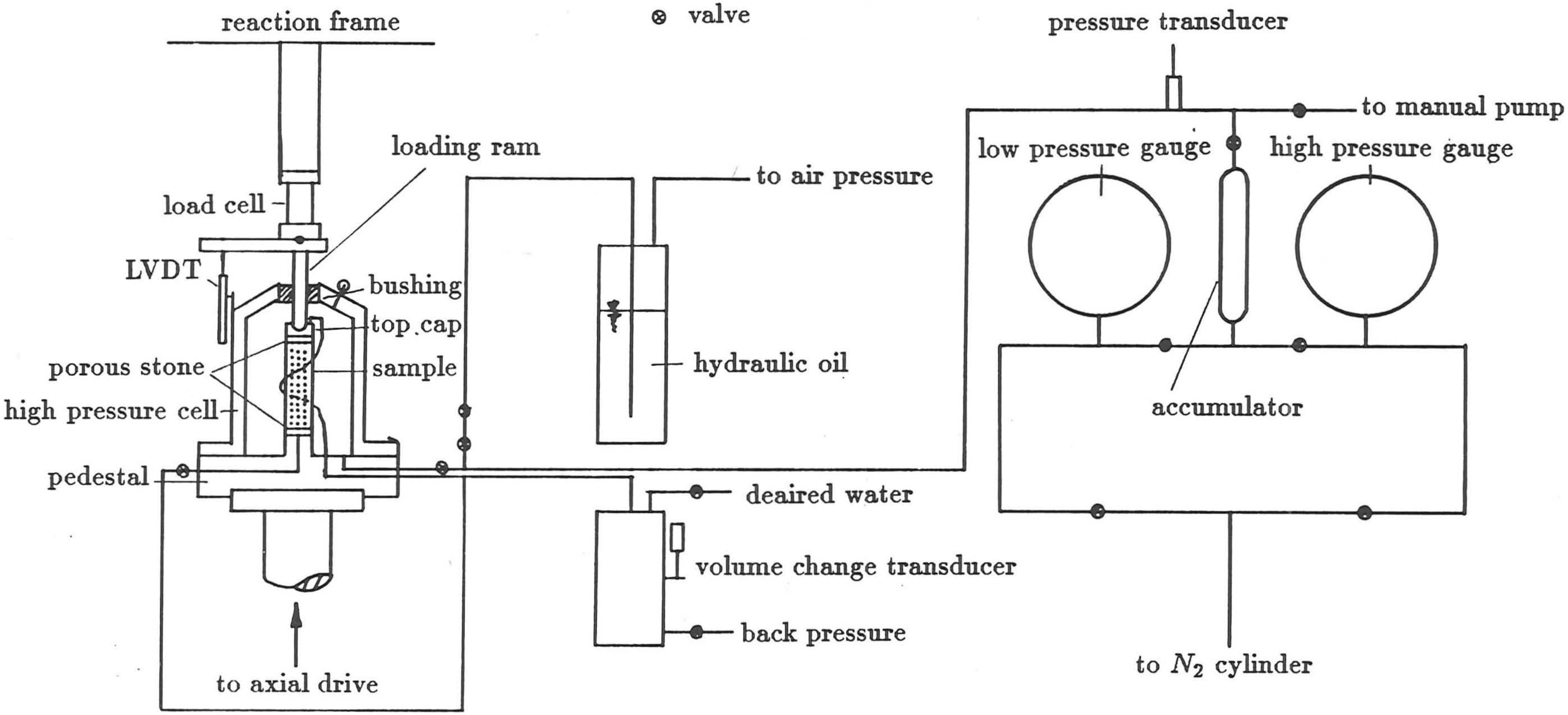

Fig 2.3 Layout of high pressure triaxial setup.

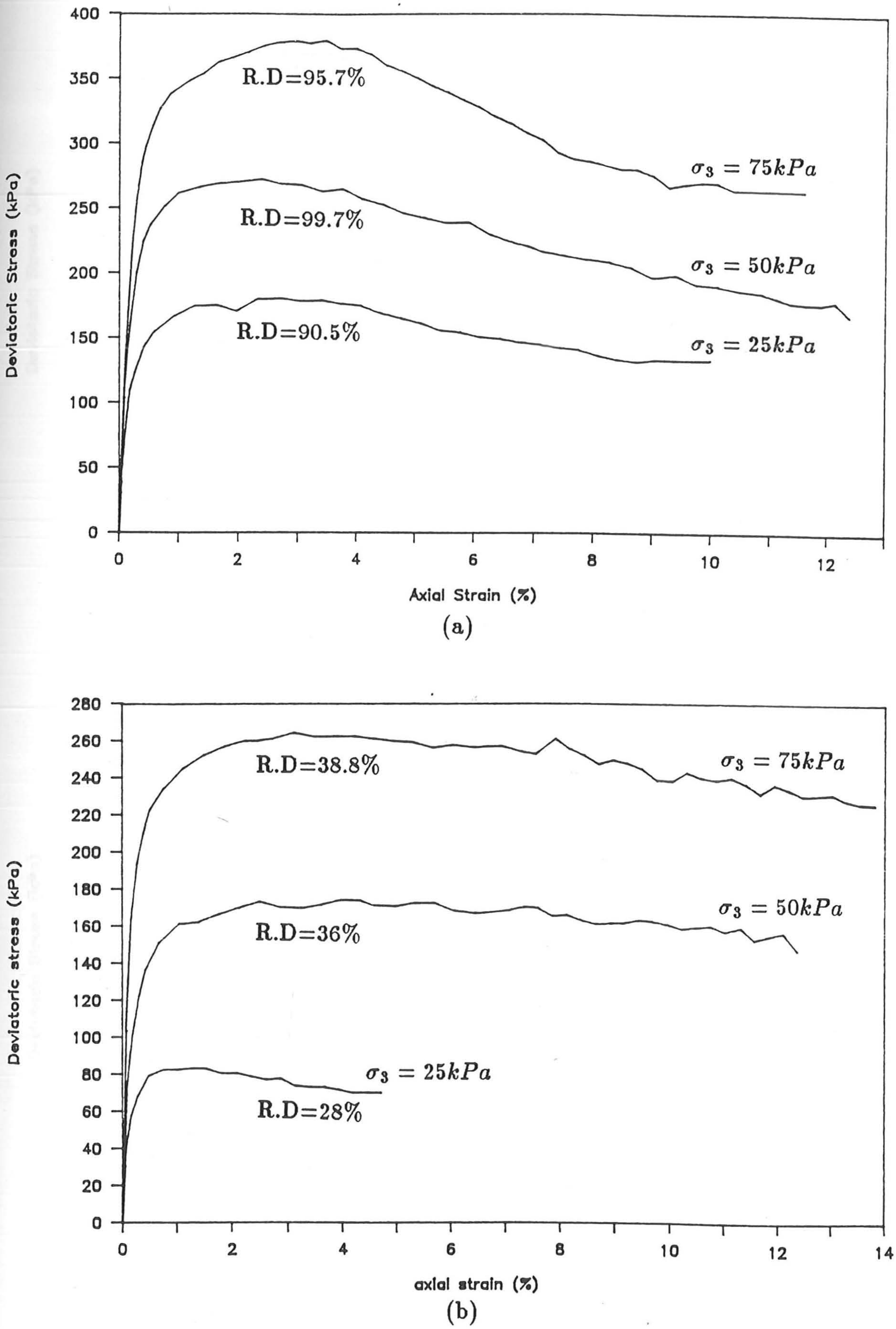

Fig 2.4 Low pressure triaxial tests on 14/25 sand.

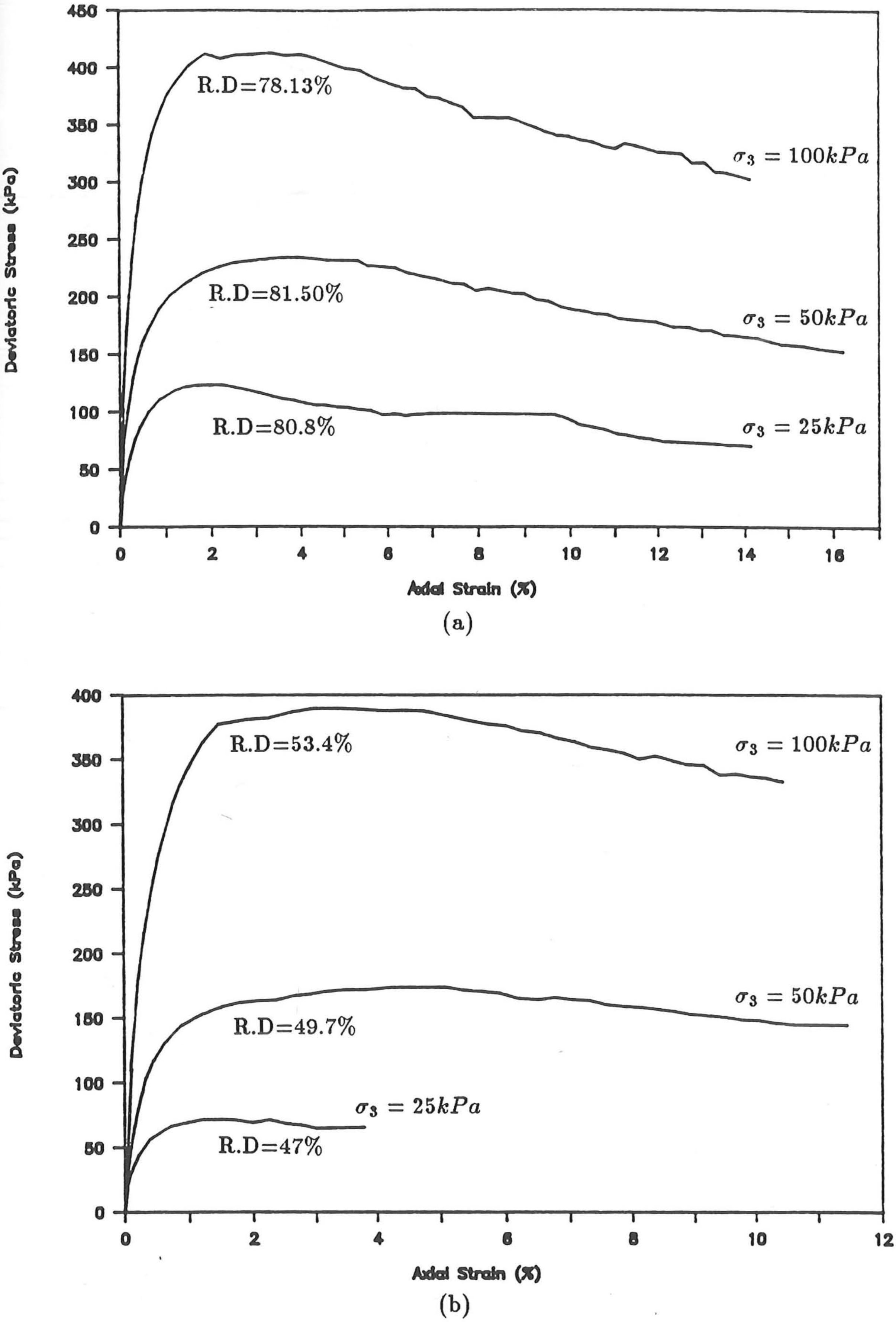

Fig 2.5 Low pressure triaxial tests on 52/100 sand.

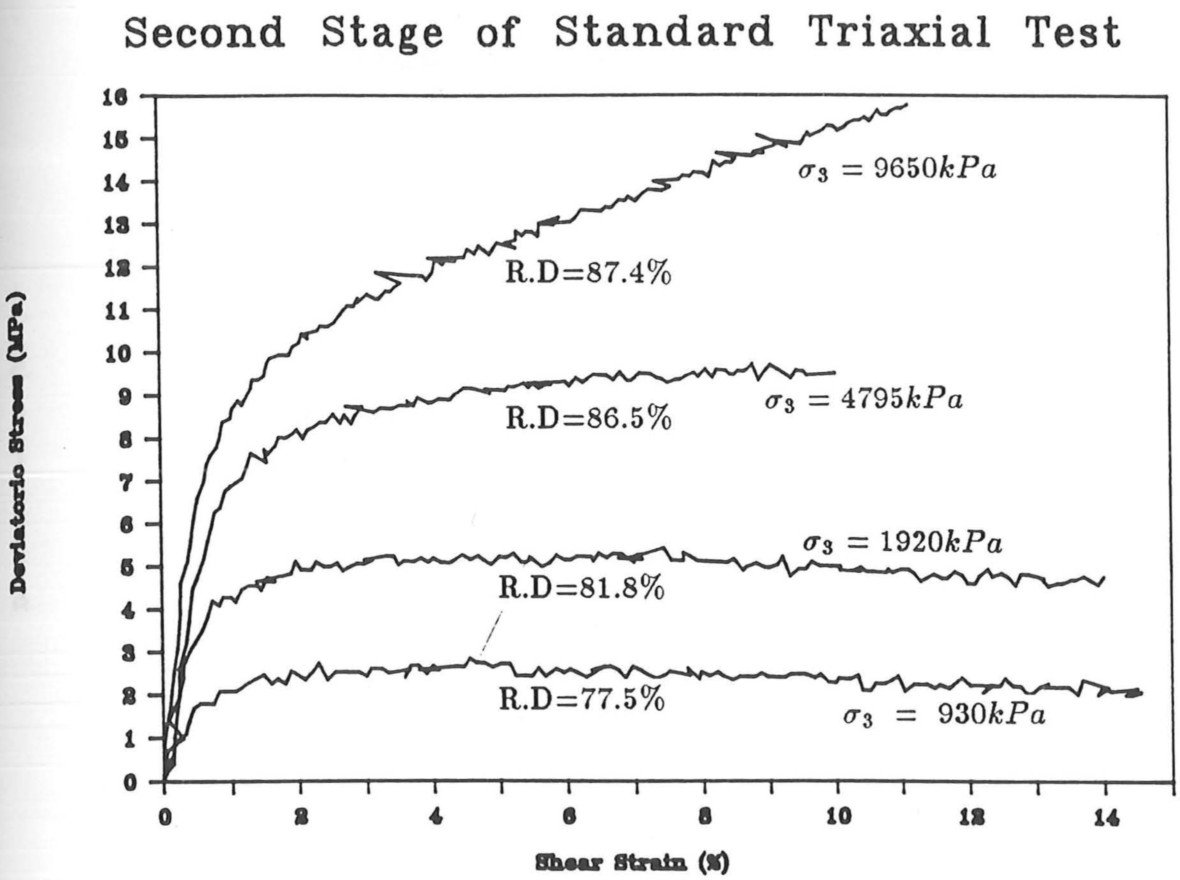

(a)

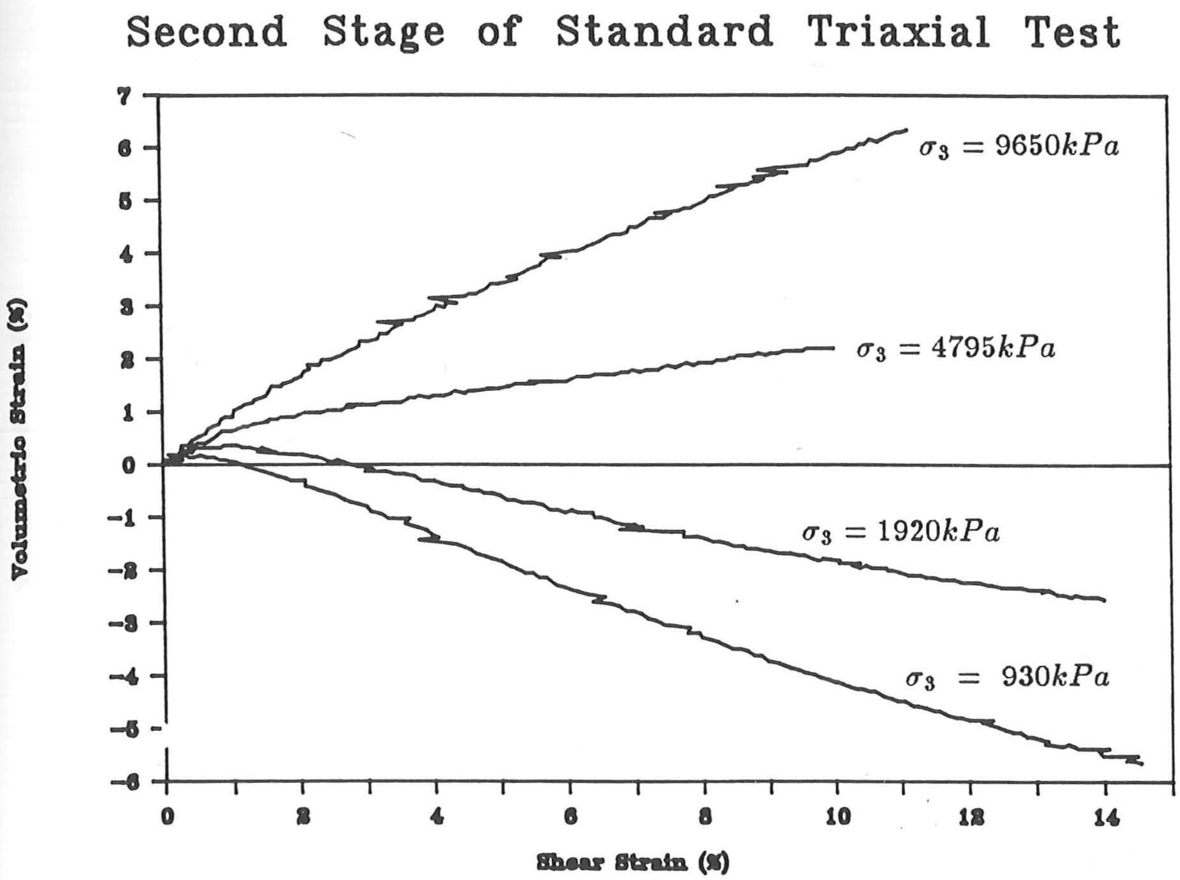

(b)

Fig 2.6 High pressure triaxial tests on 14/25 sand.

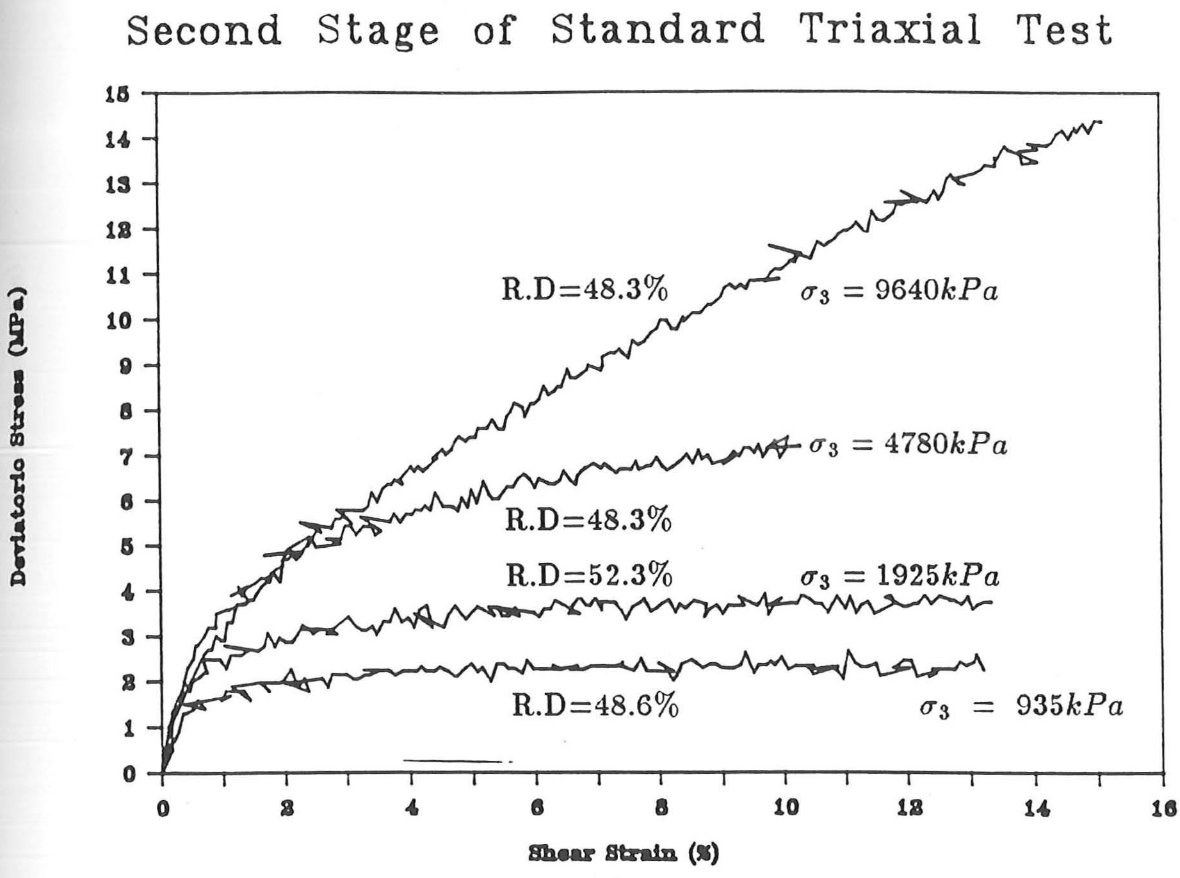

(a)

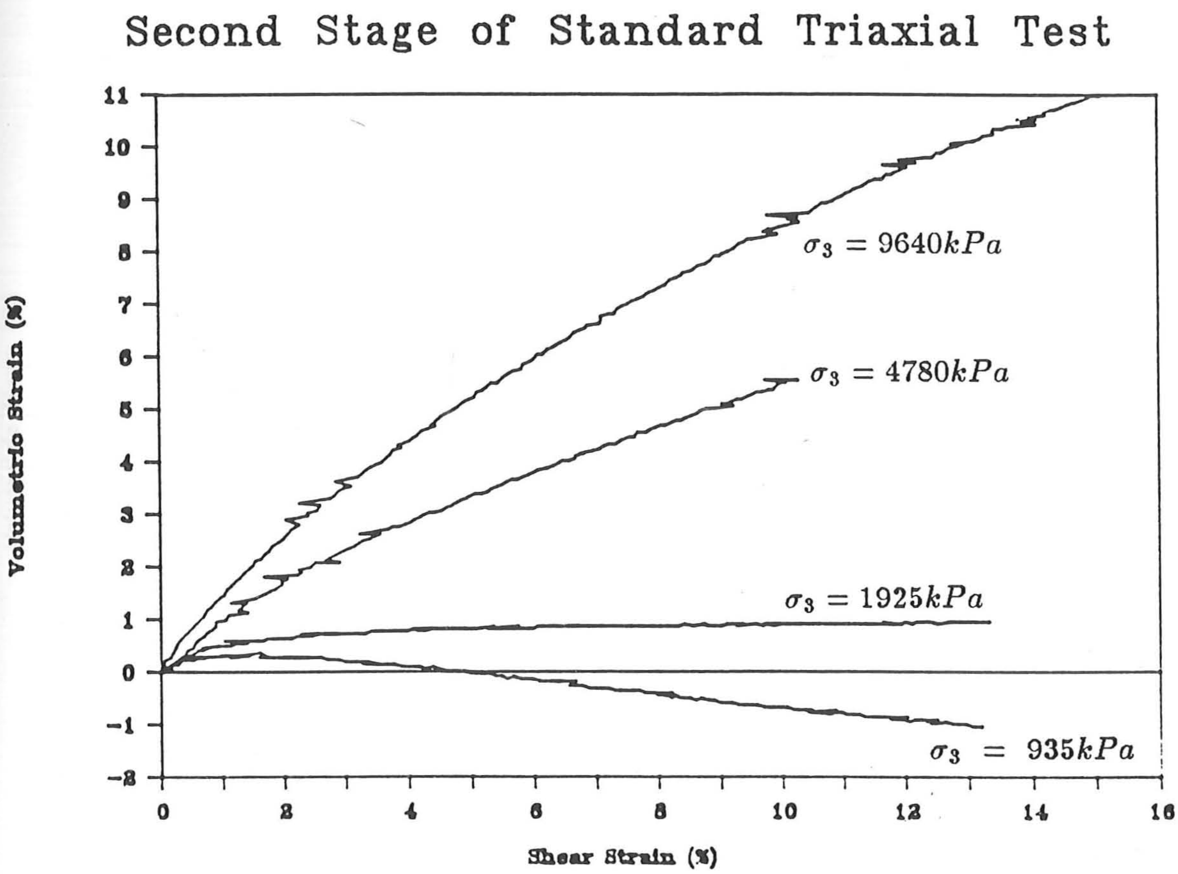

(b)

Fig 2.7 High pressure triaxial tests on 14/25 sand.

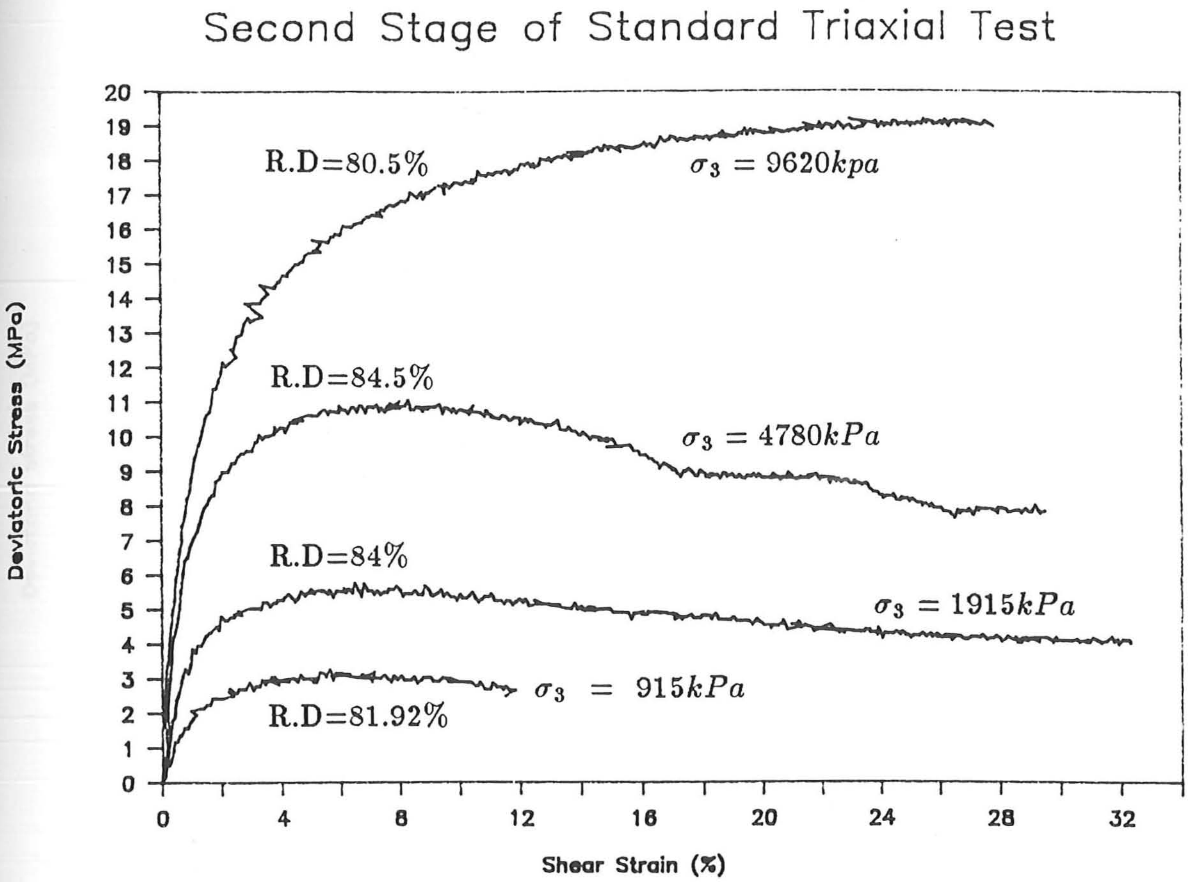

(a)

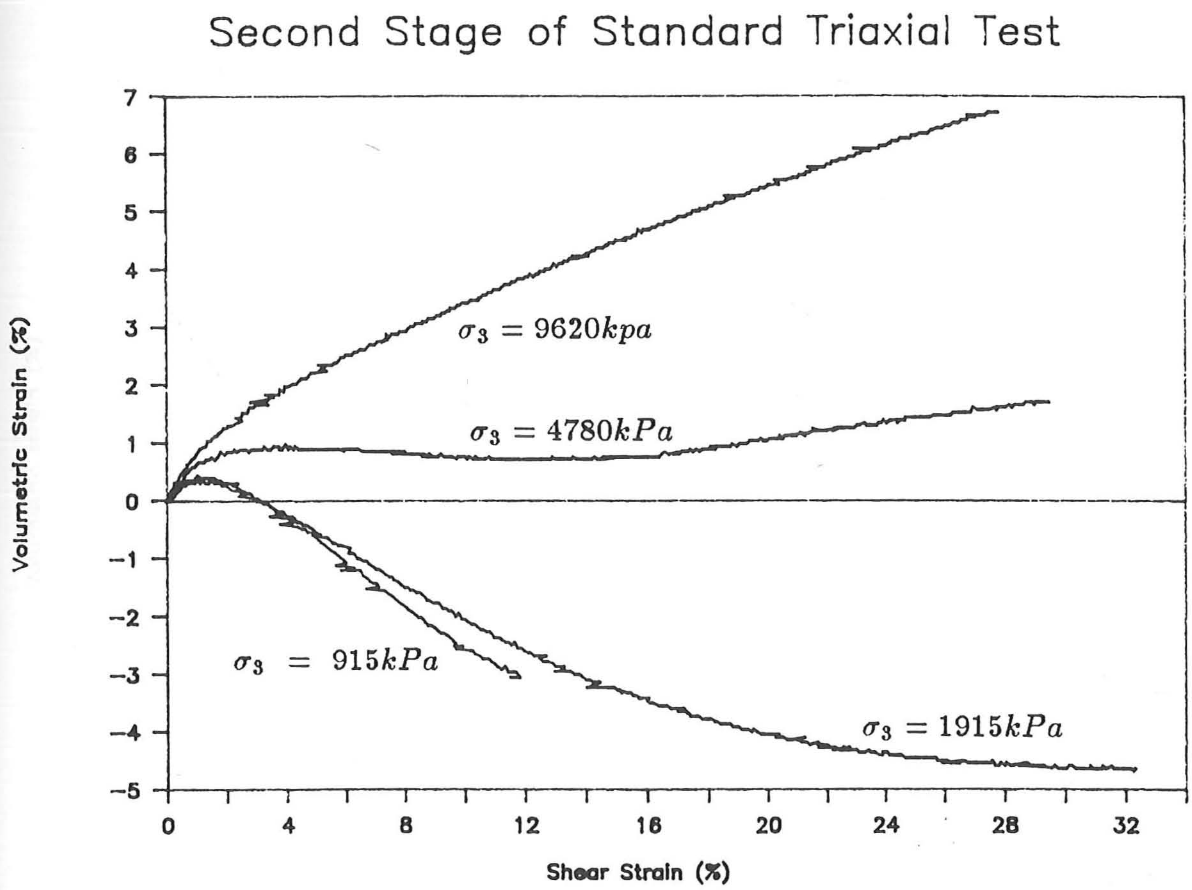

(b)

Fig 2.8 High pressure triaxial tests on 52/100 sand.

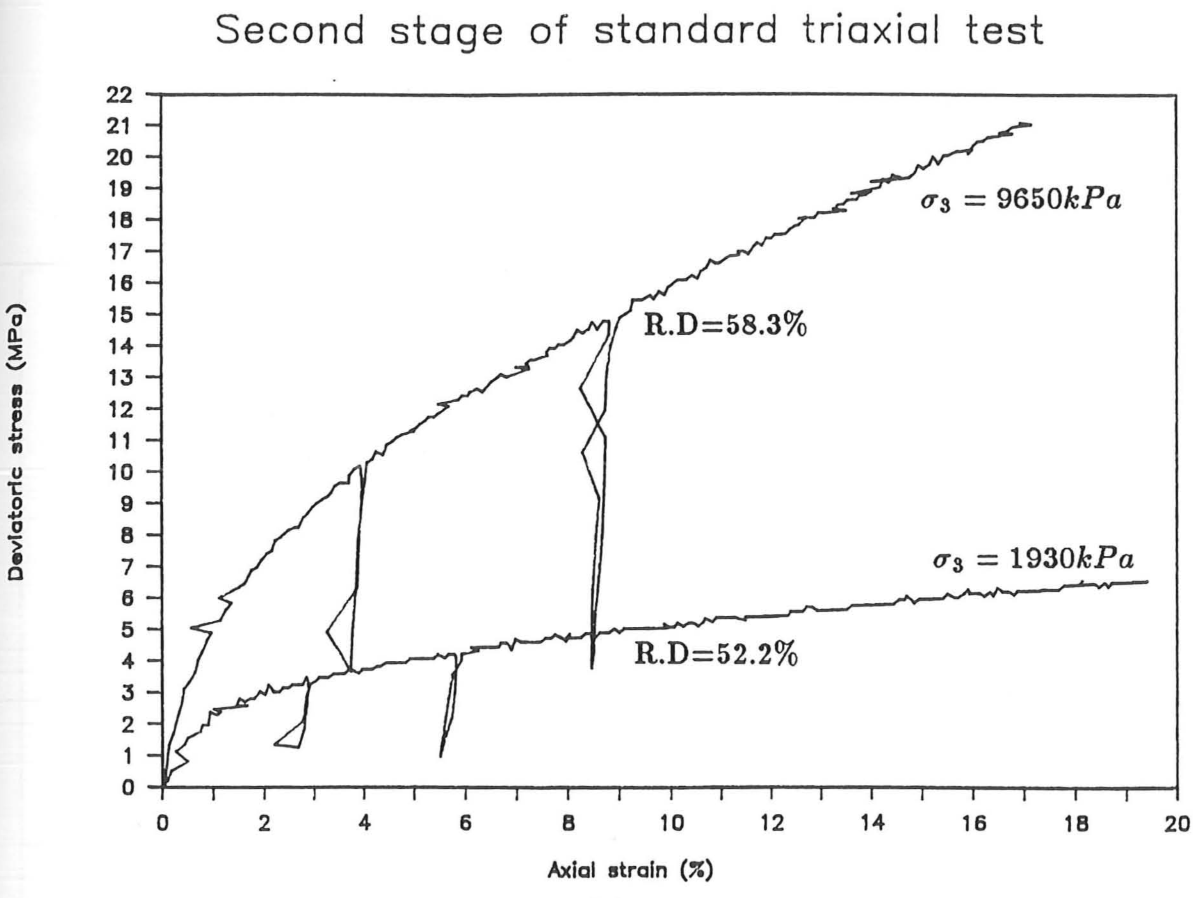

(a)

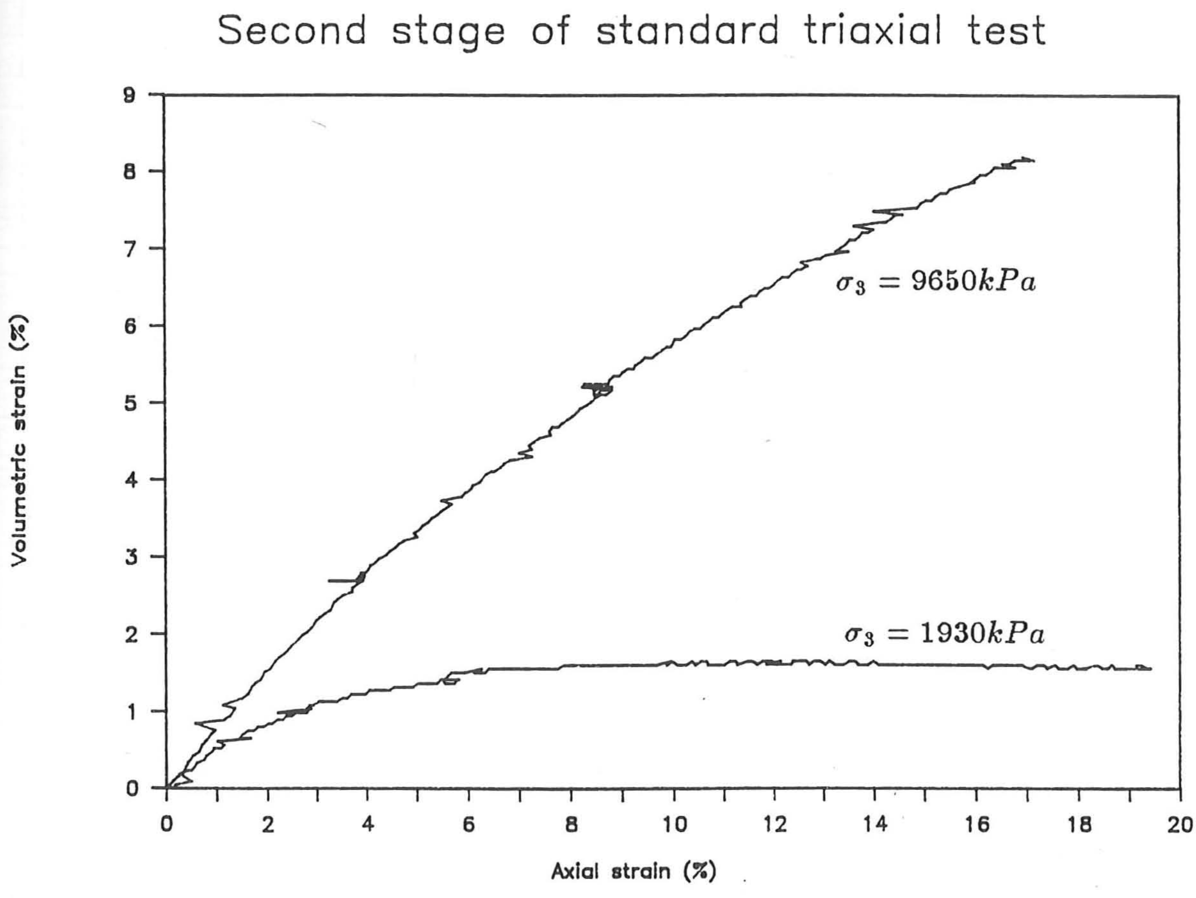

(b)

Fig 2.9 High pressure triaxial tests on 52/100 sand.

Fig 2.10 (a)

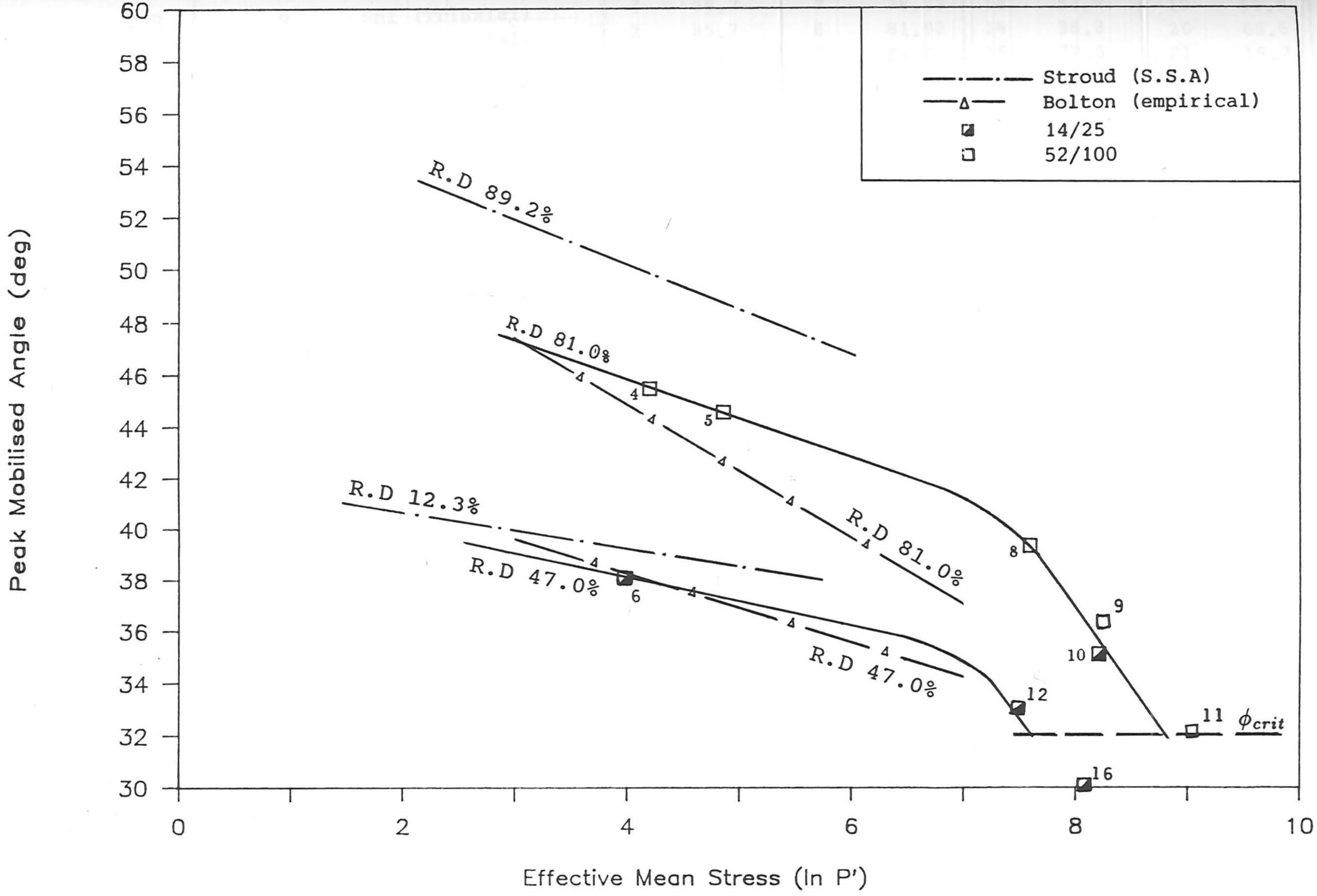

Fig 2.10 Plots of ϕ_p against ln p'.

Fig 2.10 (b)

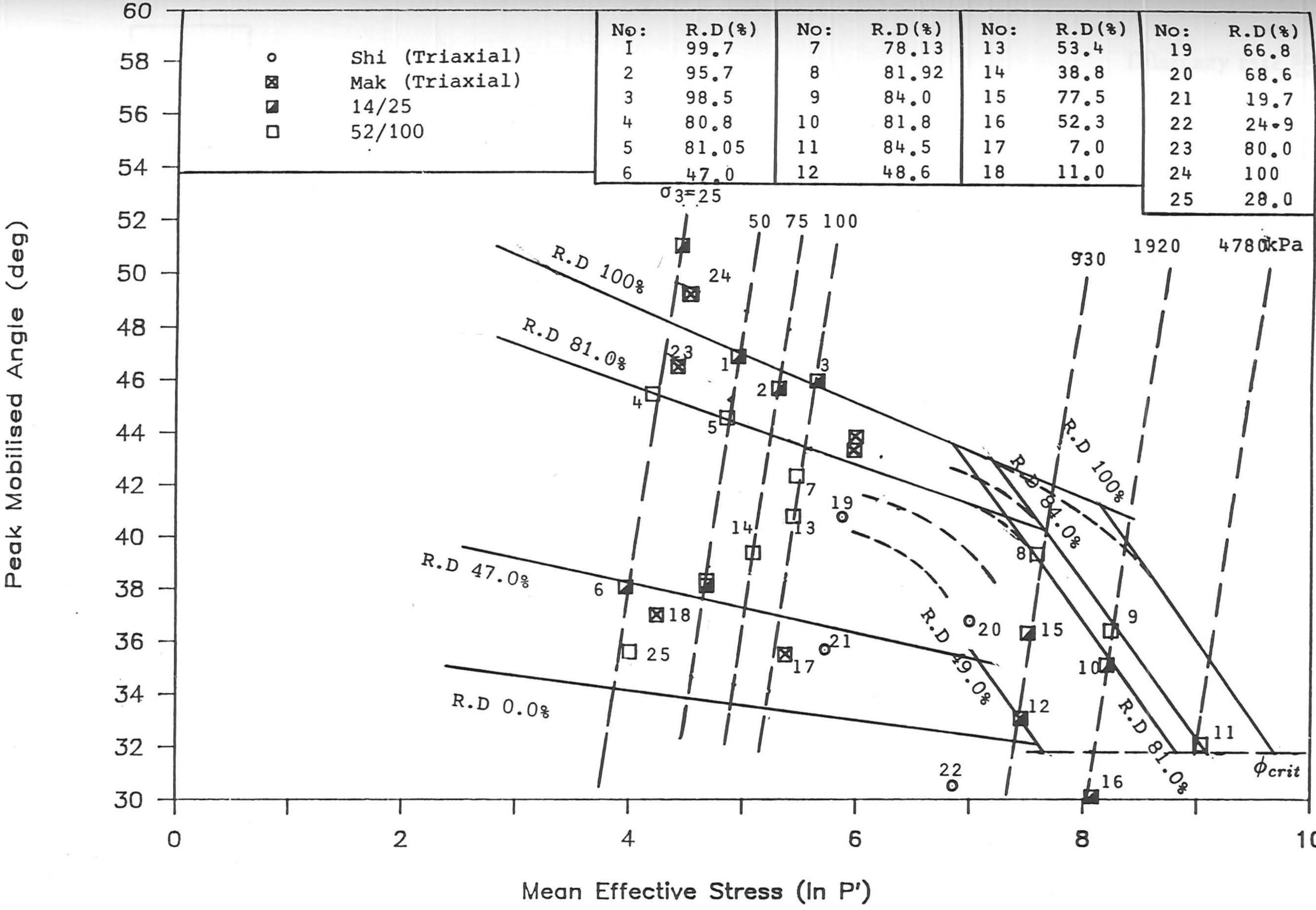

Fig 2.10 Plots of ϕ_p against In p'.

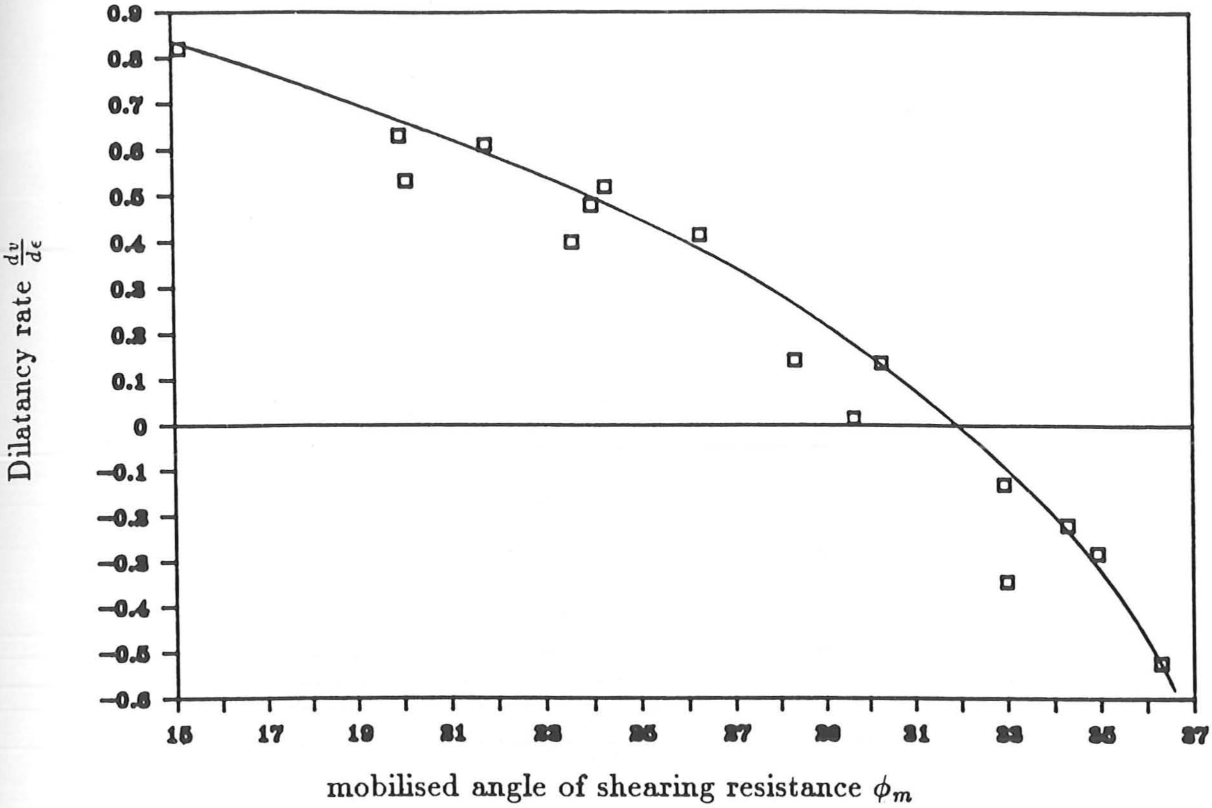

Fig 2.11 Plot of dilatancy rate against ϕ_m.

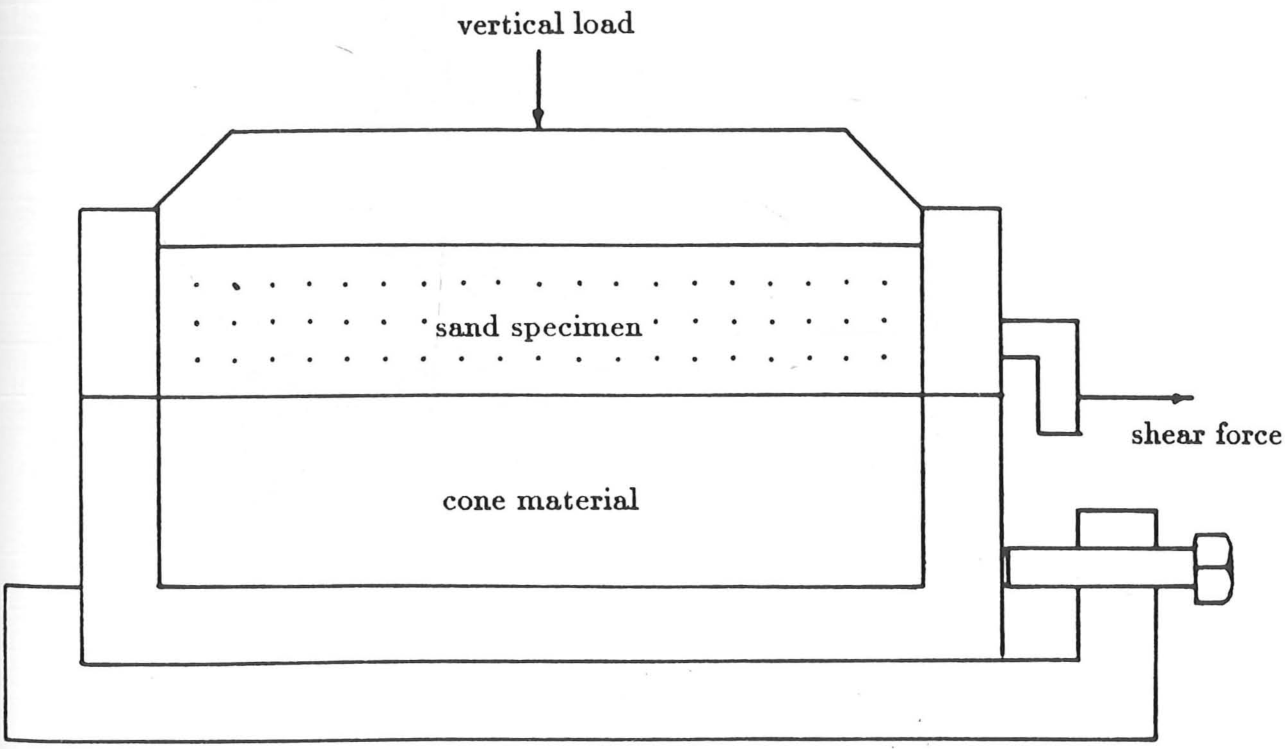

Fig 2.12 Cross-sectional view of direct shear test.

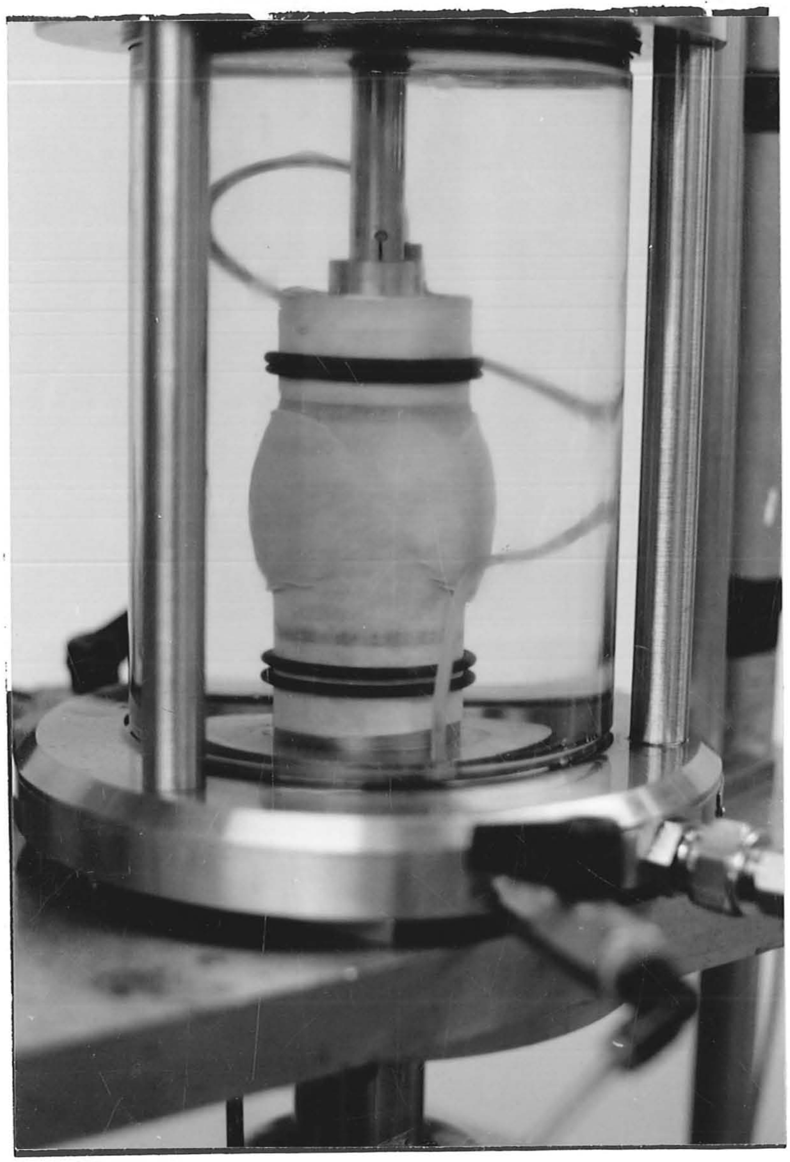

Fig 2.13 Photo shows the rupture planes in a triaxial test.

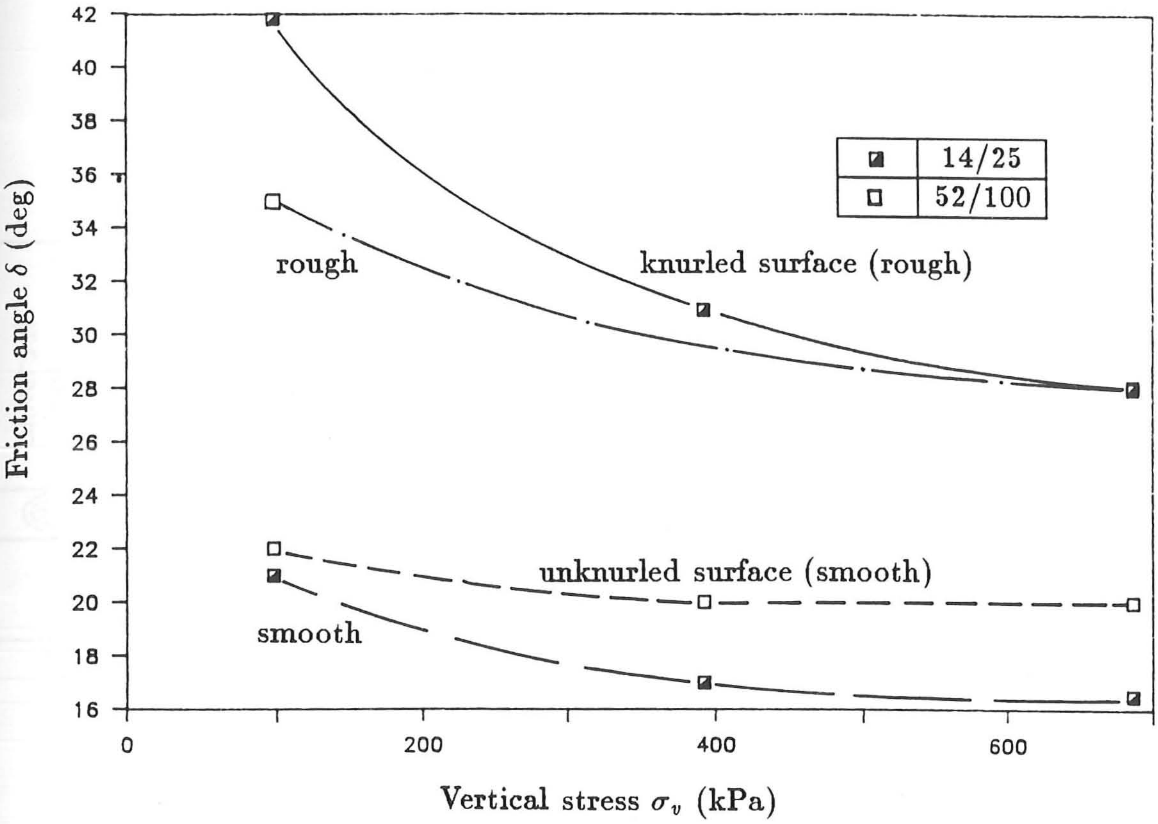

Fig 2.14 Values of δ for a given roughness and normal stress.

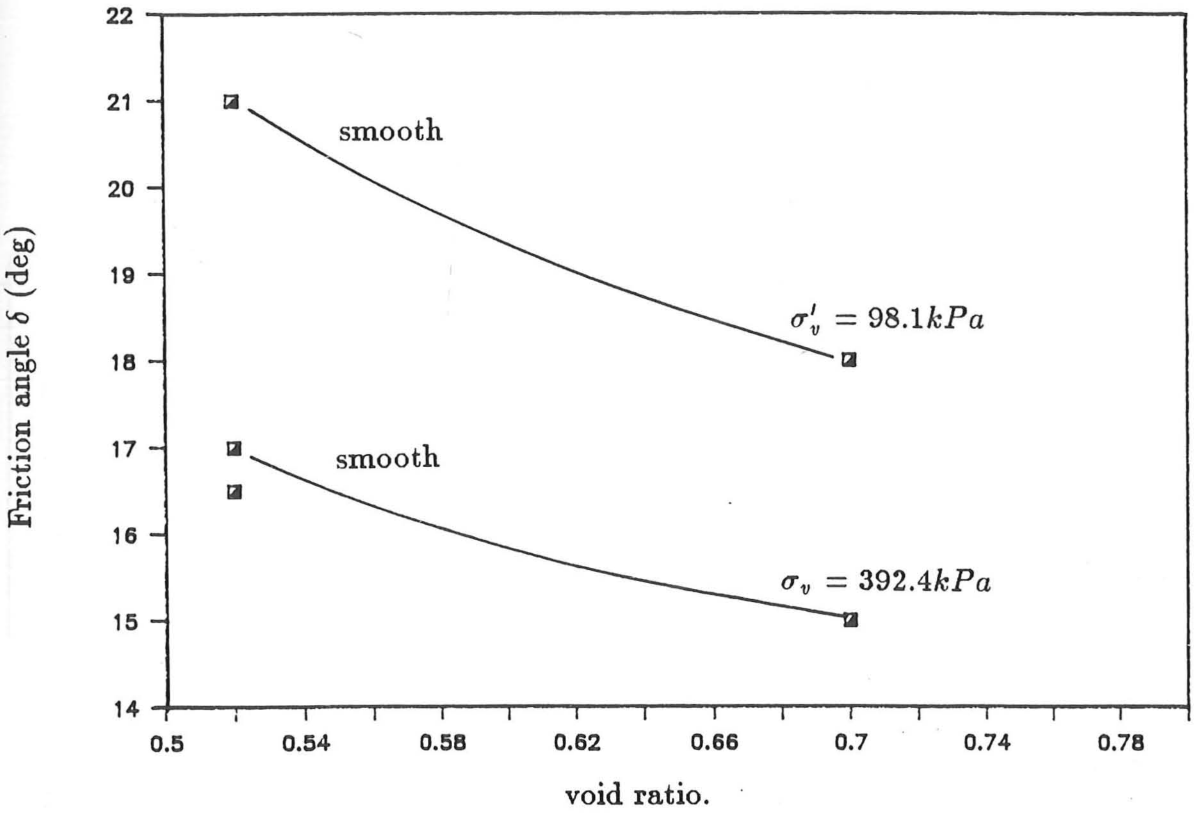

Fig 2.15 Values of δ for different void ratio.
14/25 sand

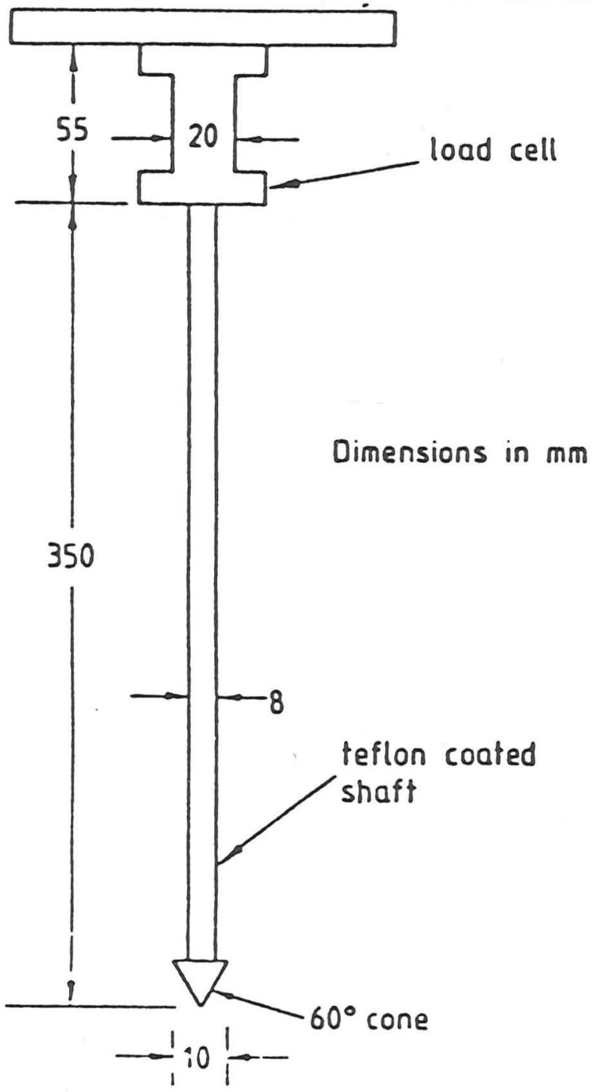

Fig 3.1 Mark I penetrometer.

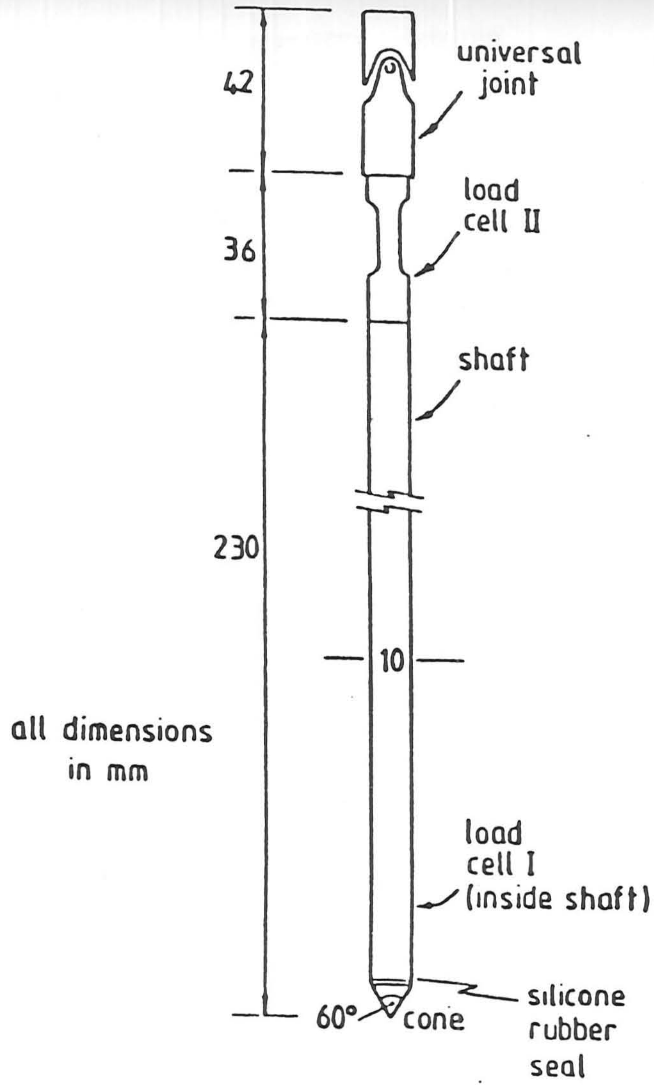

Fig 3.2 Mark II penetrometer.

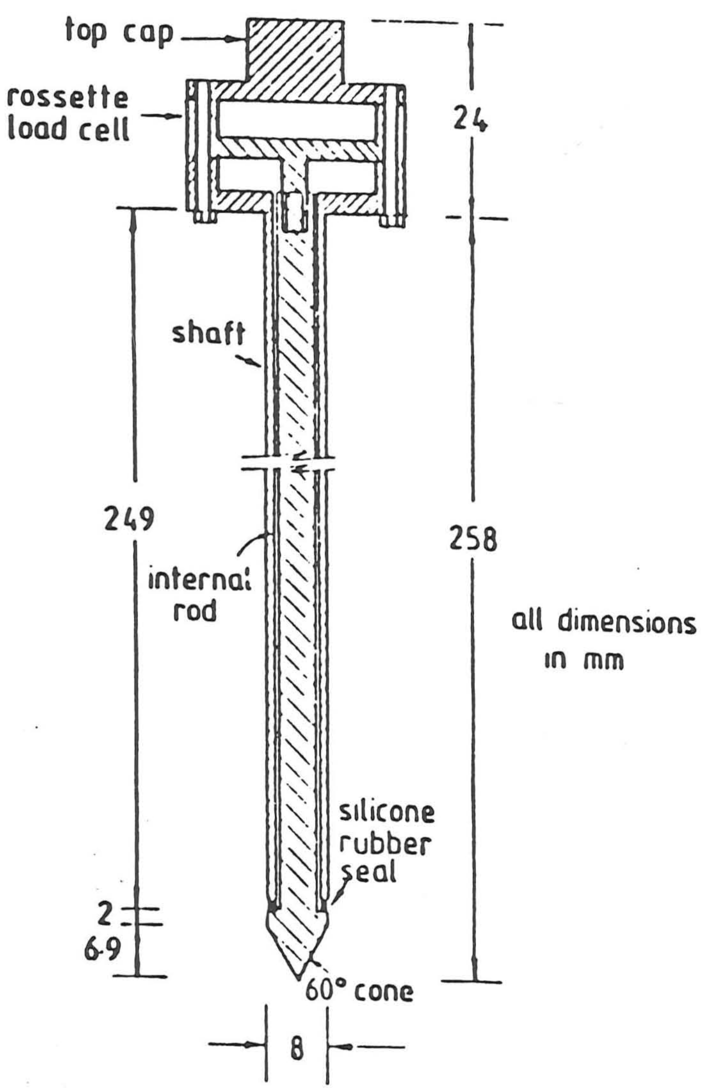

Fig 3.3 Mark III penetrometer.

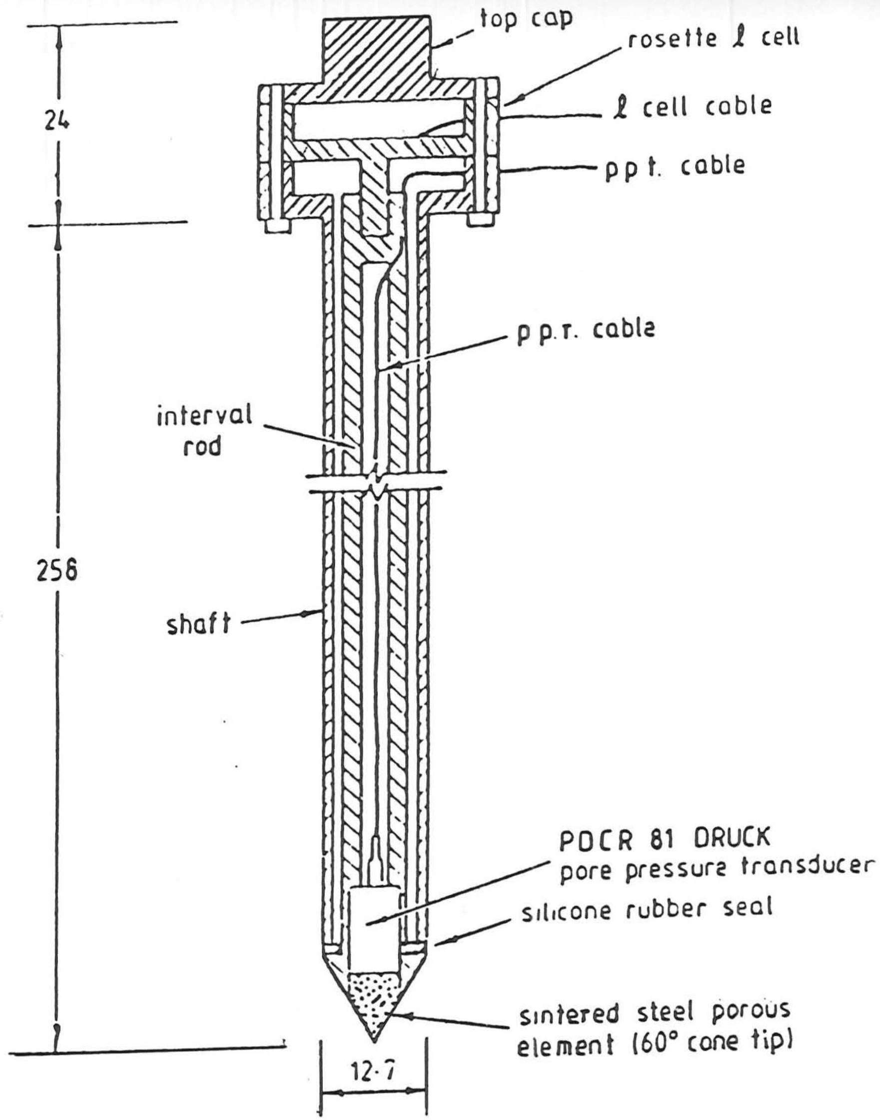

Fig 3.4 Piezocone.

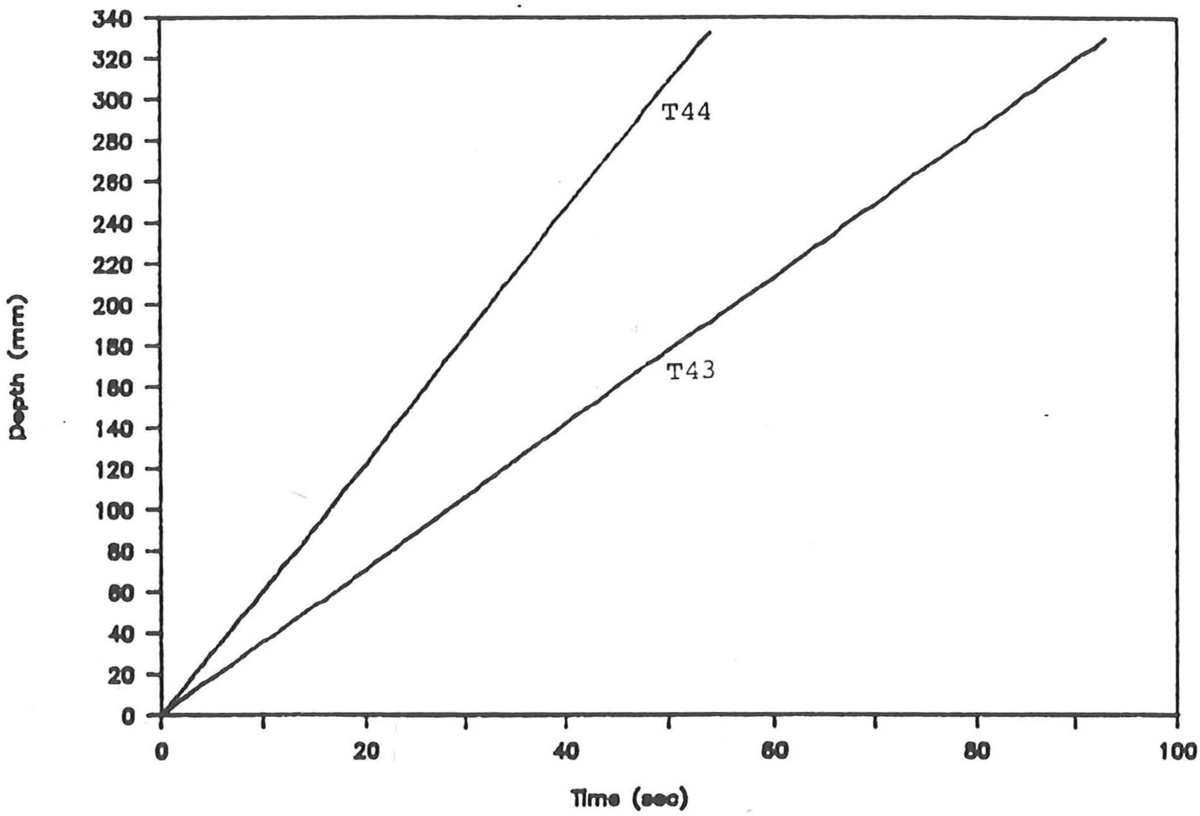

Fig 3.5 Penetration rate recorded with new arrangement of rotary potentiometer.

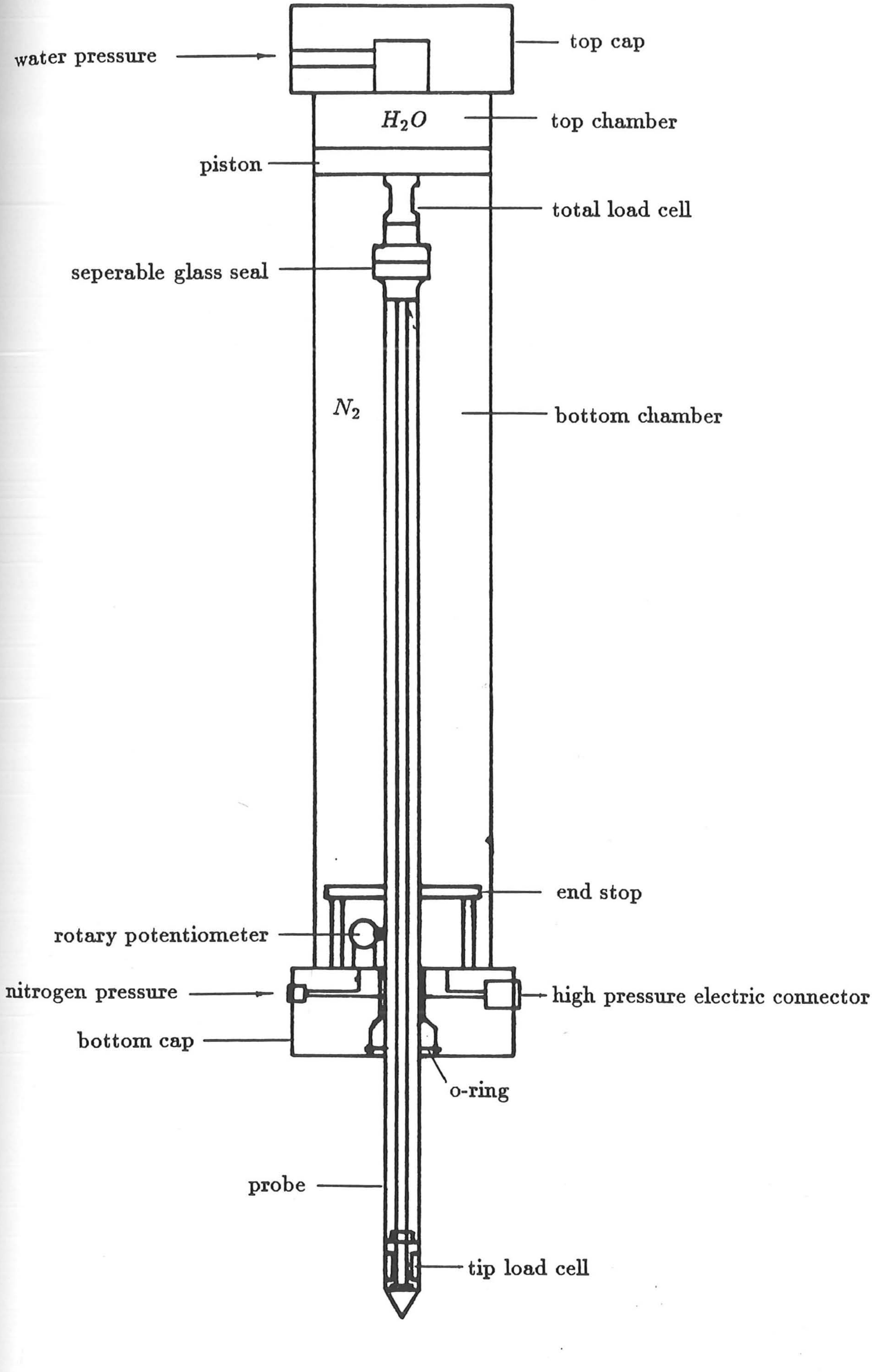

Fig 3.6 The penetrometer assembly.

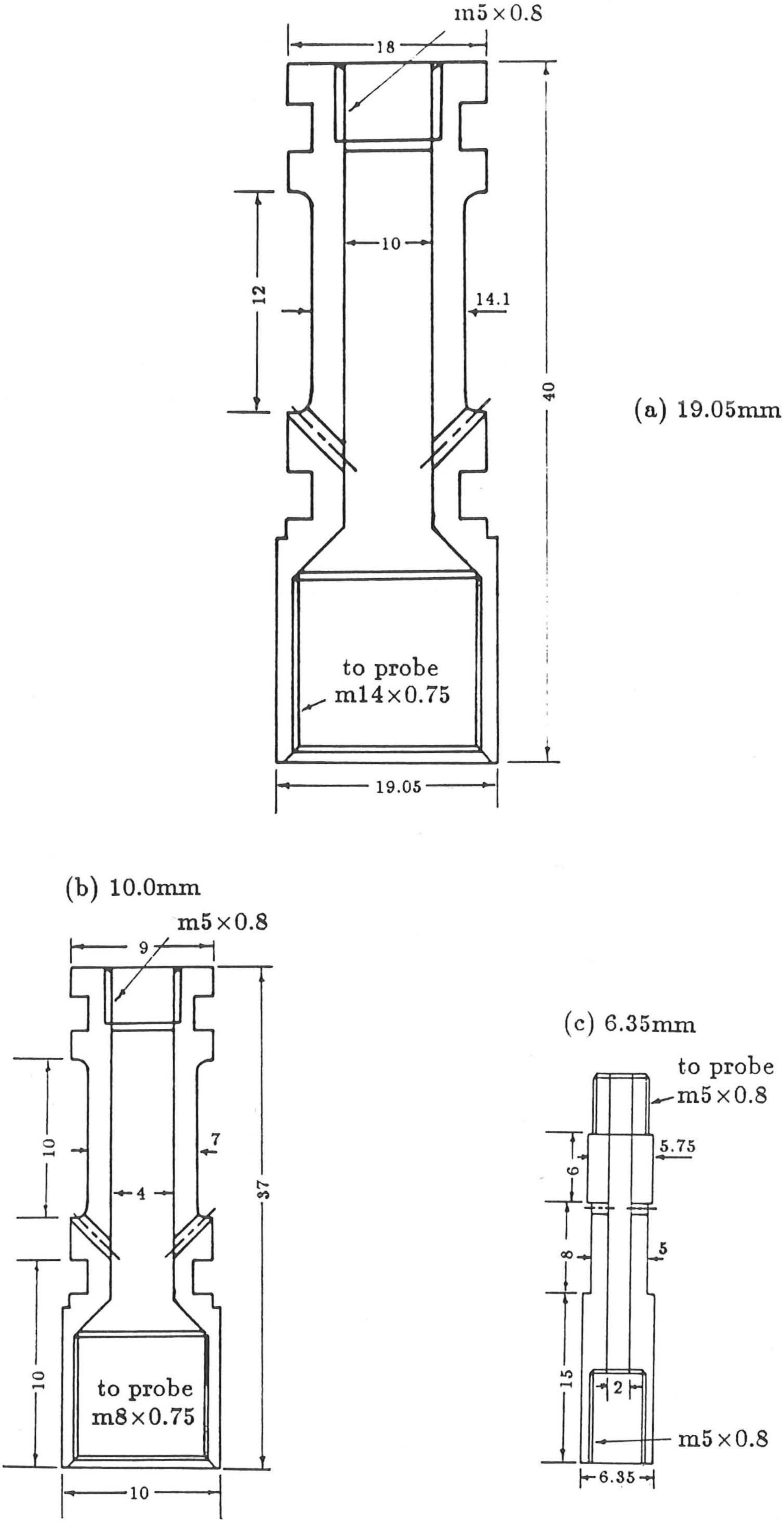

Fig 3.7 Tip load cells.
(all dimensions in mm)

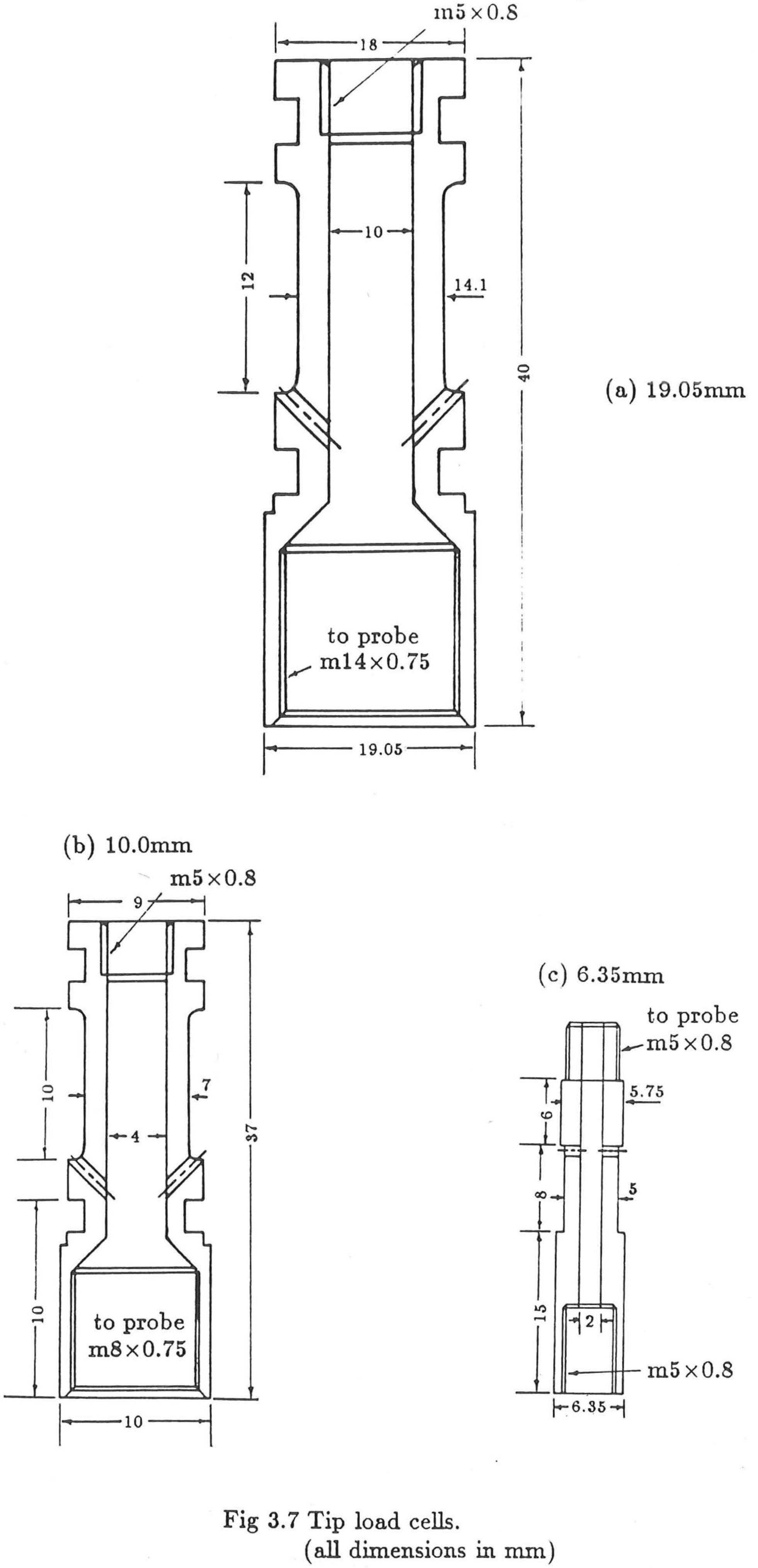

Fig 3.7 Tip load cells.
(all dimensions in mm)

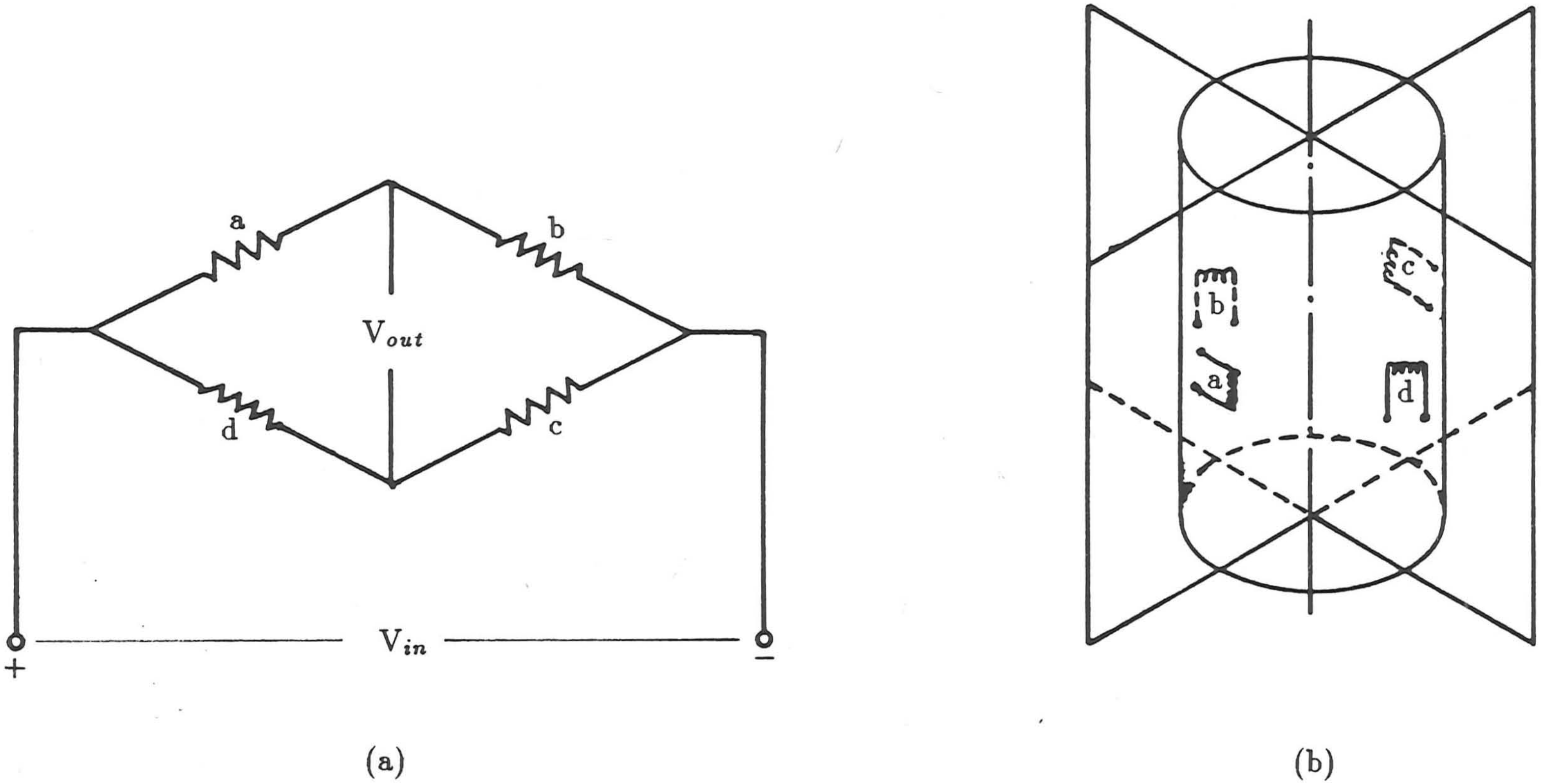

Fig 3.8 Arrangement of the bridge for strain gauges.

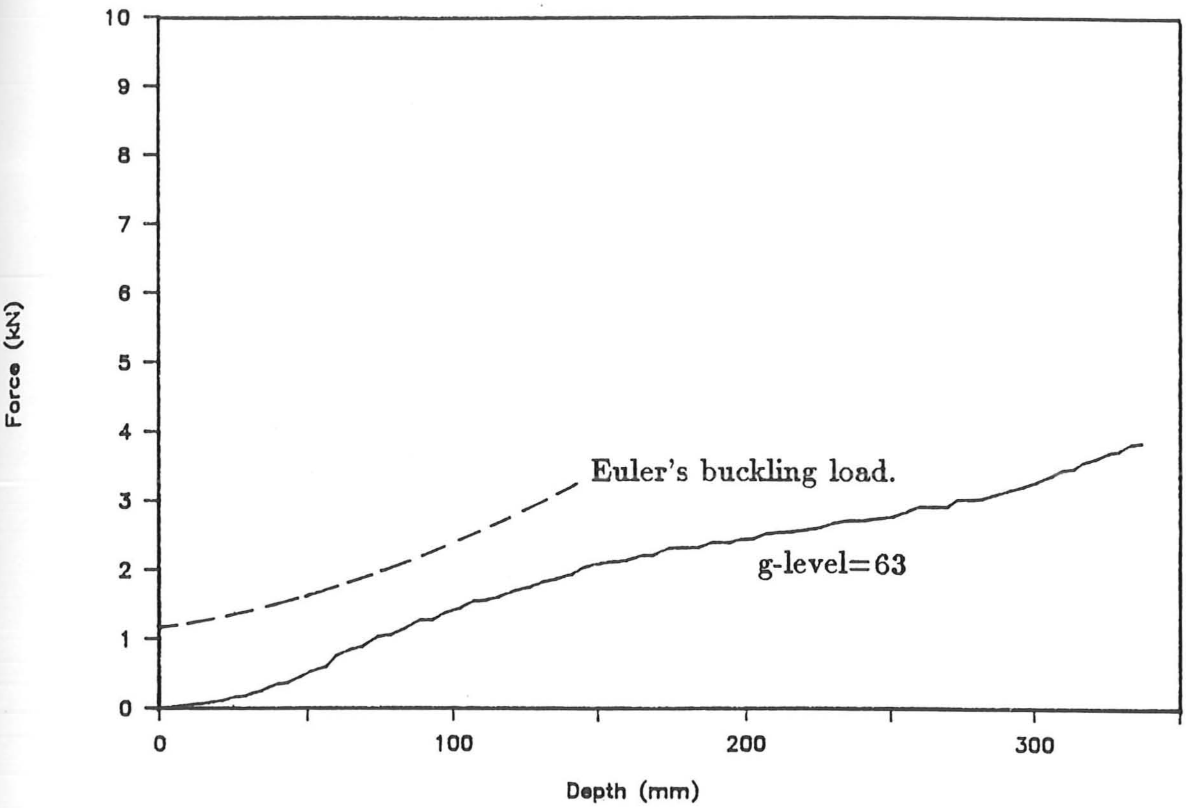

(a) 6.35mm diameter Probe
(14/25 sand, void ratio=0.519).

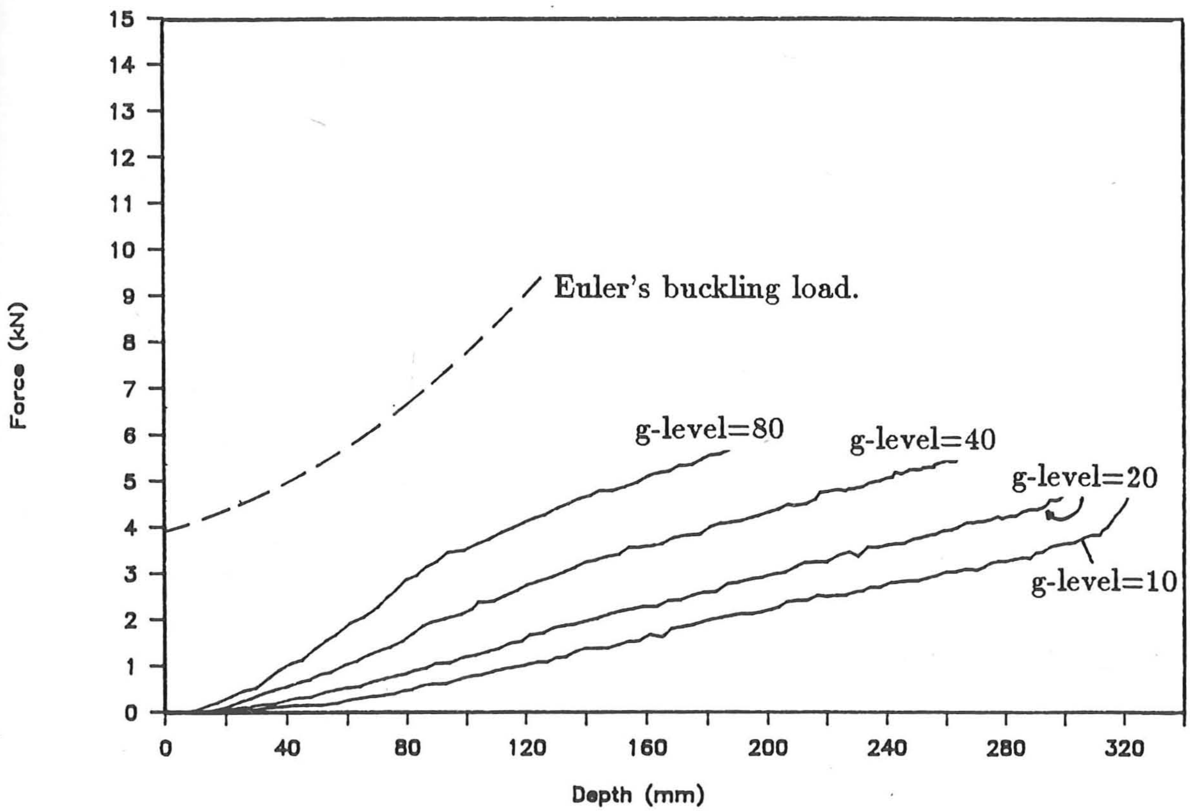

(b) 10.0mm diameter probe
(14/25 sand, void ratio=0.50)

Fig 3.9 Check for Euler's buckling load.

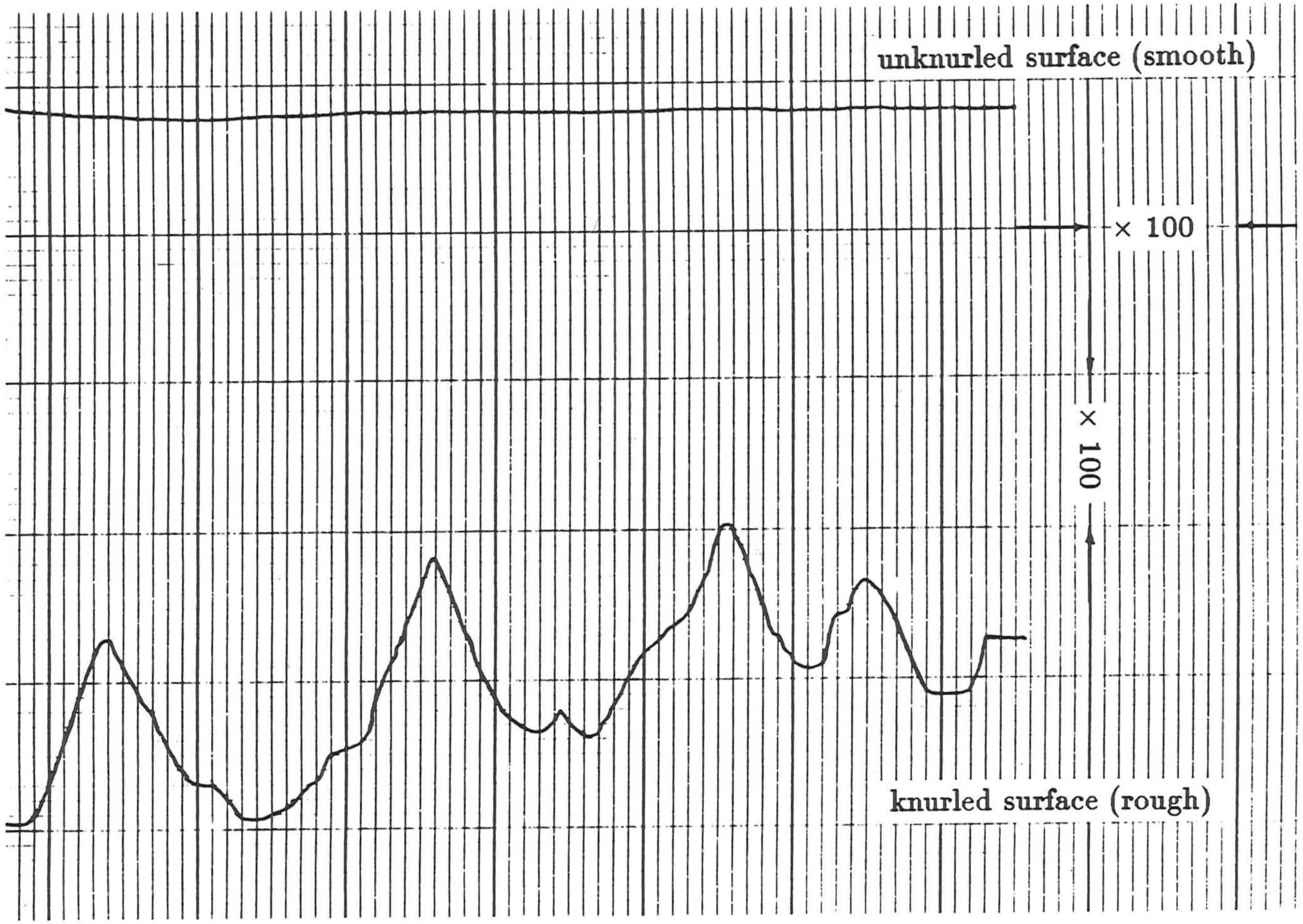

Fig 3.10 Surface finished of knurled and unknurled cones.

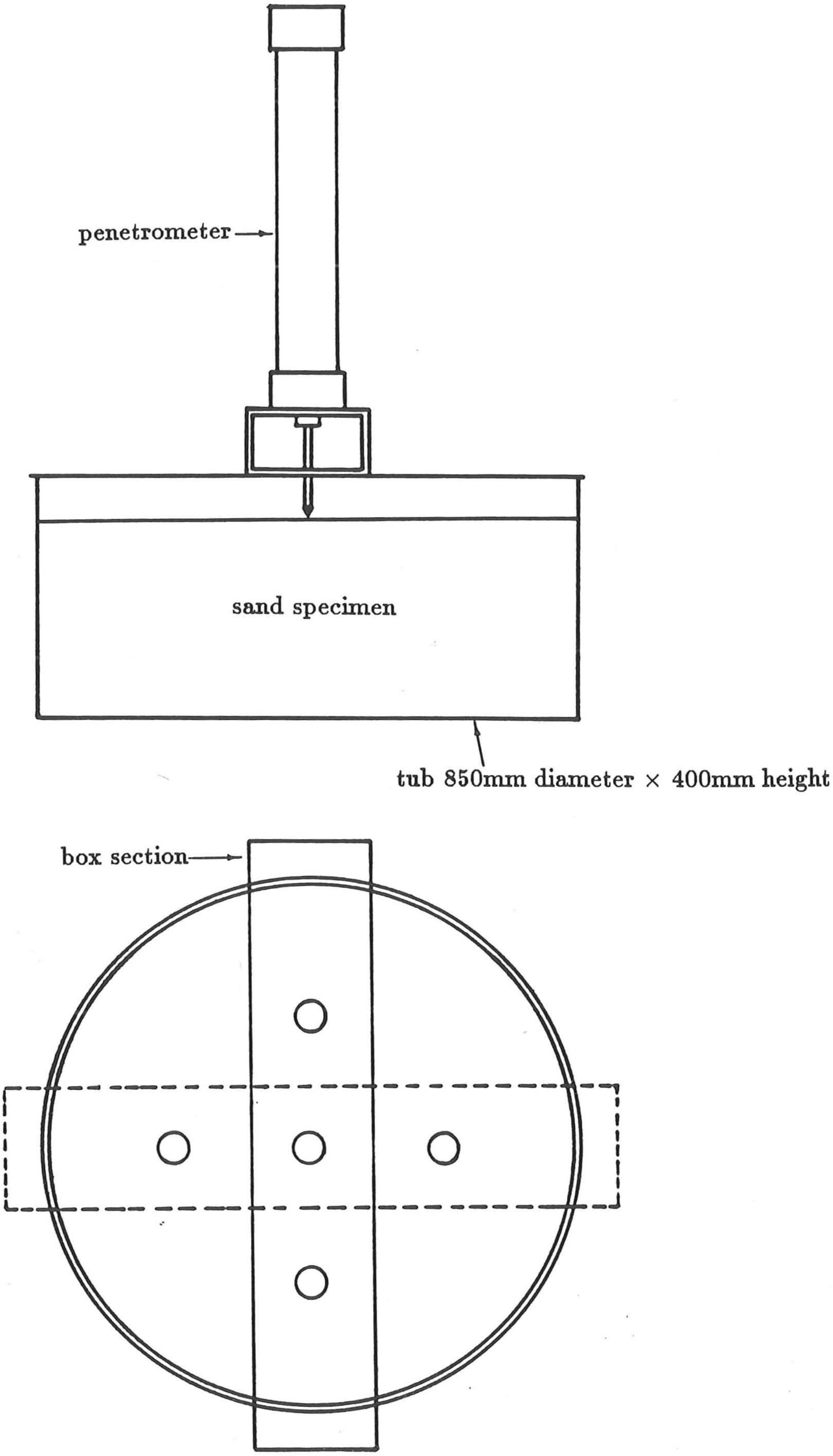

Fig 3.11 The assembled package for centrifuge tests.

Fig 3.12(a)

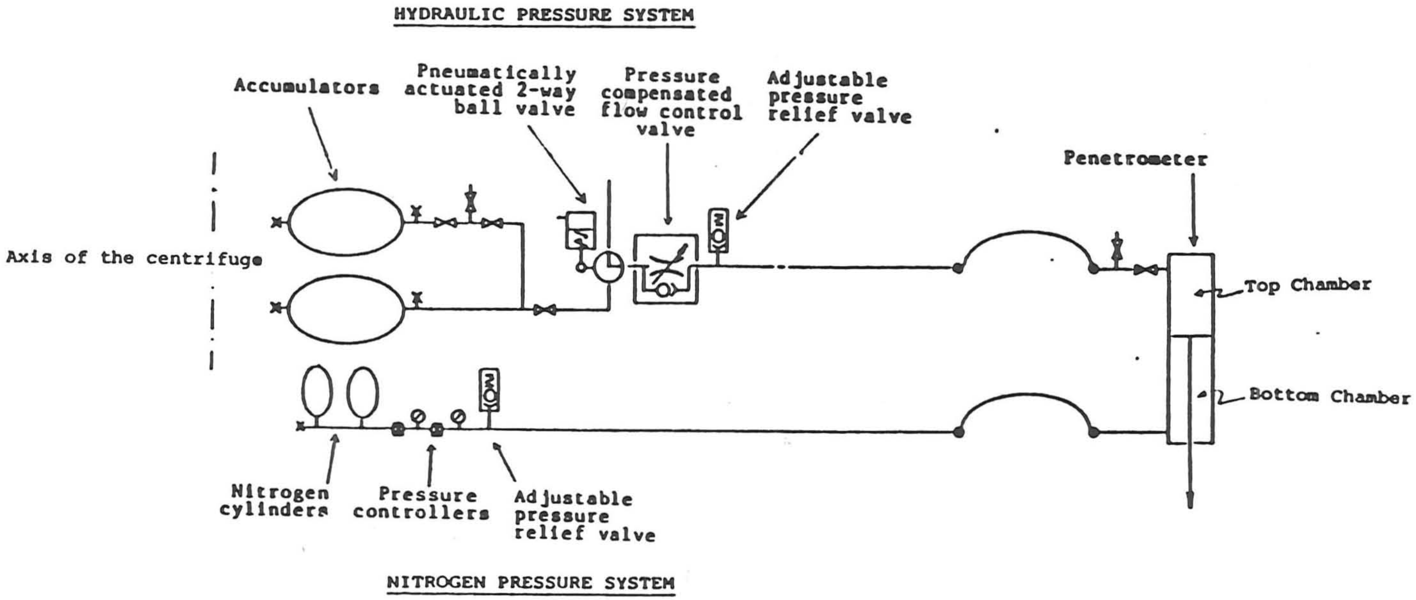

Fig 3.12 Schemetic diagram of hydraulic and pressure control system.

Fig 3.12 (b)

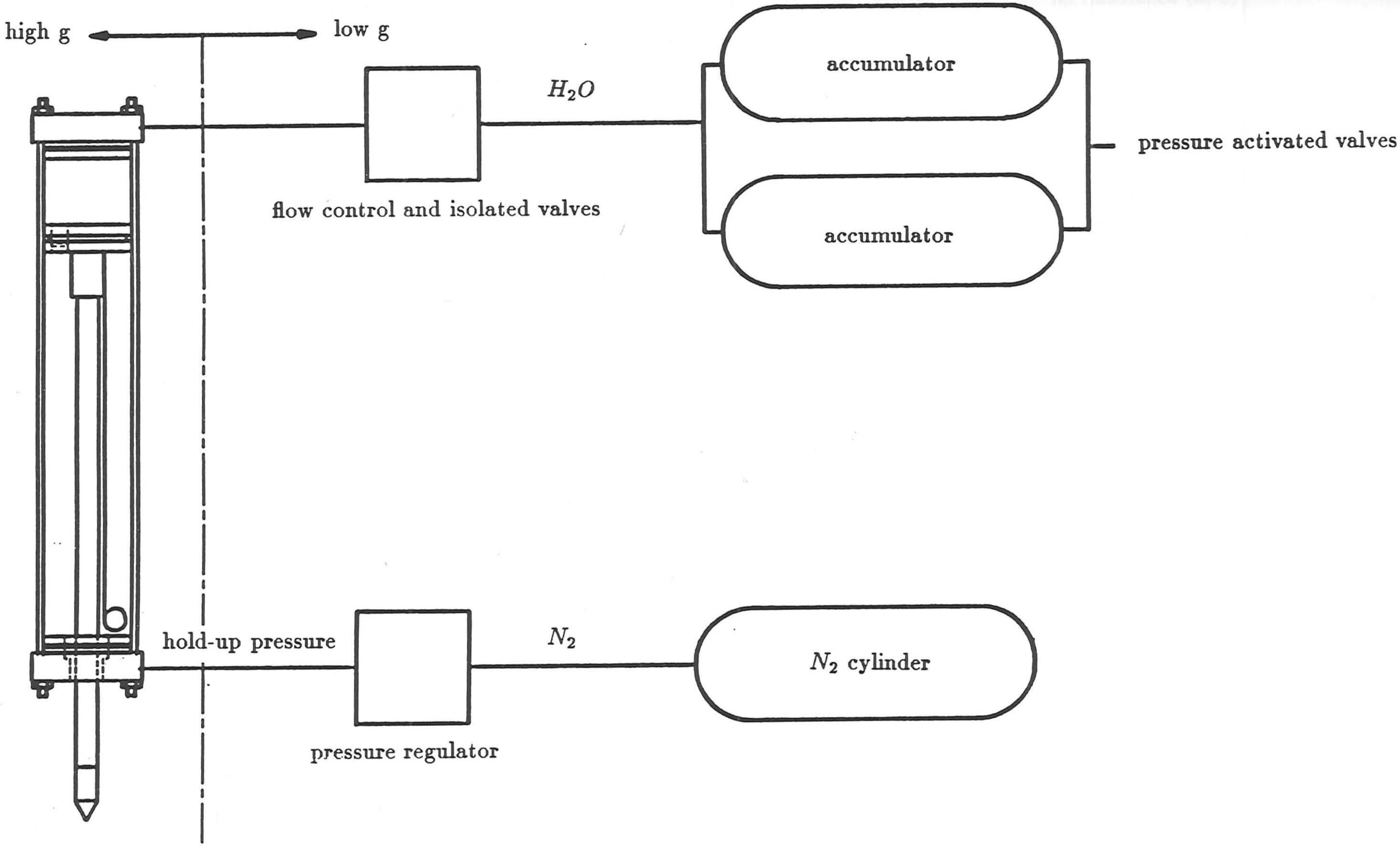

Fig 3.12 Schemetic diagram of hydraulic and pressure control system.

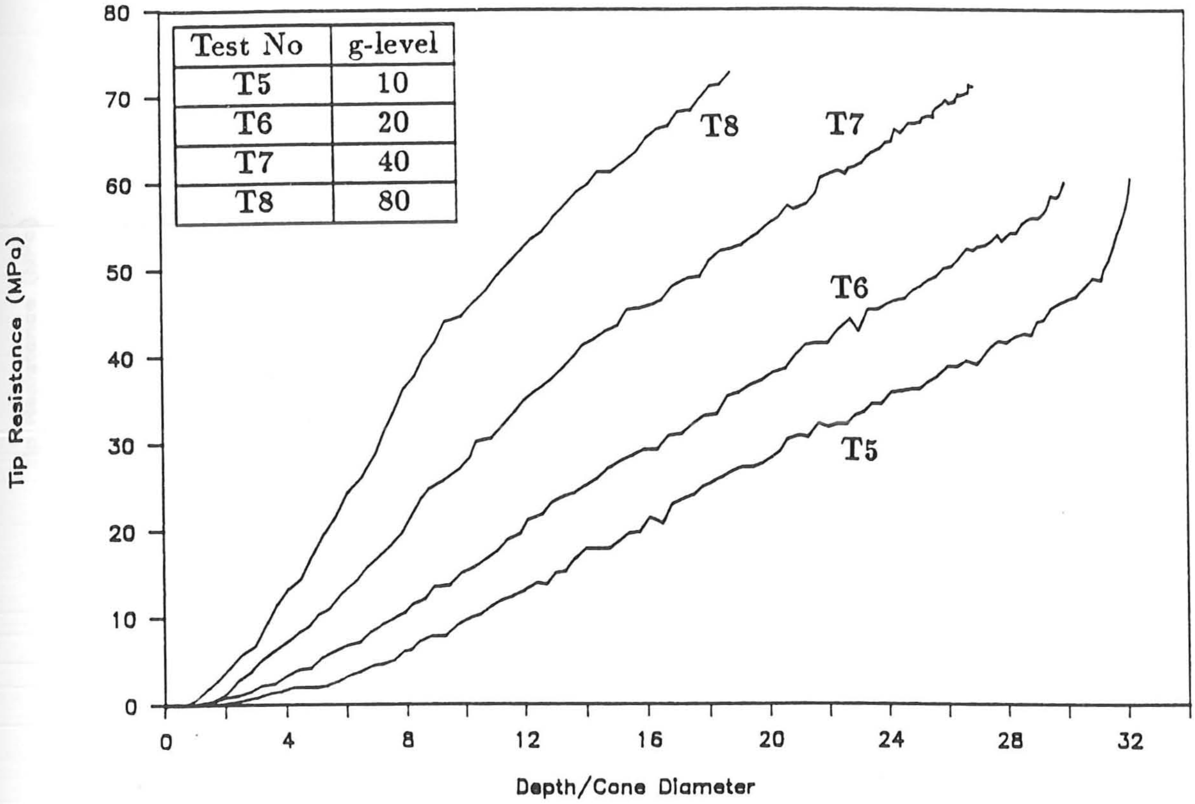

Fig 3.13 Stress level effects.
(14/25 sand, void ratio=0.50, cone diameter=10.0mm)

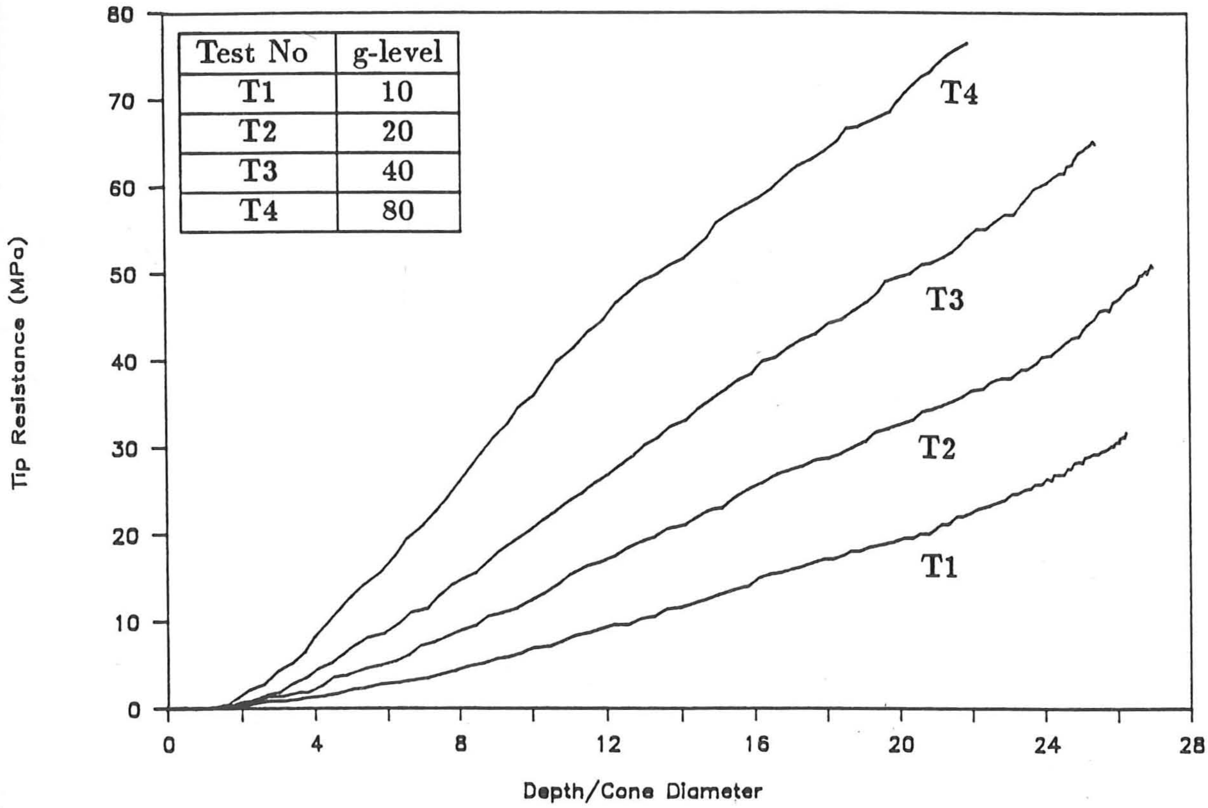

Fig 3.14 Stress level effects.
(Fontainbleau sand, void ratio=0.622, cone diameter=10.0mm)

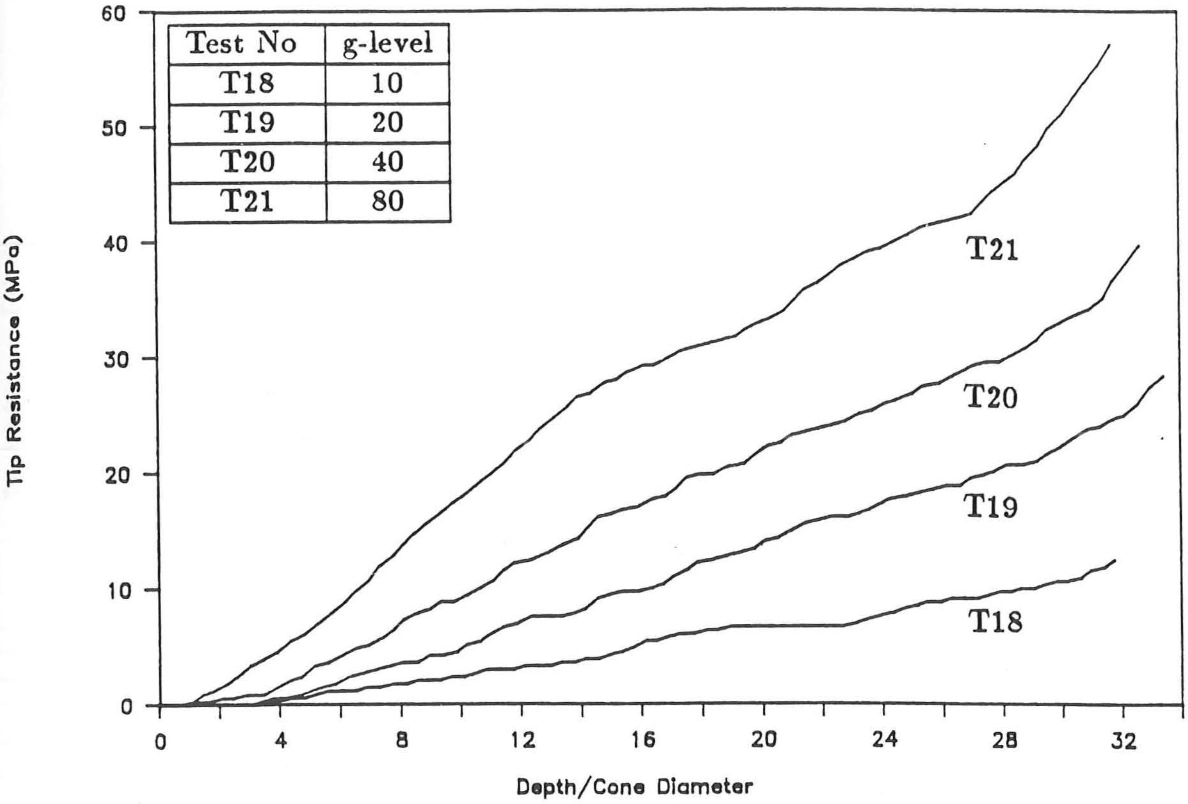

Fig 3.15 Stress level effects.
(52/100 sand, void ratio=0.657, cone diameter=10.0mm)

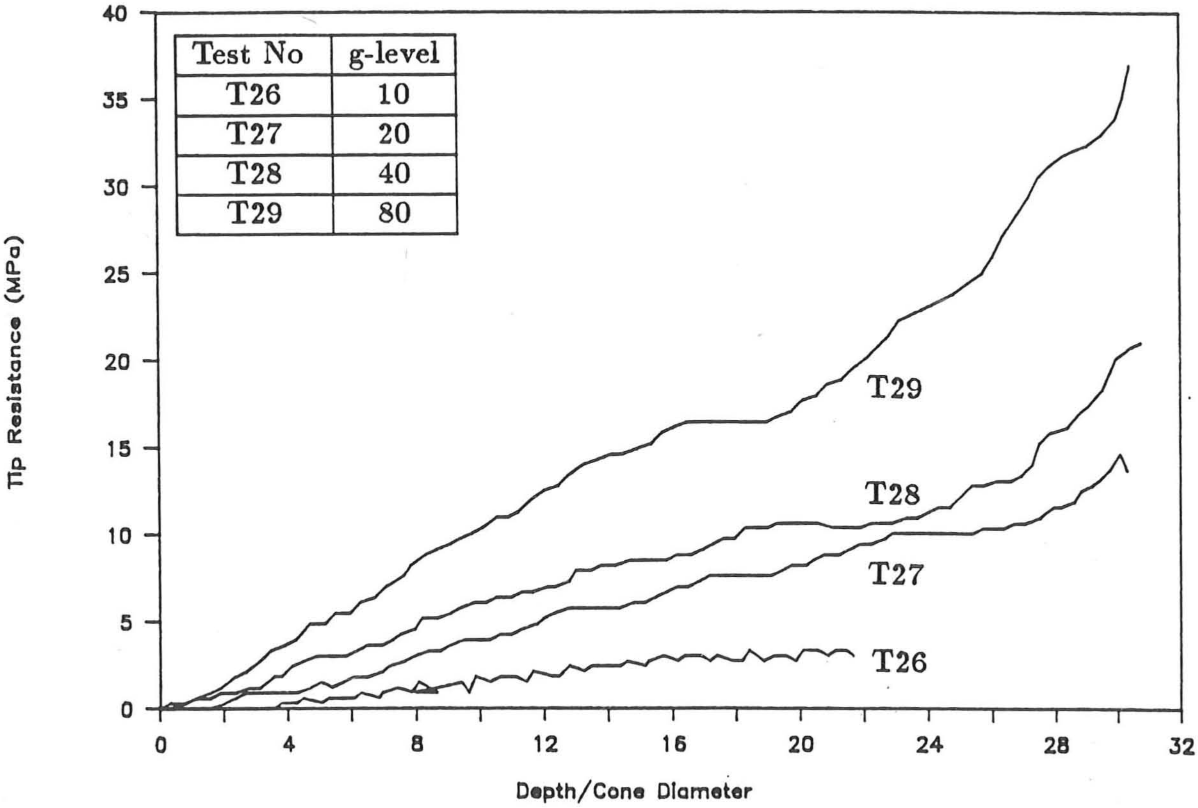

Fig 3.16 Stress level effects.
(52/100 sand, void ratio=0.743, cone diameter=10.0mm)

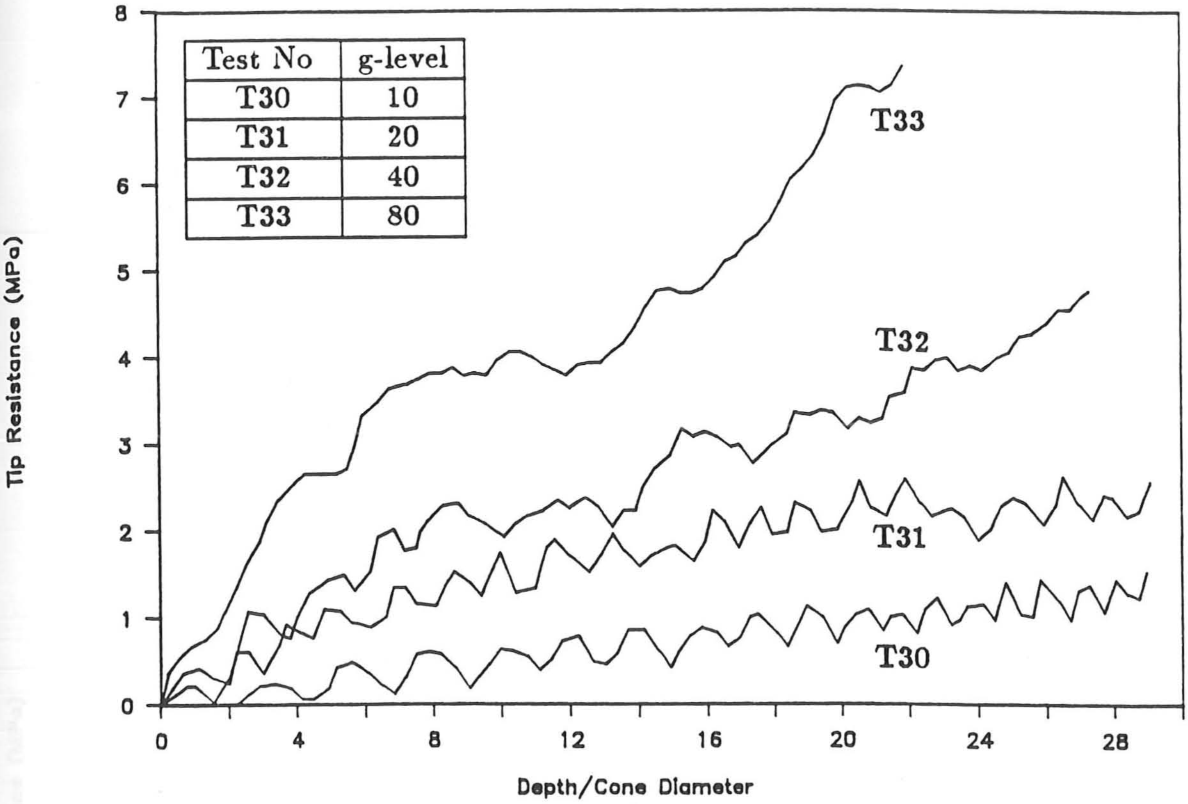

Fig 3.17 Stress level effects.
(52/100 sand, void ratio=0.909, cone diameter=10.0mm)

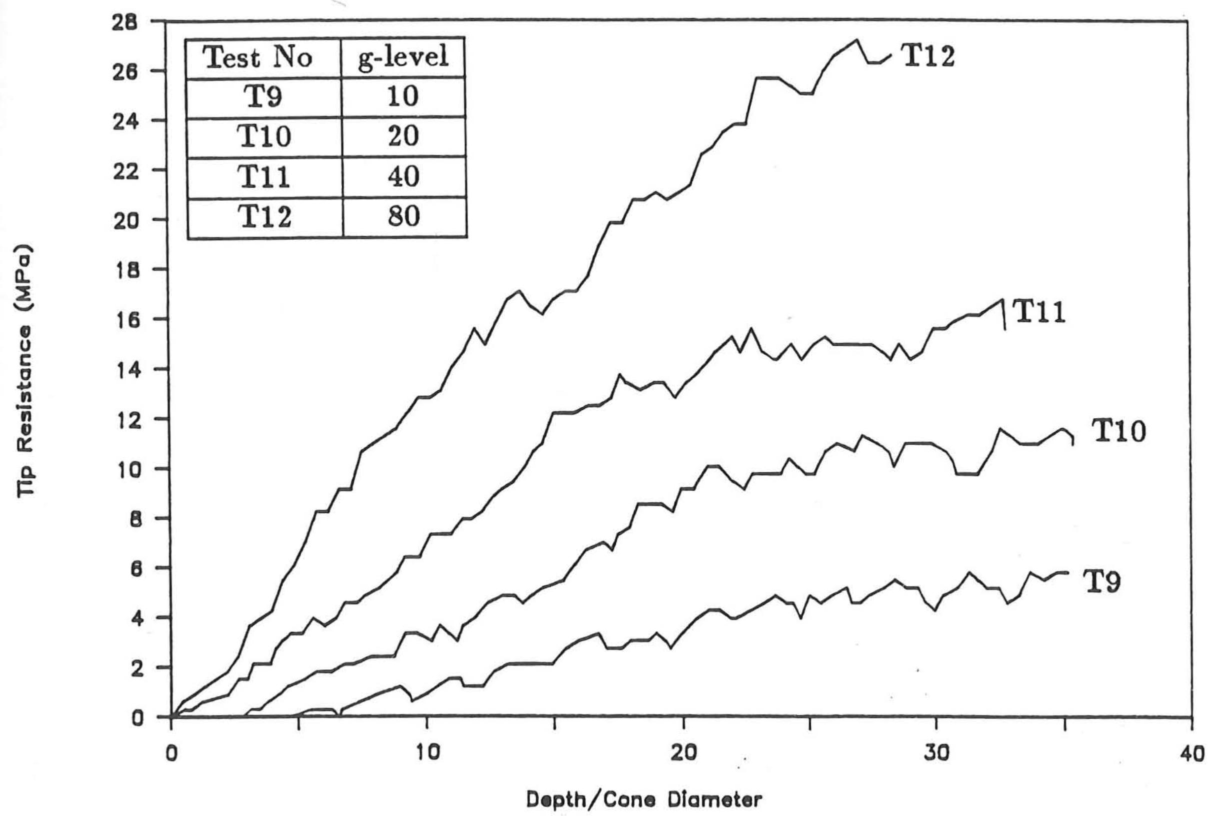

Fig 3.18 Stress level effects.
(14/25 sand, void ratio=0.671, cone diameter=10.0mm)

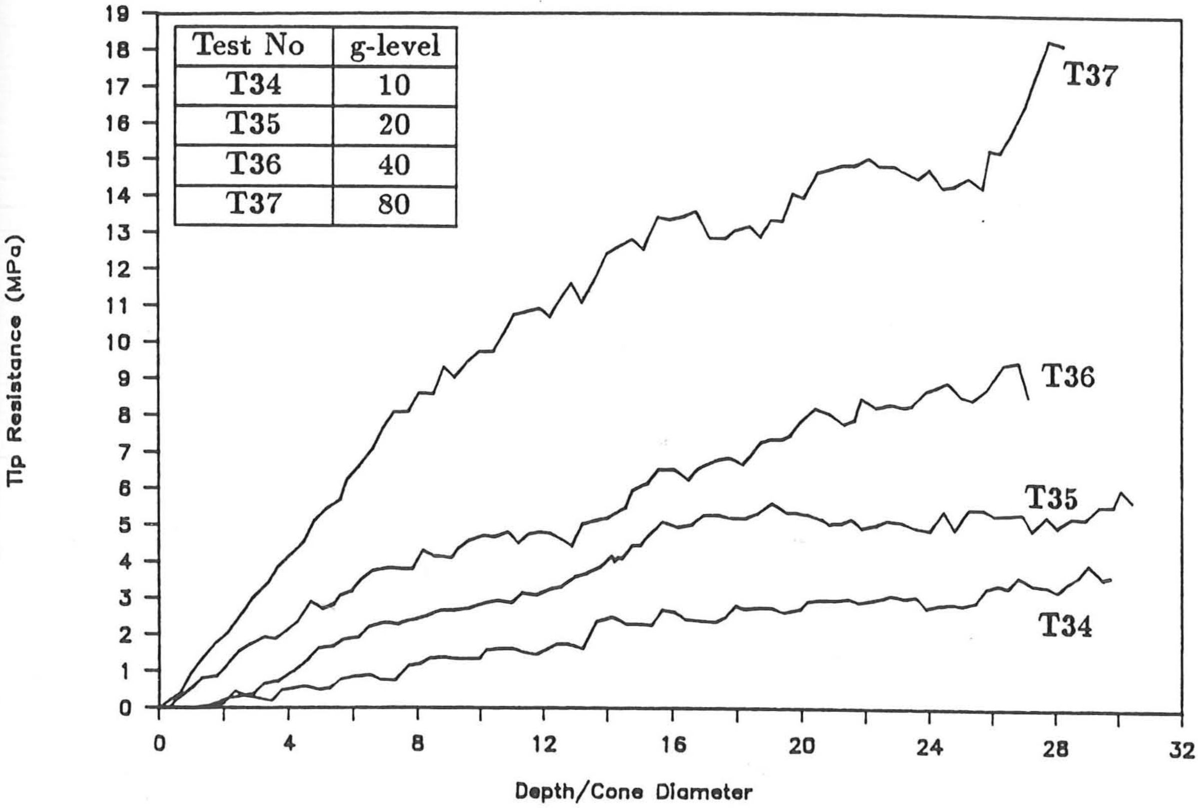

Fig 3.19 Stress level effects.

(14/25 sand, void ratio=0.741, cone diameter=10.0mm)

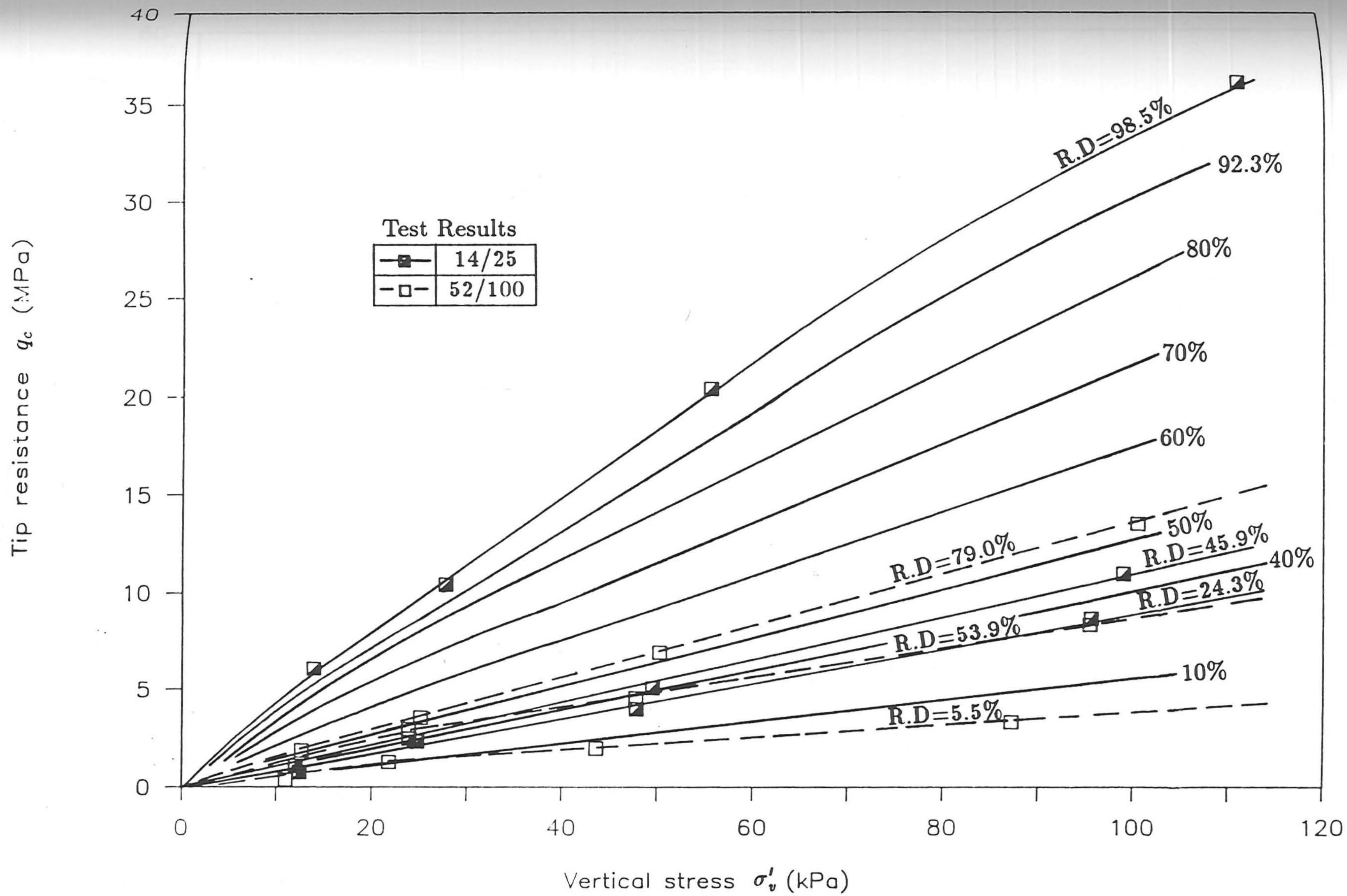

Fig 3.20(a) $\frac{D}{B} = 8$

Fig 3.20 Relationship between q_c, σ_v and R.D for normally consolidated sand.

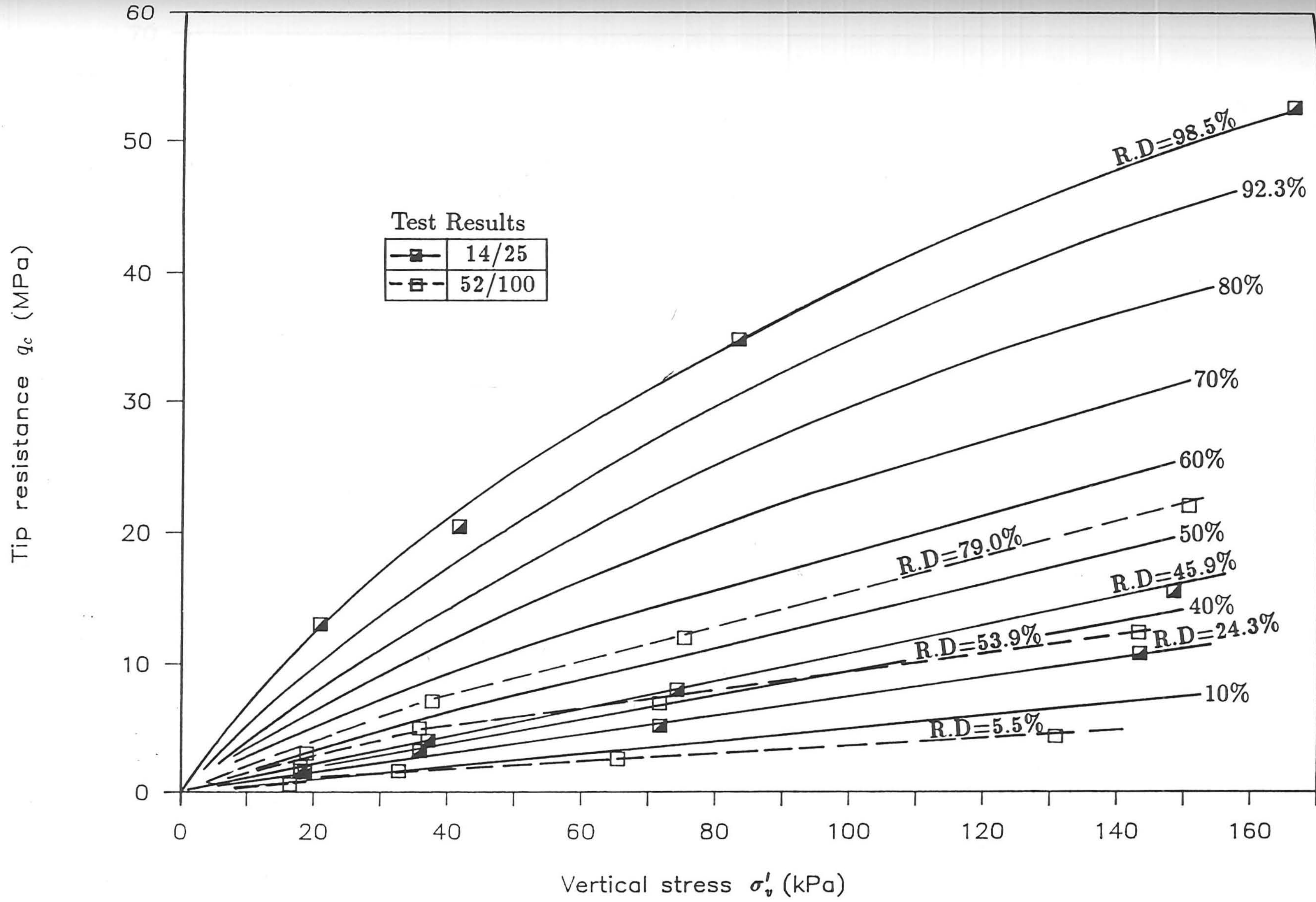

Fig 3.20(b) $\frac{D}{B} = 12$

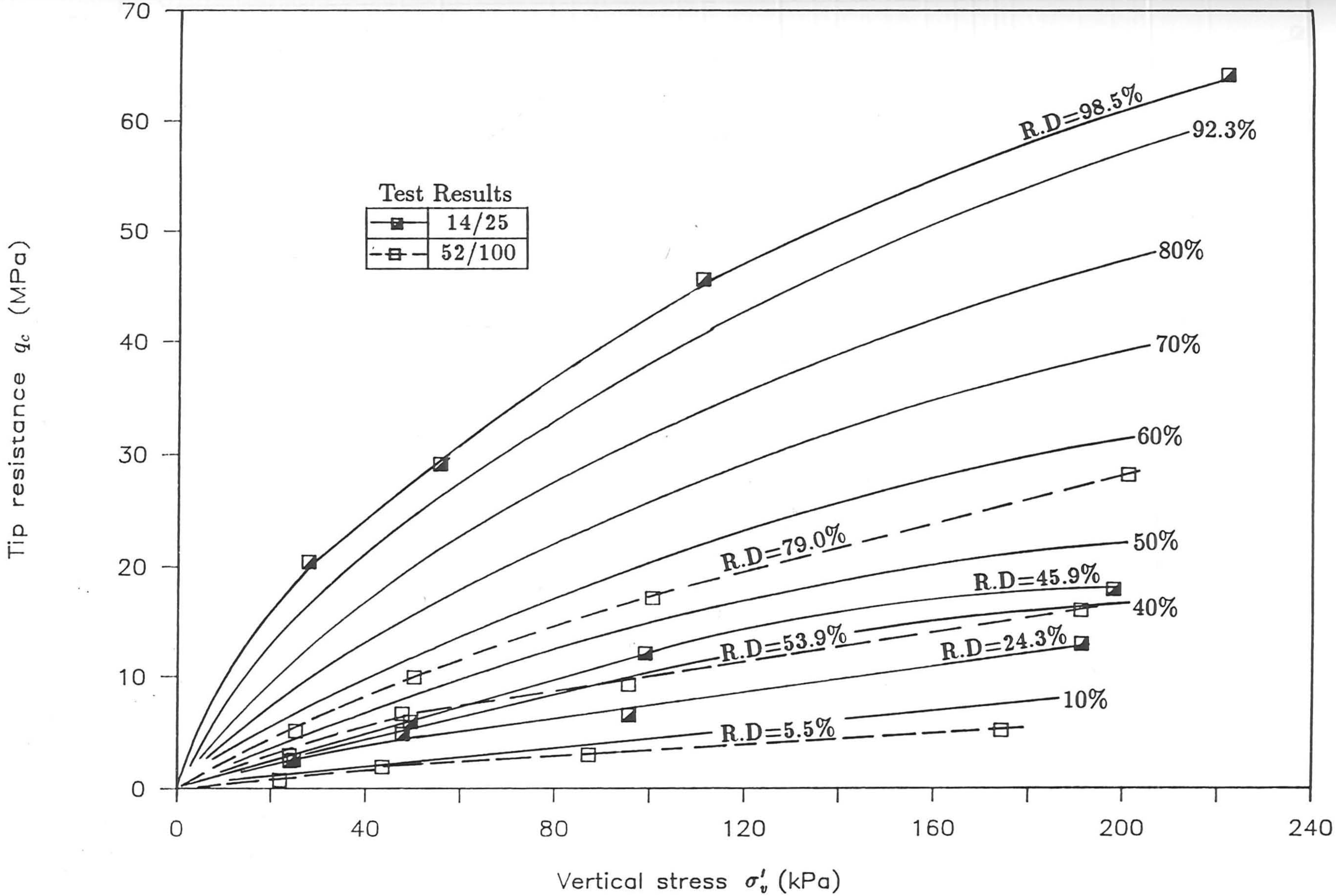

Fig 3.20(c) $\frac{D}{B} = 16$

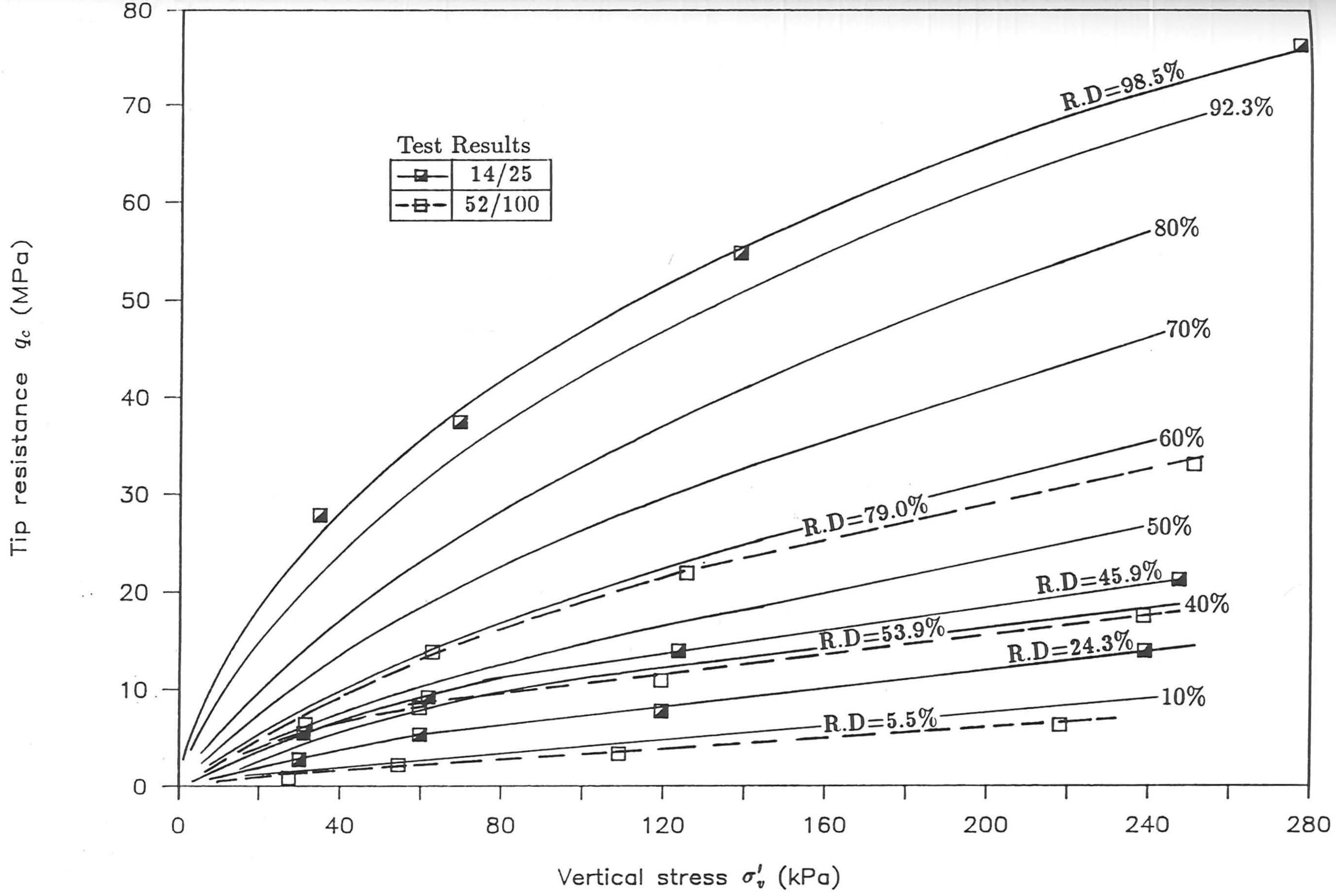

Fig 3.20(d) $\frac{D}{B} = 20$

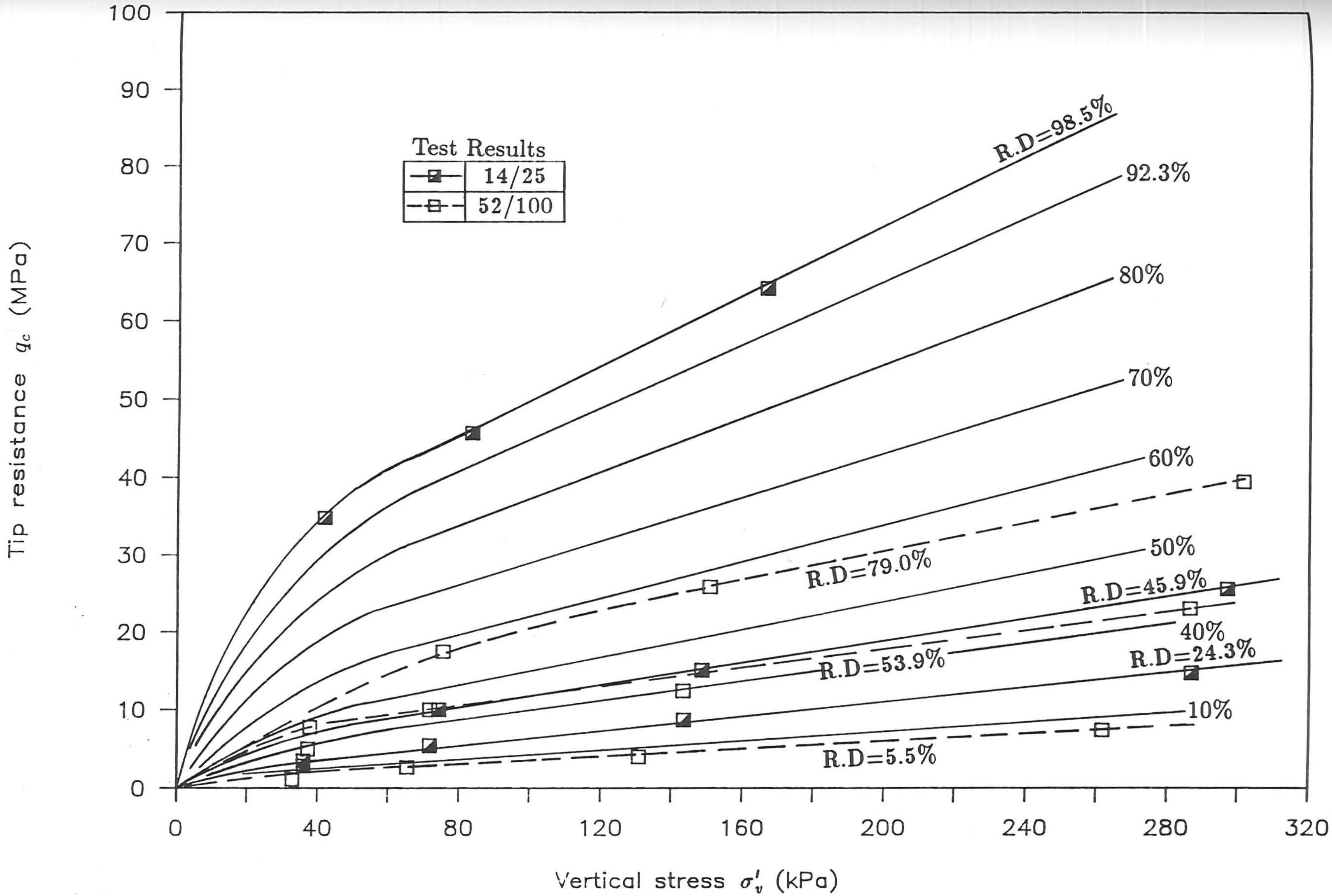

Fig 3.20 (e) $\frac{D}{B} = 24$

Fig 3.20 Relationship between q_c, σ_v and R.D for normally consolidated sand.

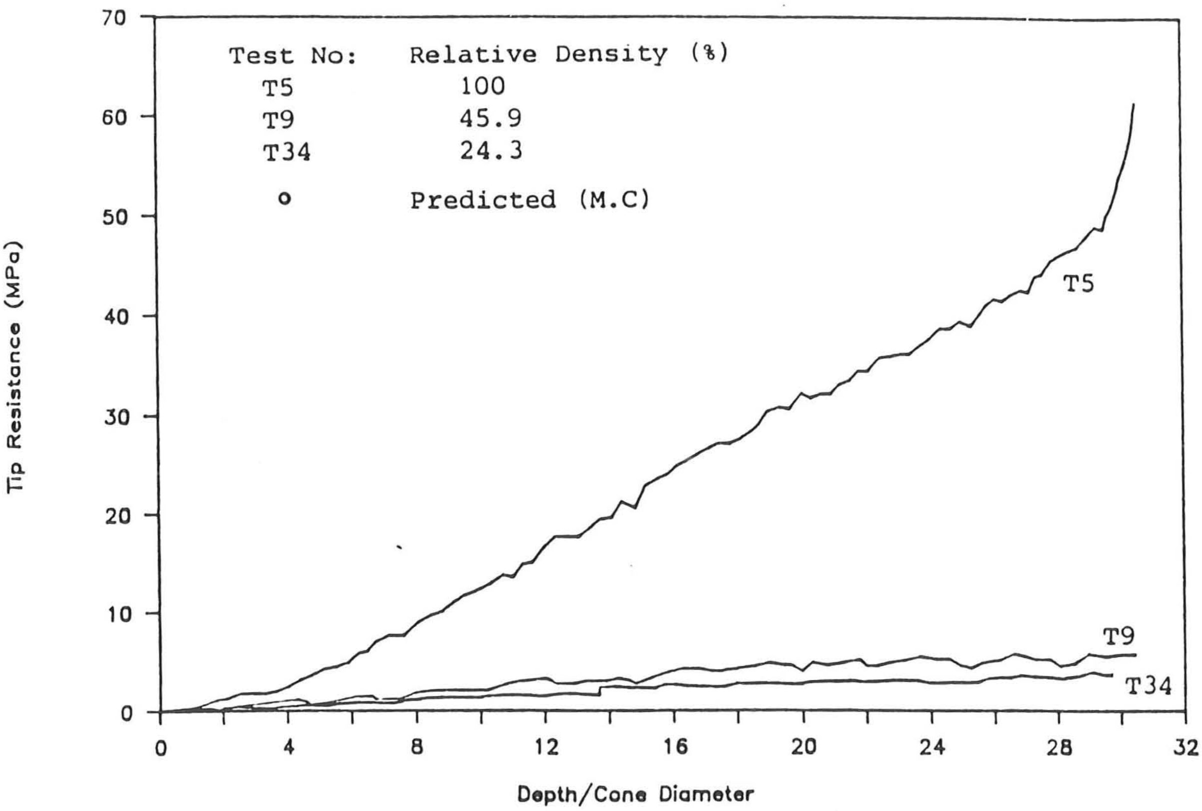

Fig 3.21 Relative density effects (14/25 sand, g-level=10).

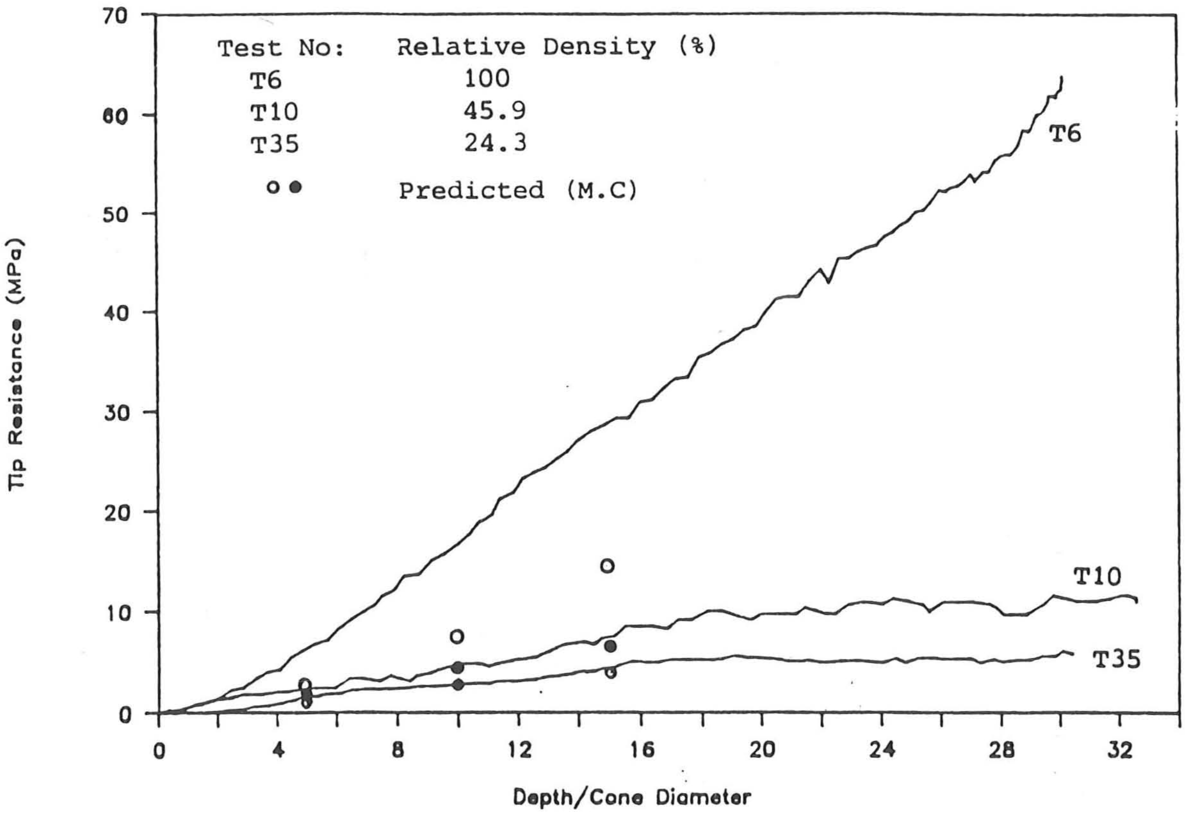

Fig 3.22 Relative density effects (14/25 sand, g-level=20).

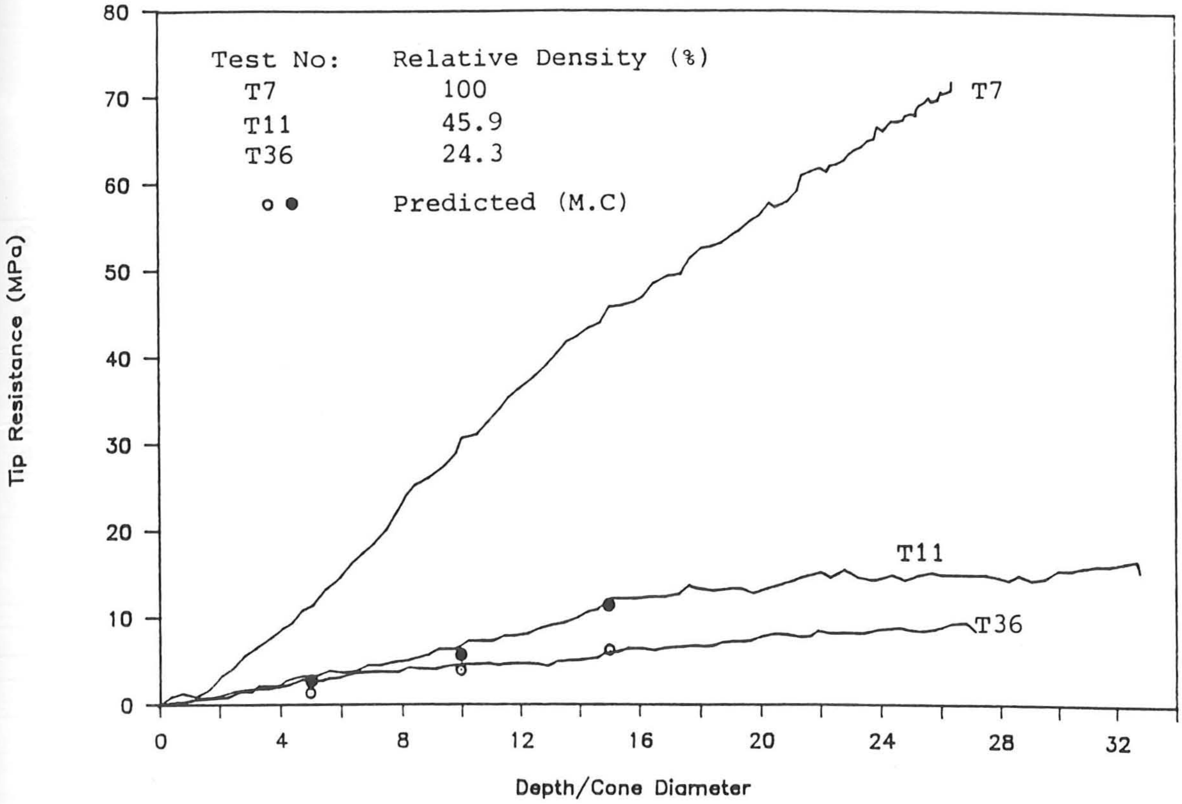

Fig 3.23 Relative density effects (14/25 sand, g-level=40).

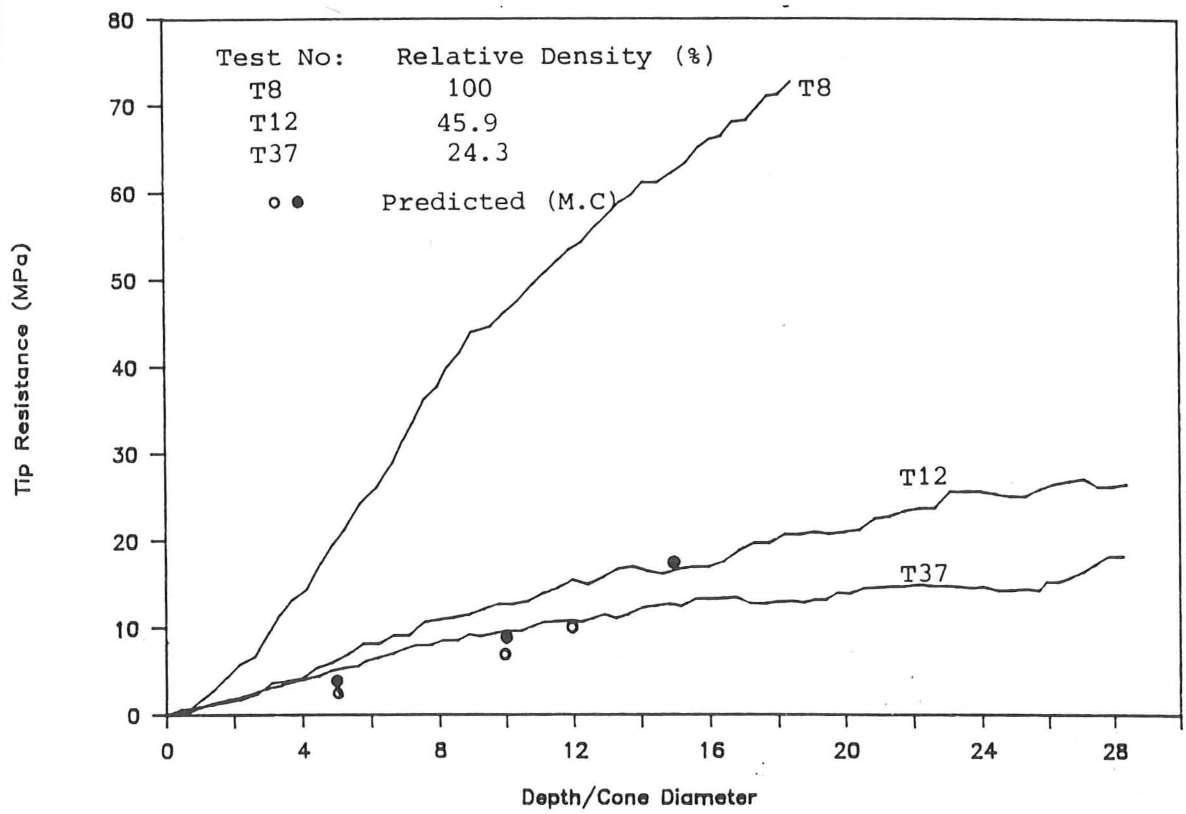

Fig 3.24 Relative density effects (14/25 sand, g-level=80).

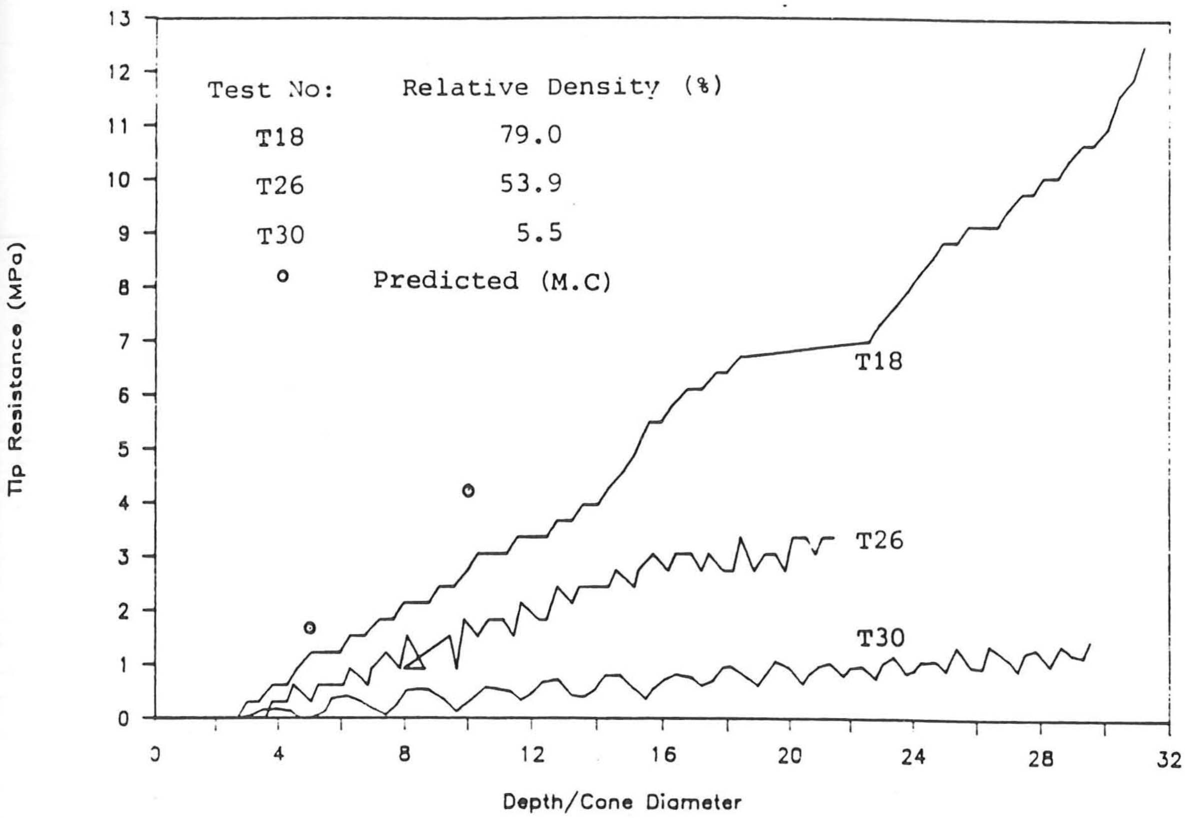

Fig 3.25 Relative density effects (52/100 sand, g-level=10).

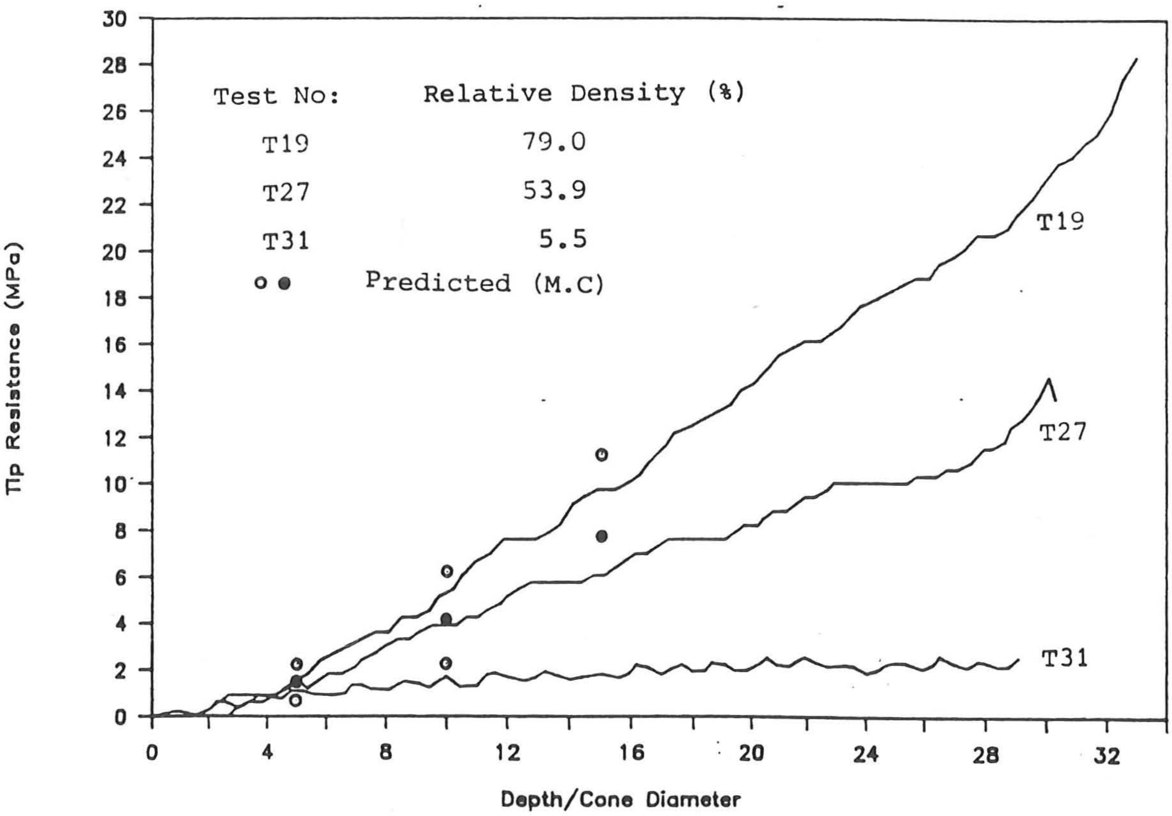

Fig 3.26 Relative density effects (52/100 sand, g-level=20).

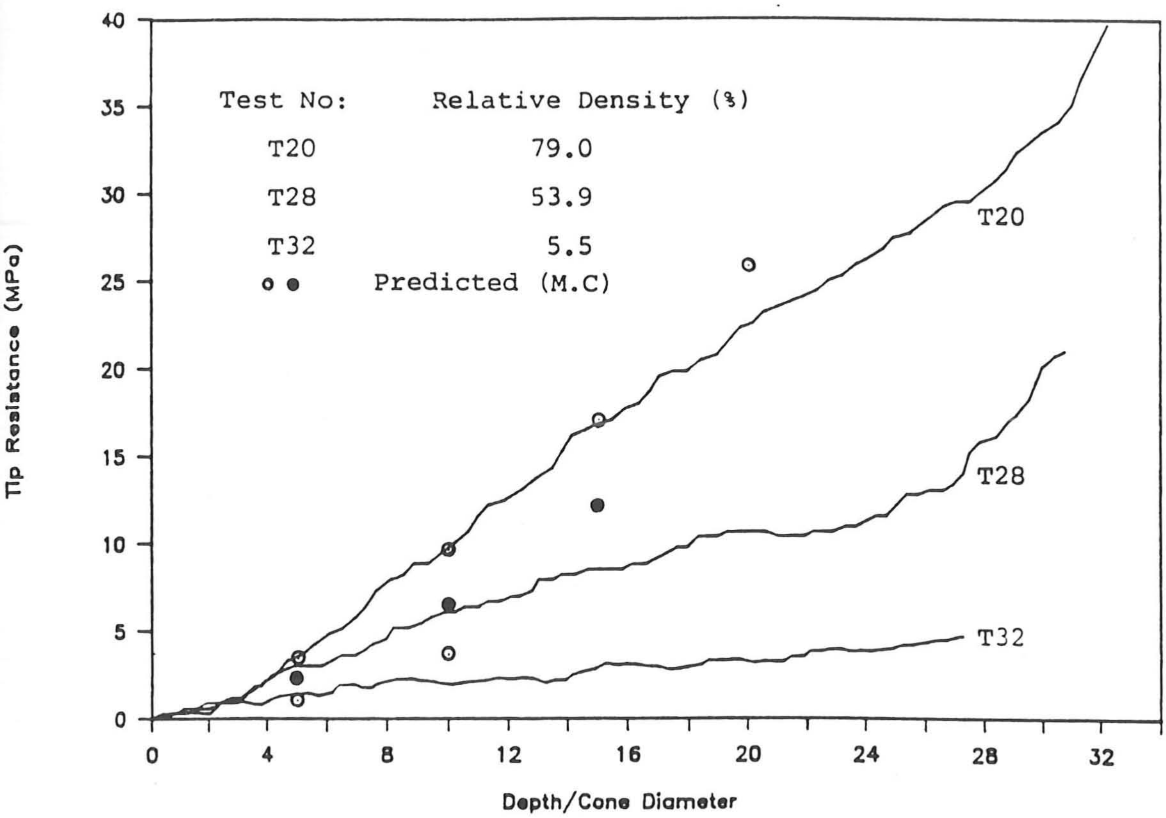

Fig 3.27 Relative density effects
(52/100 sand, g-level=40).

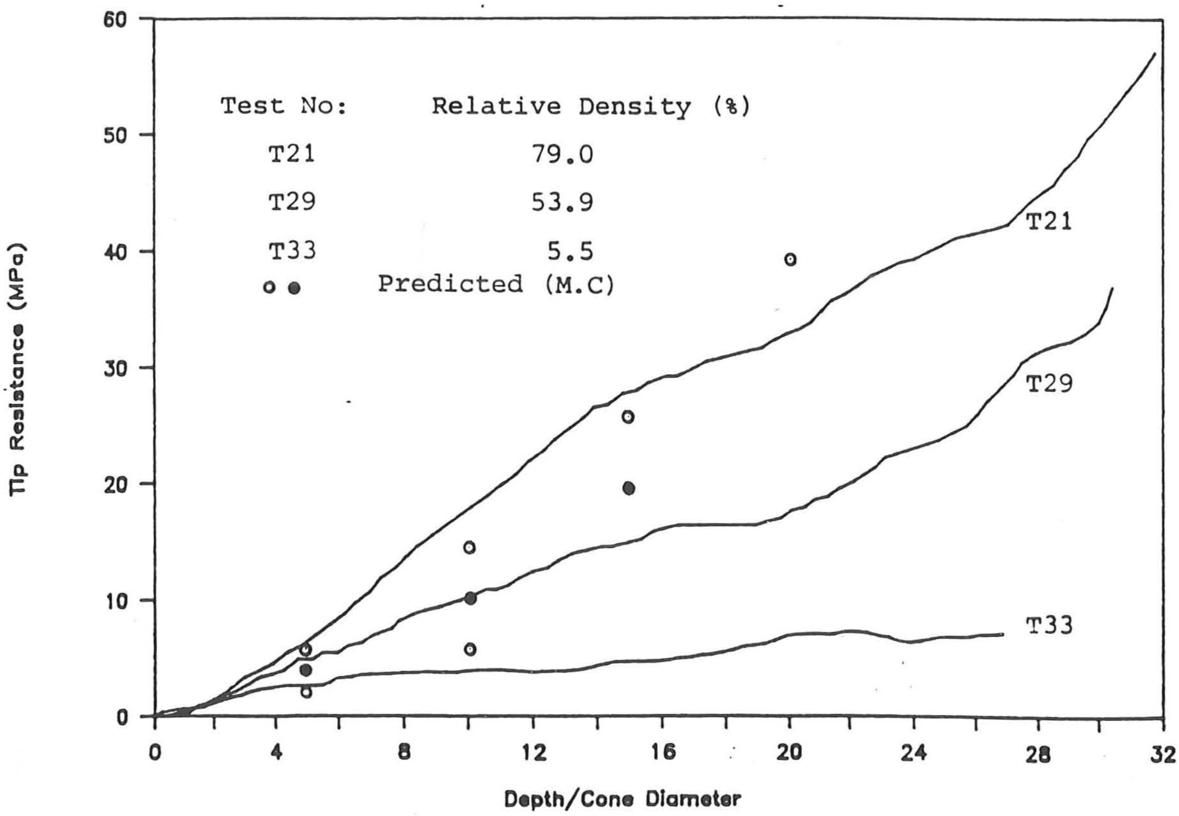

Fig 3.28 Relative density effects
(52/100 sand, g-level=80).

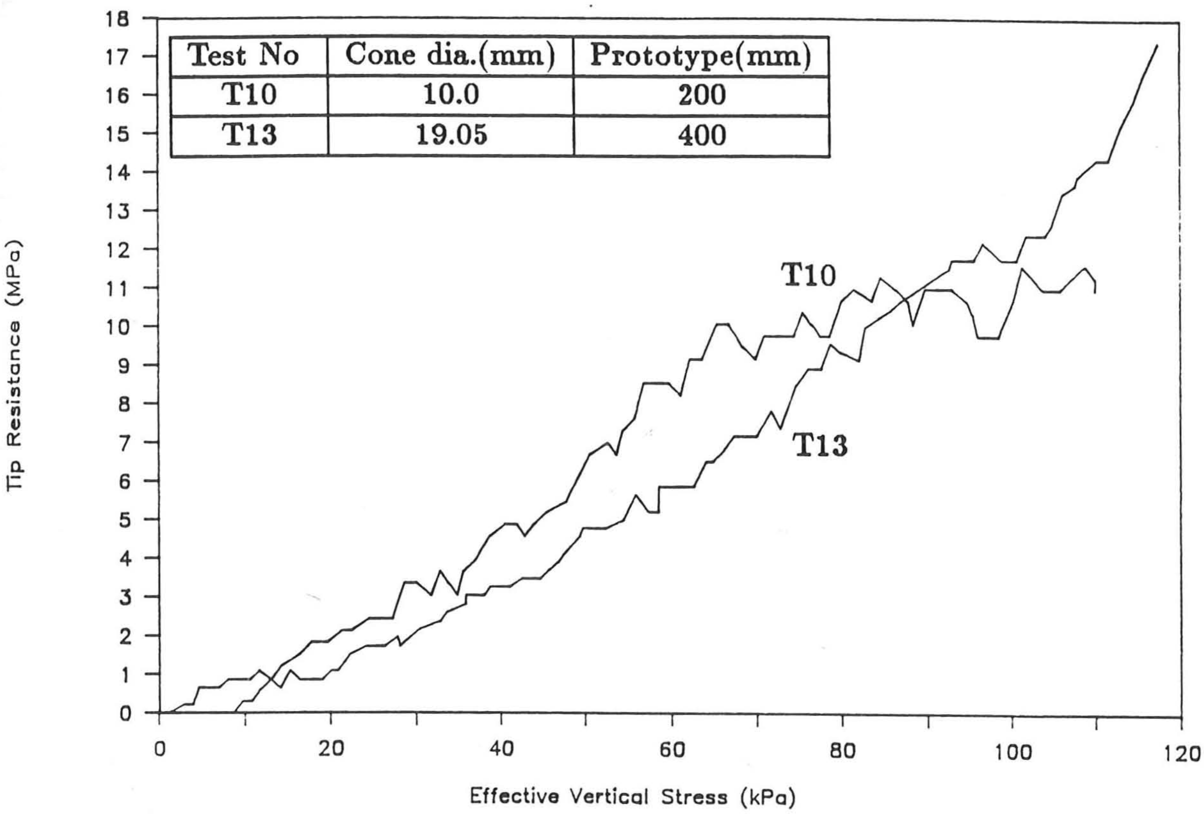

Fig 3.29 Scale effects
(14/25 sand).

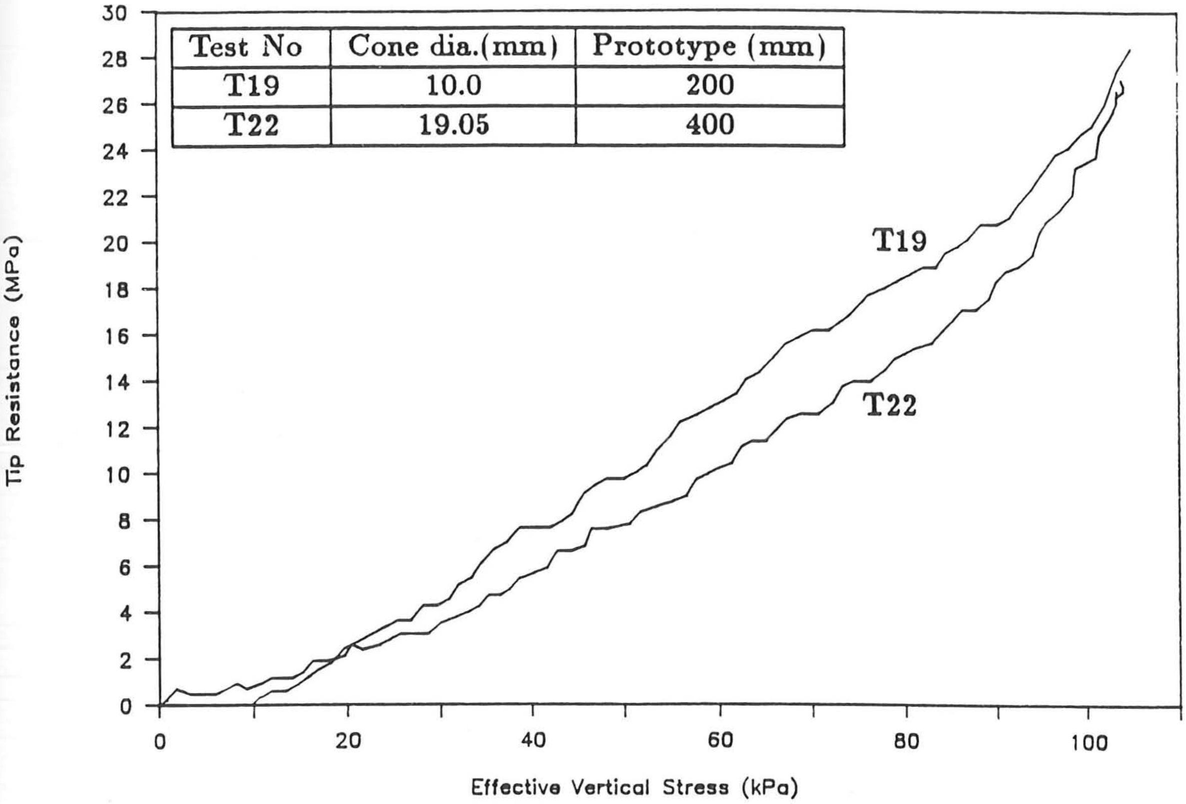

Fig 3.30 Scale effects
(52/100 sand).

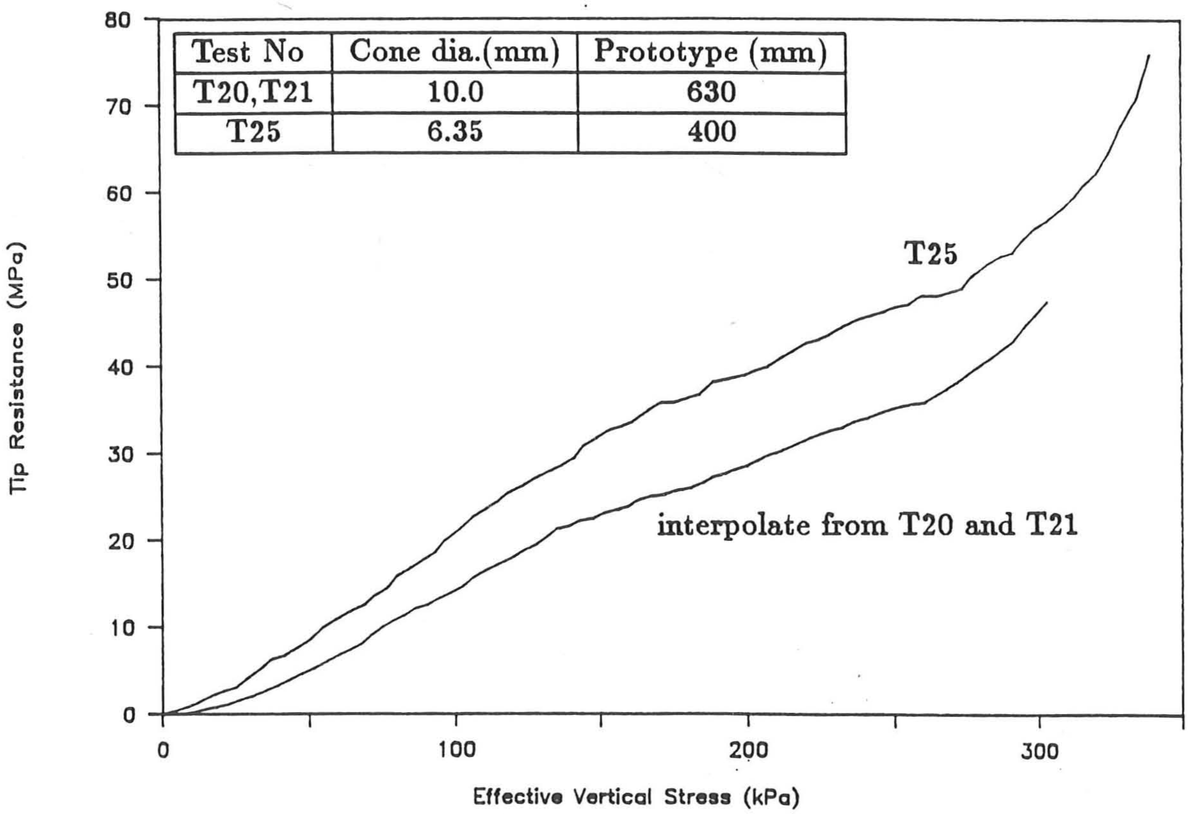

Fig 3.31 Scale effects
(52/100 sand).

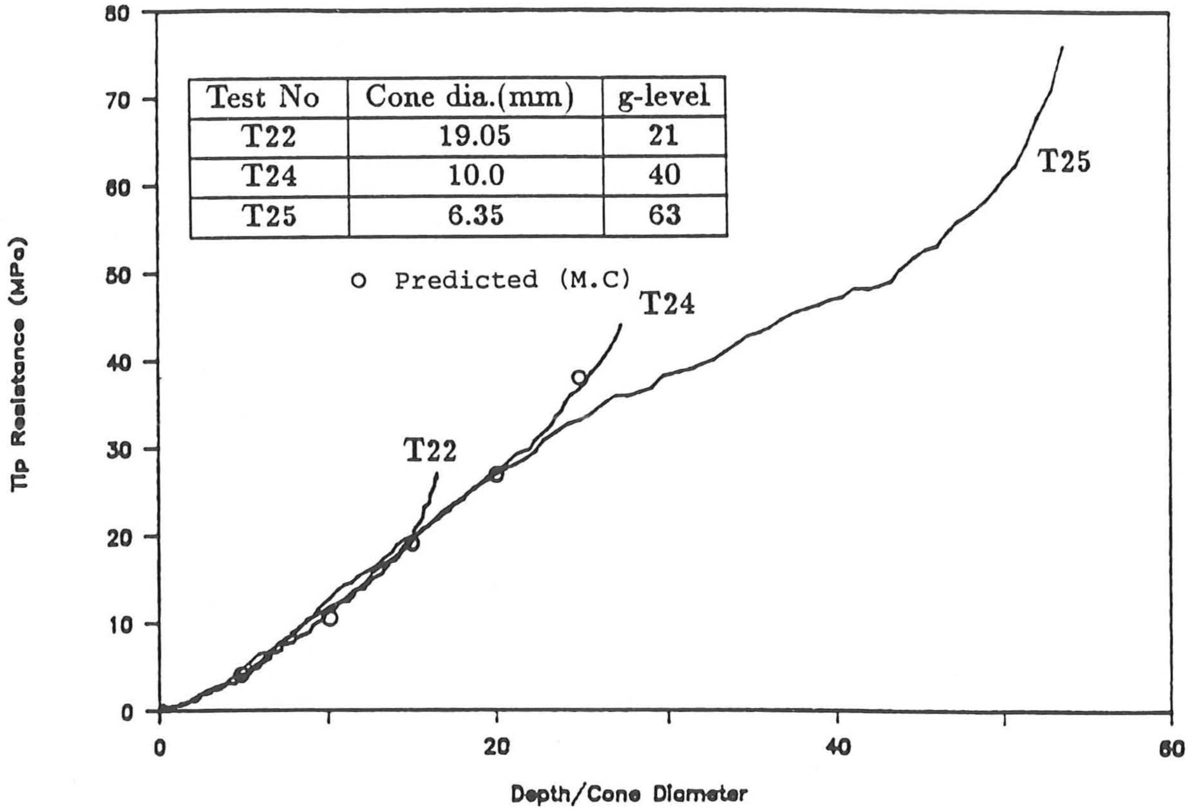

Fig 3.32 Grain size effects
(52/100 sand, void ratio=0.646).

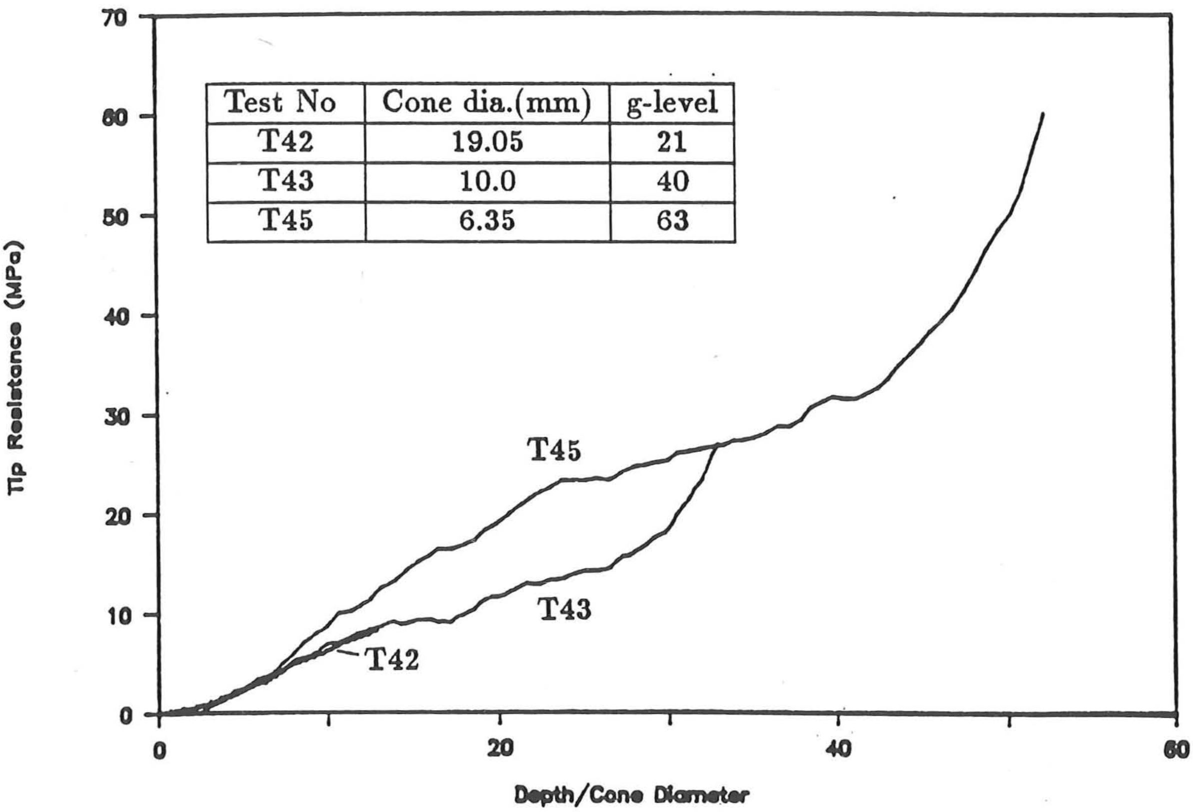

Fig 3.33 Grain size effects
(52/100 sand, void ratio=0.71).

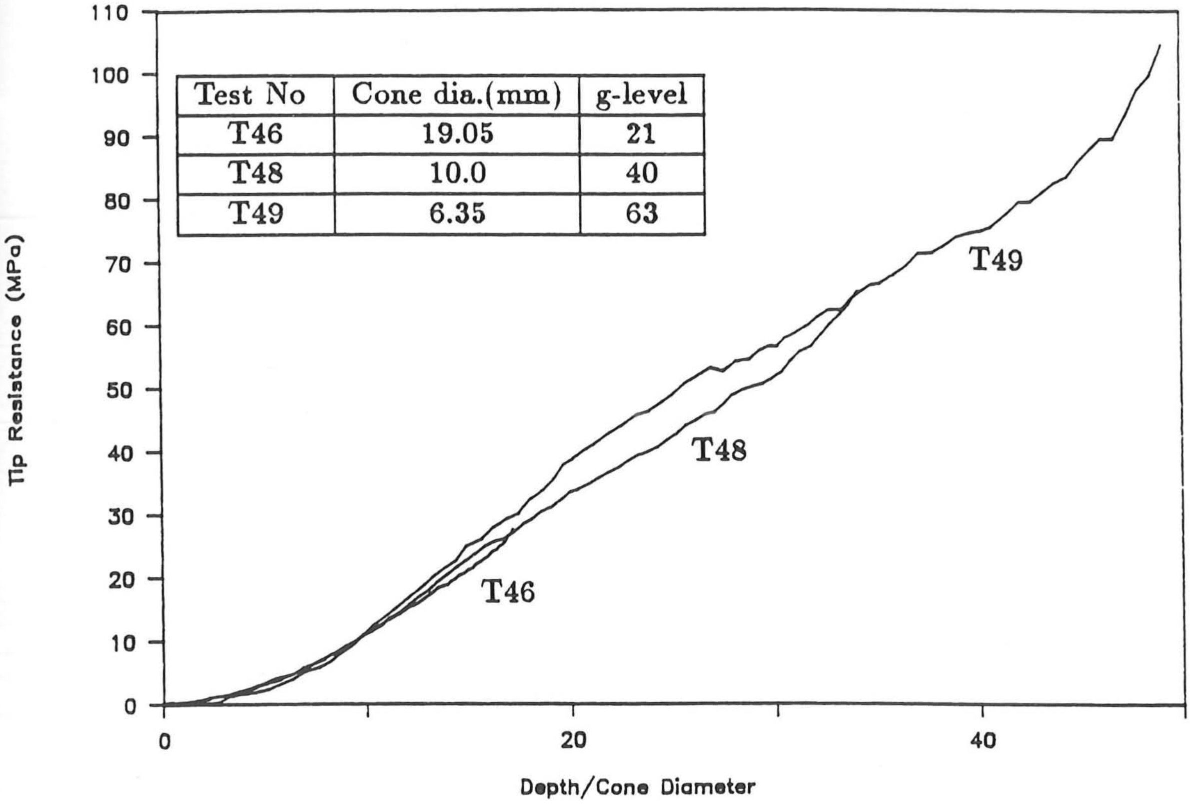

Fig 3.34 Grain size effects
(25/52 sand, void ratio=0.524).

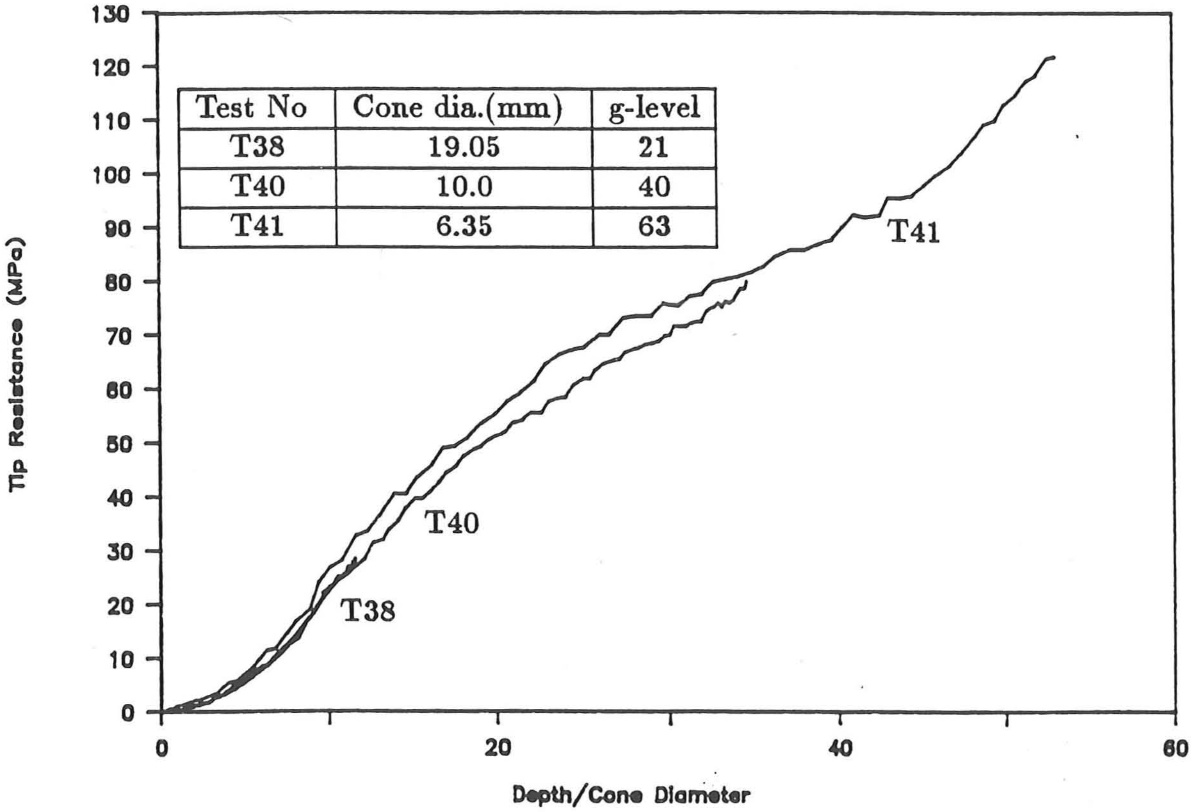

Fig 3.35 Grain size effects
(14/25 sand, void ratio=0.519).

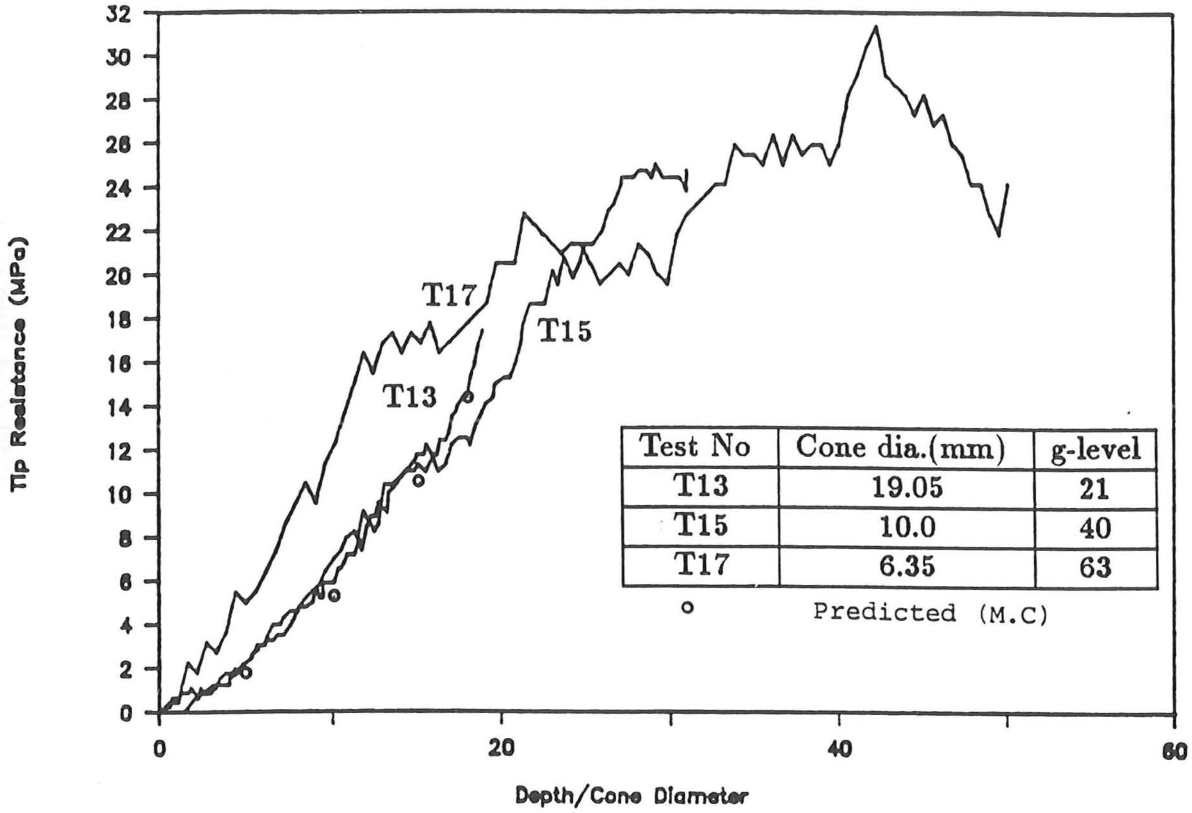

Fig 3.36 Grain size effects
(14/25 sand, void ratio=0.671).

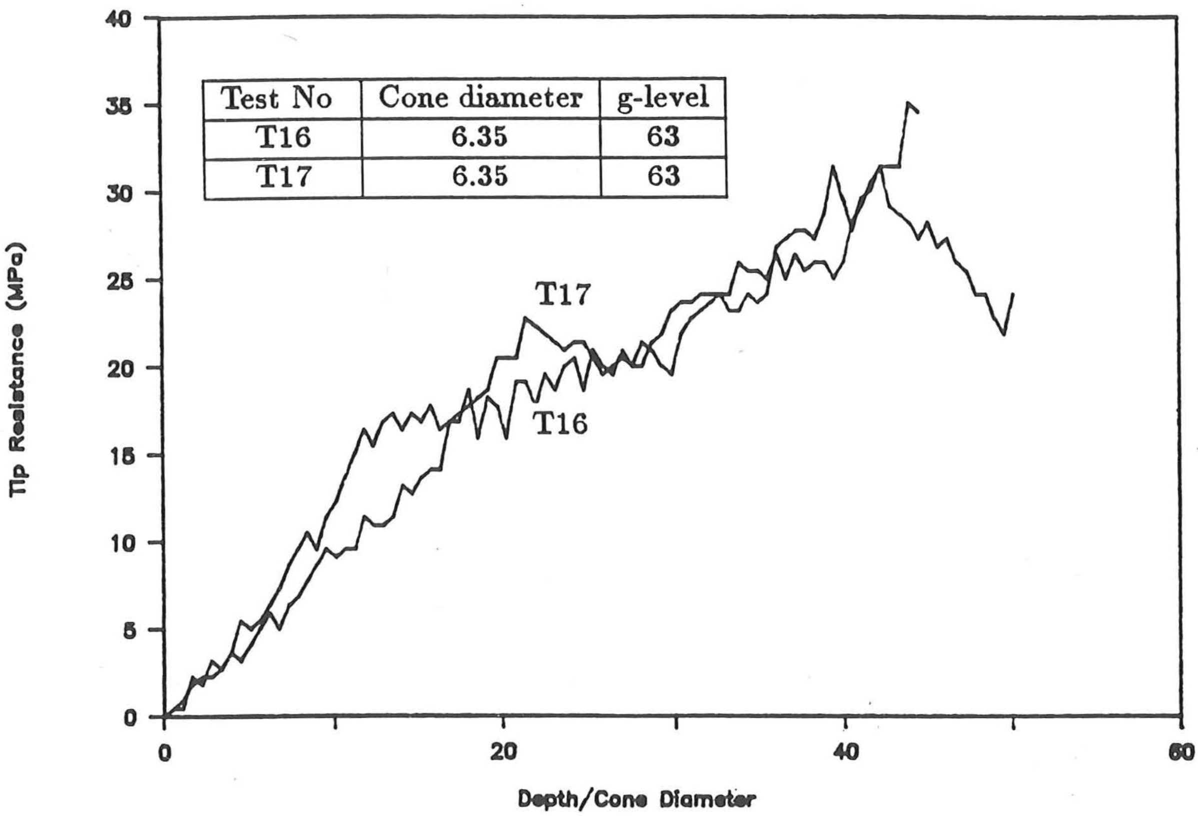

Fig 3.37 Grain size effects
(14/25 sand, void ratio=0.671).

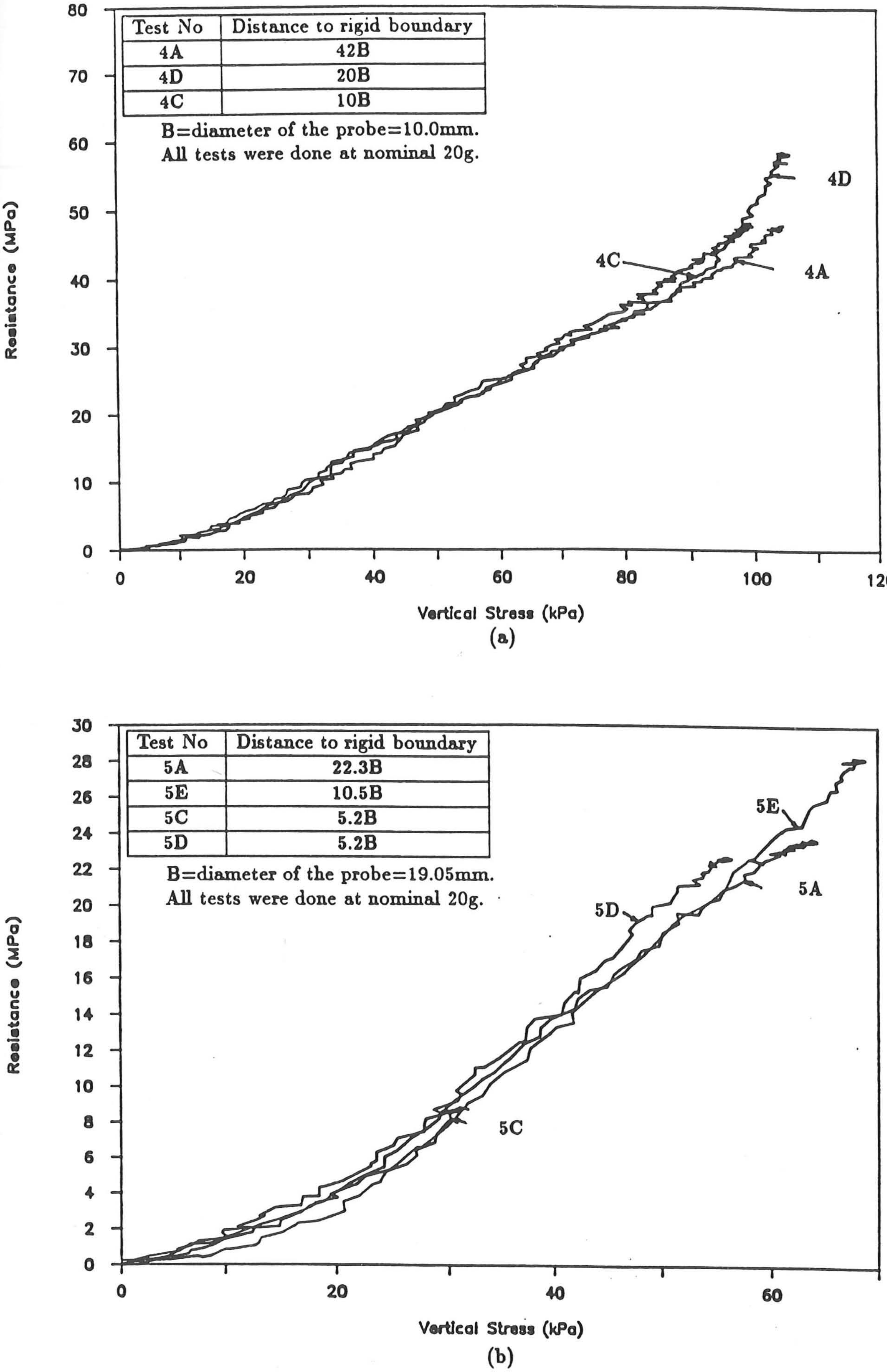

Fig 3.38 Boundary effects on tip resistance.

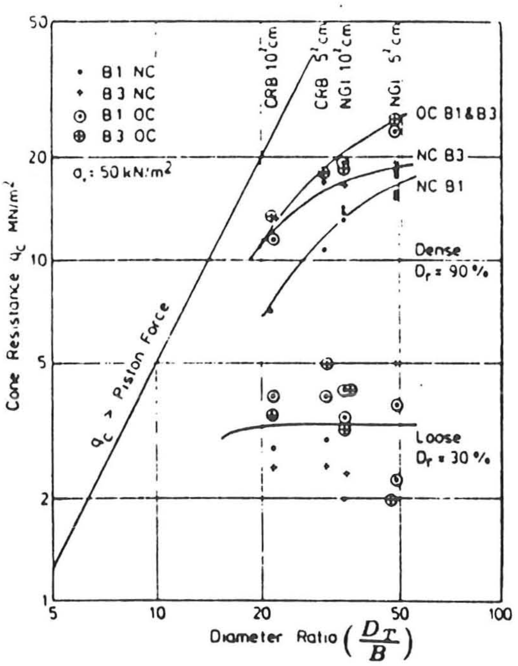

Fig 3.39 Chamber size effects on tip resistance (after Parkin and Lunne, 1982).

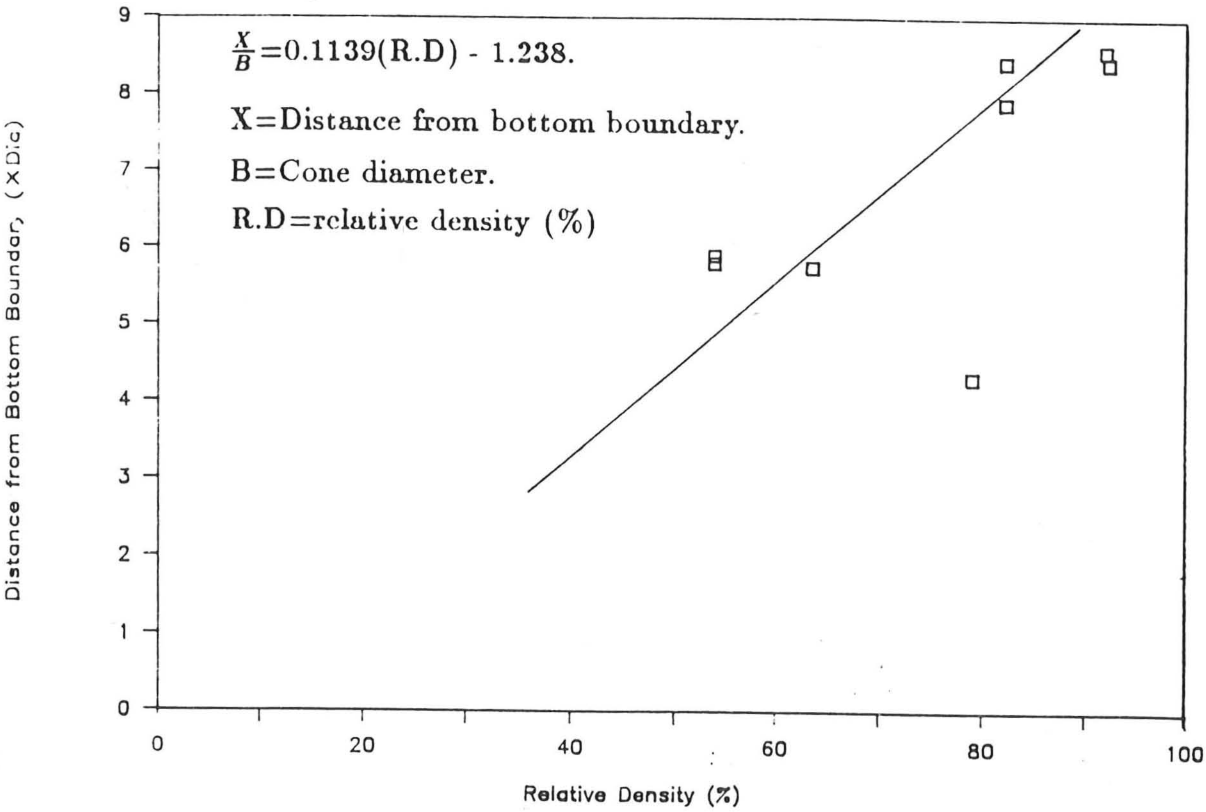

Fig 3.40 Bottom boundary effects.

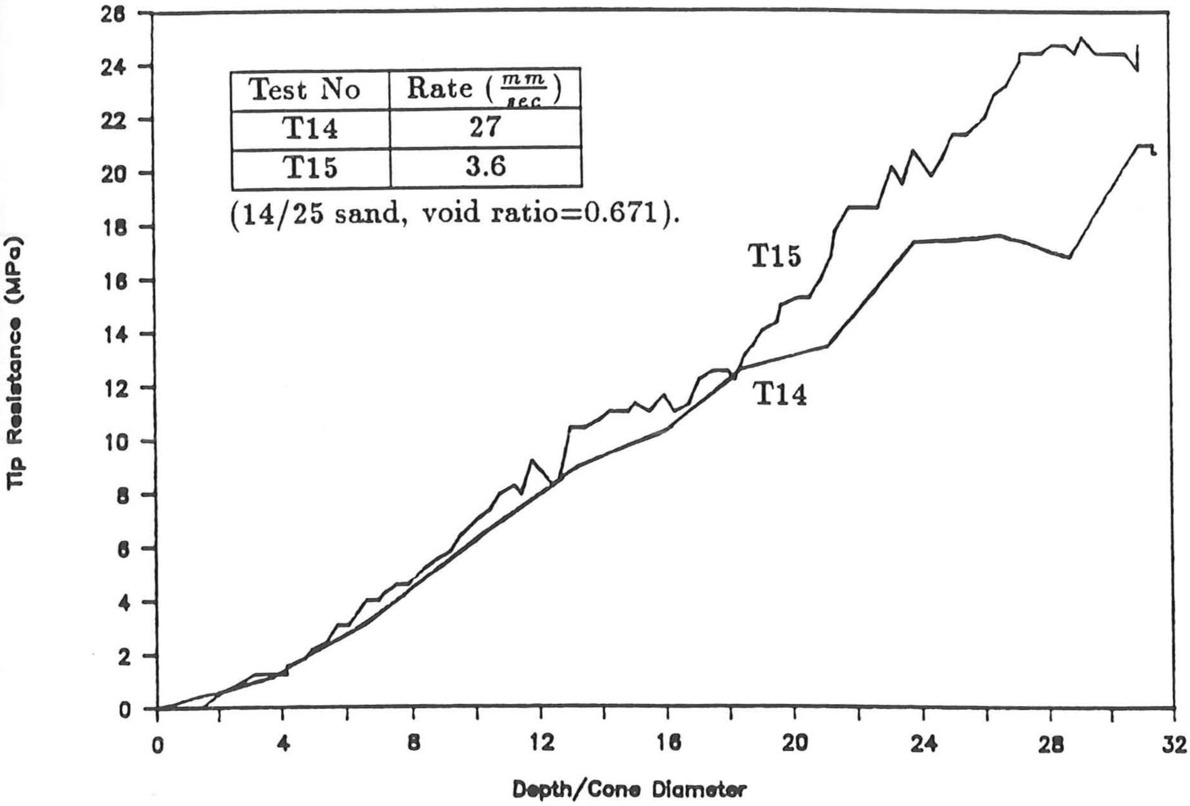

(a)

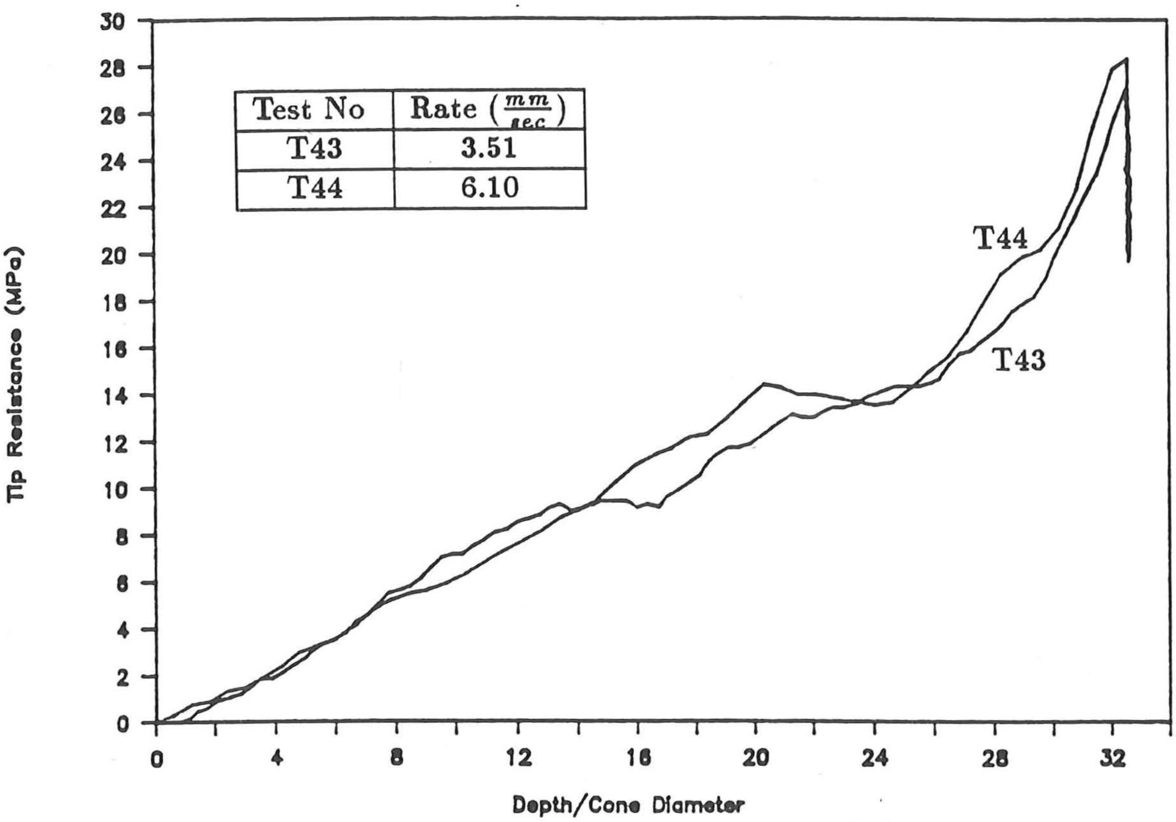

(b)

Fig 3.41 Penetration rate effects

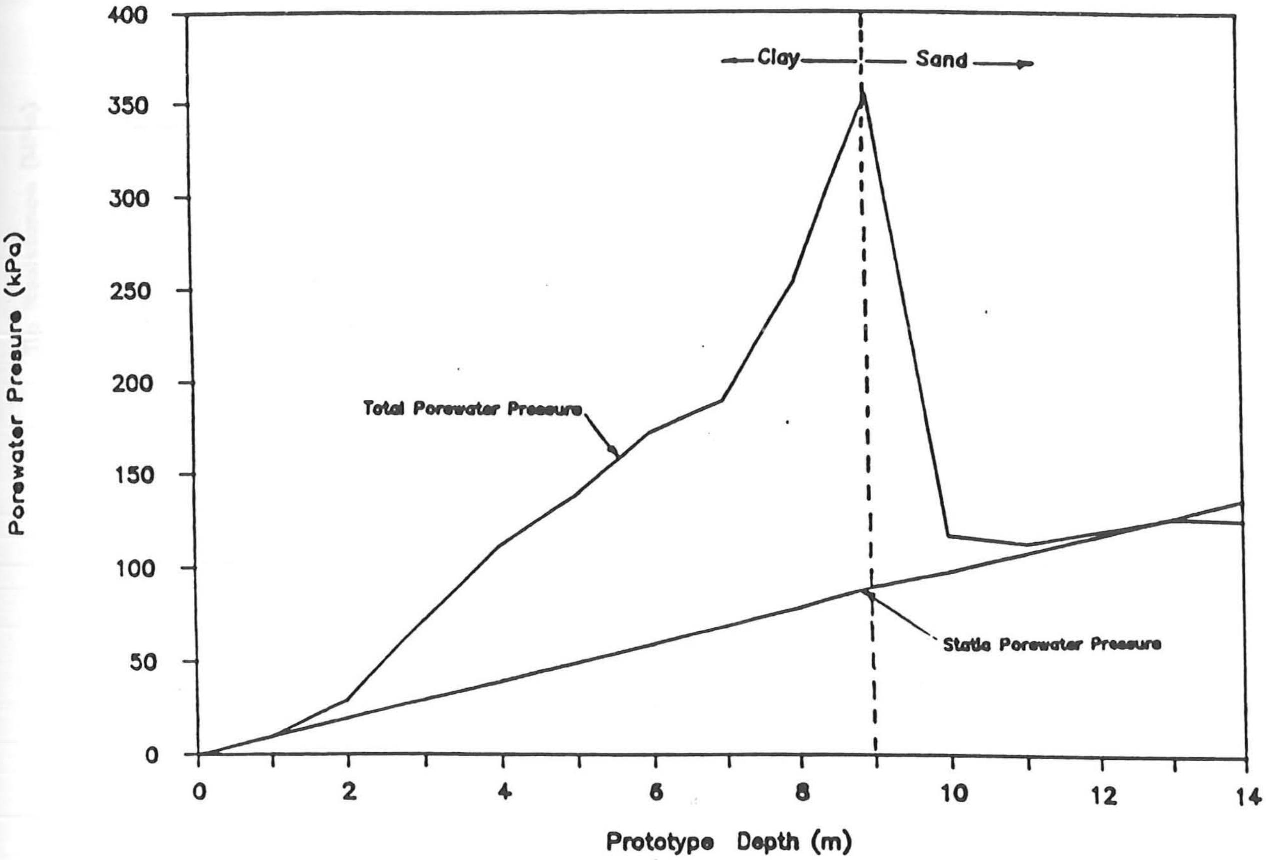

Fig 3.42 Excess pore pressure generated in clay
(after Springman, 1987)

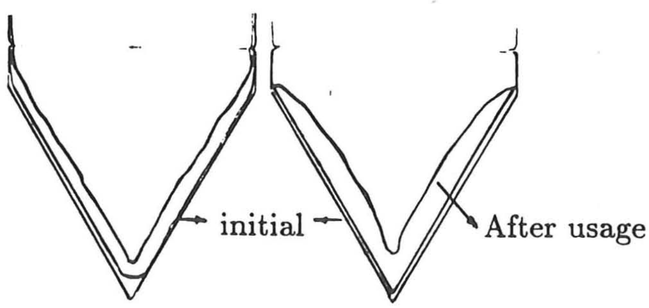

Fig 3.43 Wear and tear of the cone face
(after Schaap and Zuidberg, 1982).

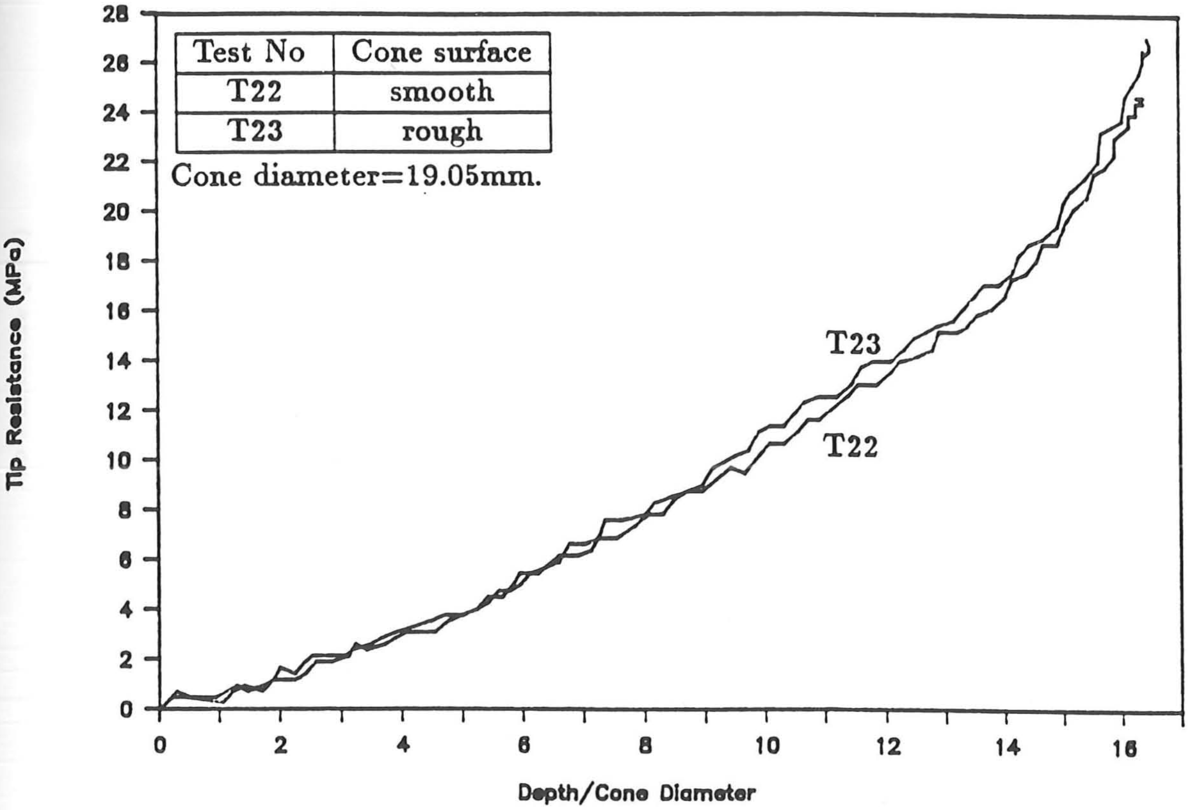

Fig 3.44(a) 52/100 sand, void ratio=0.646.

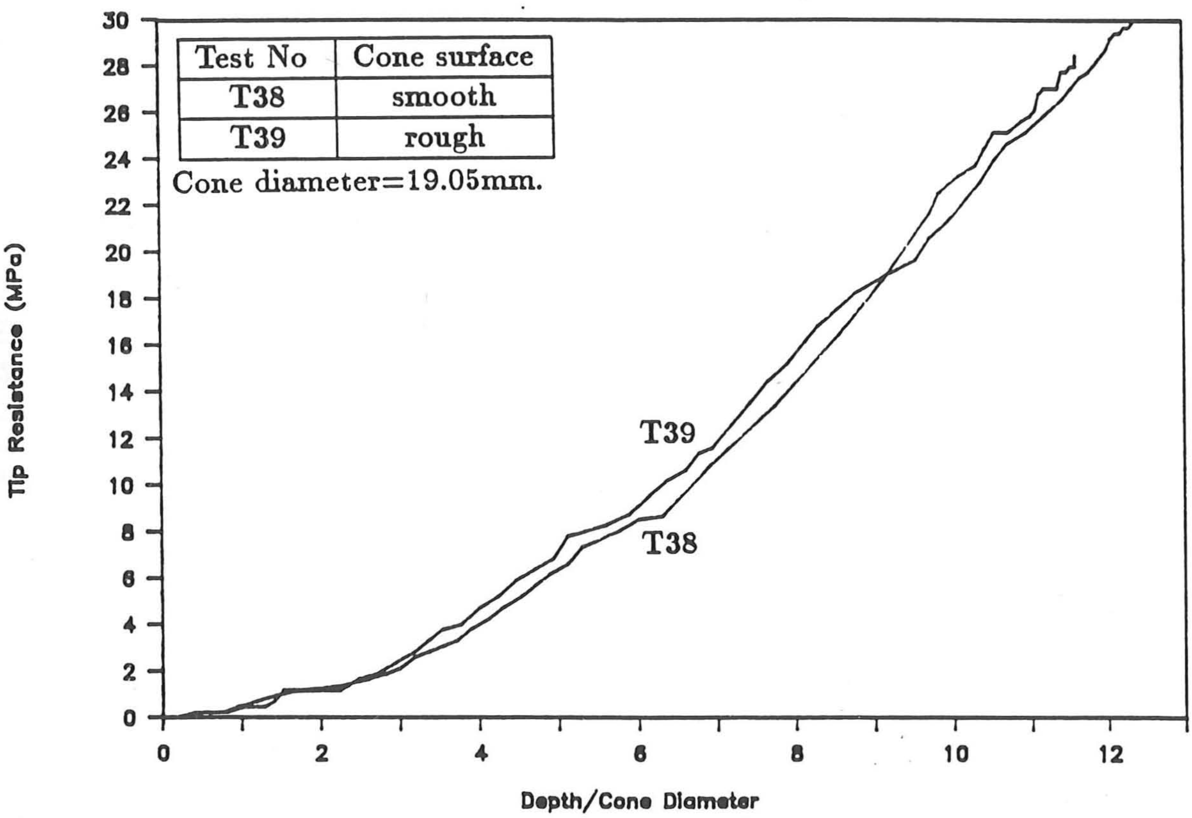

Fig 3.44(b) 14/25 sand, void ratio=0.519.

Fig 3.44 Roughness effects on tip resistance.

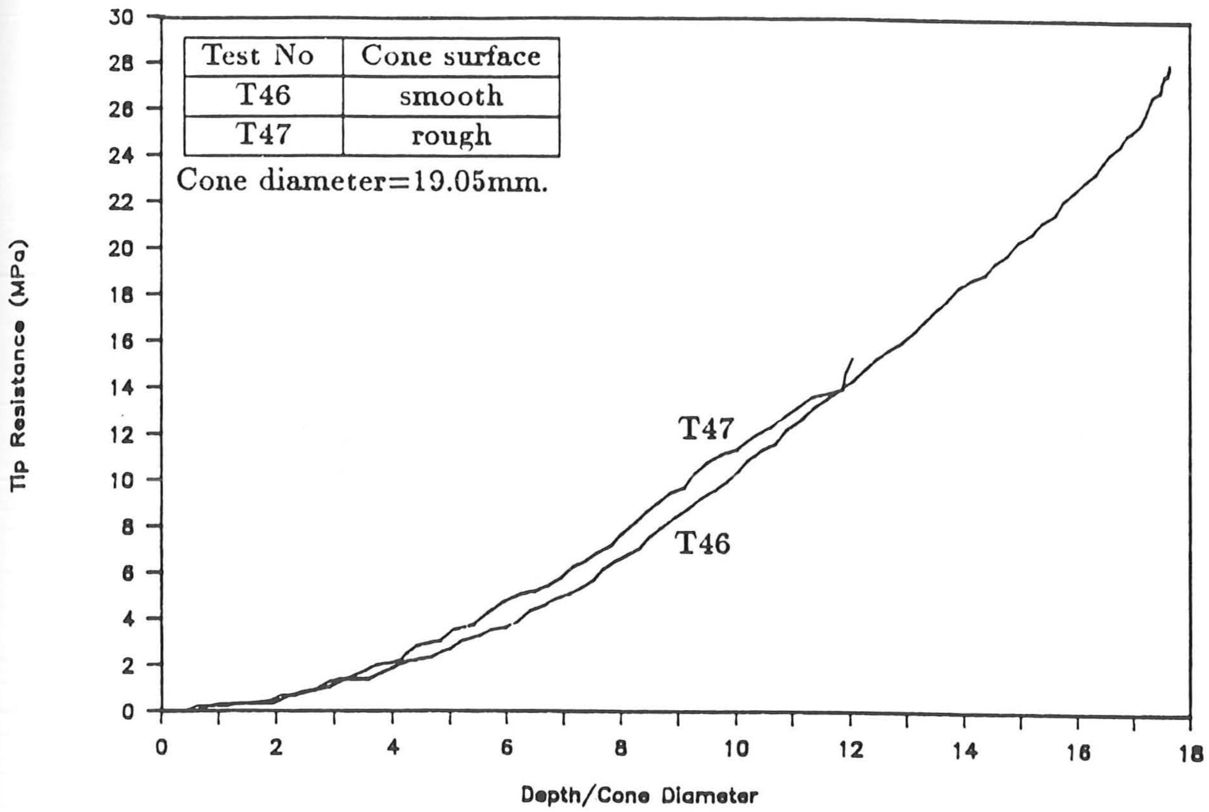

Fig 3.44 (c) 25/52 sand, void ratio=0.524.

Fig 3.44 Roughness effects on tip resistance.

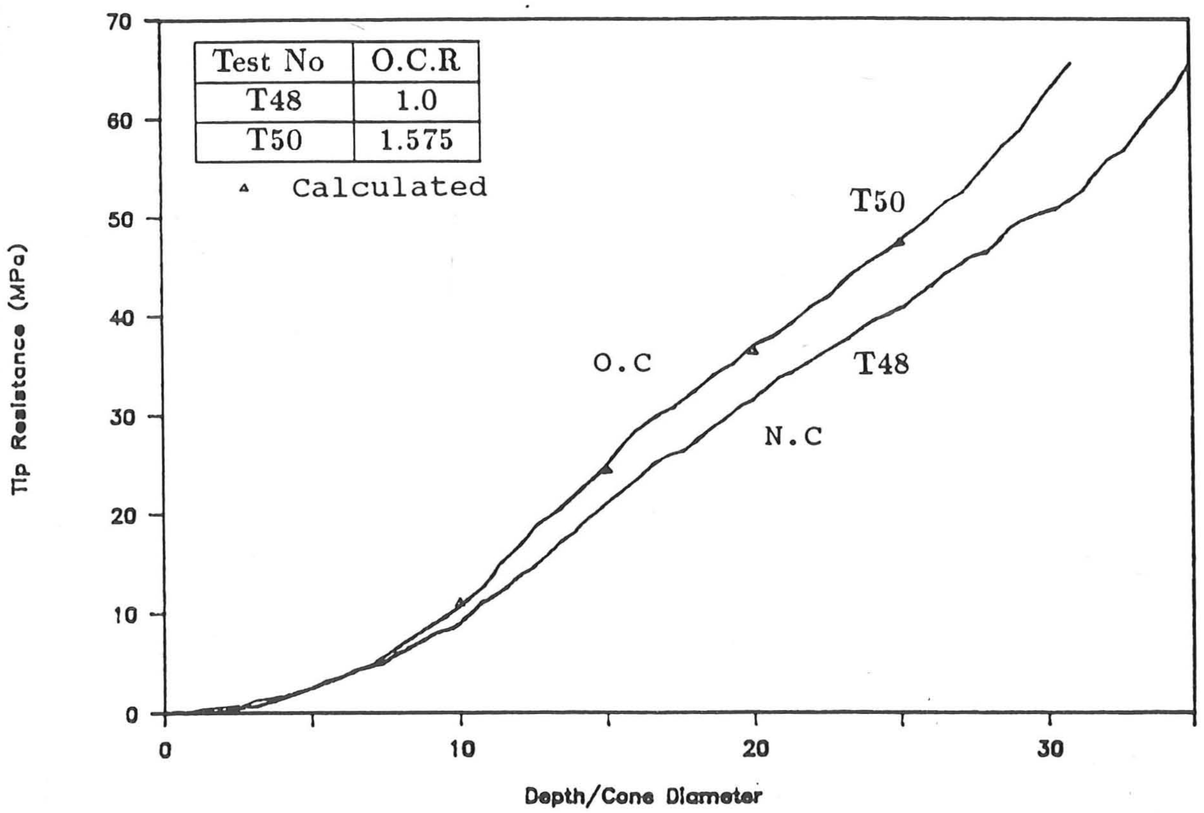

Fig 3.45 Overconsolidation effects on tip resistance
(25/52 sand, void ratio=0.524).

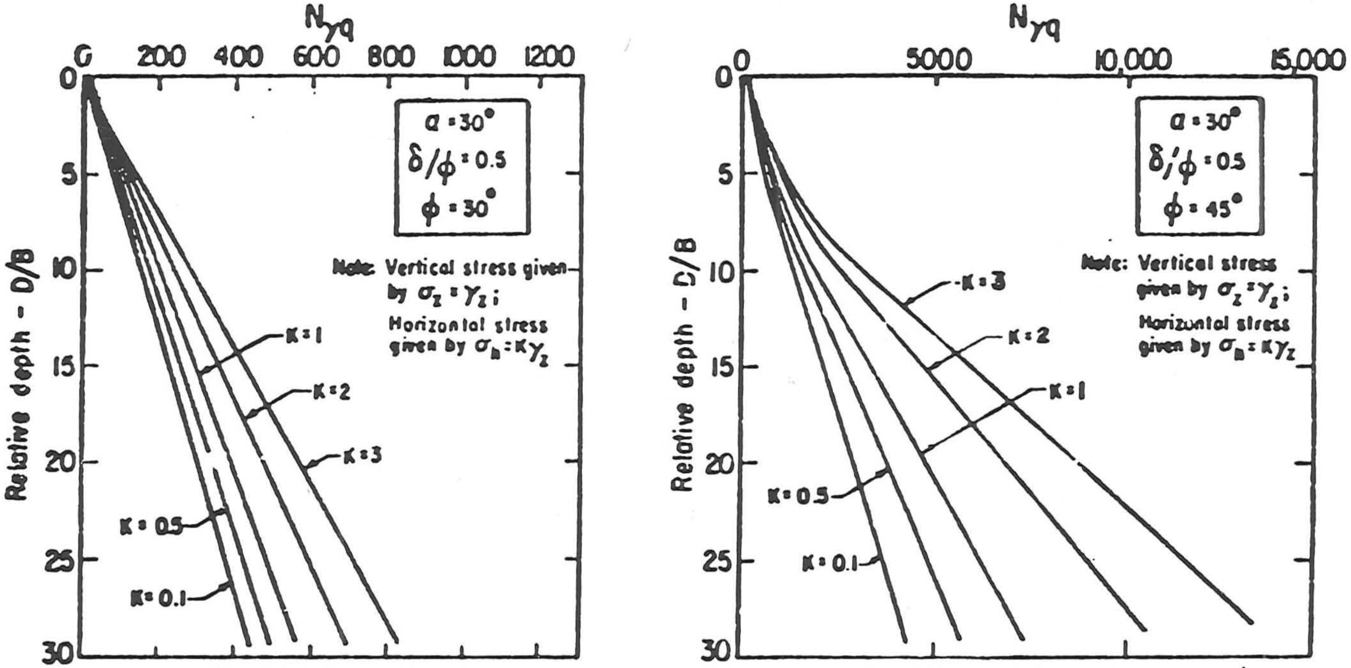

Fig 3.46 Effect of initial horizontal stresses on bearing capacity factors (after Durgunoglu and Mitchell, 1975).

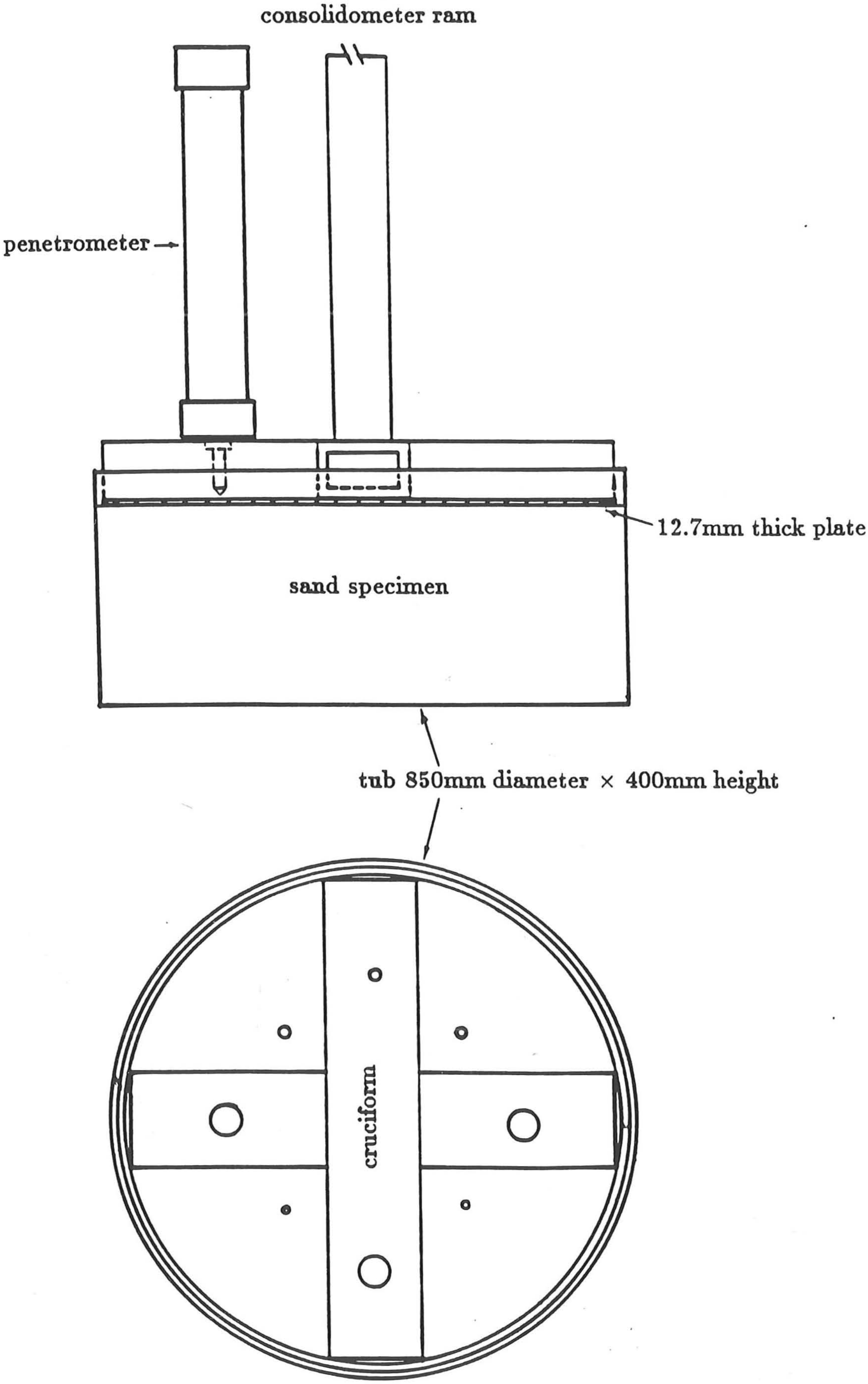

Fig 4.1 The assembled package for laboratory floor 1g tests.

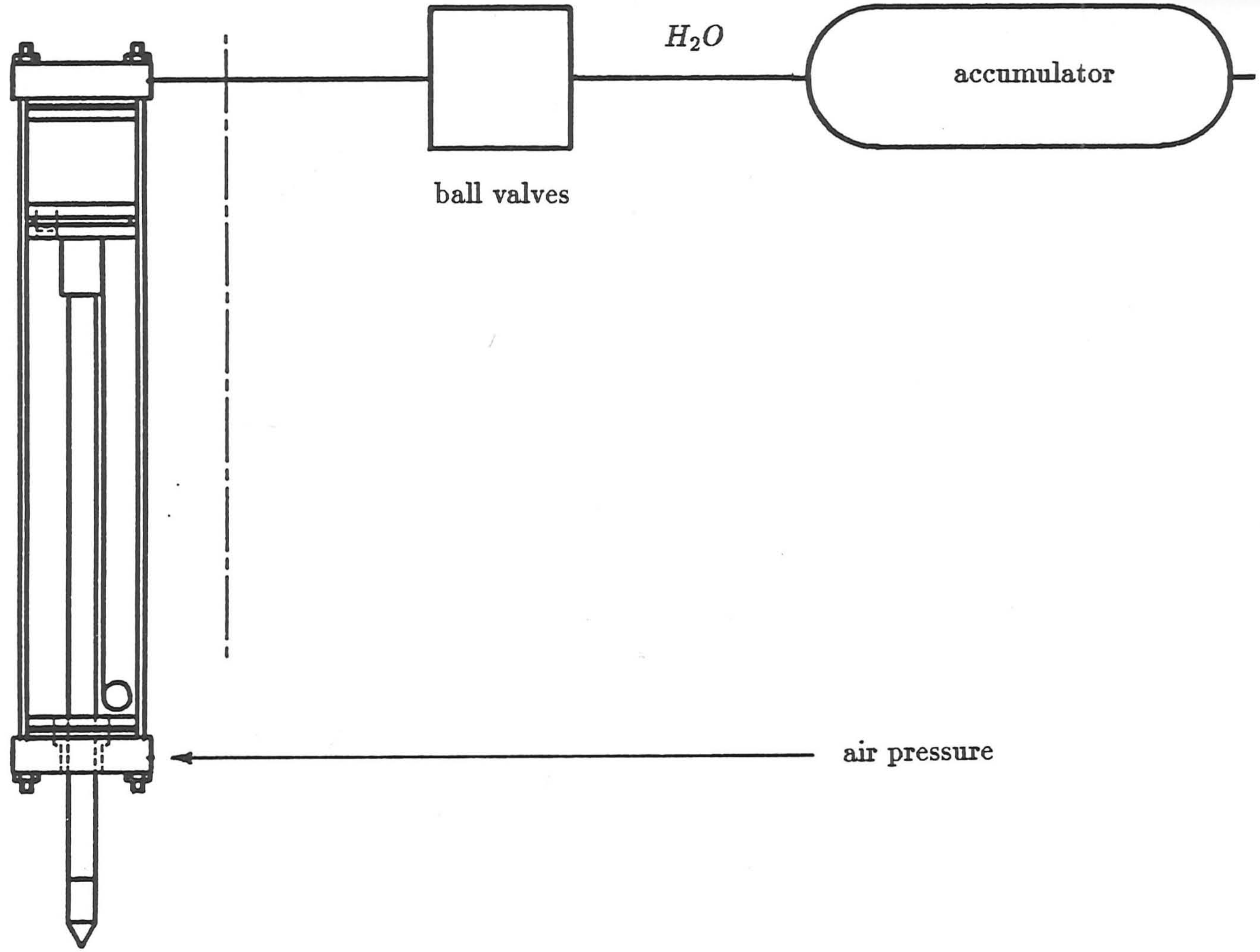

Fig 4.2 Hydraulic and pressure control system.

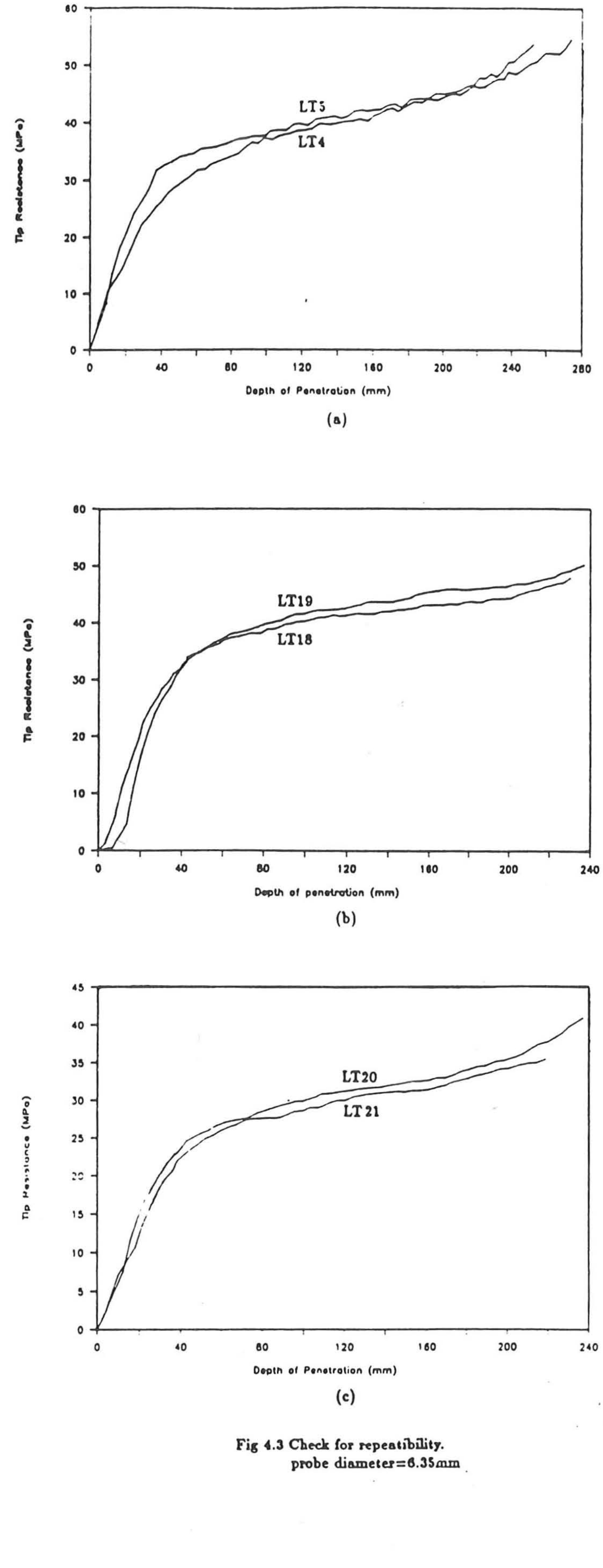

Fig 4.3 Check for repeatibility.
probe diameter=6.35mm

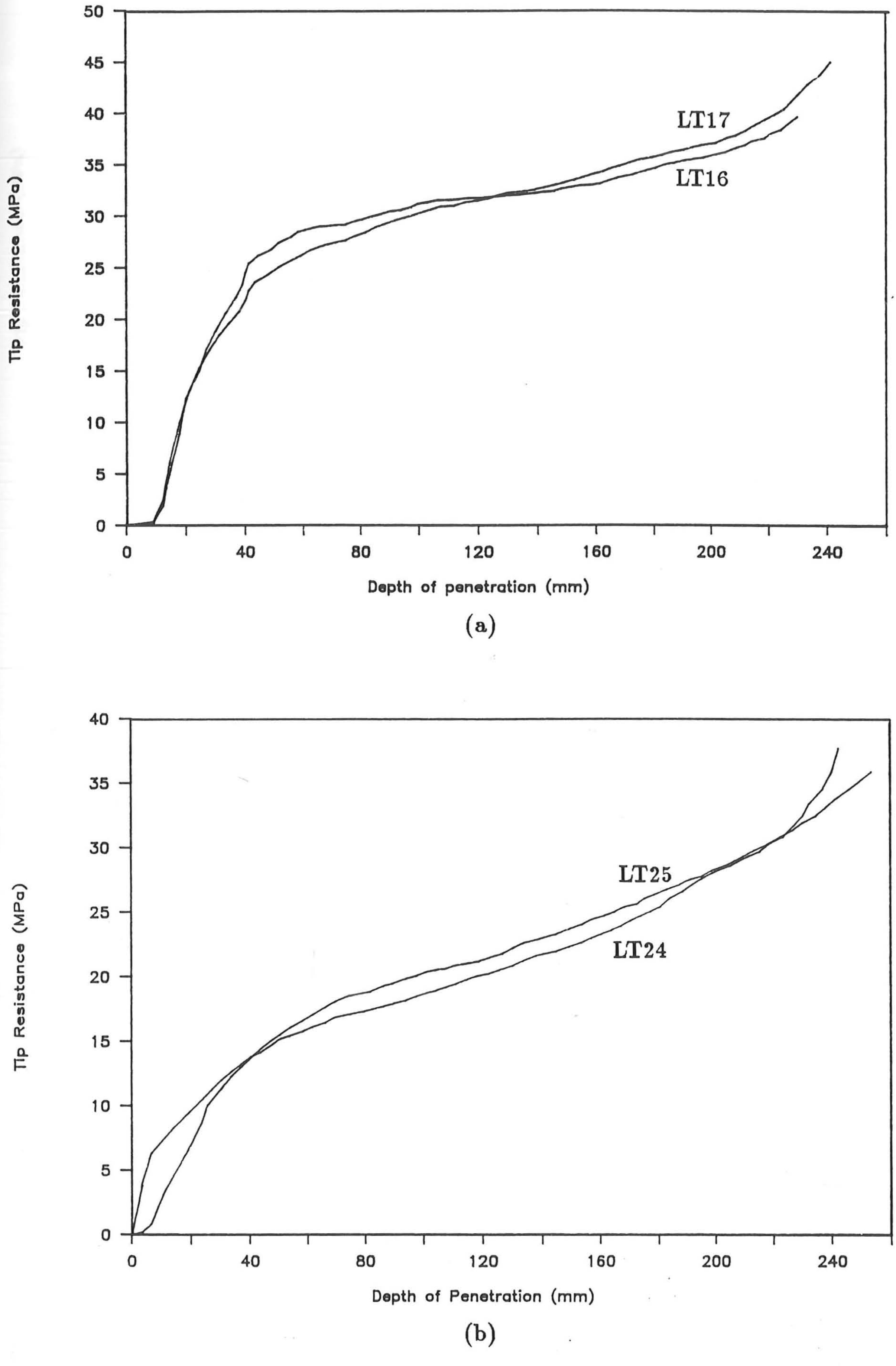

Fig 4.4 Check for repeatibility.
probe diameter=10.0mm

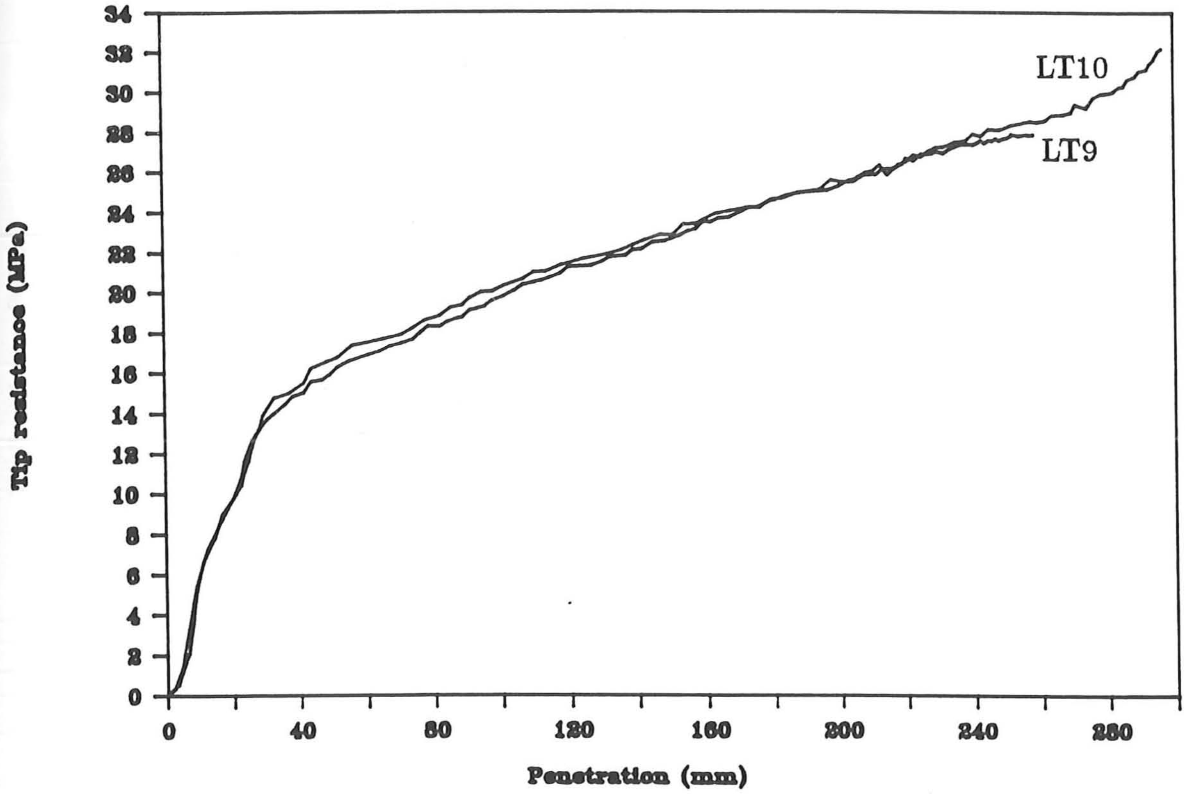

(a)

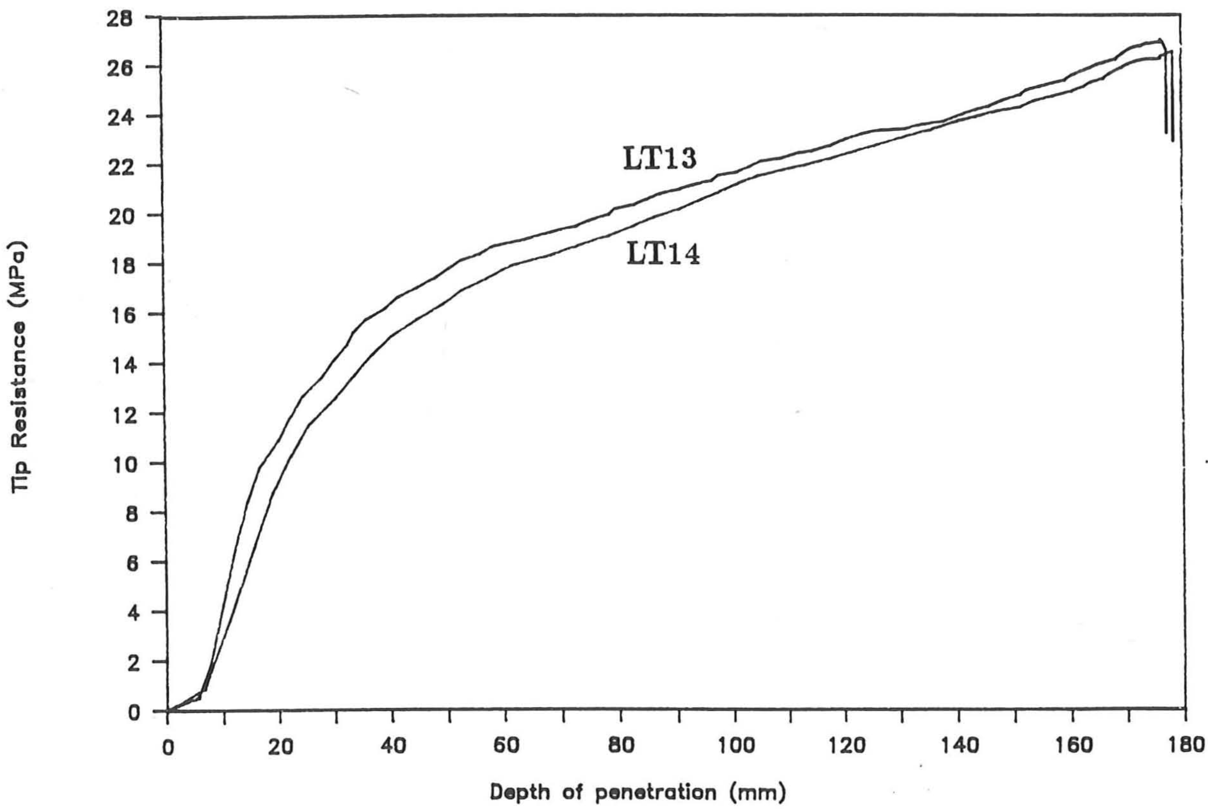

(b)

Fig 4.5 Check for repeatibility
probe diameter=19.05mm

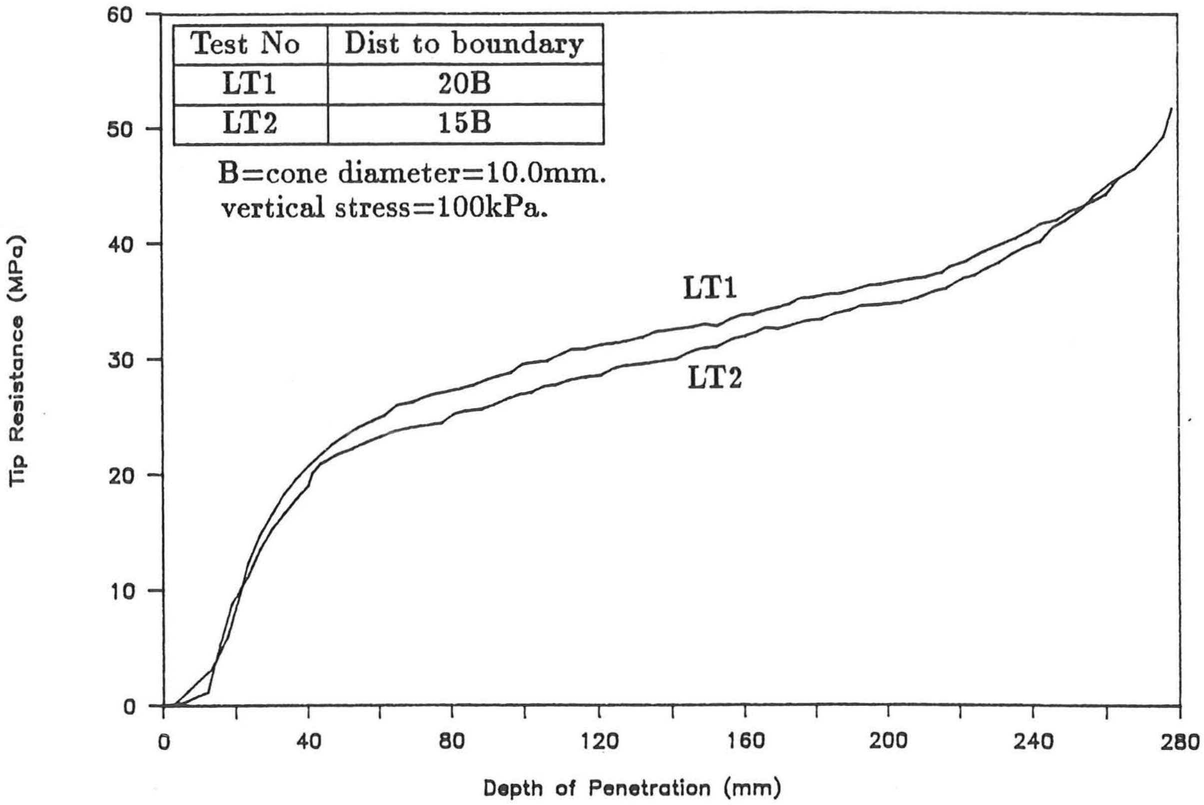

(a)

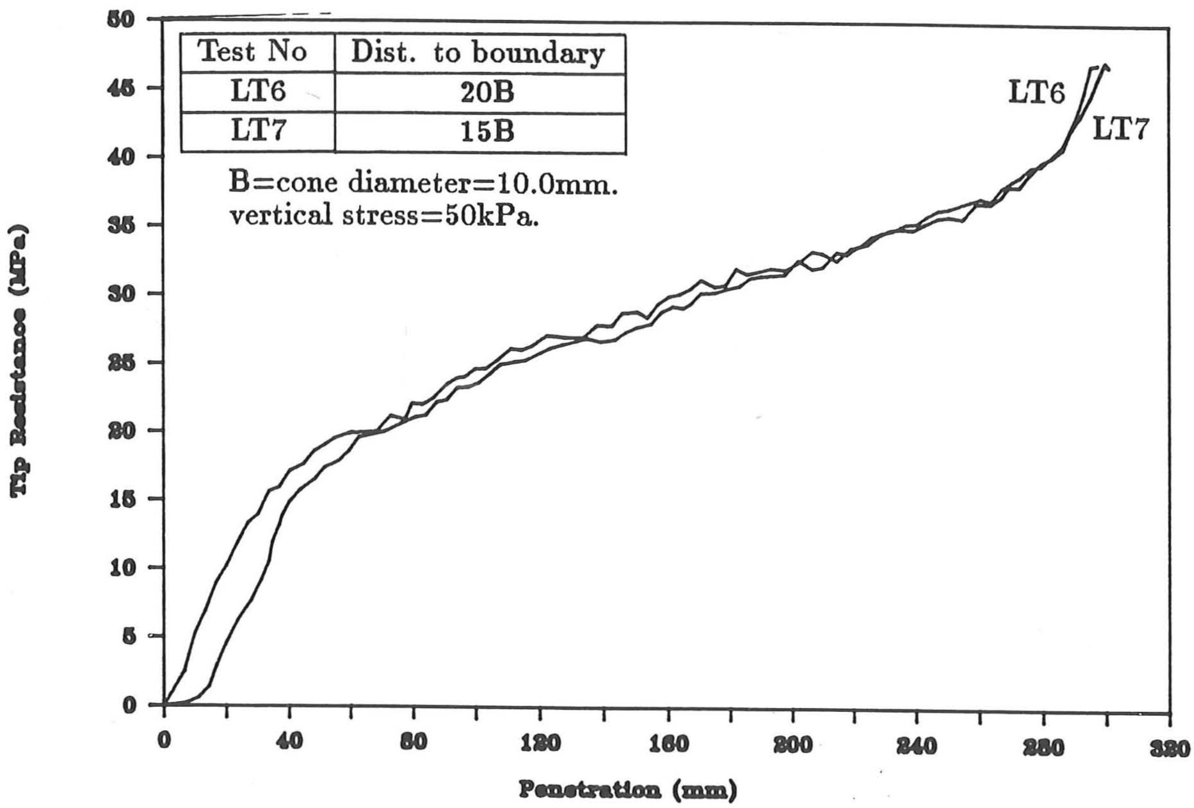

(b)

Fig 4.6 Boundary effects on tip resistance.

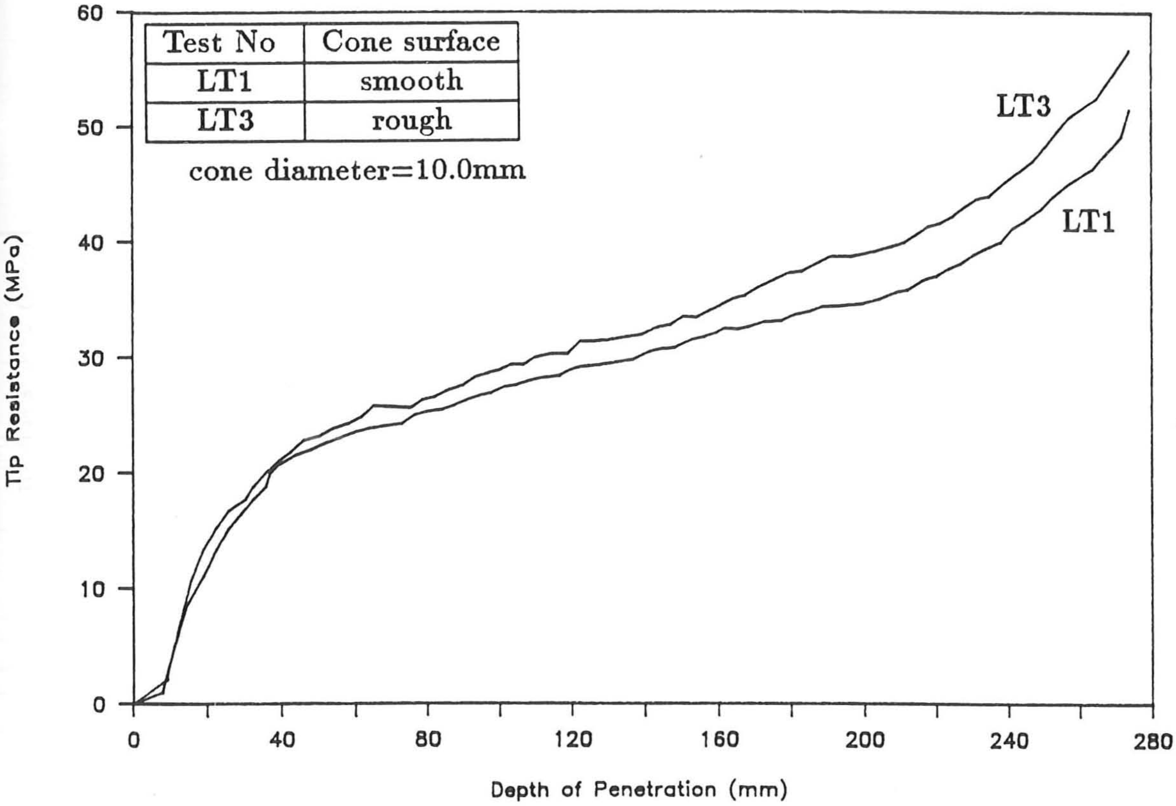

Fig 4.7(a) 25/52 sand

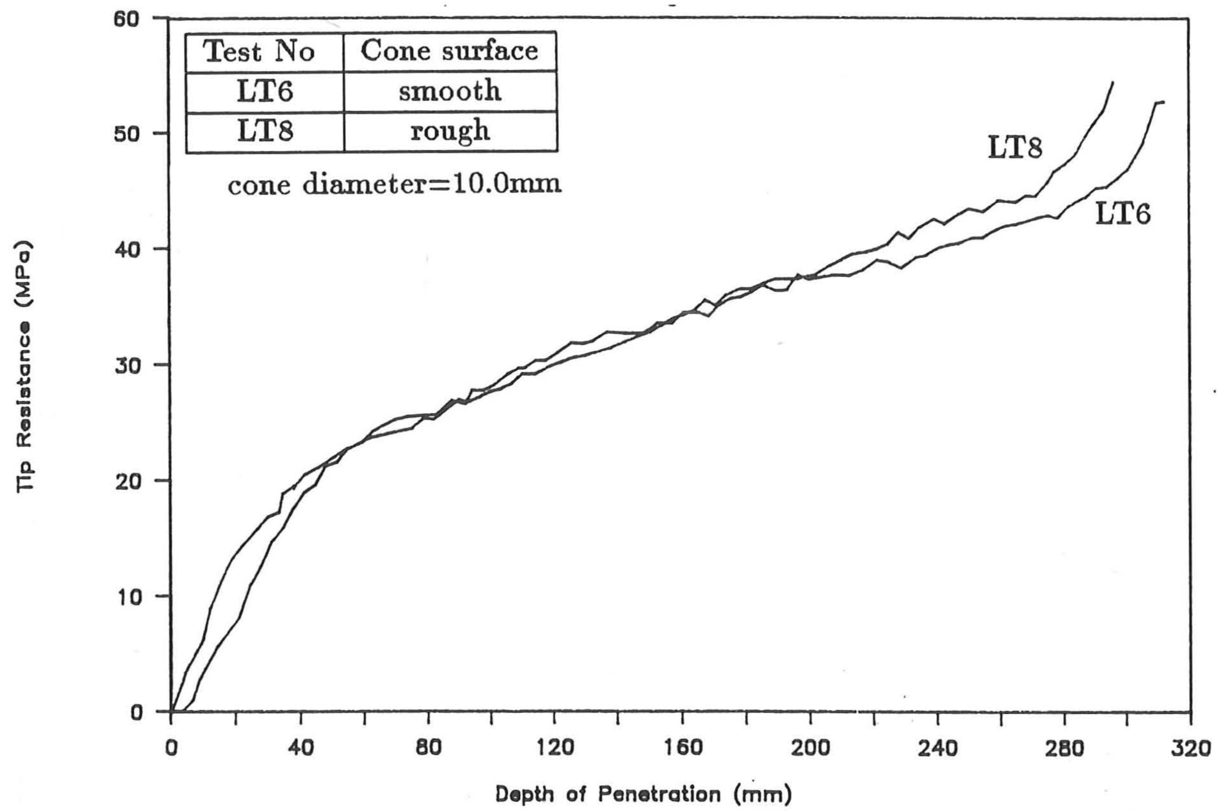

Fig 4.7(b) 14/25 sand

Fig 4.7 Roughness effects on tip resistance.

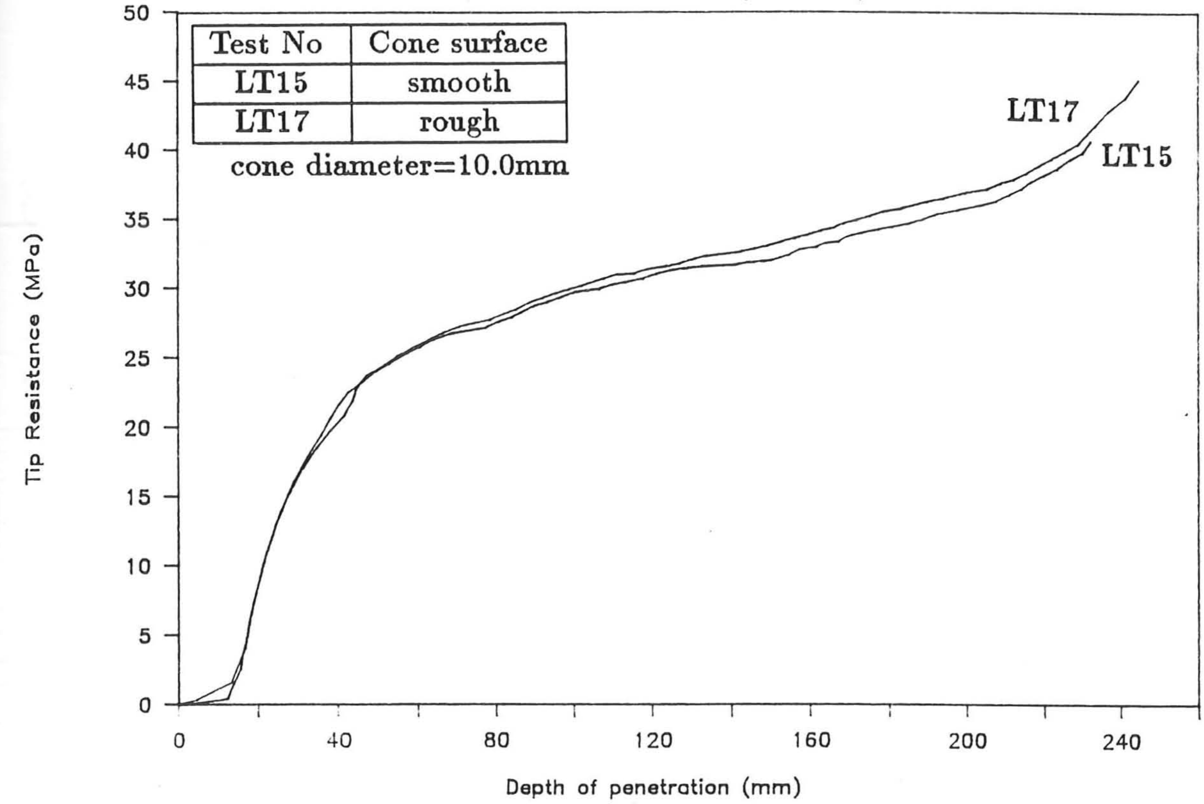

Fig 4.7 (c) 52/100 sand

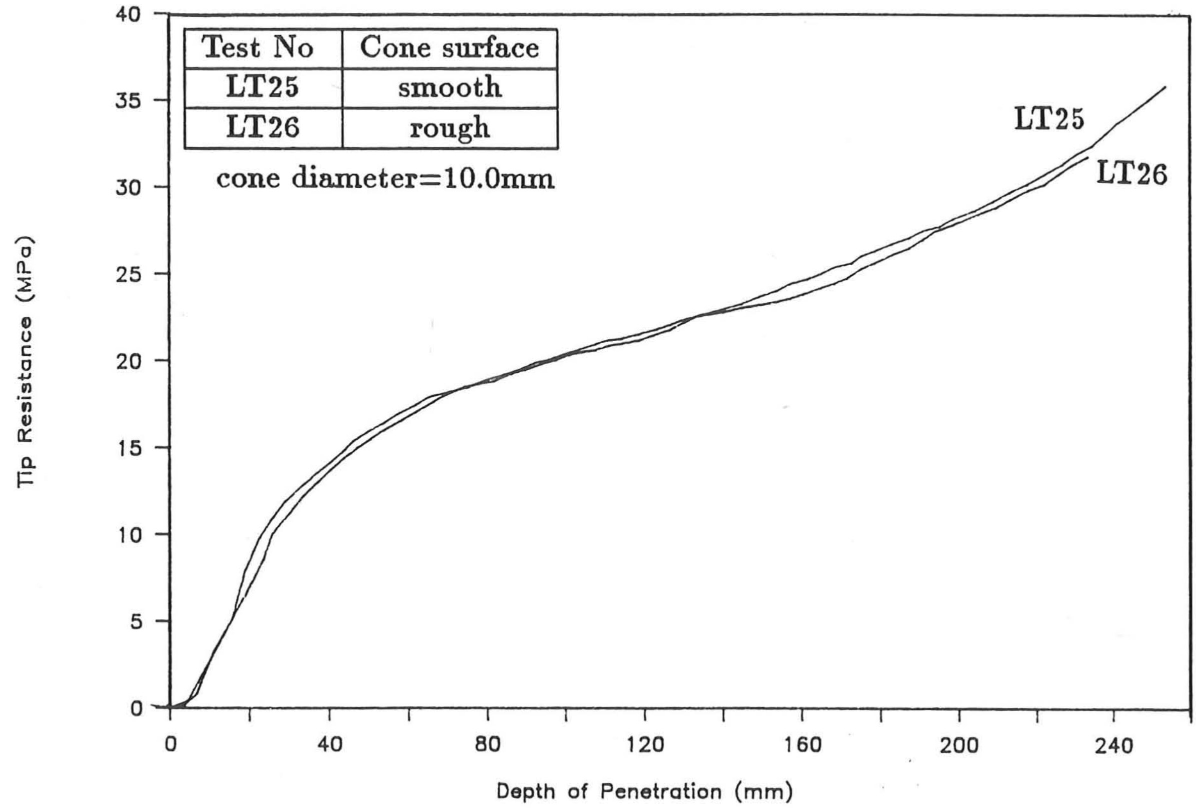

Fig 4.7 (d) Fontainbleau sand

Fig 4.7 Roughness effects on tip resistance.

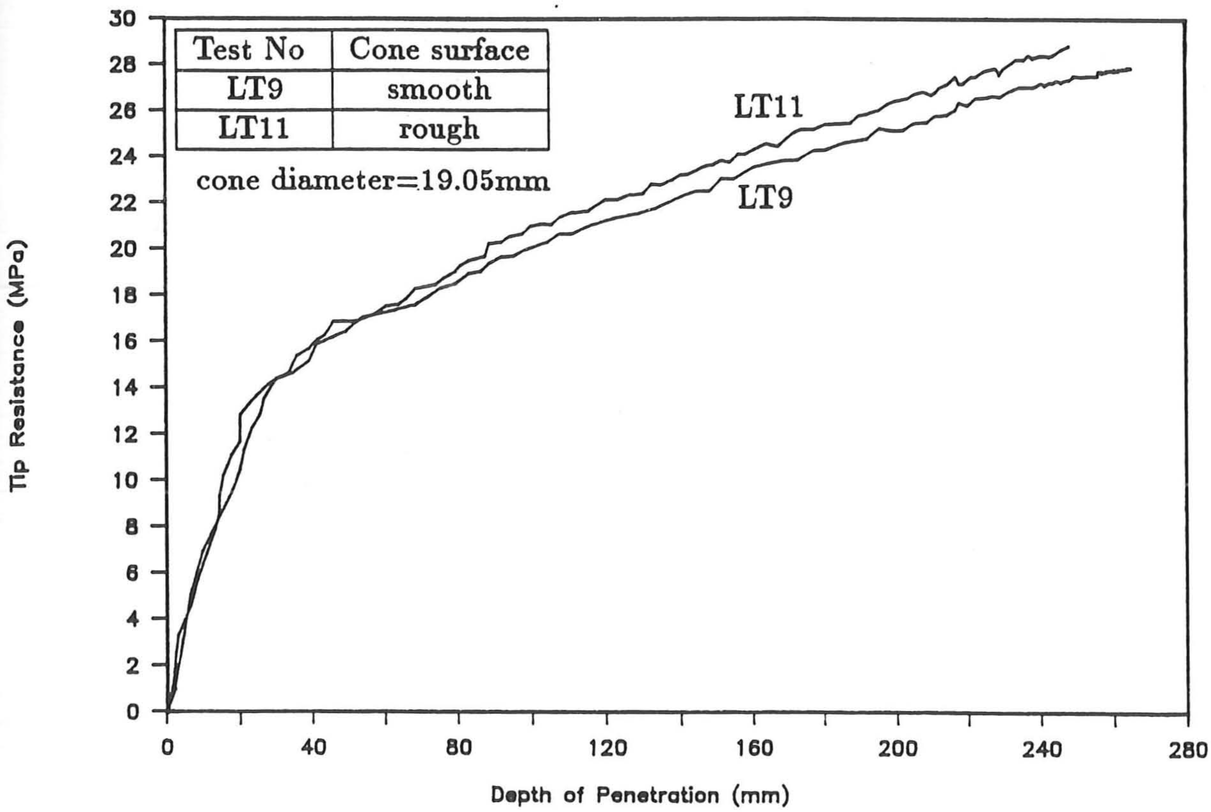

Fig 4.8(a) 14/25 sand

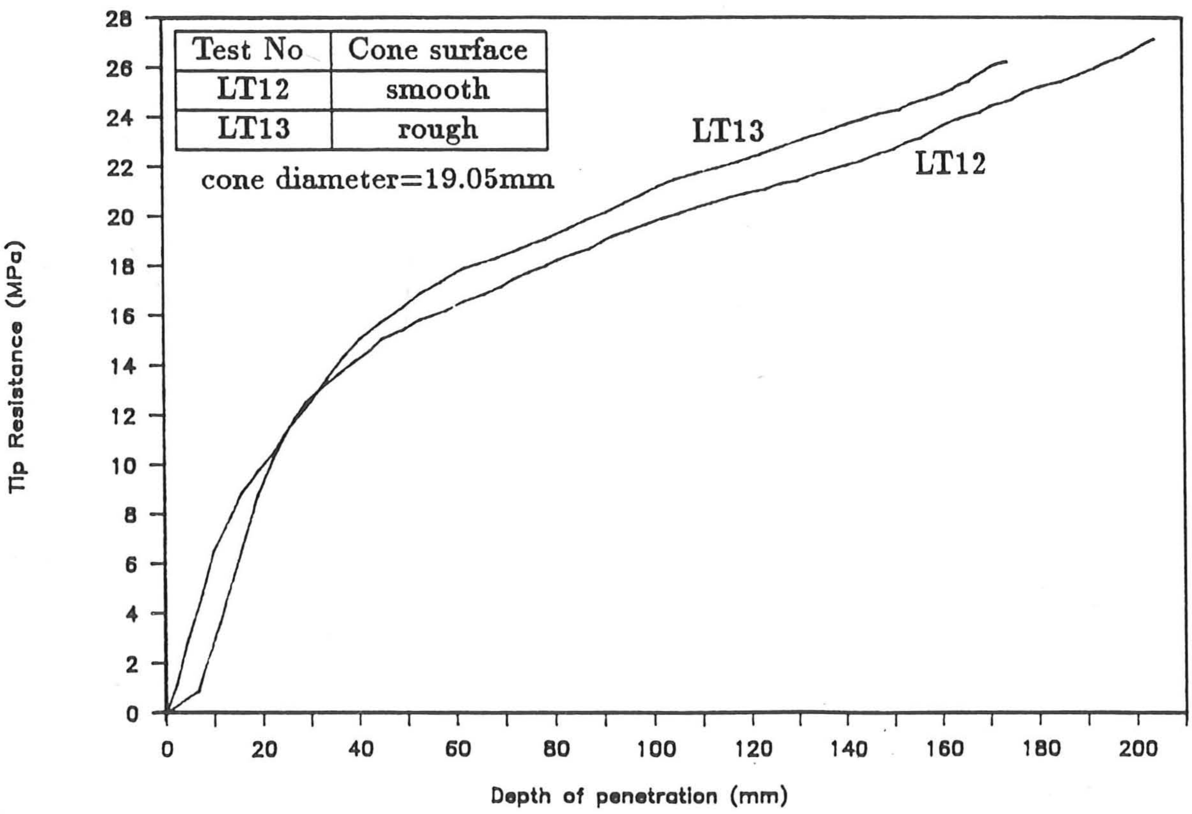

Fig 4.8 (b) 52/100 sand

Fig 4.8 Roughness effects on tip resistance.

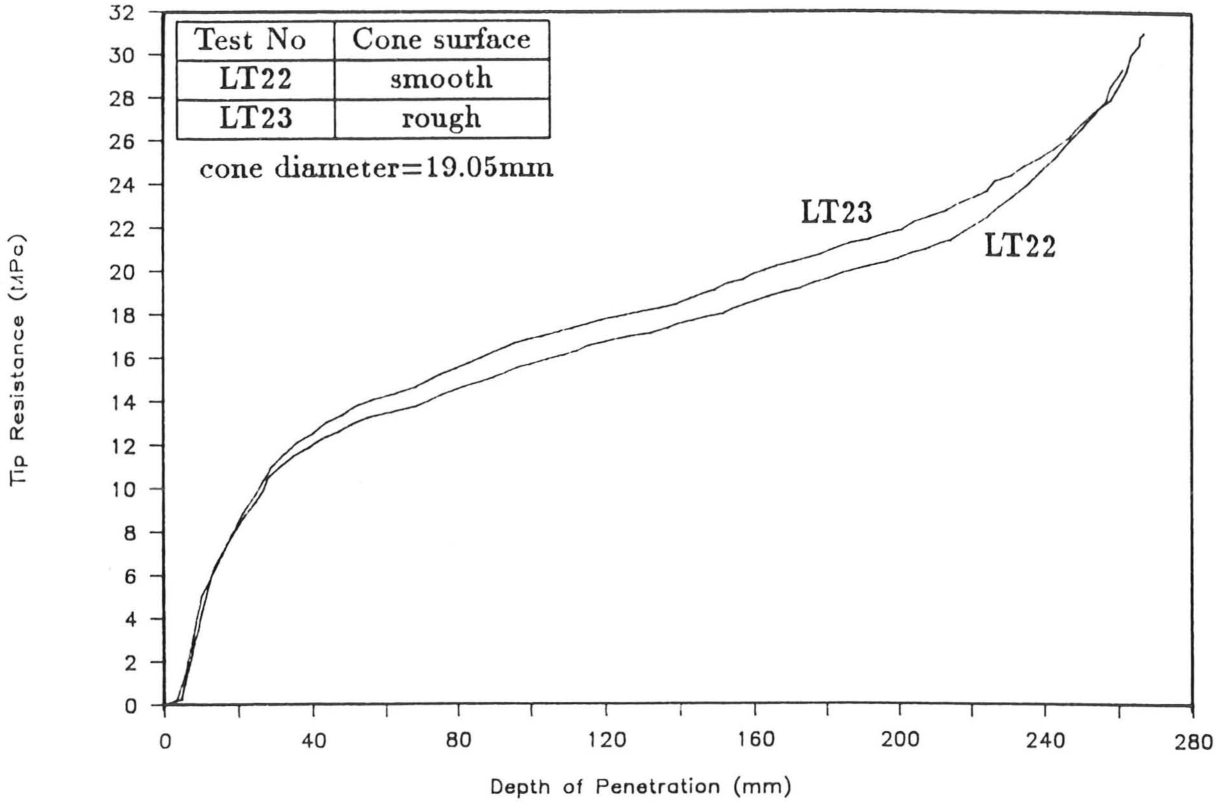

Fig 4.8 (c) Fontainbleau sand

Fig 4.8 Roughness effects on tip resistance.

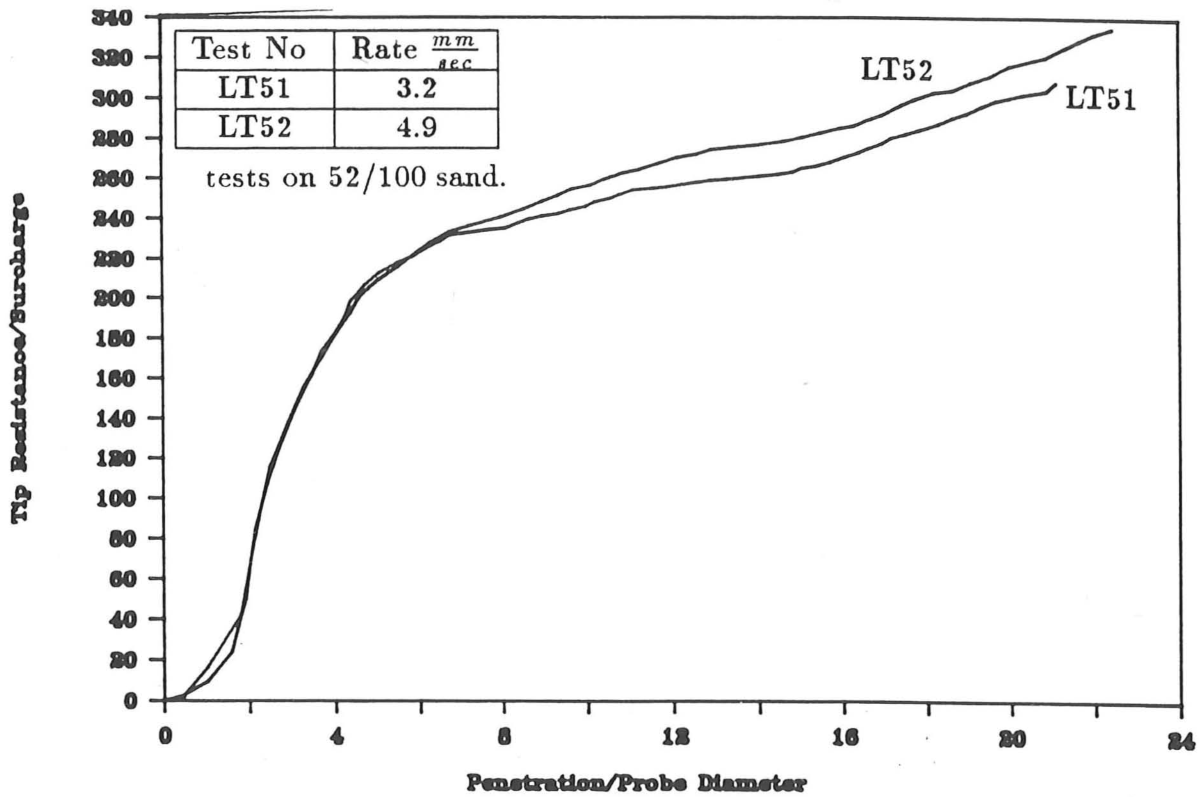

Fig 4.9 Penetration rate effects on tip resistance.
cone diameter=10.0mm

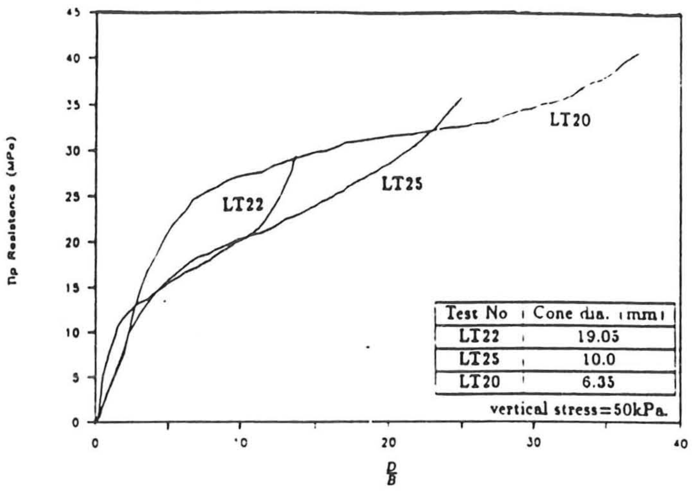

(a) Fontainbleau sand

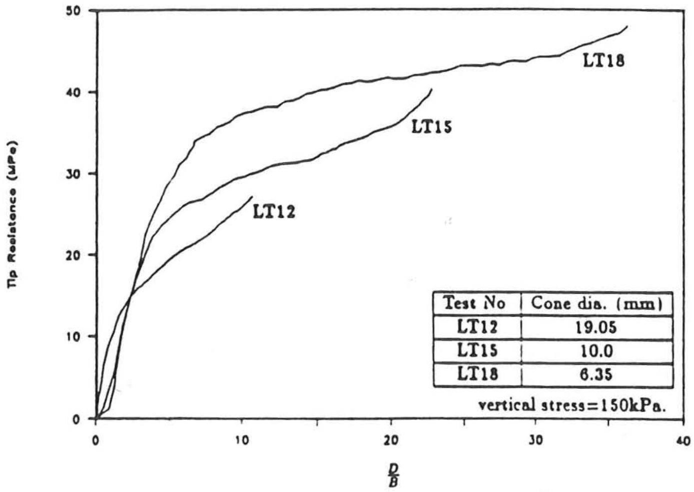

(b) 52/100 sand

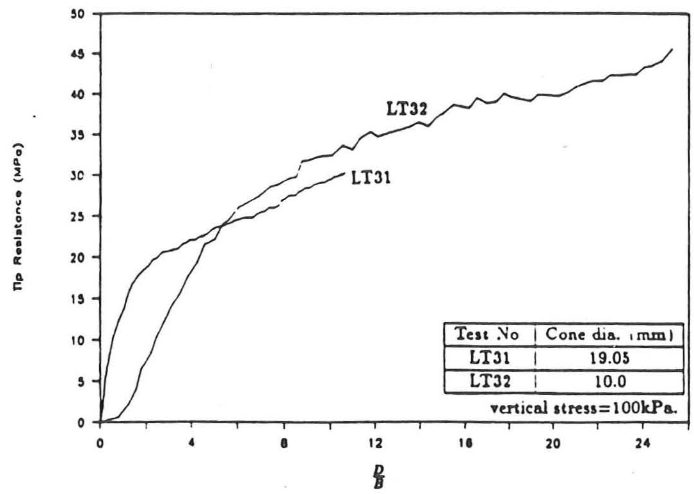

(c) 14/25 sand

Fig 4.10 Scale effects on tip resistance.

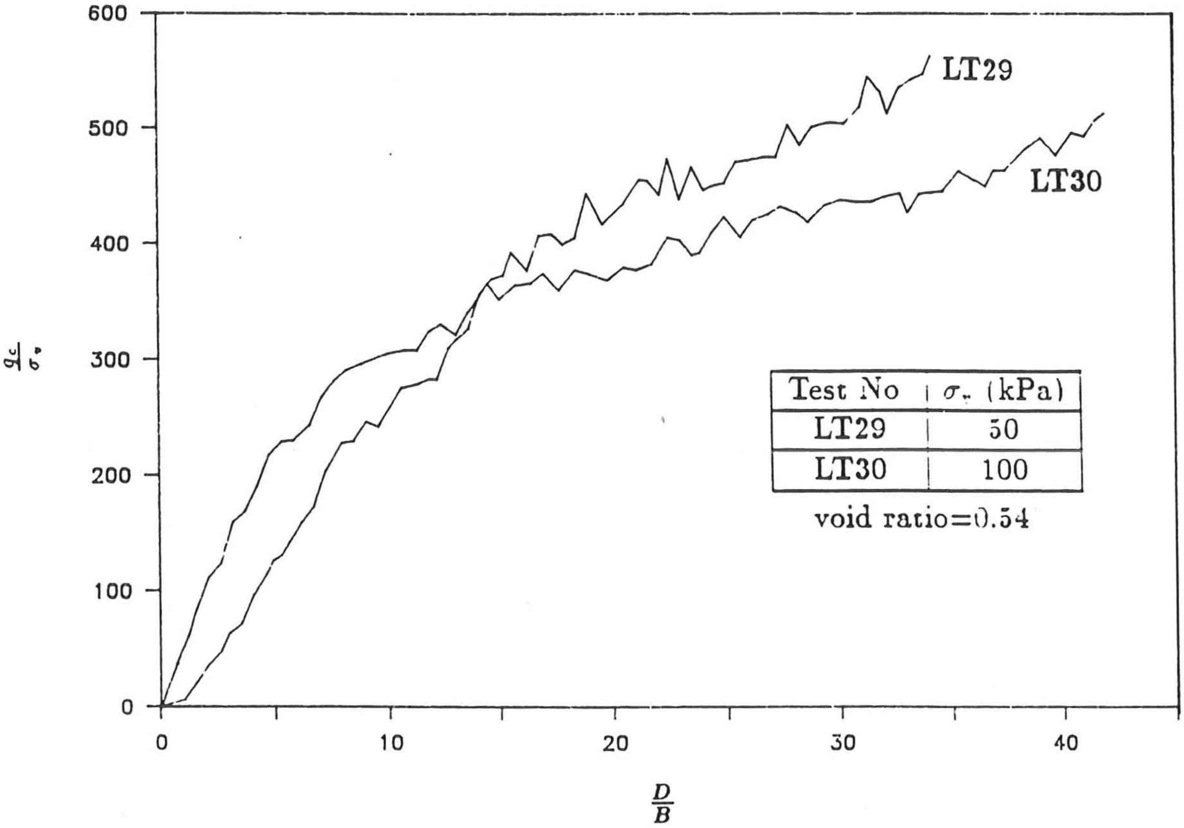

(a)

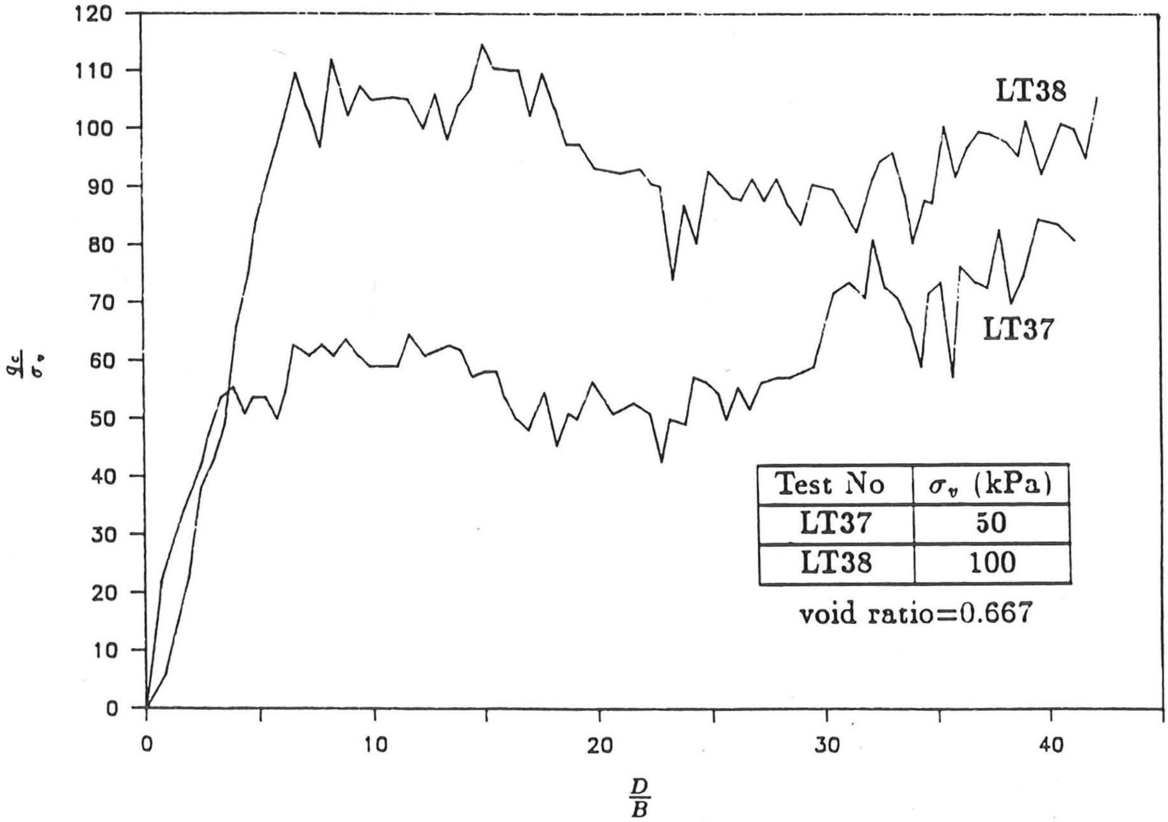

(b)

Fig 4.11 Stress level effects on tip resistance.
cone diameter=6.35mm

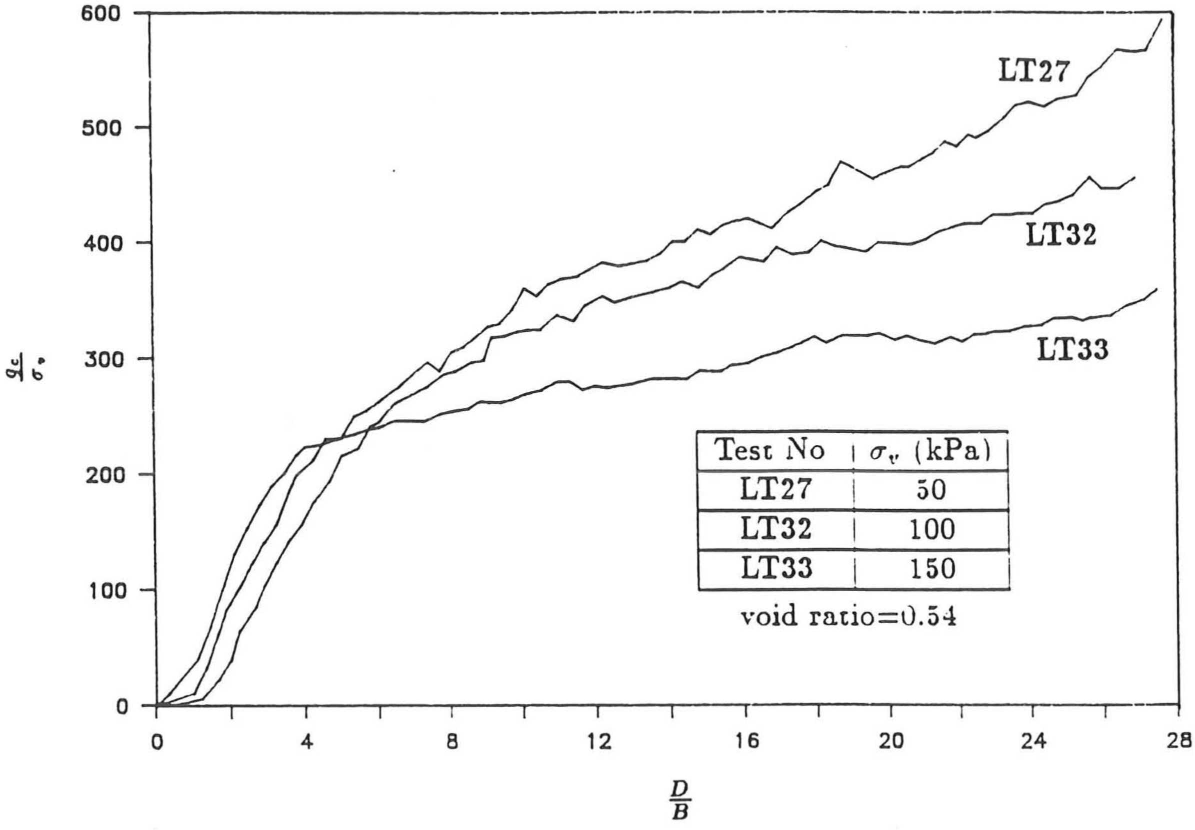

(a)

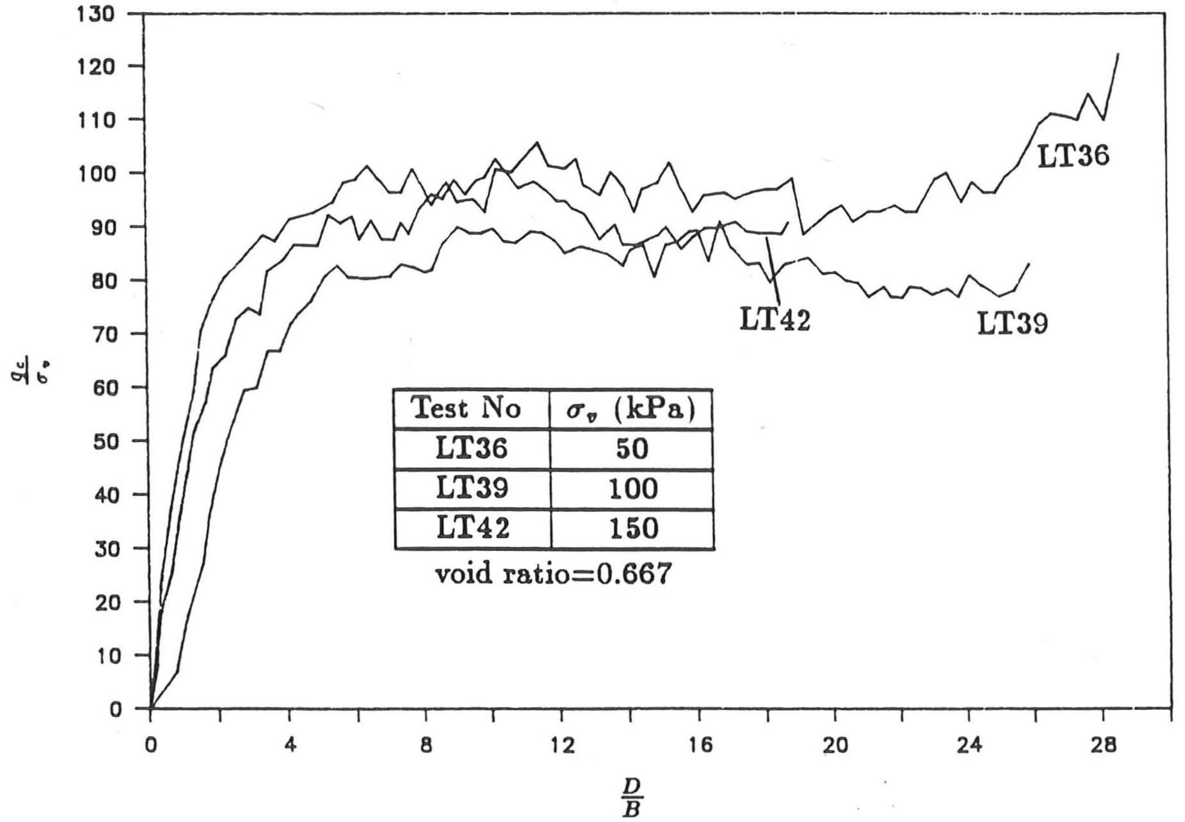

(b)

Fig 4.12 Stress level effects on tip resistance.
cone diameter=10.0mm

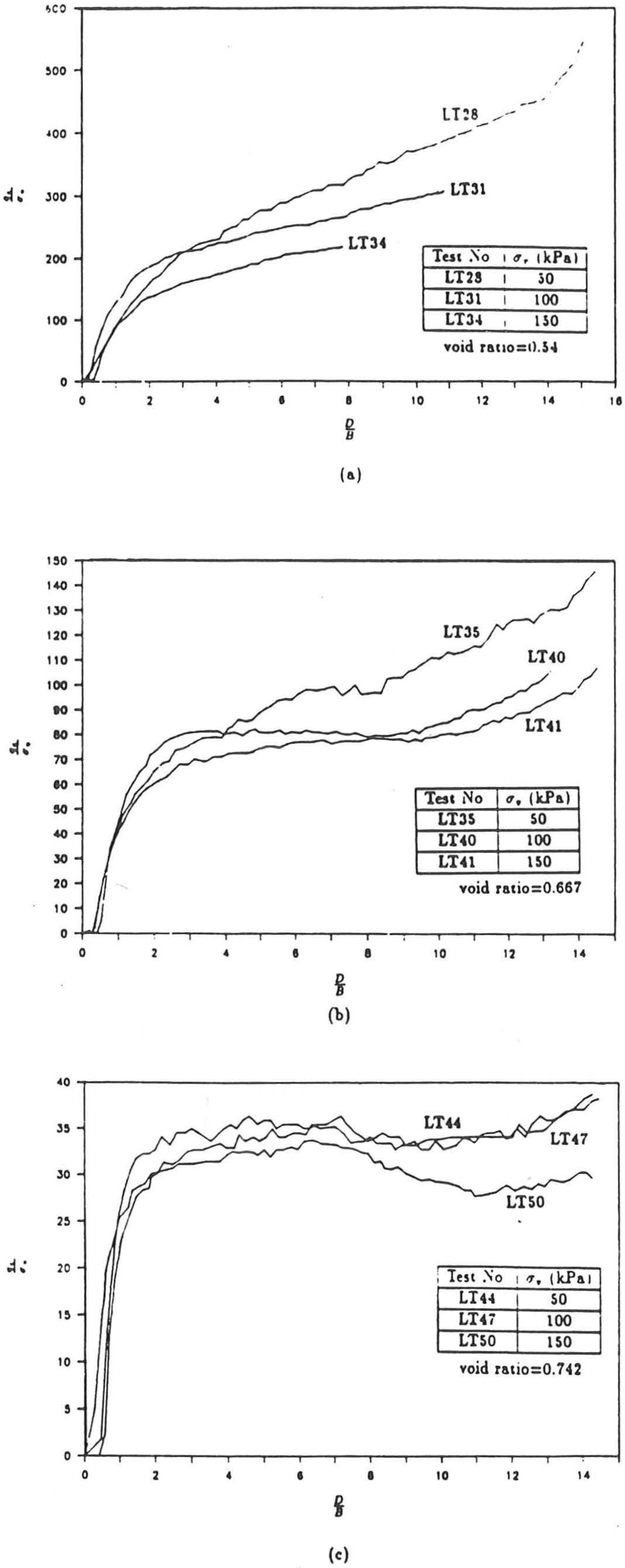

Fig 4.13 Stress level effects on tip resistance.
cone diameter=19.05mm

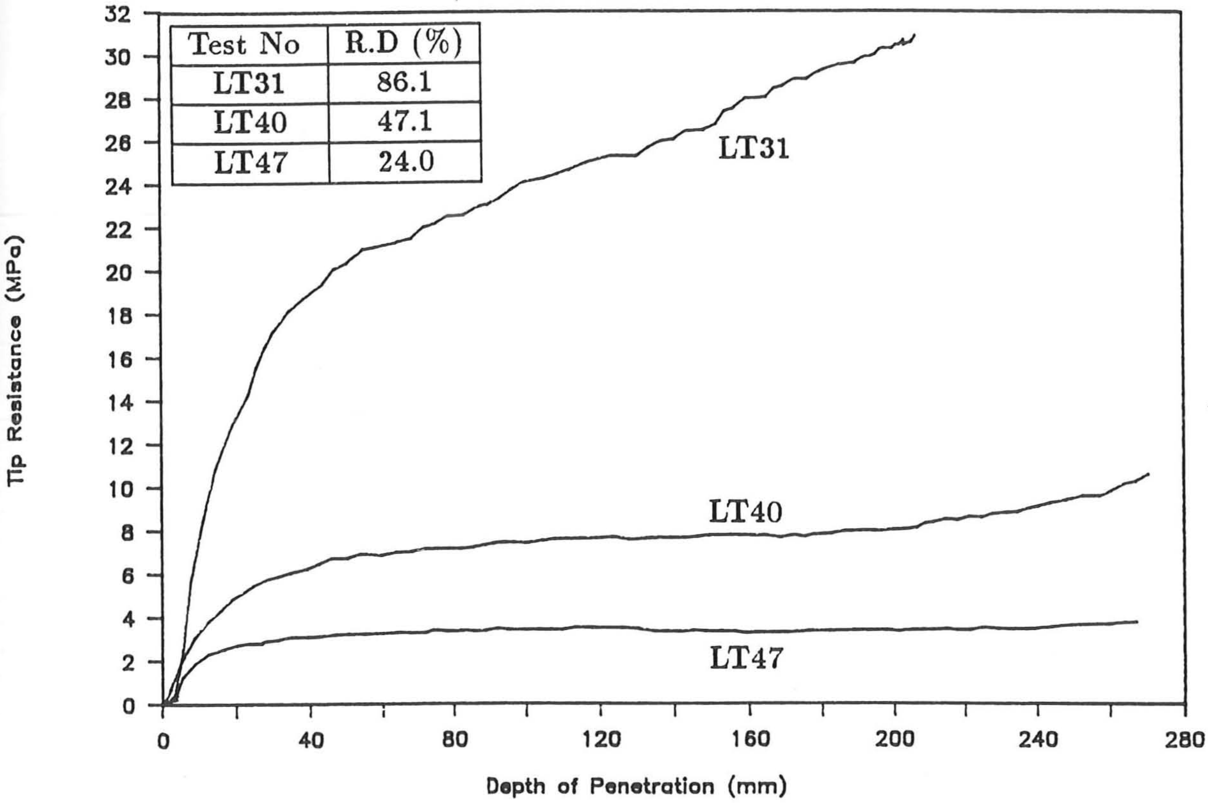

(a) vertical stress=100kPa

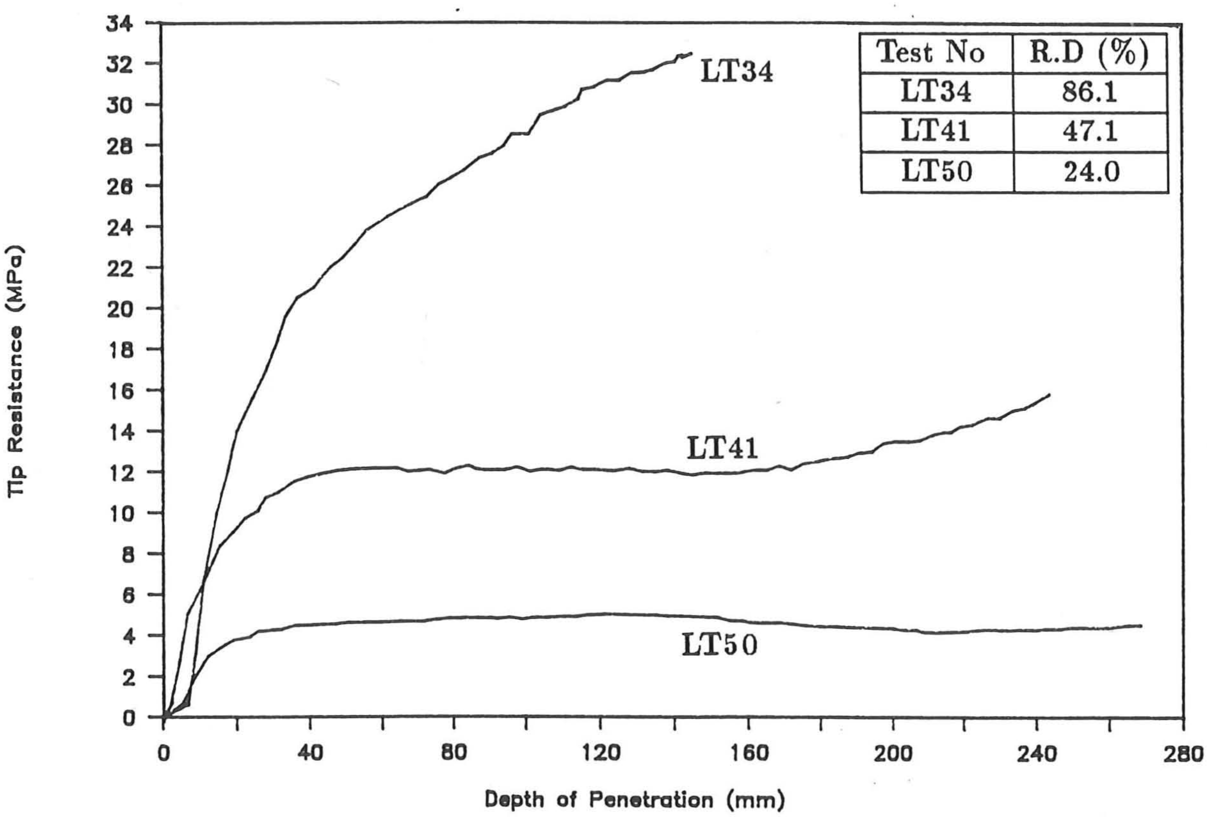

(b) vertical stress=150kPa

Fig 4.14 Relative density effects on tip resistance.
cone diameter=19.5mm

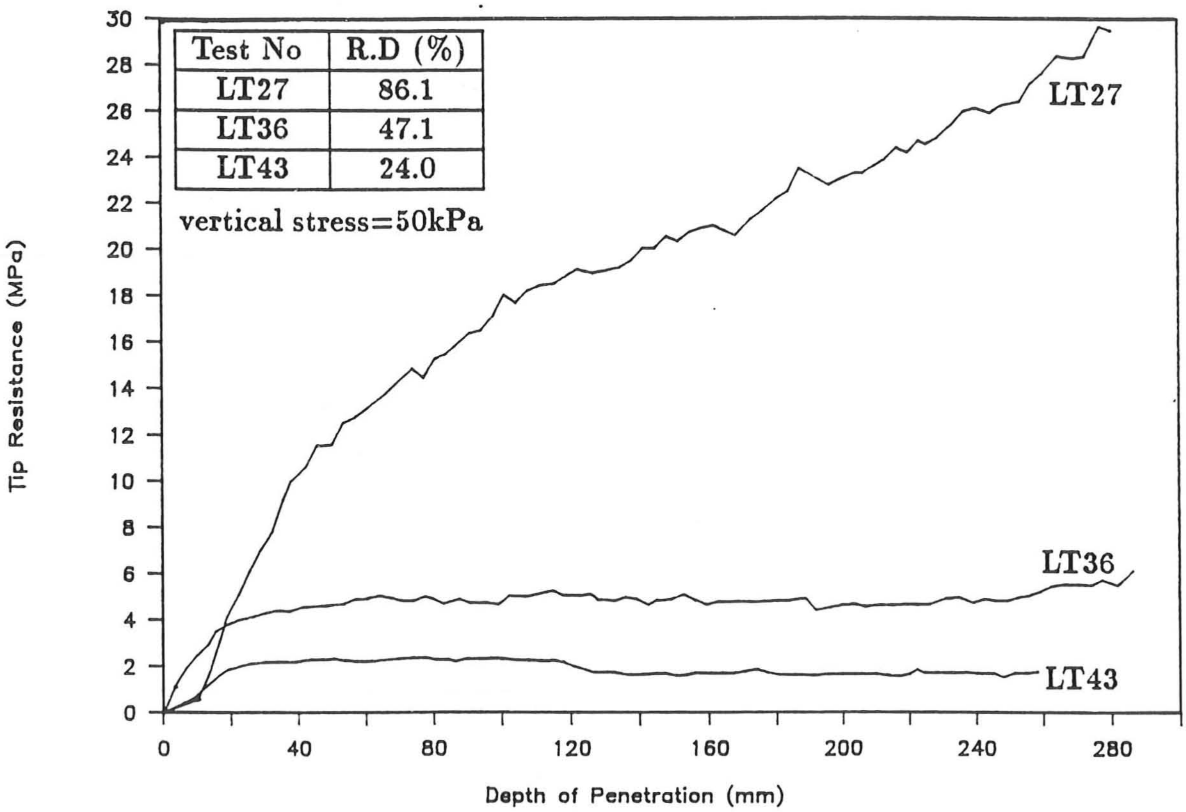

Fig 4.15(a)

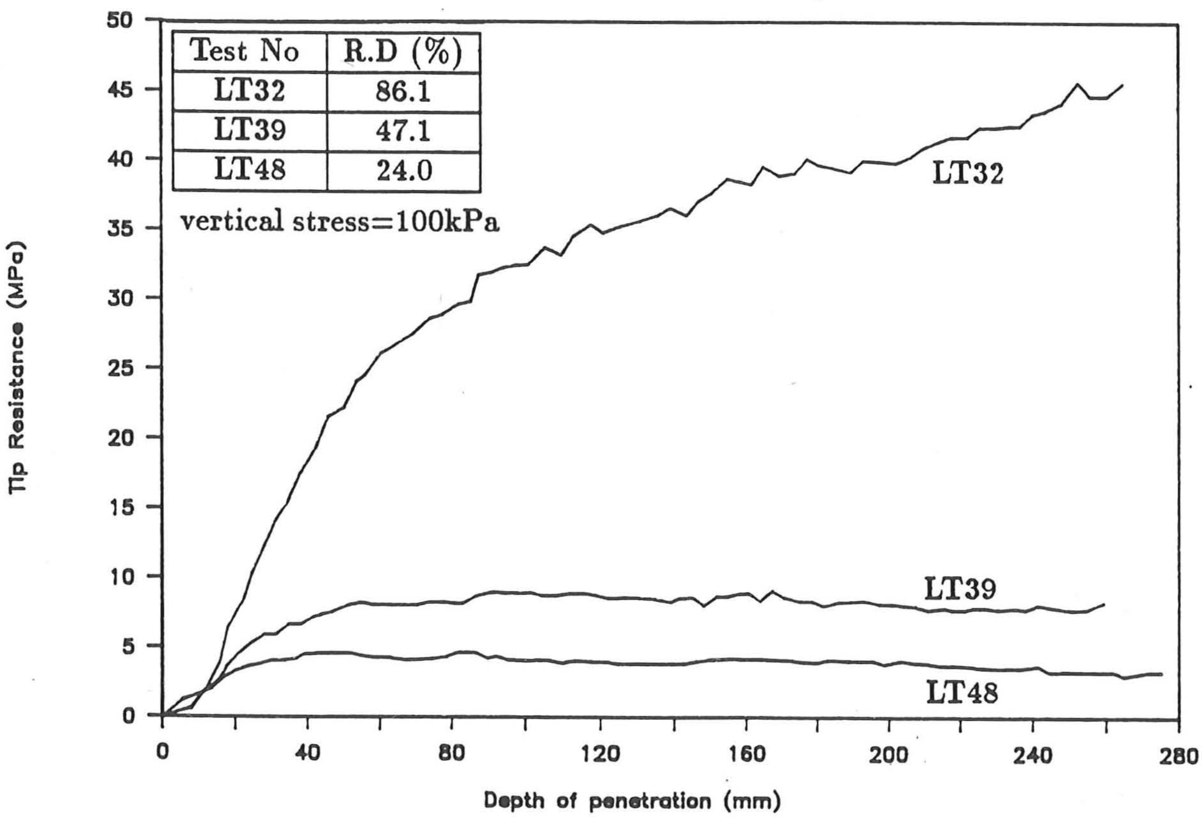

Fig 4.15(b)

Fig 4.15 Relative density effects on tip resistance.
cone diameter=10.0mm

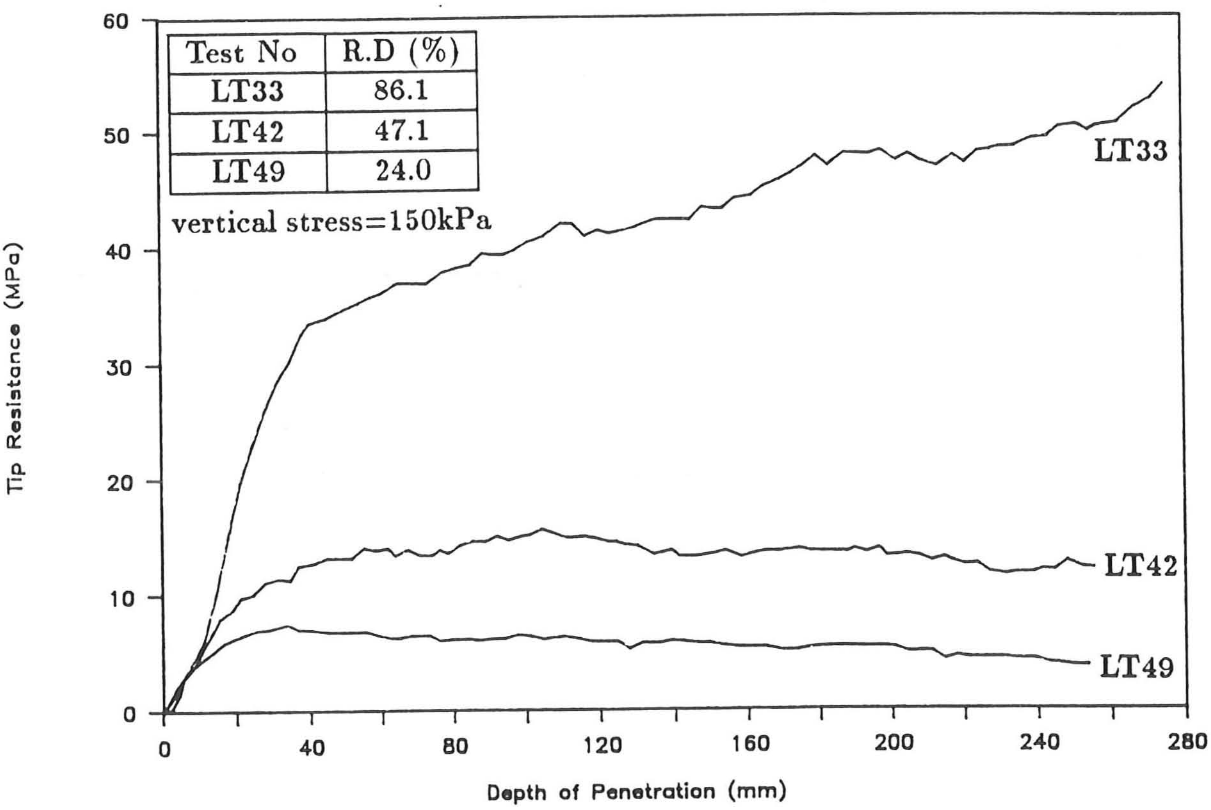

Fig 4.15(c)

Fig 4.15 Relative density effects on tip resistance.
cone diameter=10.0mm

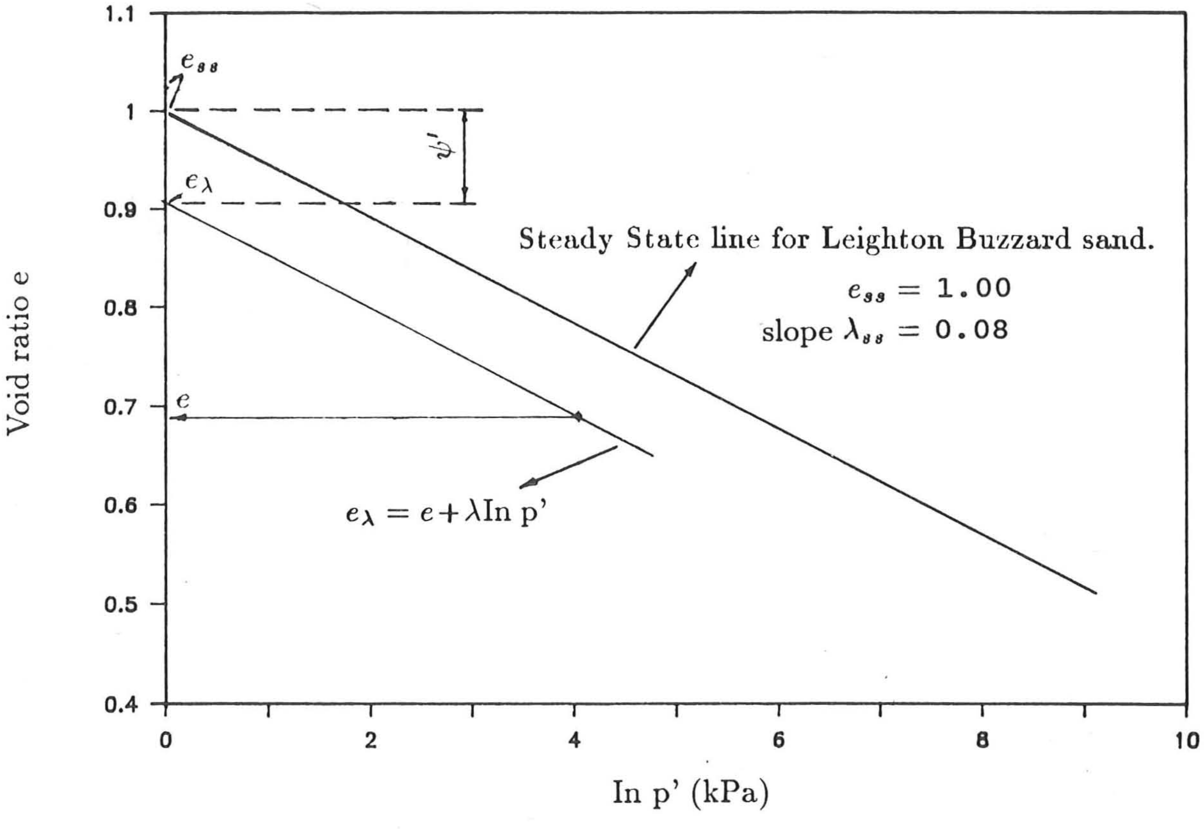

Fig 4.16 State parameter $\psi' = e_\lambda - e_{ss}$

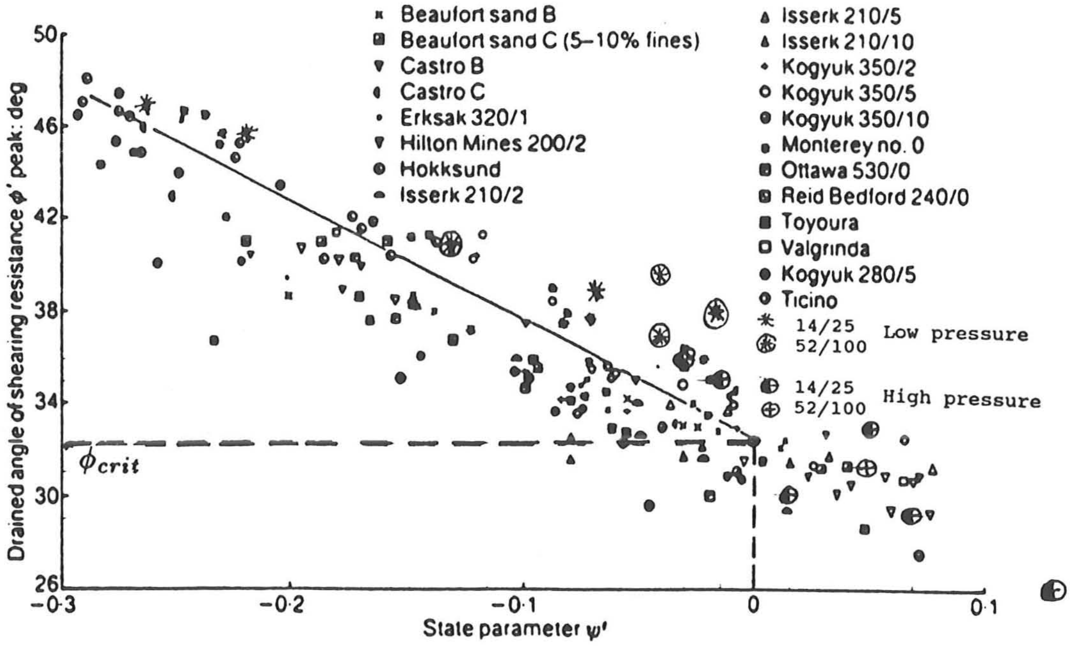

Fig 4.17 Drained mobilised angle of shearing resistance ϕ_p' and state parameter ψ' relationship. (after Been and Jefferies, 1987)

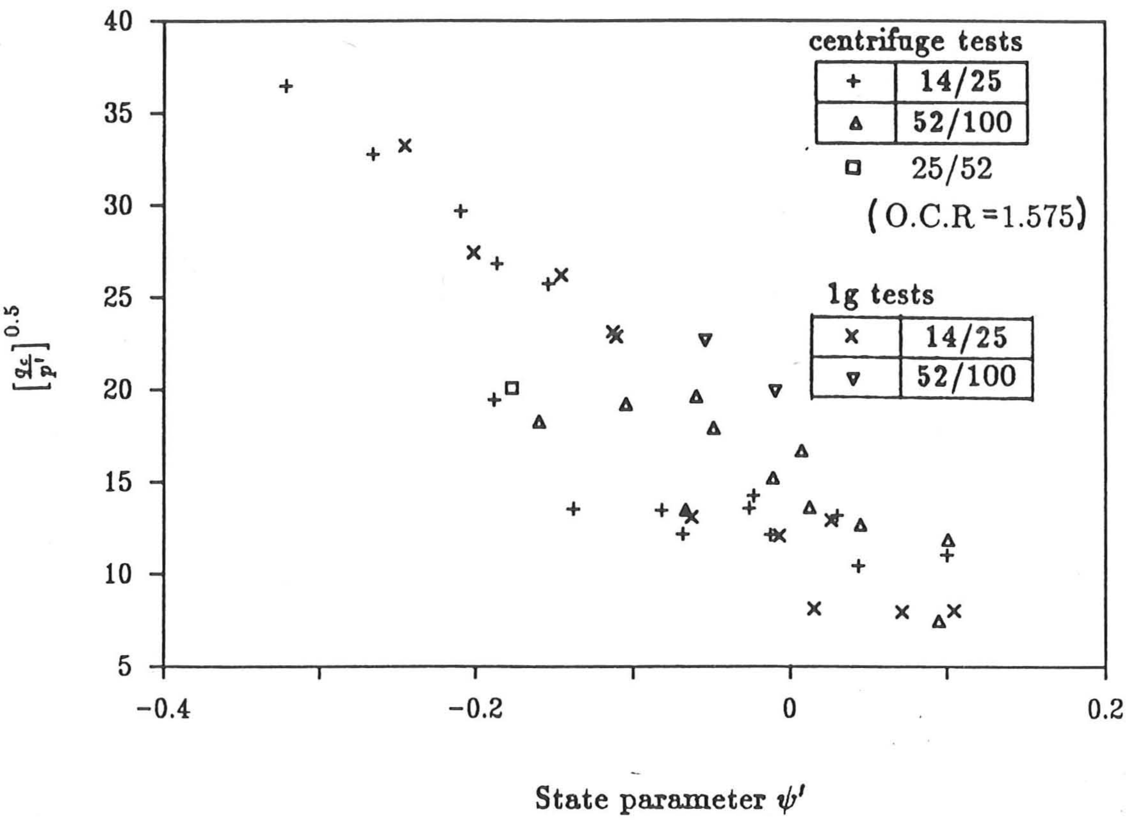

Fig 4.18 Normalised tip resistance q_c with mean normal effective stress p' and state parameter ψ' relationship for Leighton Buzzard sand.

(a) Meyerhof

(b) Terzaghi

Fig 5.1 Different failure mechanism assumptions for deep penetration.

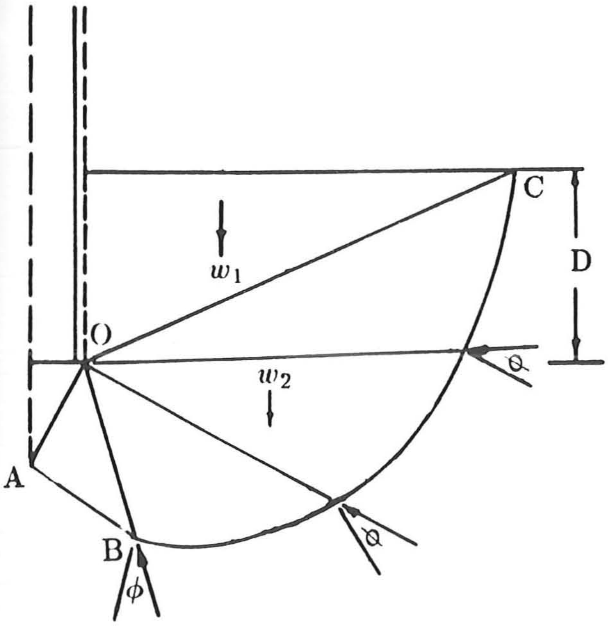

(a) shallow penetration

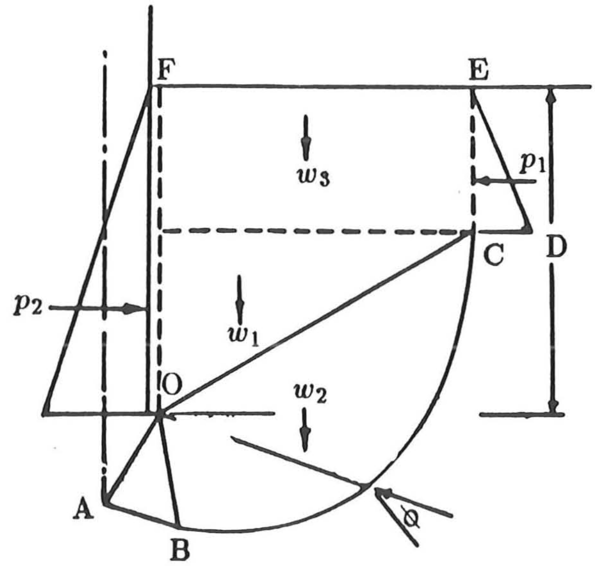

(b) deep penetration

Fig 5.2 The assumed failure mechanism.
(after Durgunoglu and Mitchell, 1975)

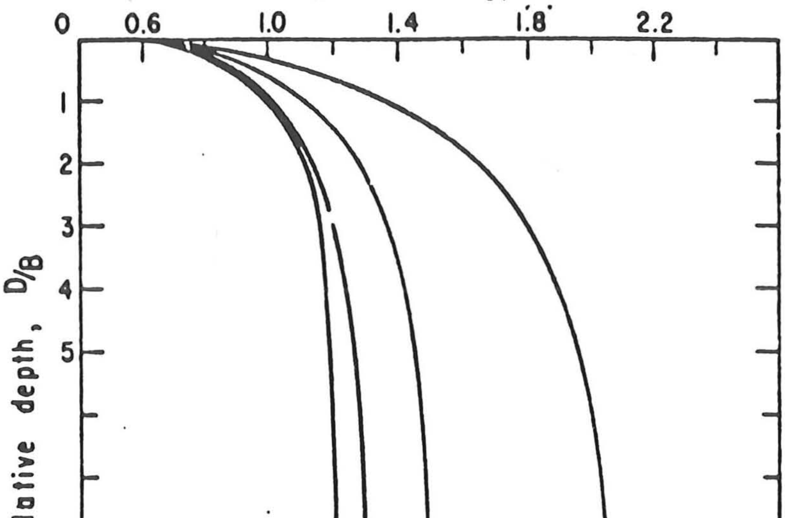

Fig 5.3 Relationship between shape factors $s_{q\gamma}$
relative depth $\frac{D}{B}$ and ϕ.

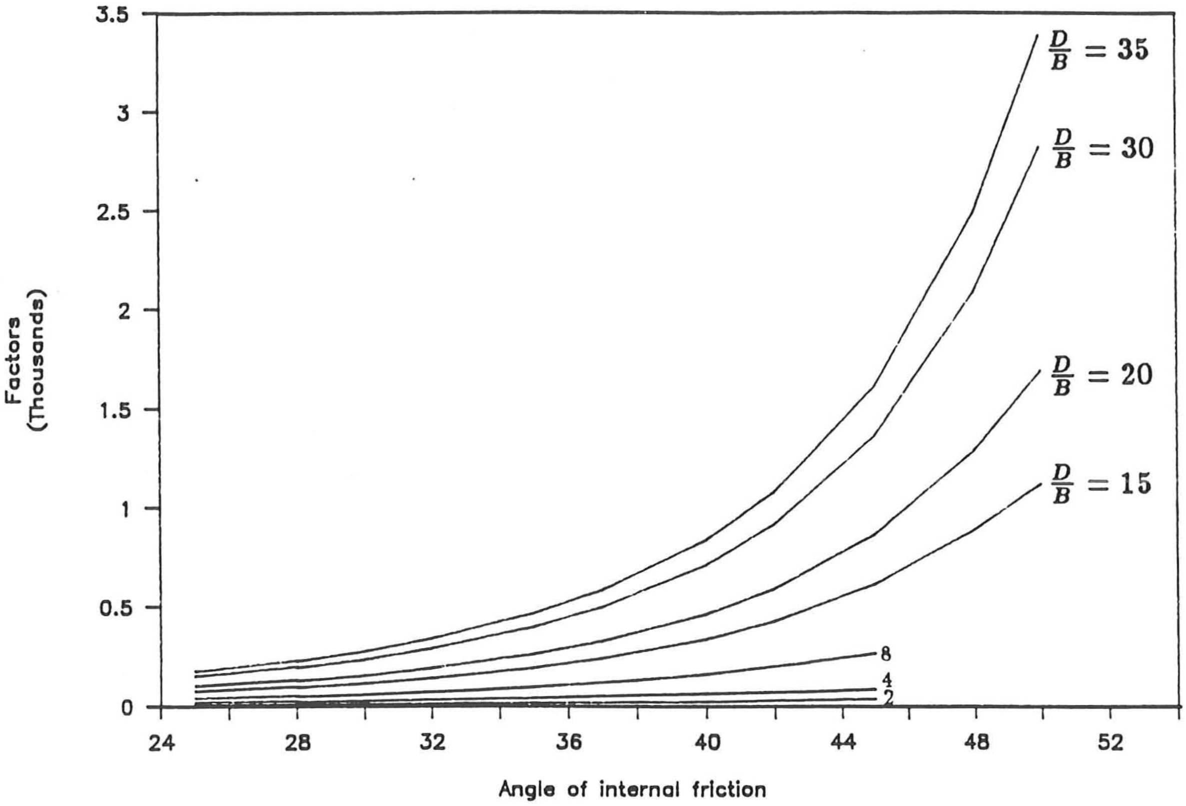

Fig 5.4 (a) perfectly smooth $\frac{\delta}{\phi} = 0$

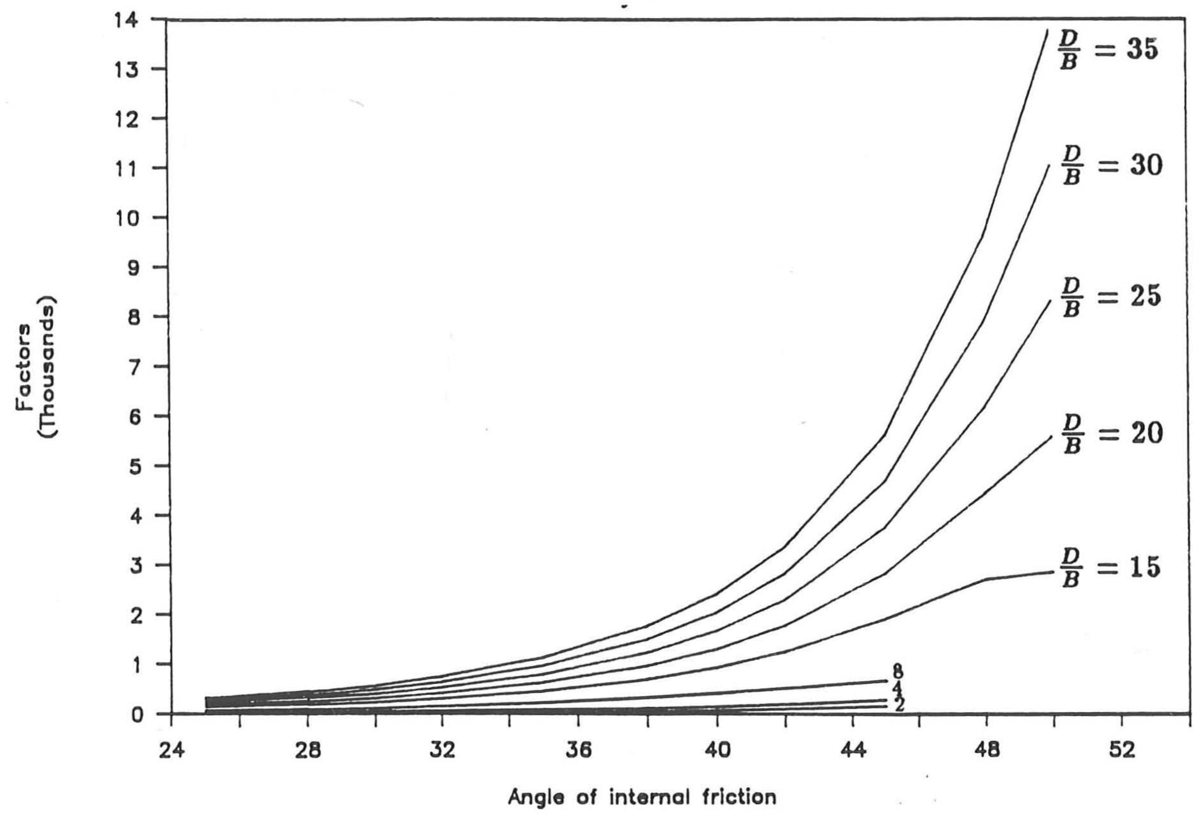

Fig 5.4 (b) partially rough $\frac{\delta}{\phi} = 0.5$

Fig 5.4 Relationship between bearing capacity factors $N_{q\gamma}$, realtive density $\frac{D}{B}$ and ϕ

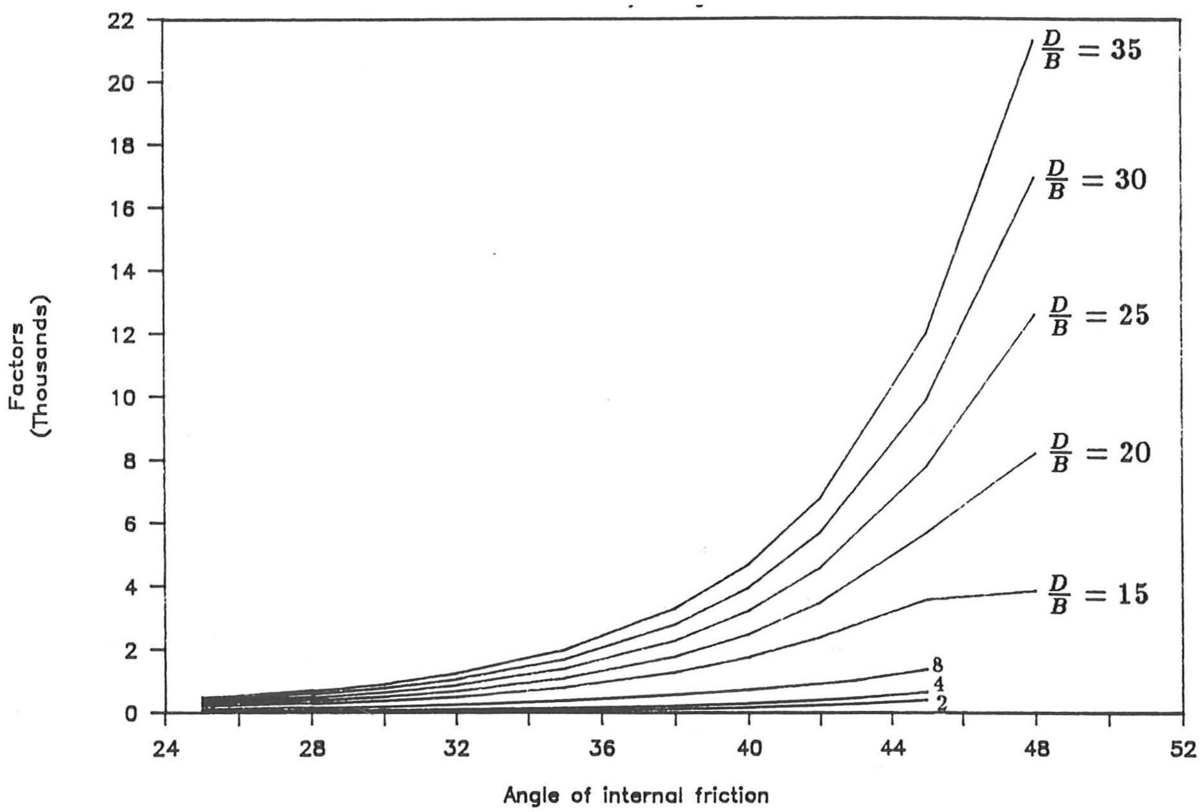

Fig 5.4(c) perfectly rough $\frac{\delta}{\phi} = 1.0$

Fig 5.4 Relationship between bearing capacity factors $N_{q\gamma}$, relative density $\frac{D}{B}$ and ϕ

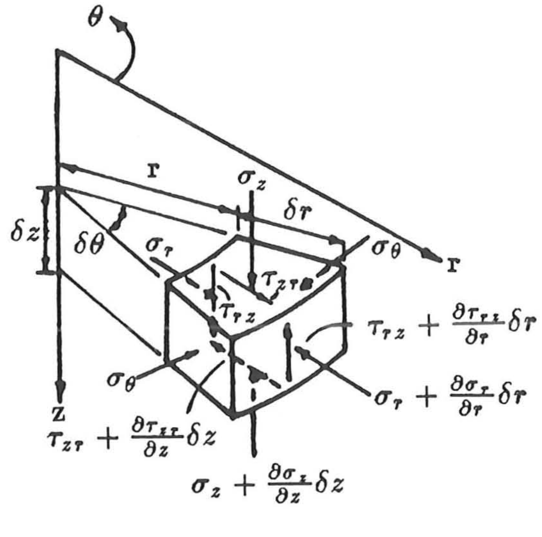

Fig 5.5 Stress components acting on an element.

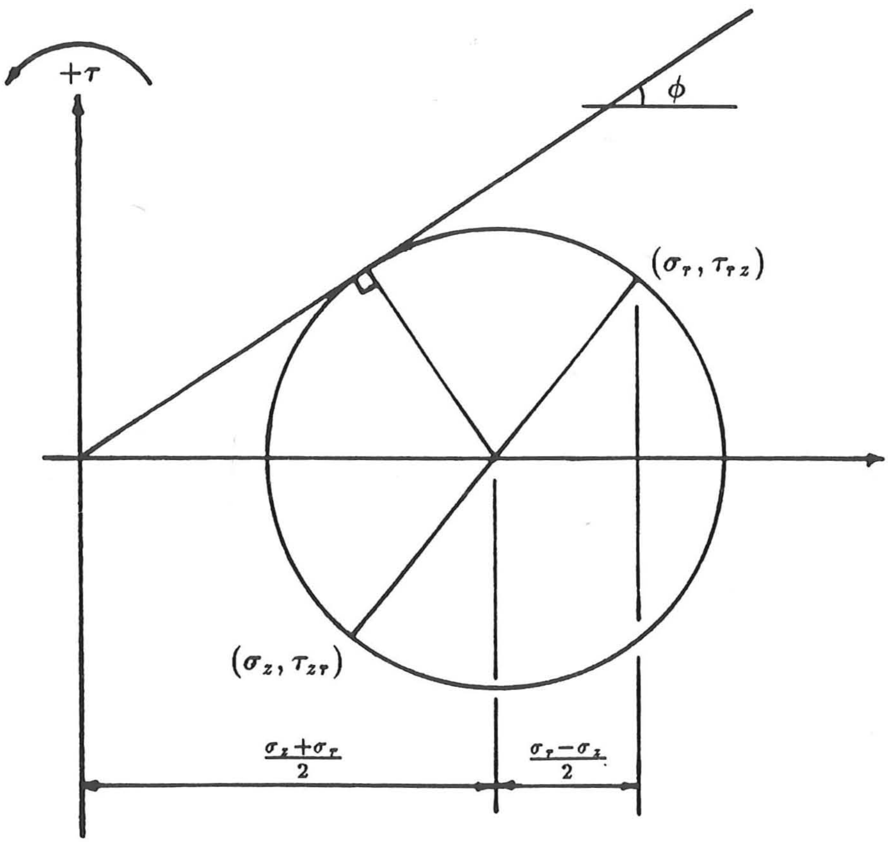

Fig 5.6 Mohr-coulomb failure criterion.

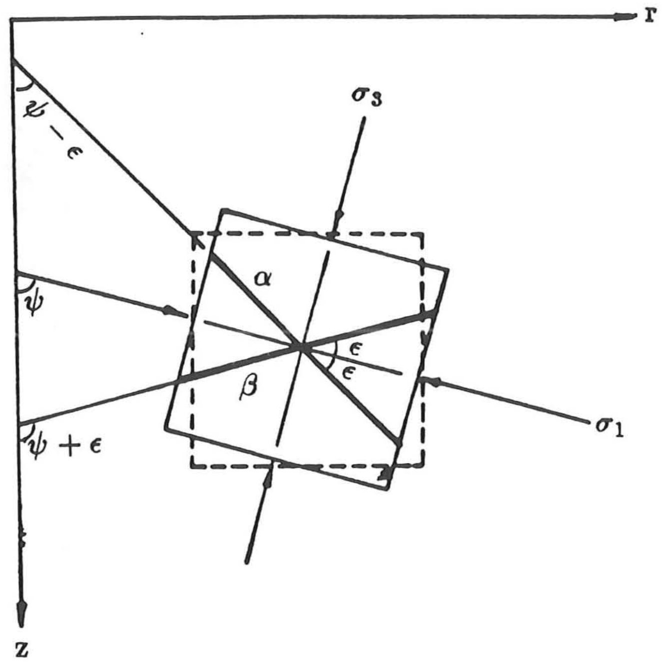

Fig 5.7 Sign convention.

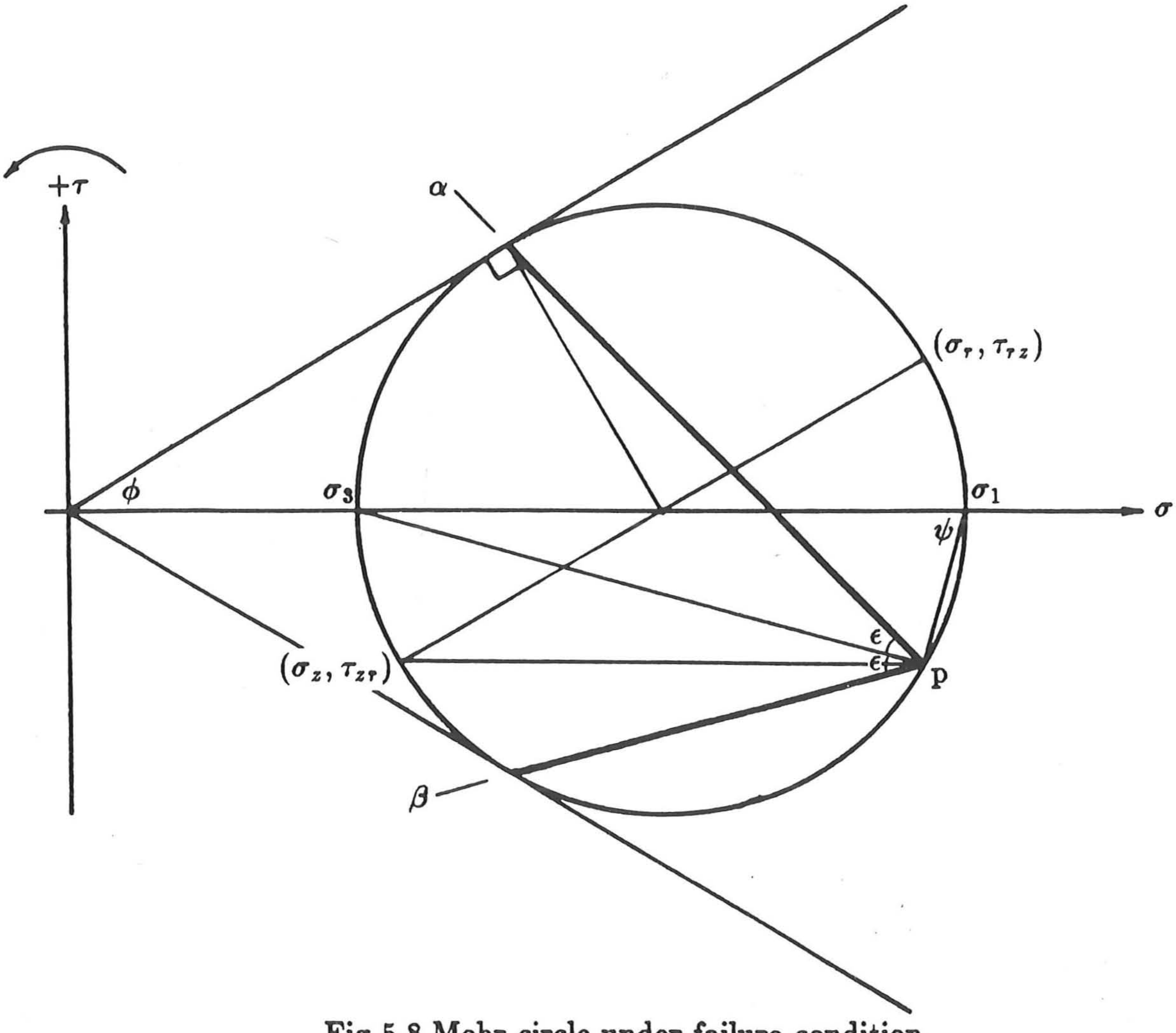

Fig 5.8 Mohr circle under failure condition.

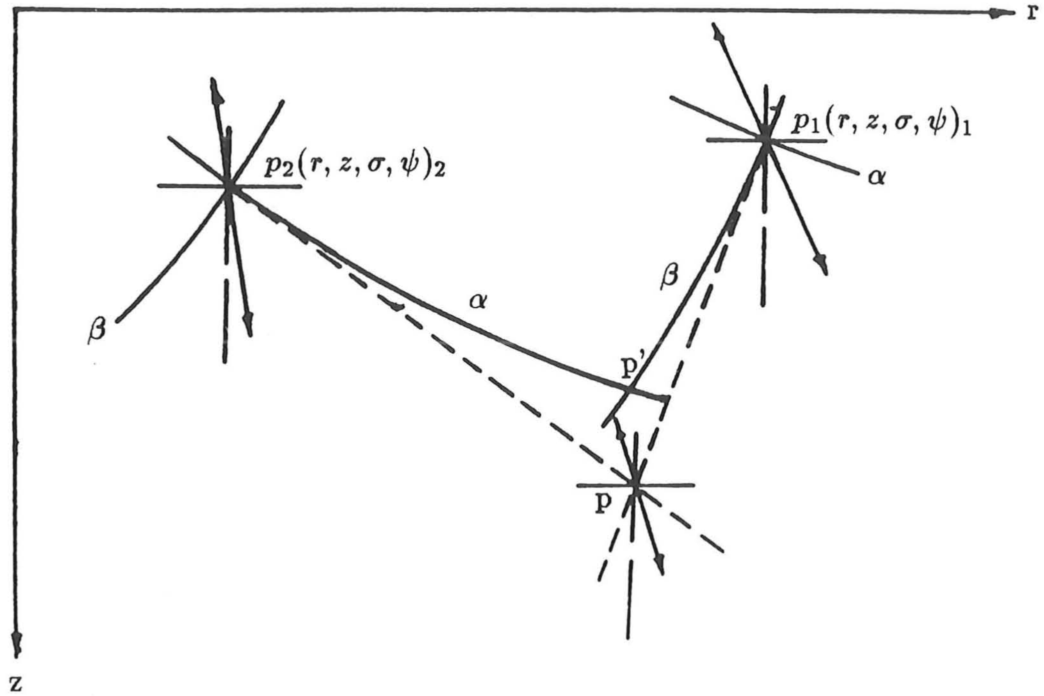

Fig 5.9 To solve an unknown point p.

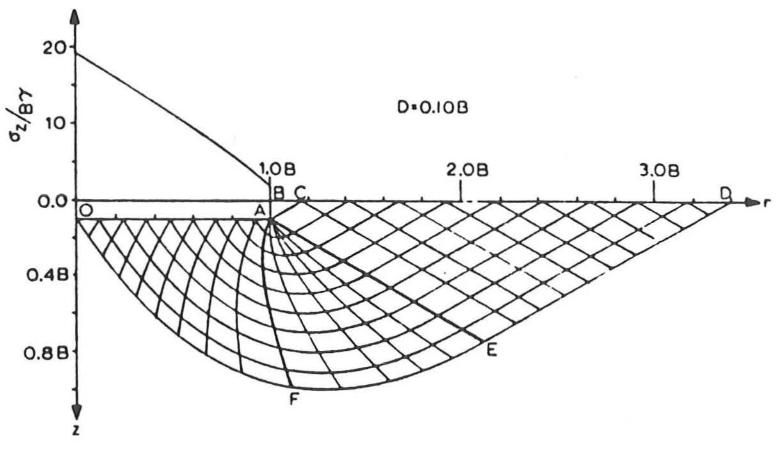

Fig 5.10 Stress characteristics with penetration effects
(after Larkin, 1968)

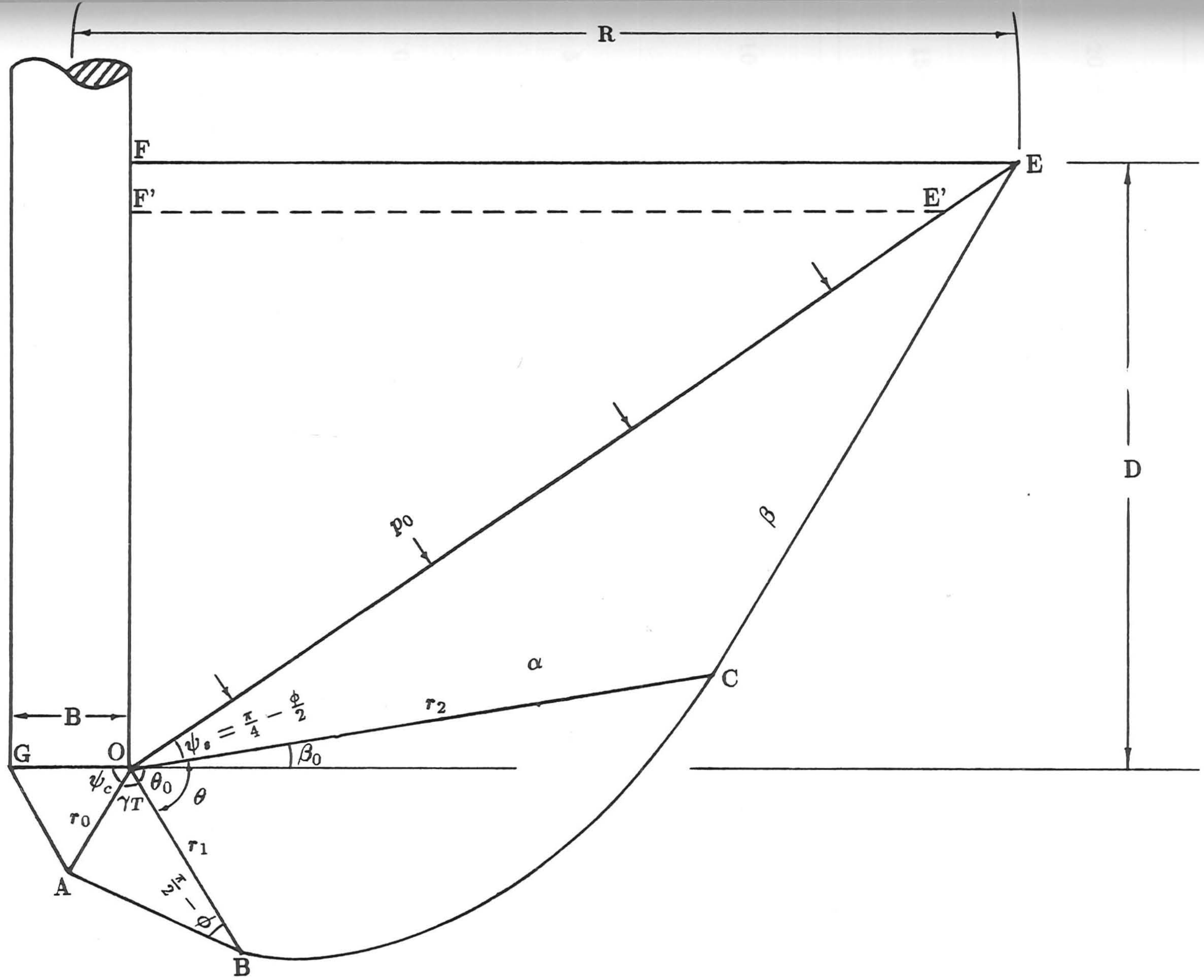

Fig 5.11 The assume failure mechanism due to penetration effect.

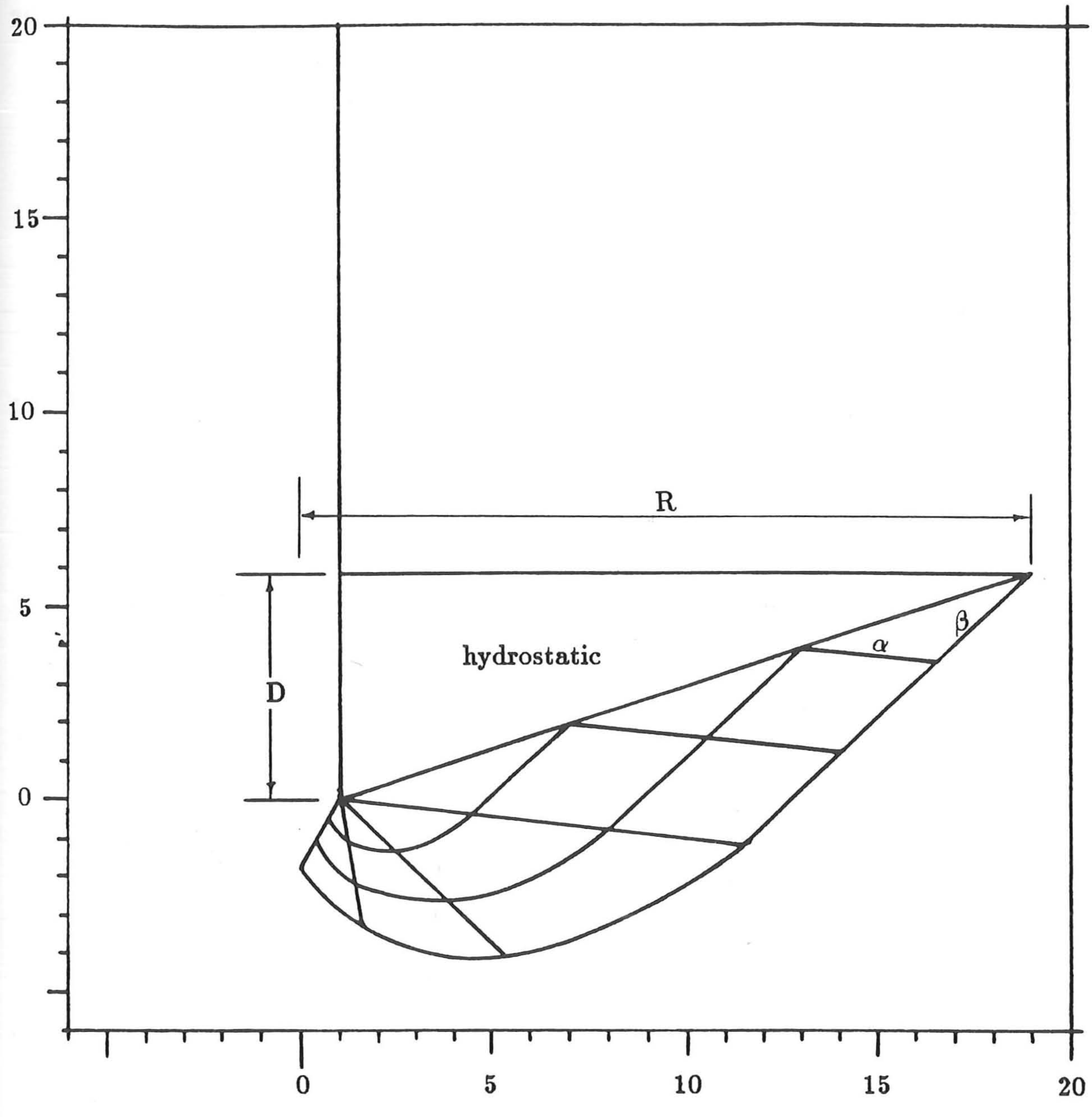

Fig 5.12(a) $\phi = 40°$, $\frac{D}{B} = 3$, $\frac{\delta}{\phi} = 1.0$

Fig 5.12 Stress characteristics net with penetration effect.

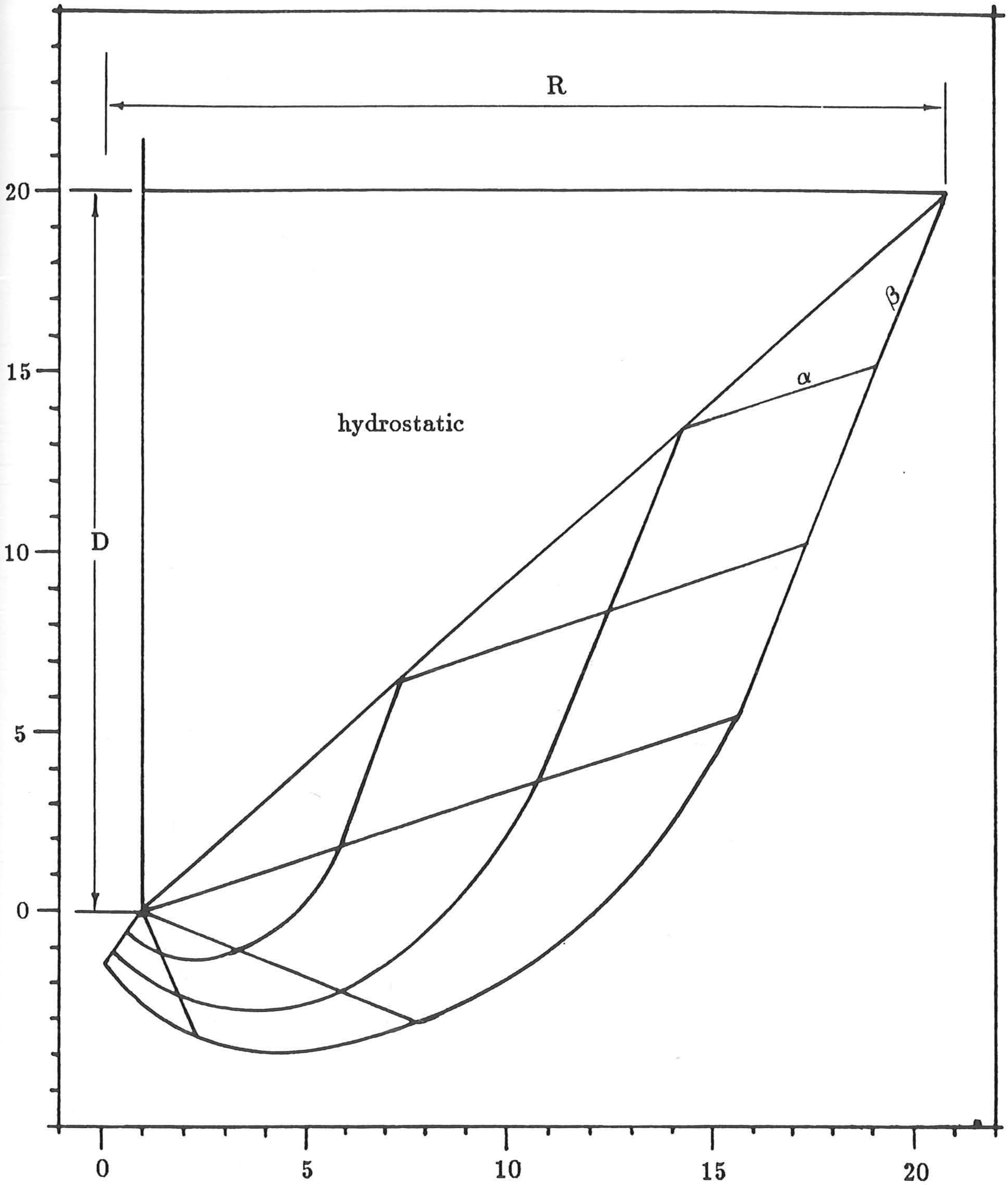

Fig 5.12 (b) $\phi = 40°$, $\frac{D}{B} = 10$, $\frac{\delta}{\phi} = 1.0$

Fig 5.12 Stress characteristics net with penetration effect.

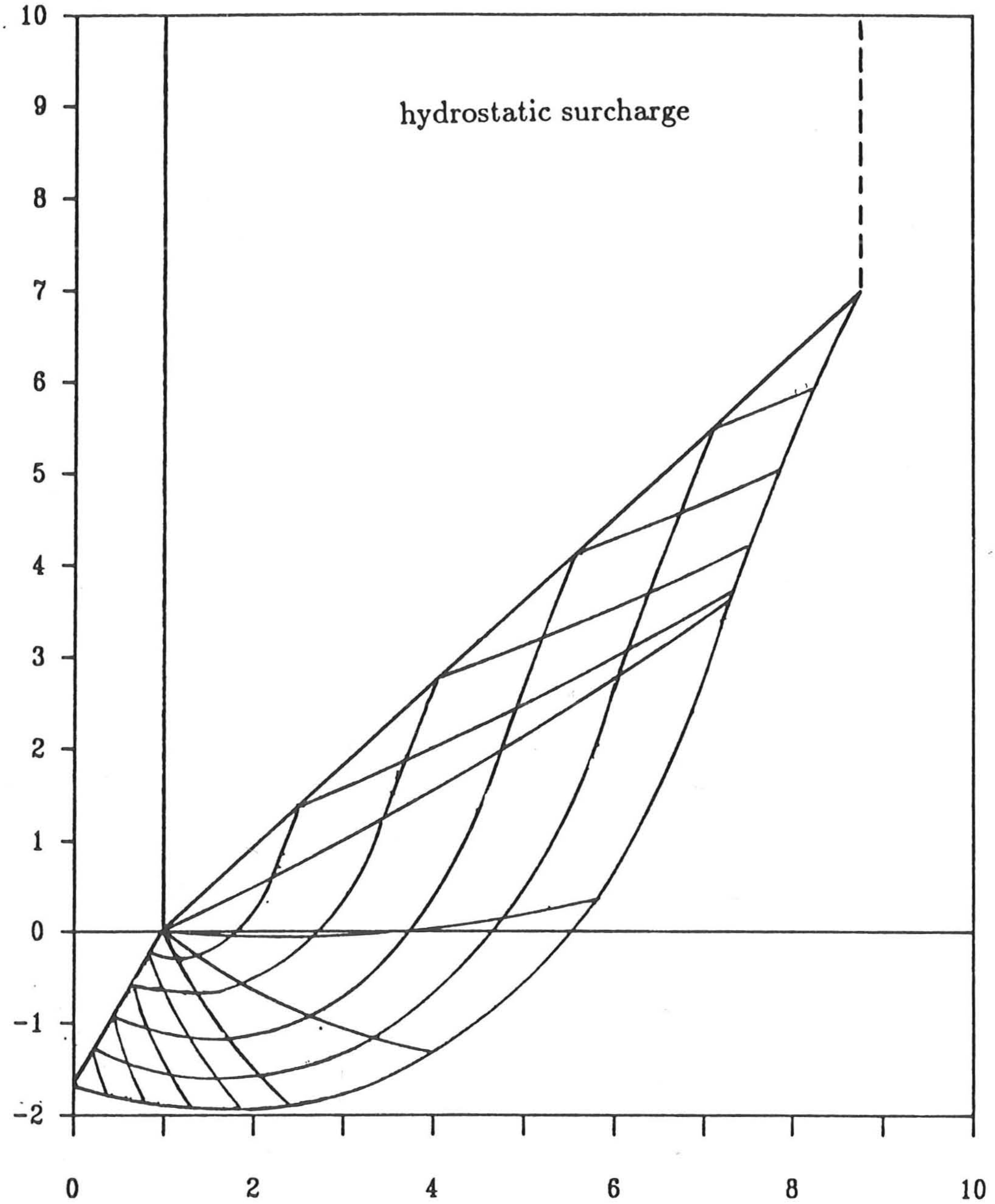

Fig (5.12)c Variable $\phi_p=46^\circ, \phi_{cr}=32^\circ$ D/B=10 $\delta=21^\circ$

Fig 5.12 Stress characteristics net with penetration effect for test T25 (Axisymmetric case)

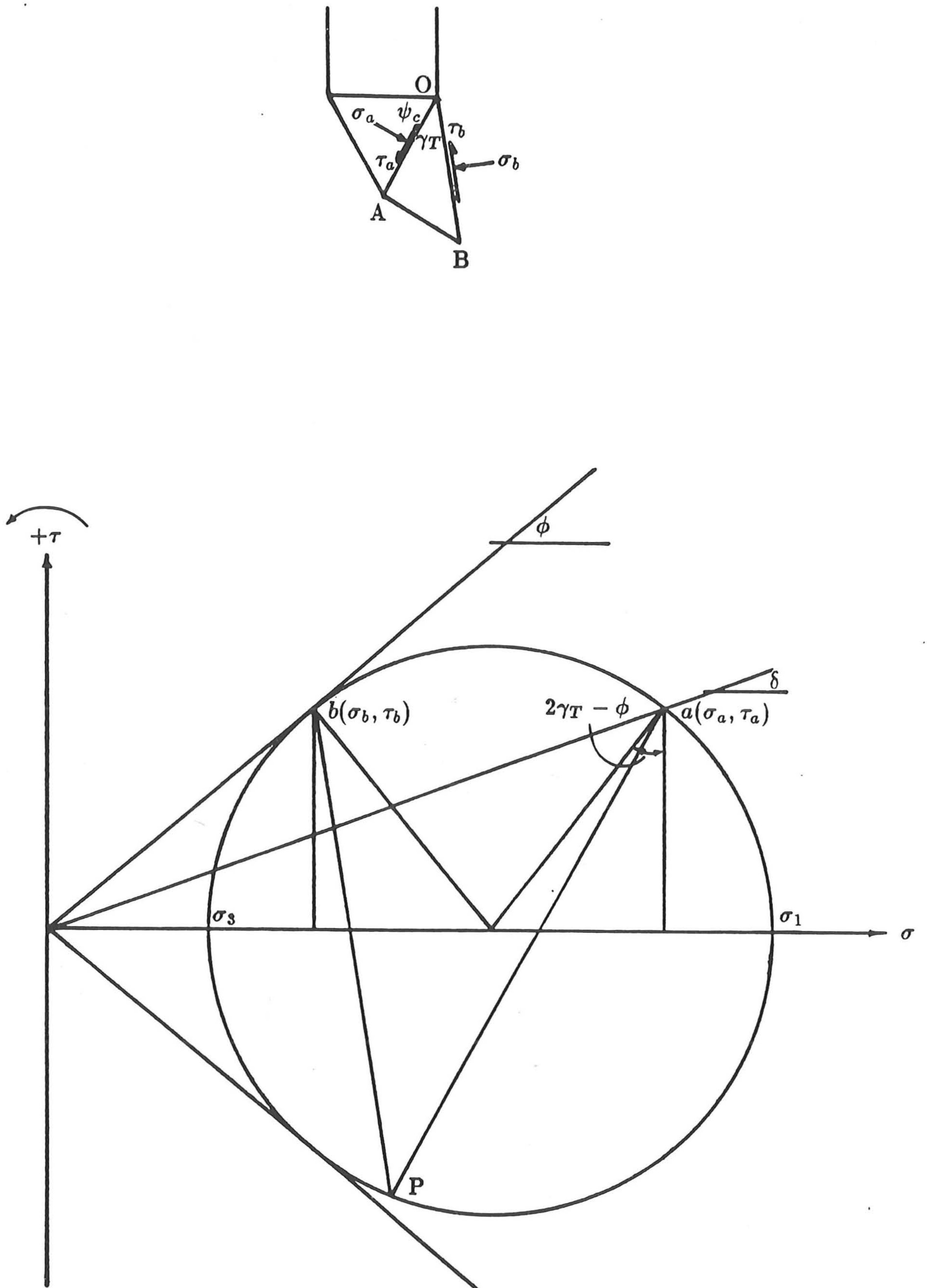

Fig 5.13 Mohr circle to determine angle γ_T.

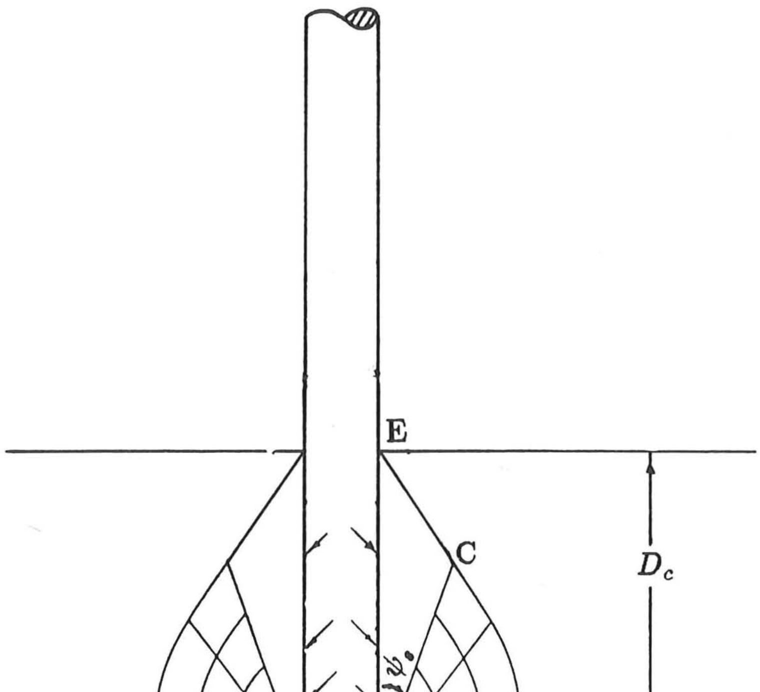

Fig 5.14 Definition of characteristic depth.

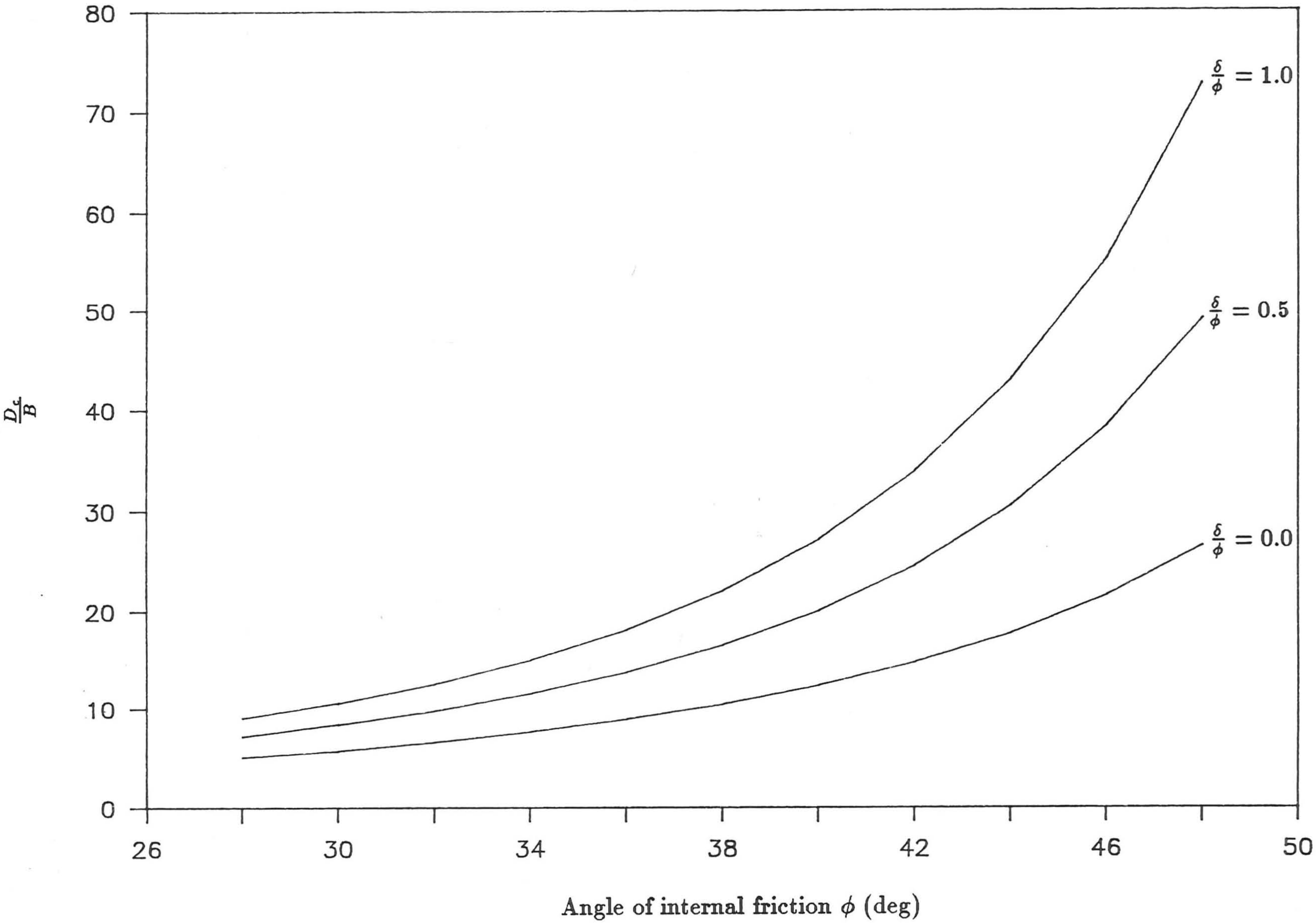

Fig 5.15 Values of $\frac{D_c}{B}$ for a given $\frac{\delta}{\phi}$ and ϕ.

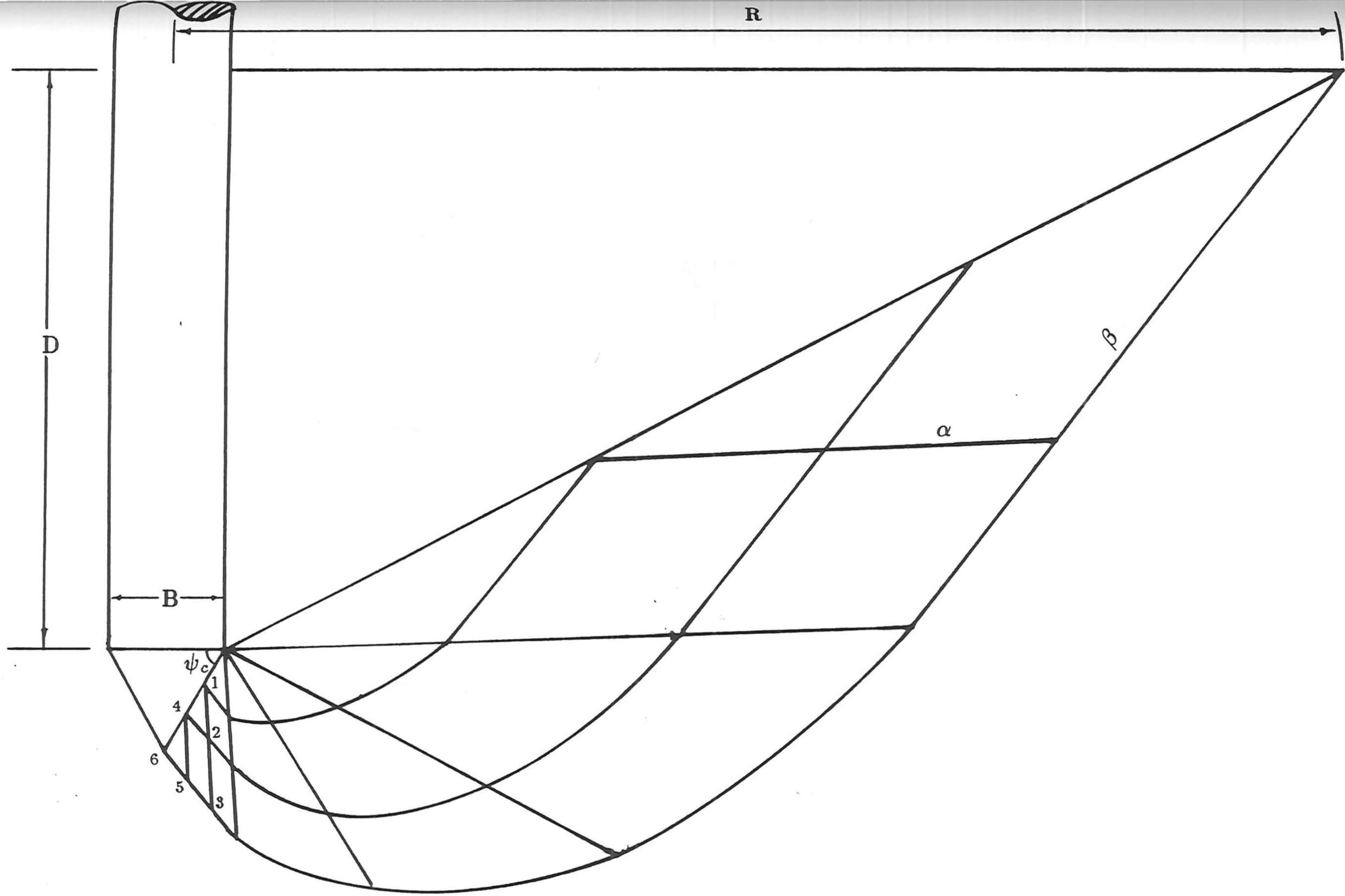

Fig 5.16 Example of stress characteristics net.
$(\frac{D}{B} = 5, \frac{\delta}{\phi} = 0.5, \phi = 40°)$.

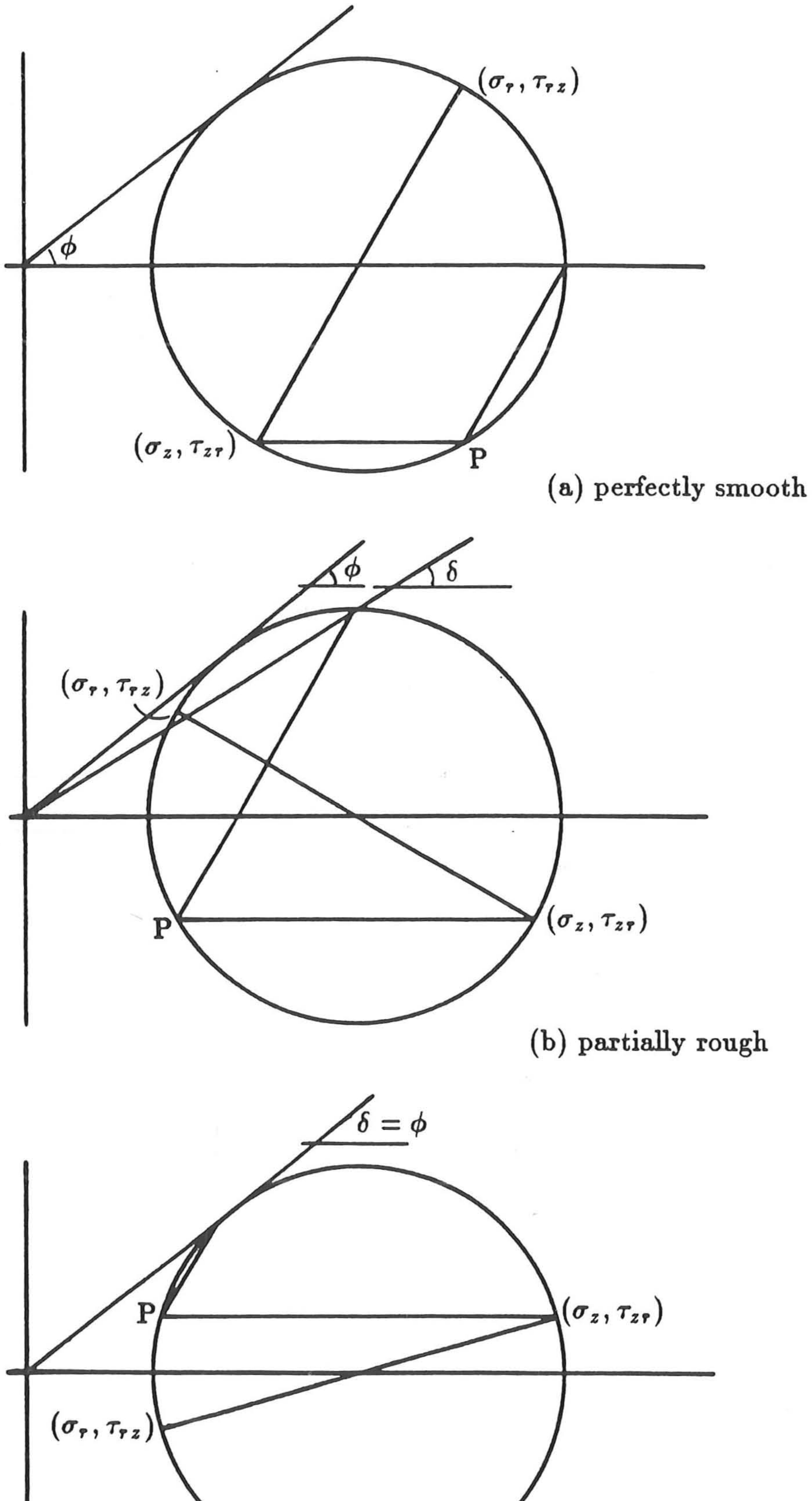

(a) perfectly smooth

(b) partially rough

(c) perfectly rough

Fig 5.17 Change of stress components on the Mohr circle for different roughness.

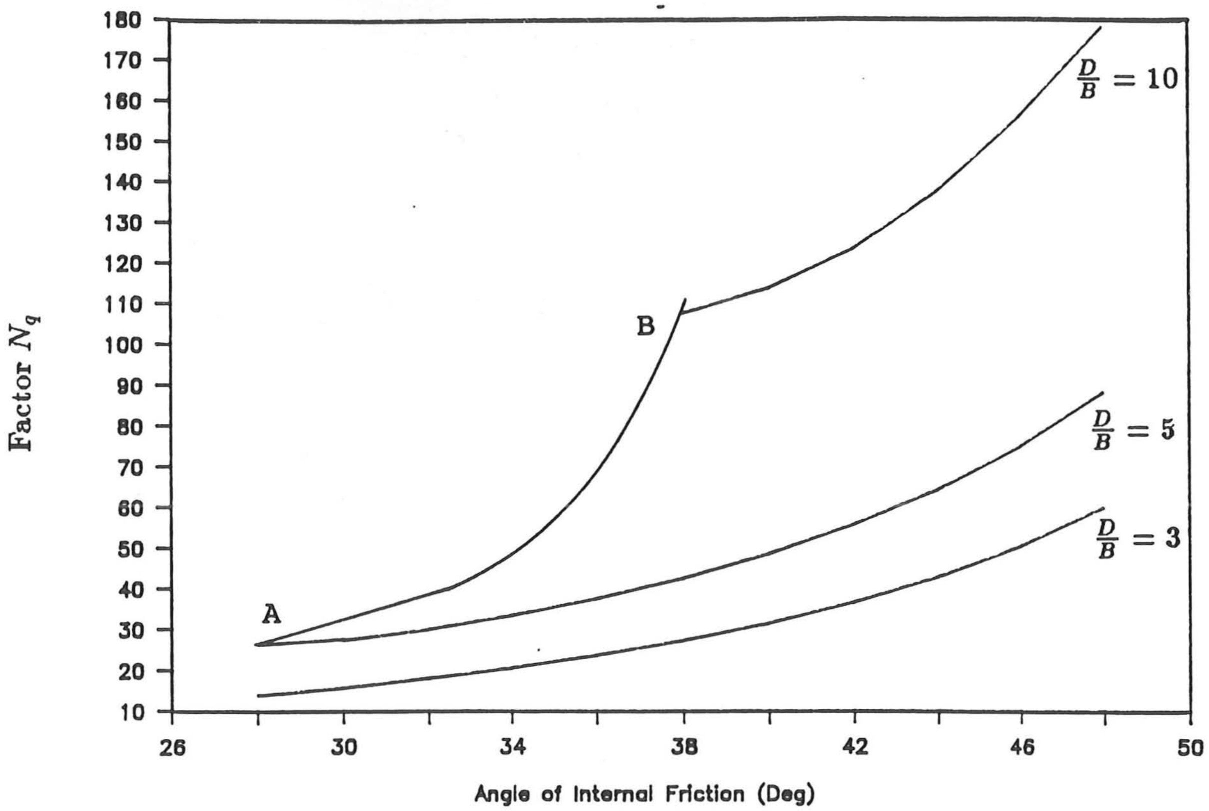

Fig 5.18 (a) Perfectly smooth $\frac{\delta}{\phi} = 0$.

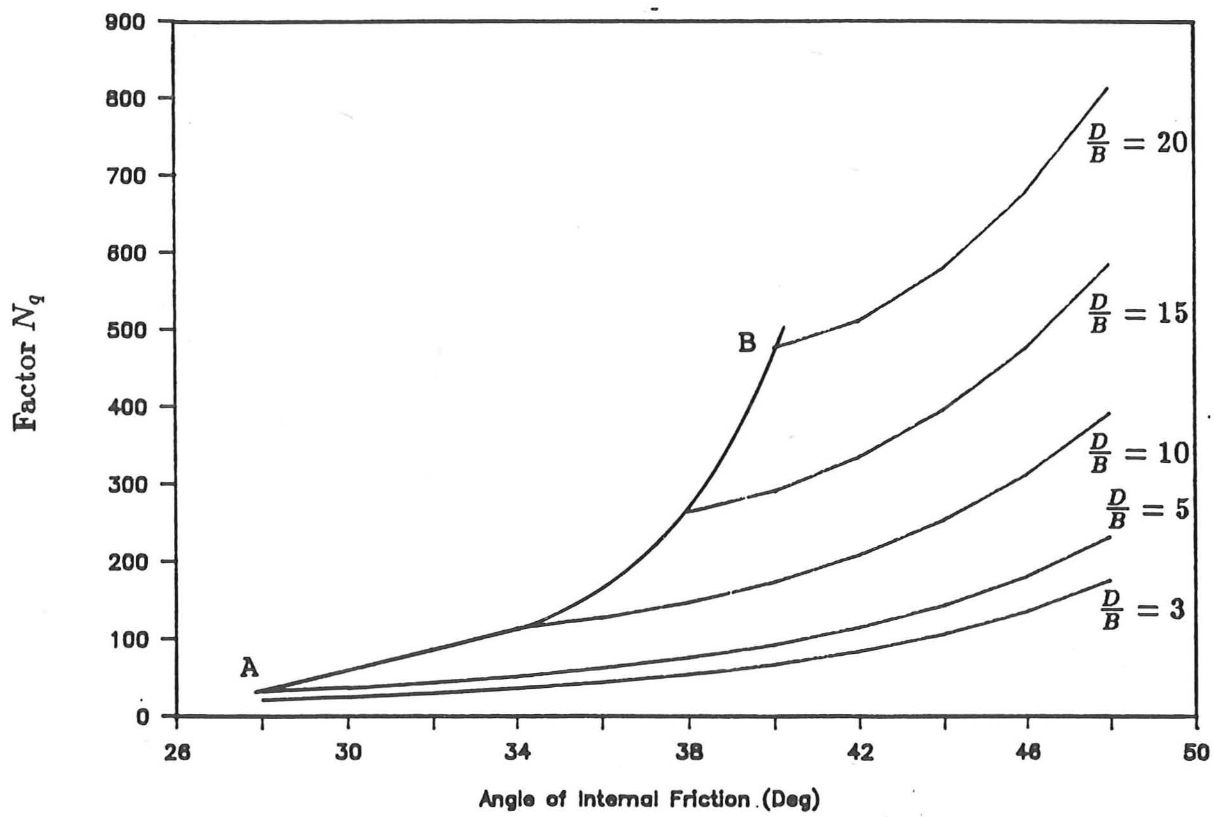

Fig 5.18(b) Partially rough $\frac{\delta}{\phi} = 0.5$

Fig 5.18 Relationship between bearing capacity factors N_q, relative depth $\frac{D}{B}$ and ϕ_{pc} from method of characteristics (Plane strain case).

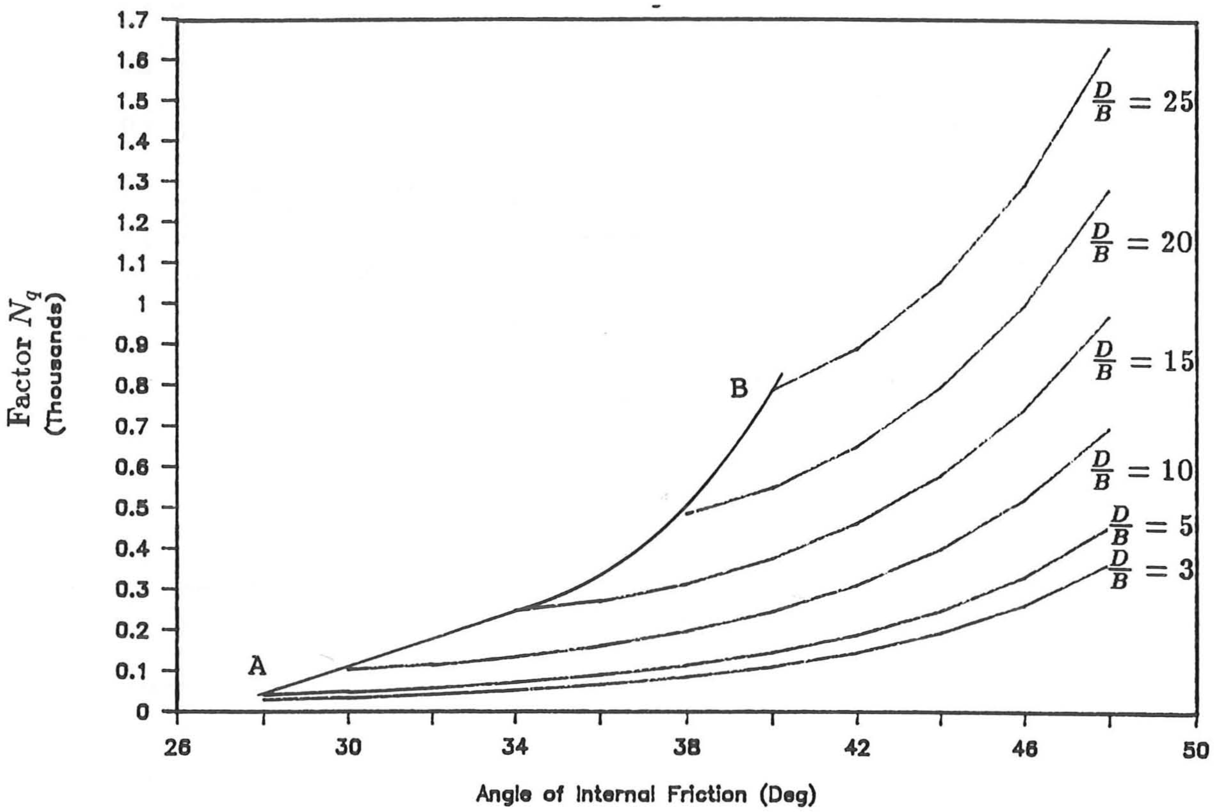

Fig 5.18(c) Perfectly rough $\frac{\delta}{\phi} = 1.0$

Fig 5.18 Relationship between bearing capacity factors N_q, relative depth $\frac{D}{B}$ and ϕ_{pc} from method of characteristics (Plane strain case).

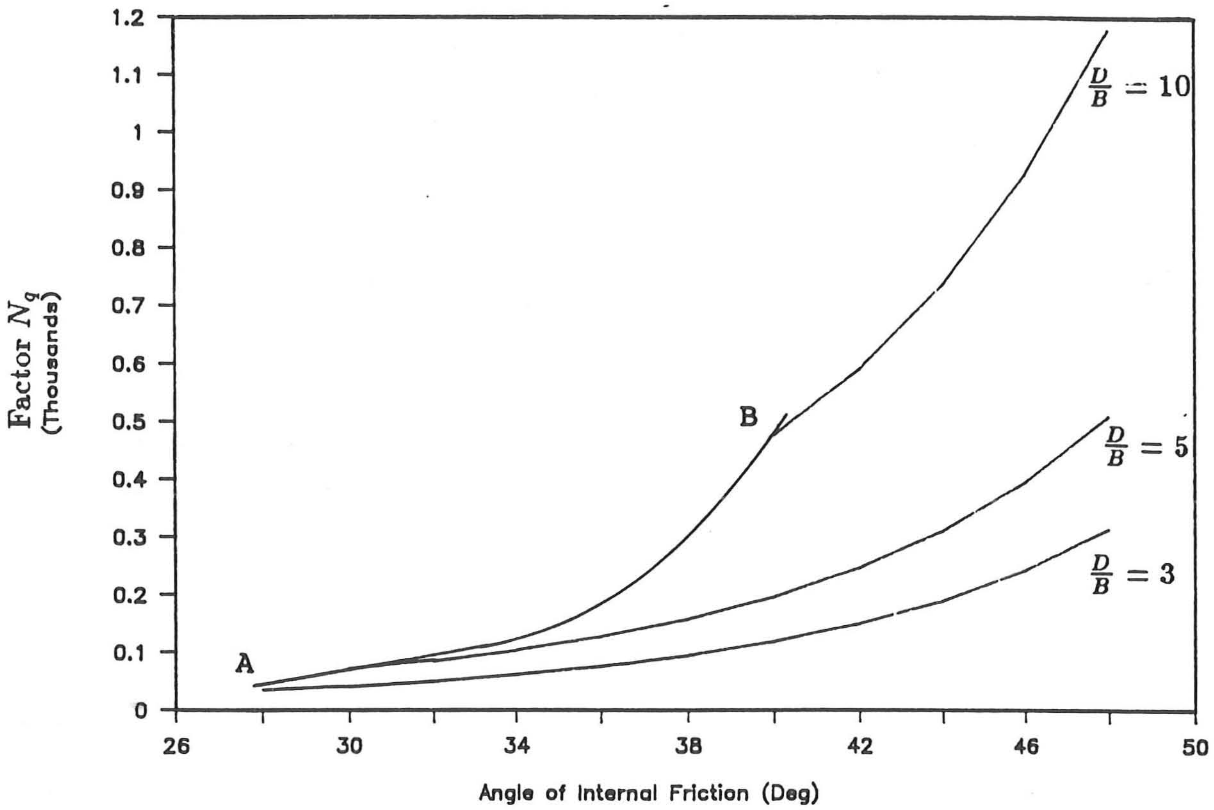

Fig 5.19(a) Perfectly smooth $\frac{\delta}{\phi} = 0$.

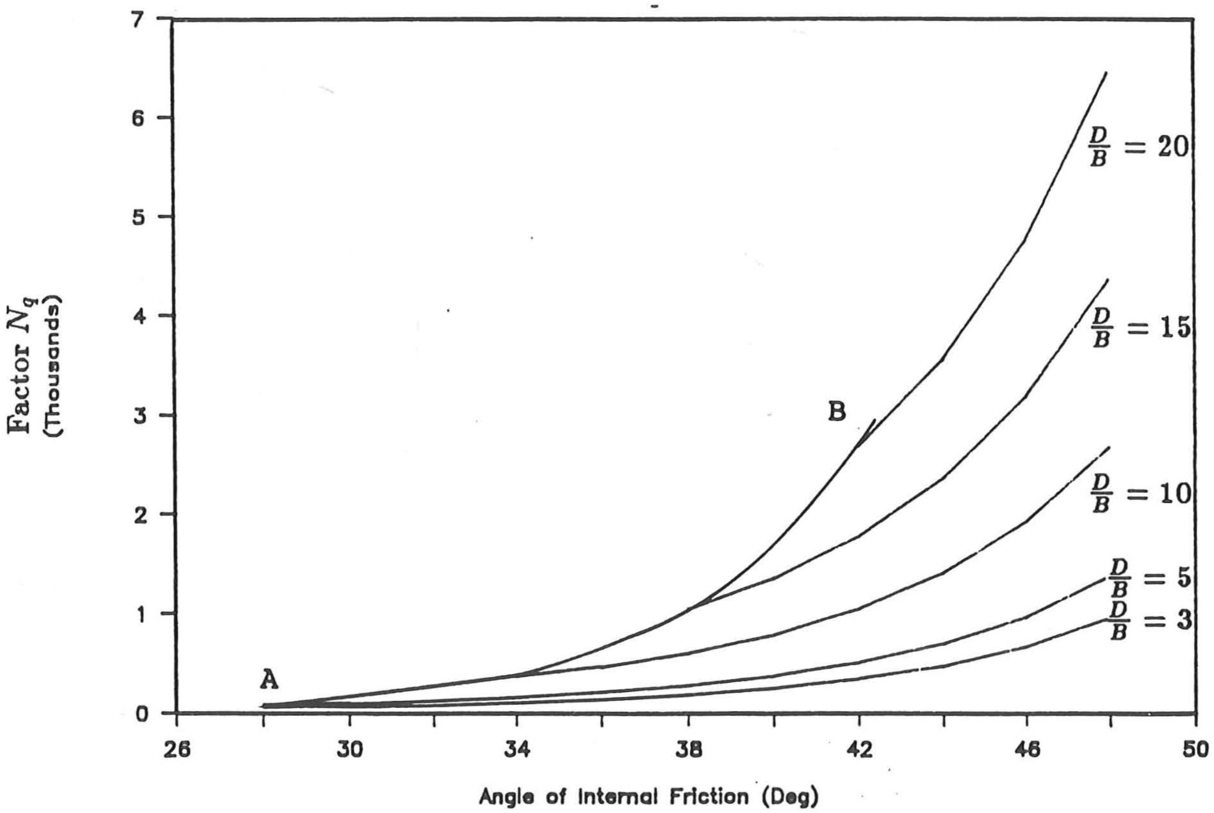

Fig 5.19(b) Partially rough $\frac{\delta}{\phi} = 0.5$

Fig 5.19 Relationship between bearing capacity factors N_q, relative depth $\frac{D}{B}$ and ϕ_{pc} from method of characteristics (axisymmetric case).

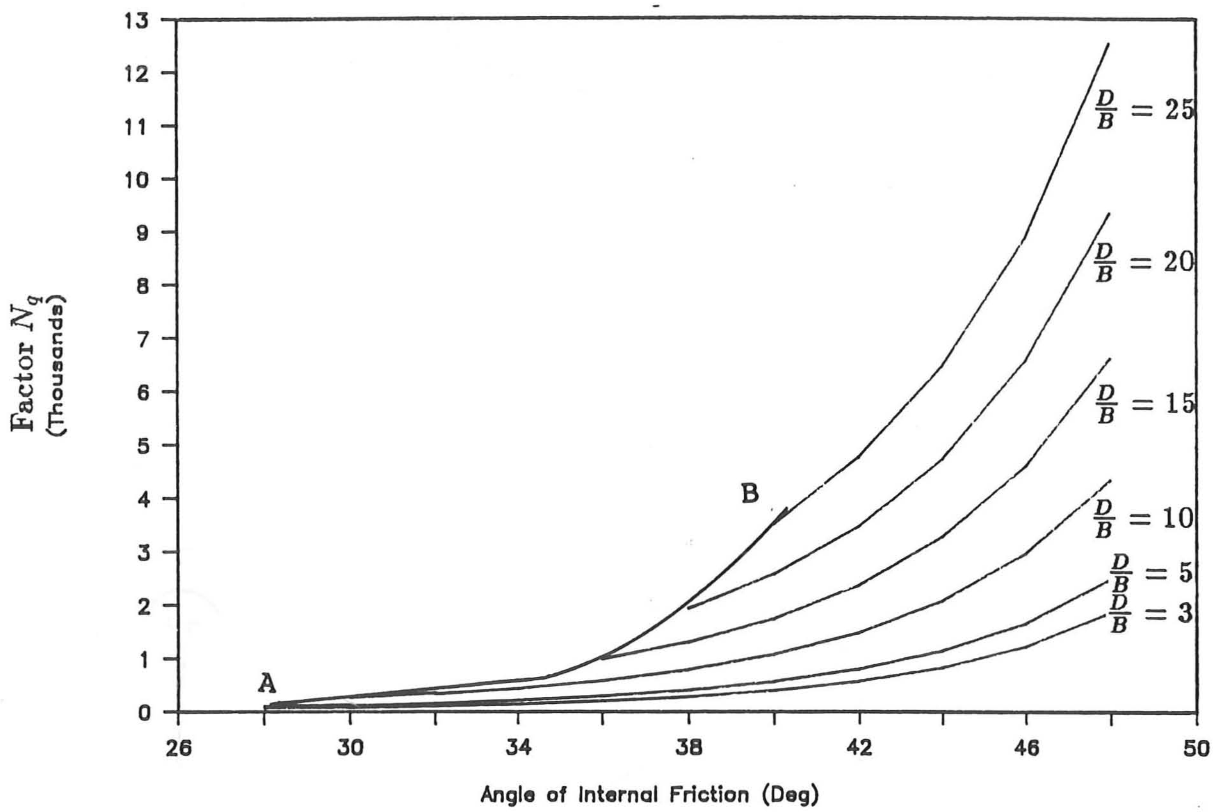

Fig 5.19(c) Perfectly rough $\frac{\delta}{\phi} = 1.0$

Fig 5.19 Relationship between bearing capacity factors N_q, relative depth $\frac{D}{B}$ and ϕ_{pc} from method of characteristics (axisymmetric case).

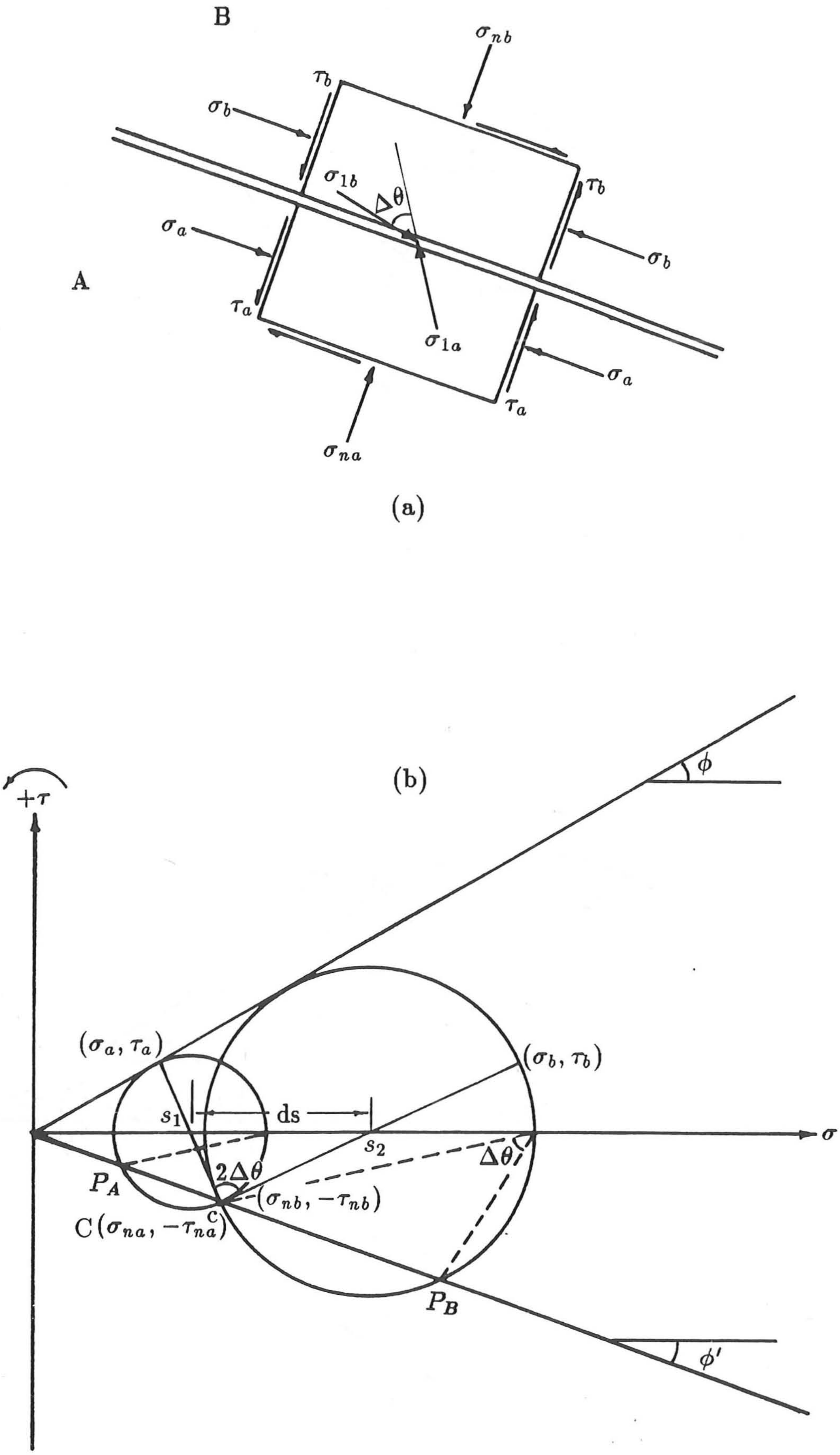

Fig 5.20 Directions of major principal stress across a discontinuity.

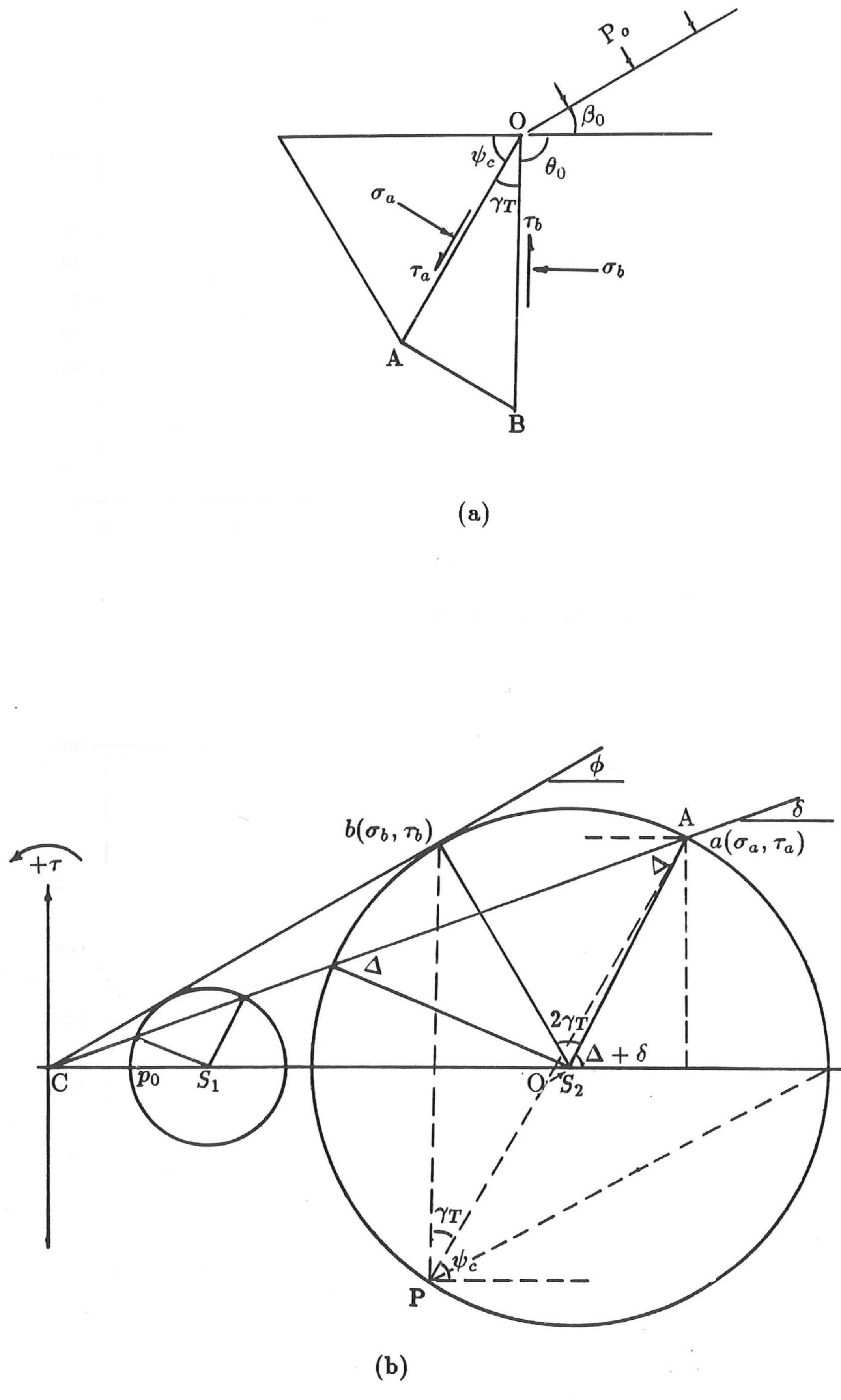

Fig 5.21 Change of stress across a fan of discontinuities.

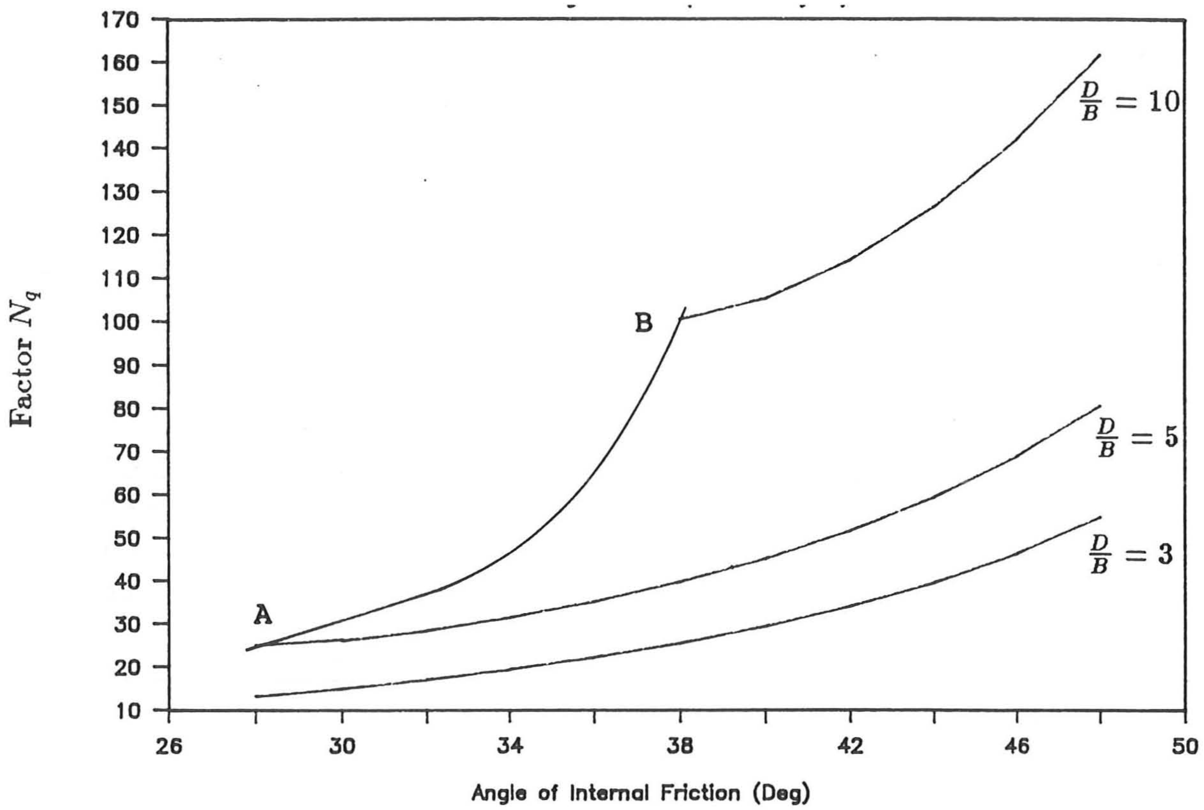

Fig 5.22 (a) Perfectly smooth $\frac{\delta}{\phi} = 0$.

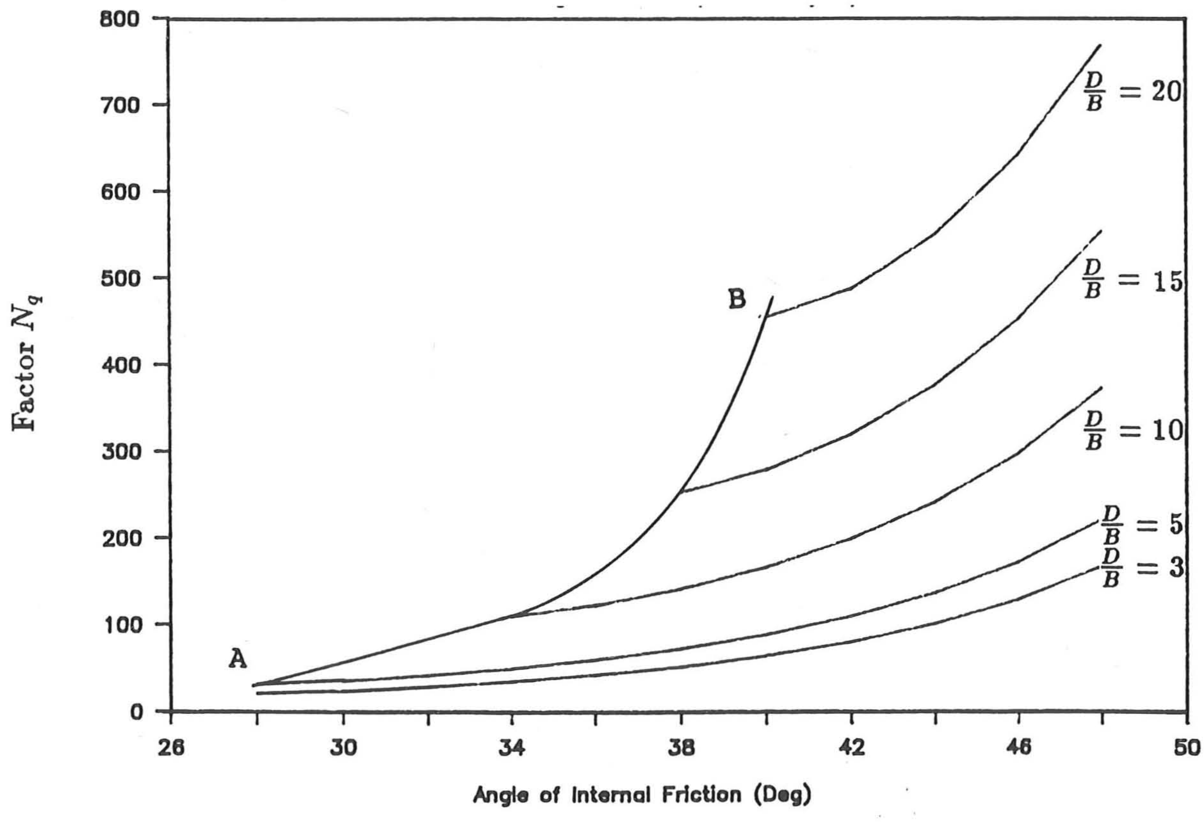

Fig 5.22 (b) Partially rough $\frac{\delta}{\phi} = 0.5$

Fig 5.22 Relationship between bearing capacity factors N_q, relative depth $\frac{D}{B}$ and ϕ_{pc} from limit analysis (Plane strain case).

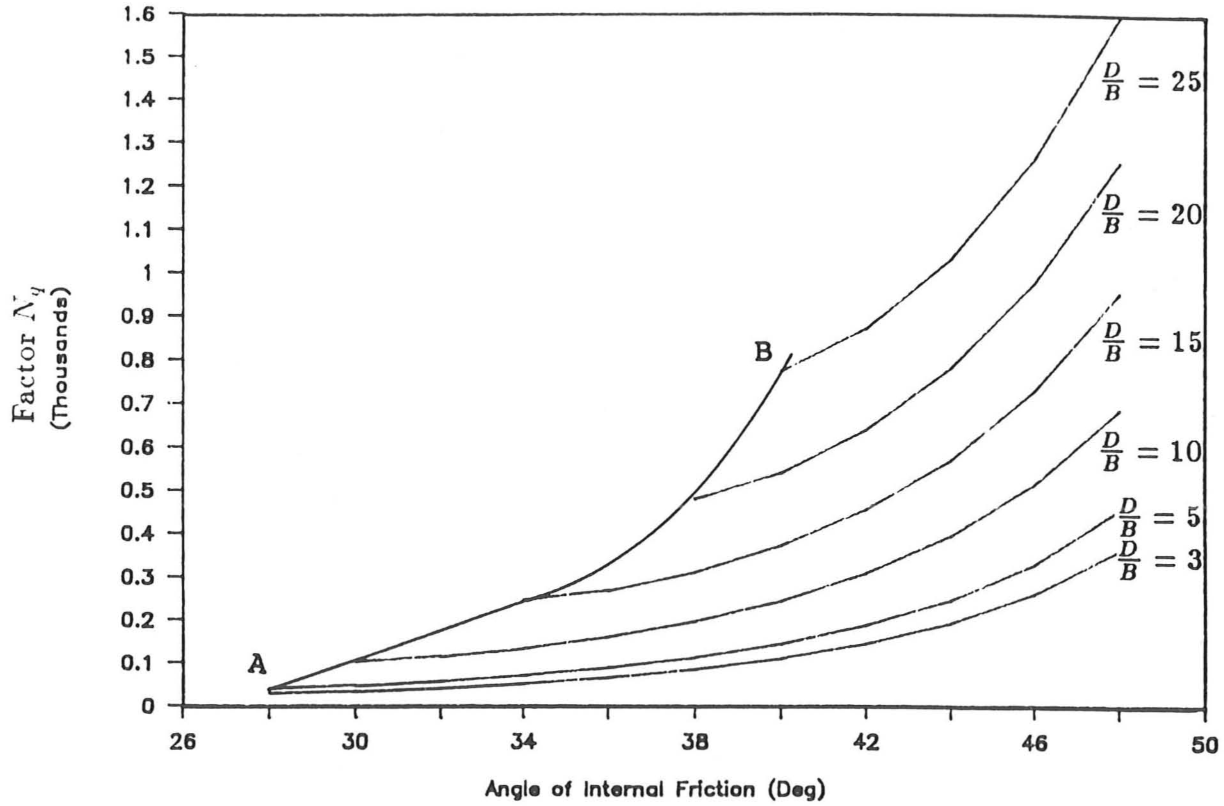

Fig 5.22(c) Perfectly rough $\frac{\delta}{\phi} = 1.0$

Fig 5.22 Relationship between bearing capacity factors N_q, relative depth $\frac{D}{B}$ and ϕ_{pc} from limit analysis (Plane strain case).

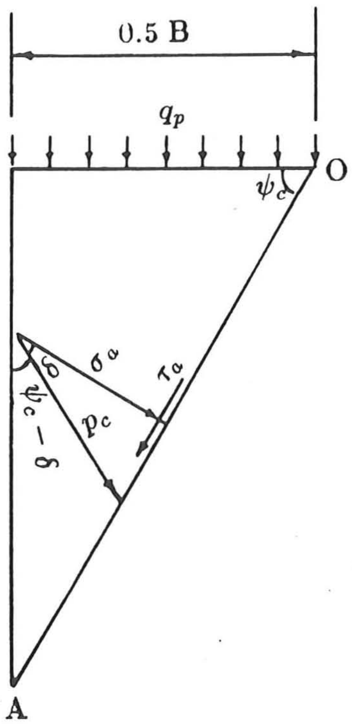

Fig 5.23 Equilibrium of forces.

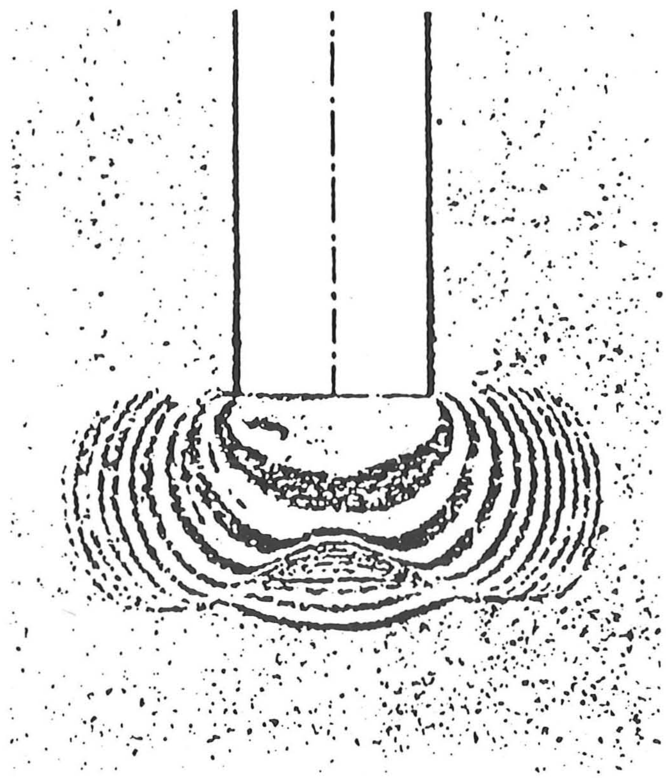

Fig 6.1 Failure patterns under pile point
(after Vesic, 1977).

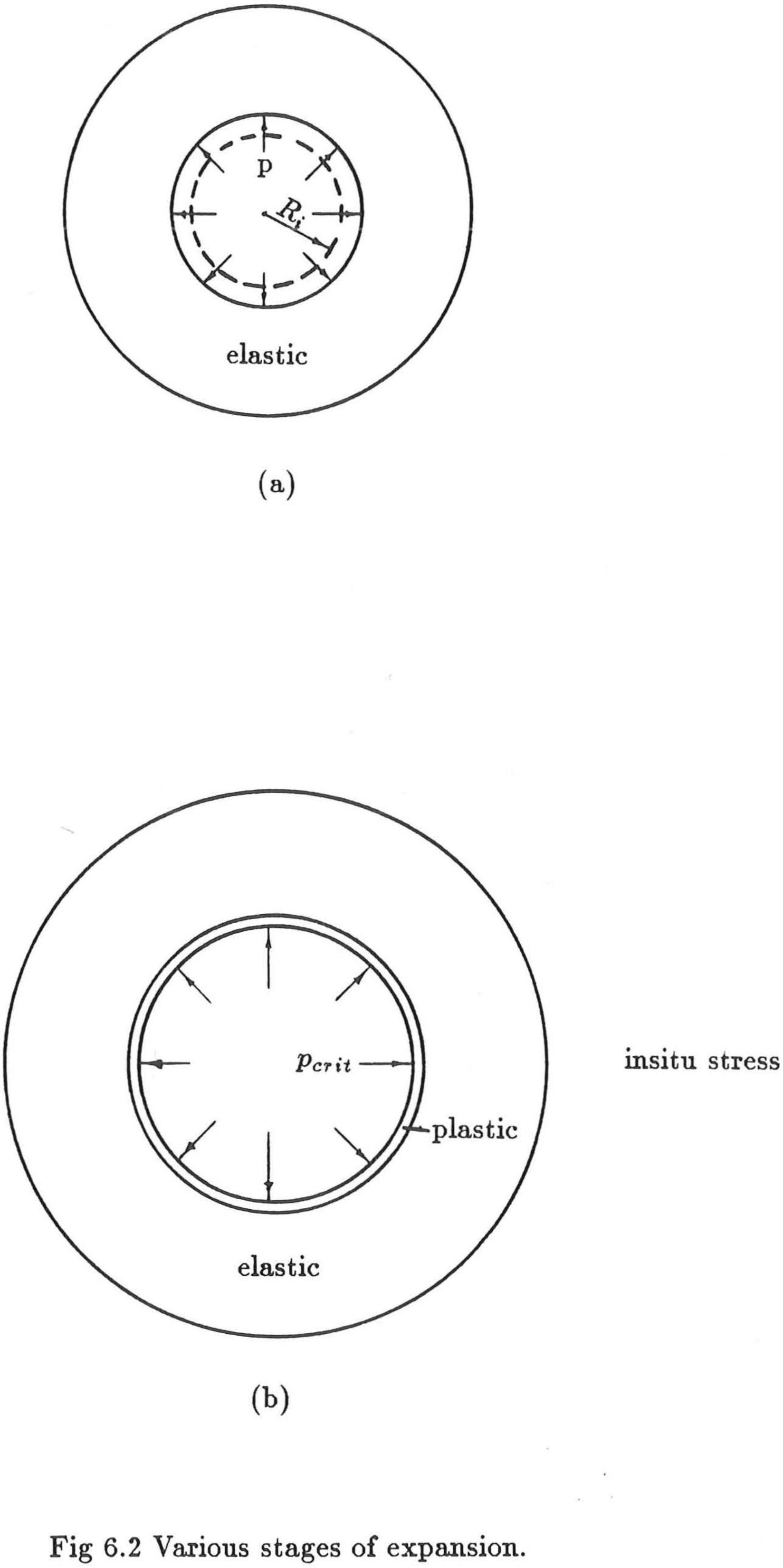

Fig 6.2 Various stages of expansion.

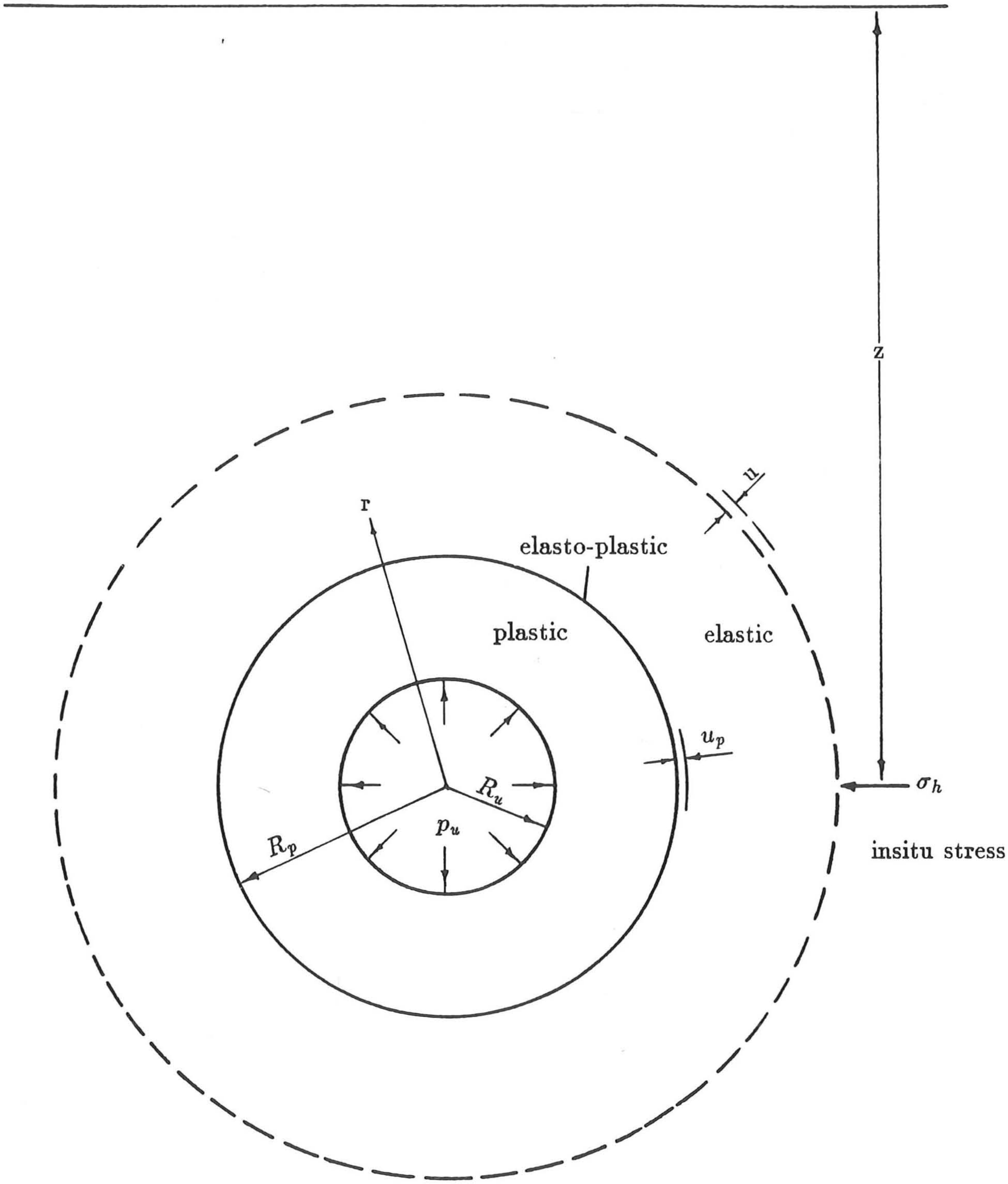

Fig 6.3 The expanding cavity.

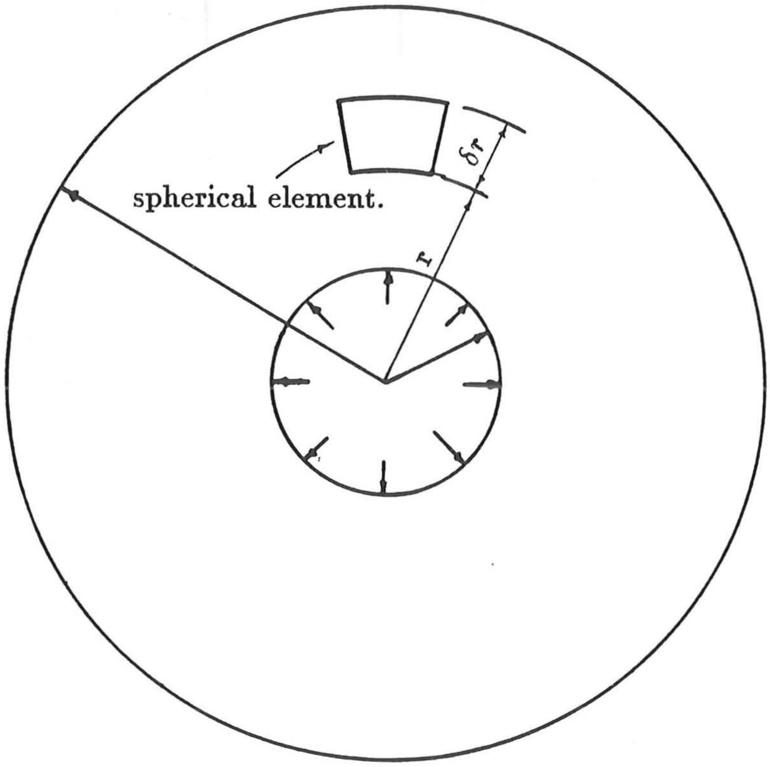

(a)

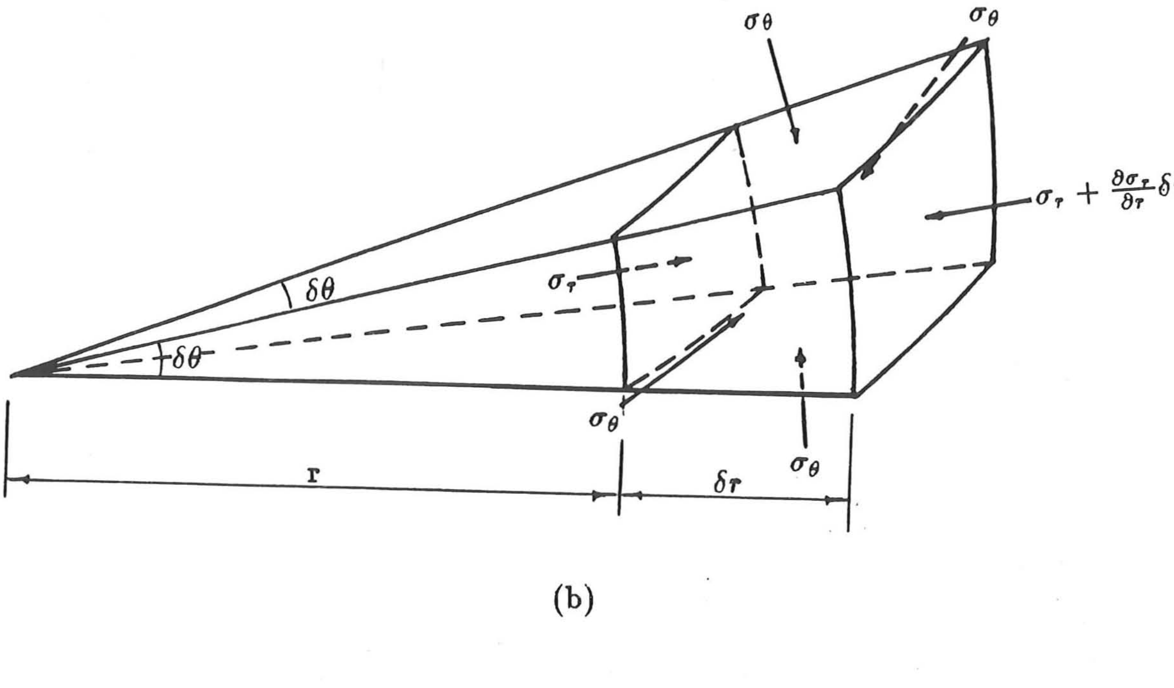

(b)

Fig 6.4 Stress components of a spherical element.

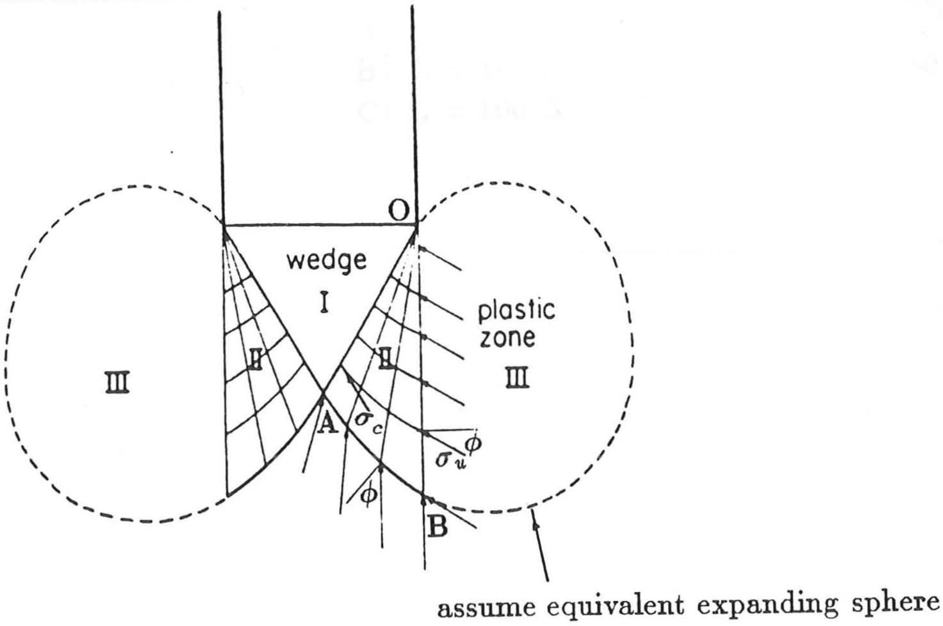

Fig 6.5 Assumed failure pattern under pile point.
(after Vesic, 1977)

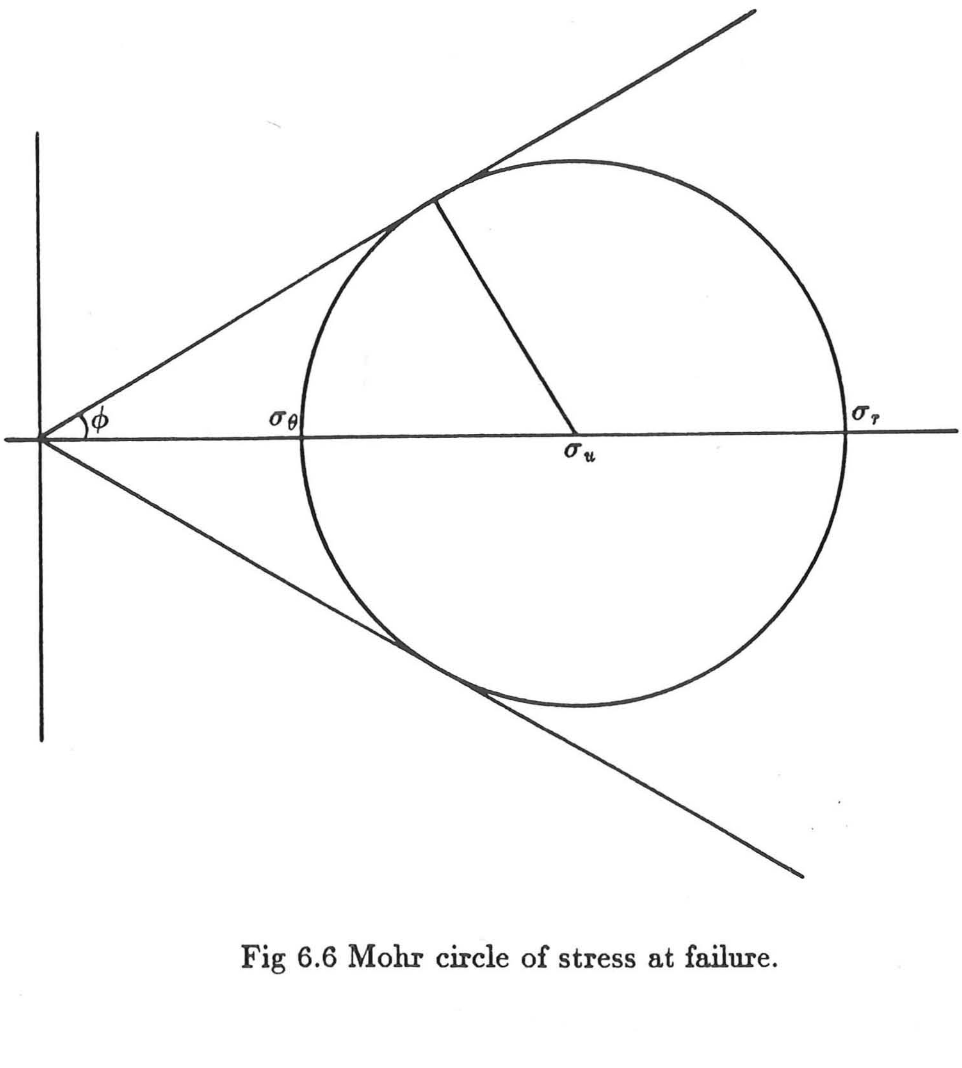

Fig 6.6 Mohr circle of stress at failure.

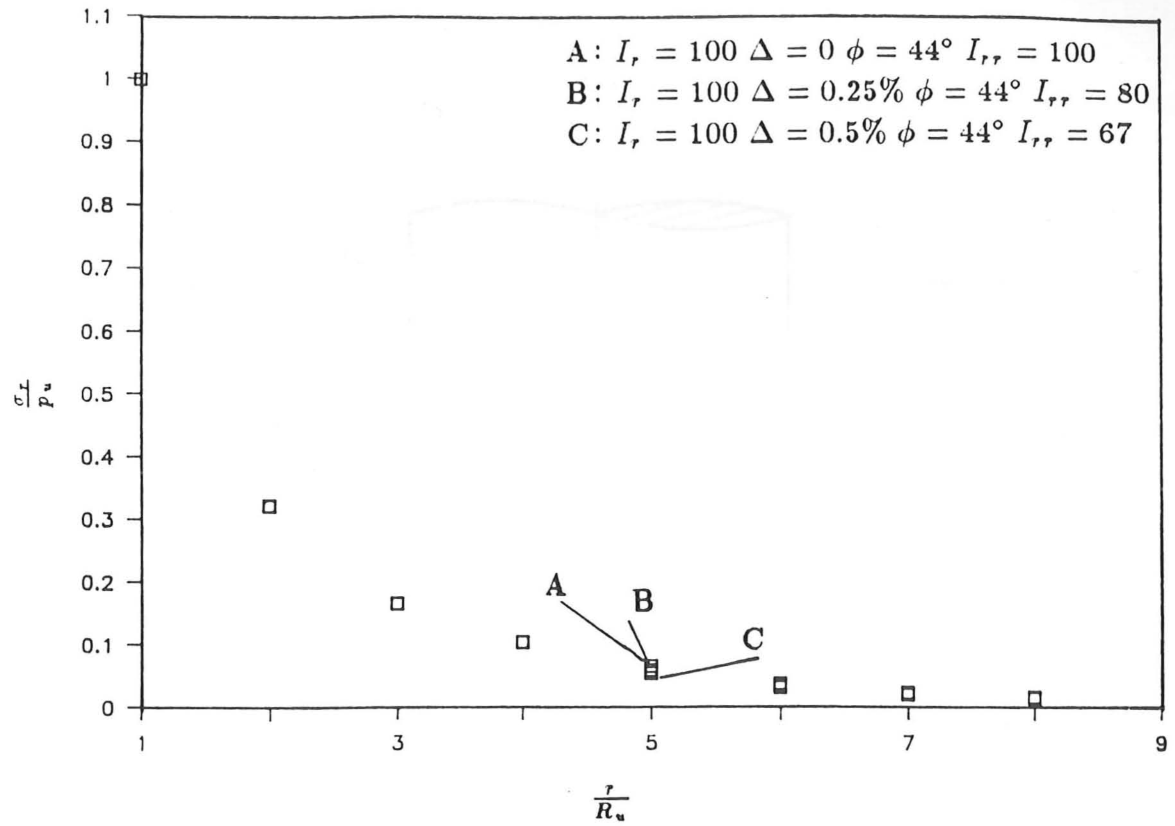

Fig 6.7 Variation of radial stress σ_r with radius r.

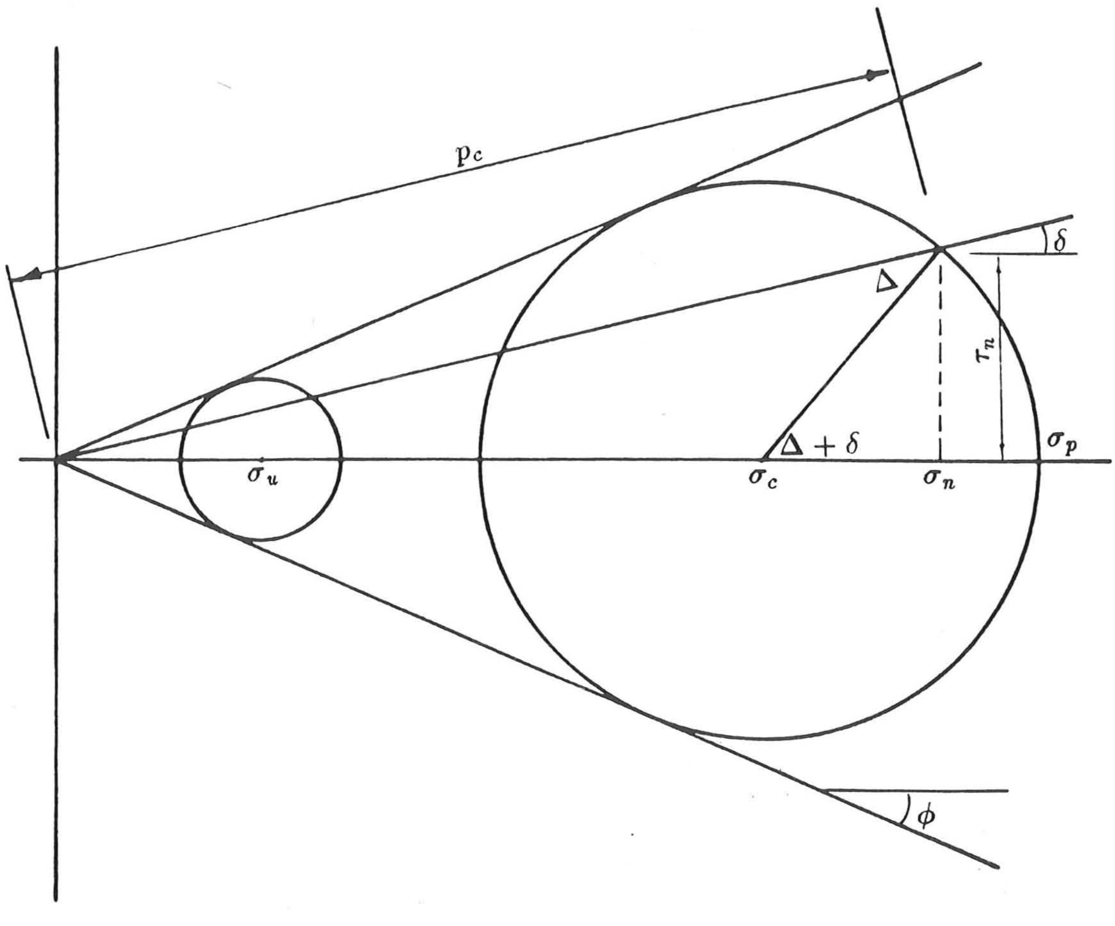

Fig 6.8 Mohr circle of stress.

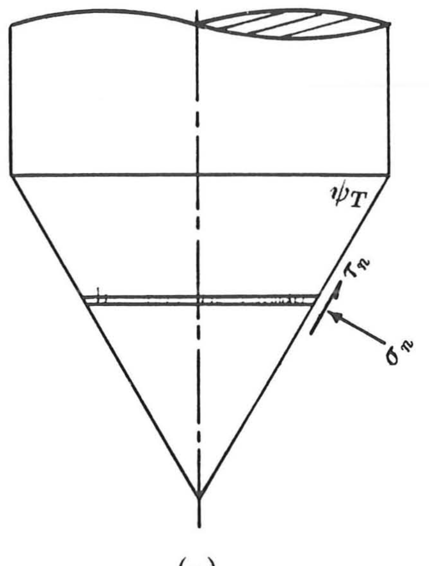

(a)

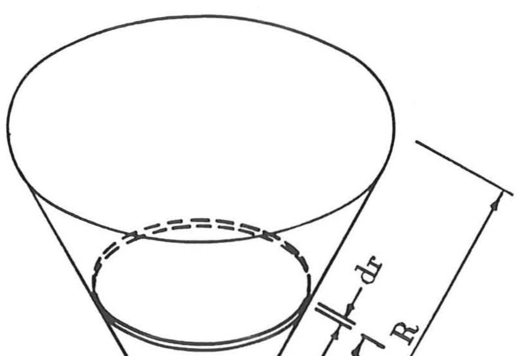

(b)

Fig 6.9 Equilibrium of forces.